PhD Dissertation

Electrochemical Model-Based Advanced Battery Control Systems

Eduardo Miguel

Director: Unai Iraola
Co-Director: Emilie Bekaert

Mondragon Goi Eskola Politeknikoa
Electronics and Computing Department

CiC Energigune
Structure & Surface Analysis Departament

January 14, 2020

Electrochemical Model-Based Advanced Battery Control Systems

Eduardo Miguel

Director: Unai Iraola
Mondragon Goi Eskola Politeknikoa
Electronics and Computing Department

Co-Director: Emilie Bekaert
CiC Energigune
Structure & Surface Analysis Departament

Submitted in partial fulfilment of the requirements
for the Degree of Doctor of Philosophy under the program:
Mechanical and Electrical Energy Engineering

Thesis Committee:
President: Dr. Gregory L. Plett (University of Colorado Colorado Springs)
Vocal: Dr. M. Scott Trimboli (University of Colorado Colorado Springs)
Vocal: Dr. Mikel Oyarbide Urquizu (CIDETEC)
Vocal: Dr. Egoitz Martinez-Laserna (IKERLAN)
Secretary: Dr. Iosu Aizpuru Larrañaga (Mondragon Unibertsitatea)

January 14, 2020

Abstract

Nowadays energetic scenario is changing, improving the actual energy mix, and using cleaner and more sustainable energy generation and consumption methods. Renewable energies are key within this context for a more environmentally friendly energy generation. The intermittent nature of these energy sources boost the use of energy storage systems. A more efficient energy consumption is also a benefit of the energy storage system since the energy generation does not need to instantly feed the demand.

Li-ion batteries are one of the most promising technology in the market, but the price per Wh and the aging of these devices are crucial for their integration. Different methods are considered to control or mitigate batteries aging, nonetheless advanced control system will enable further improvements and optimal battery utilization.

This thesis is based on the hypothesis that **aging of batteries can be controlled using physics based state of function control embedded systems**, that will enable the concept of a dynamic safe operating area. Something that will open the door to more optimized and advanced battery management.

Laburpena

Gaur egun agertoki energetikoa aldatzen ari da, mix energetikoa hobetzen eta energia sortzeko zein kontsumitzeko metodo garbiagoak nahiz iraunkorragoak erabiltzen ari dira. Testuinguru horretan, energia berriztagarriak funtsezkoak dira ingurumenarekiko errespetu handiagoa izateko. Aipatu energia iturri berriztagarrien aldizkako izaerak energia biltegiratzeko sistemen erabilera bultzatzen duela. Gainera, energia-kontsumo eraginkorragoa bermatzen dute, energia sorgailuak ez duelako zertan eskaria berehala elikatu behar.

Li-ion bateriak merkatuan teknologiarik itxaropentsuenetarikoak dira, baina Wh bakoitzaren prezioa eta gailu horien zaharkitzea funtsezkoak dira haien integraziorako. Baterien zaharkitzea kontrolatzeko edota arintzeko metodo desberdinak daude. Hala ere, kontrol sistema aurreratuak hobekuntza gehiago eskaini eta baterien erabilera hobea ahalbidetuko dute.

Tesi honen hipotesi nagusia da **fisikan oinarritutako modeloz osaturiko egoera kontrol sistema txertatuekin baterien zaharkitzea kontrola daitekeela**, funtzionamendu eremu seguru dinamikoaren kontzeptua ahalbidetuz eta metaketa sistemen kudeaketa optimizatuagoei eta aurreratuagoei ateak irekiz.

Resumen

Hoy en día, el escenario energético está cambiando, mejorando el mix energético y utilizando métodos de generación y consumo de energía más limpios y sostenibles. Las energías renovables son clave en este contexto para una generación de energía más respetuosa con el medio ambiente. La naturaleza intermitente de estas fuentes de energía impulsa el uso de sistemas de almacenamiento de energía. Siendo un consumo de energía más eficiente también un beneficio derivado del uso de sistemas de almacenamiento de energía, ya que la energía no ha de ser forzosamente generada en el mismo instante en que se demanda.

Las baterías de iones de litio son una de las tecnologías más prometedoras del mercado, siendo el precio por Wh y el envejecimiento de estos dispositivos cruciales para su integración. Se pueden considerar diferentes métodos para controlar o mitigar el envejecimiento de las baterías, sin embargo, los sistema de control avanzado permitirán mejoras adicionales y la utilización óptima de las baterías.

Esta tesis se basa en la hipótesis de que **el envejecimiento de las baterías se puede controlar utilizando sistemas embarcados de control del estado basados en modelos electroquímicos**, que permitirán validar el concepto de un área de operación dinámica segura. Algo que abrirá la puerta a una gestión de las baterías más optimizada y avanzada.

Acknowledgments

Han sido muchos los años transcurridos desde el inicio de mi carrera académica hasta escribir esta tesis, a lo largo de los cuales he tenido la gran suerte de contar con el apoyo y la ayuda de mucha gente a la que me gustaría agradecérselo en estas líneas.

Primero me gustaría agradecer a Jon Andoni Barrena y a José Mª Canales la confianza que depositaron en mi cuando me brindaron la oportunidad de realizar esta tesis. Habéis sido una guía a lo largo del proceso, haciéndome crecer como investigador y a nivel personal.

A mi director de tesis Unai Iraola, por toda la paciencia y buen hacer en la tarea de acompañarme y guiarme día a día durante estos años. Por reforzar mi ideal de ética laboral desde el ejemplo. Durante este viaje has sido capaz de enseñarme a ver las tareas de investigación y el trabajo en general desde una óptica personal diferente, haciéndome evolucionar en lo profesional y personal. Aunque no siempre haya sido fácil has conseguido hacer más de lo que se te podía pedir.

A todo el departamento de electrónica de Mondragon Unibertsitaea, desde Igor Baraia que me inició en el mundo de la investigación hasta todos los compañeros a los que he ido conociendo, y que he tenido el placer de trabajar con ellos: Iosu, Txejo, Iratxo, Txef, Ander, Julen, Imanol, Santiso, Carlos, Garrido, Manex, Edurne, Dani...

I also would like to thank CICenergigune and specially Emilie Bekaert for all the new knowledge that was completely out of my initial scope. That made possible to link two different research worlds, and make me a more complete researcher. To the people there: Oier, Jon, Ane, Itziar, Maria, Begoña, Asier, Ander, Fred...

Thanks to the battery modeling team at UCCS for their help: Gregory, Scott, Albert...

Esta tesis no habría sido lo mismo sin Eneko y Laura, habéis sido dos soportes en todos los aspectos además de unos compañeros “geniales”. Espero seguir trabajando con vosotros muchos años. Laura, Eneko, Iñigo, Iker una parte de esta tesis también es vuestra.

Milesker lagunei betidanik nirekin egoteagatik eta elektronikari buruzko elkarrizketa guztiak jasan izateagatik: Egoitz, Gorka, Joseba, Eneko, Jokin...

Milesker Maddalen, zurekin tesiko momenturik gogorrenak ez zirelako hain gogorak izan, bulegotik ateratzean afaria geneukan eta.

A Casimiro por fomentar el gusto por las cosas bien hechas desde que era muy joven.

Por último, pero desde luego no menos importante, quiero agradecer a mis padres el apoyo no solo a la hora de realizar esta tesis, sino el haber sido el impulso y el soporte de toda mi carrera académica. Esto es solo una pequeña muestra del resultado de vuestro esfuerzo, no habría llegado a ser quien soy en ningún aspecto sin vuestra ayuda.

Contents

Abbreviations

ADC	**A**nalog to **D**igital **C**onverter
BCI	**B**est **C**ondition for **I**dentification
BMS	**B**attery **M**anagement **S**ystem
BPC	**B**est **P**racticable **C**ondition
CAES	**C**ompressed **A**ir **S**torage
CFC	**C**hlorofluorocarbons
DAE	**D**ifferential **A**lgebraic **E**quation
DFT	**D**ensity **F**unctional **T**heory
DMC	**D**imethyl **C**arbonate
DOD	**D**epth **O**f **D**ischarge
DRA	**D**iscrete time **R**ealization **A**lgorithm
EC	**E**thylene **C**arbonate
EDX	**E**nergy **D**ispersive **X**-ray spectroscopy
EIS	**E**lectrochemical **I**mpedance **S**pectroscopy
EMC	**E**thyl **M**ethyl **C**arbonate
ESS	**E**nergy **S**torage **S**ystem
FEM	**F**inite **E**lement **M**ethod
GITT	**G**alvanostatic **I**ntermittent **T**itration **T**echnique
ICSD	**I**norganic **C**rystal **S**tructure **D**atabase
MOA	**M**ulti-**O**ptimization **A**nalysis
MOGA	**M**ulti **O**bjective **G**enetic **A**lgorithm
MTTF	**M**ean **T**ime **T**o **F**ailure
NMP	**N**-**M**ethyl **P**yrrolidone

NMR	**N**uclear **M**agnetic **R**esonance
OCV	**O**pen **C**ircuit **V**oltage
P2D	**P**seudo **T**wo **D**imensional (model)
PDAE	**P**artial **D**ifferential **A**lgebraic **E**quation
PDE	**P**artial **D**ifferential **E**quation
PI	**P**roportional **I**ntegral
PSA	**P**article **S**ize **A**nalyzer
PWM	**P**ulse **W**idth **M**odulation
ROM	**R**educed **O**rder **M**odel
SEI	**S**olid **E**lectrolyte **I**nterphase
SEM	**S**canning **E**lectron **M**icroscopy
SOA	**S**ingle-**O**ptimization **A**nalysis / **S**afety **O**peration **A**rea
SOC	**S**tate **O**f **C**harge
SOF	**S**tate **O**f **F**unction
SOH	**S**tate **O**f **H**ealth
SP	**S**ingle **P**article (model)
SPKF	**S**igma **P**oint **K**alman **F**ilter

Chapter 1

Introduction

This chapter presents an overview of the current energetic scenario, and the reasons why energy storage will be one of the key factors in the future. Besides, as many different energy storage systems are present nowadays in this field, electrochemical devices, and more concretely Li-ion batteries are highlighted due to their advantages against other technologies. After, the drawbacks of these systems, and the possible solutions to overcome them are explained. Finally the objectives of the thesis are presented.

1.1 Framework and scope of the thesis

Todays world is in constant change, challenging humanity to adapt. Along the history of humanity energy has played a crucial role inherent to technological advance. Coal, vapor, oil or gas drove our civilization to another step allowing inventions such as cars, trains, ships or lighting. When Benjamin Franklin discovered the electricity a new huge world of possibilities was opened. We can since then transport the energy in the most efficient way known to the date.

Generation and transport of energy has become a key world-level challenge. Different energy-generation methods are used to create a so-called "Energetic mix", where oil, natural gas, coal and biofuels are the central pillars of this mix [1]. Figure 1.1 shows the different energy sources used today to generate energy, being Oil, natural gas, coal and biofuels the central pillars of the energy used all over the world.

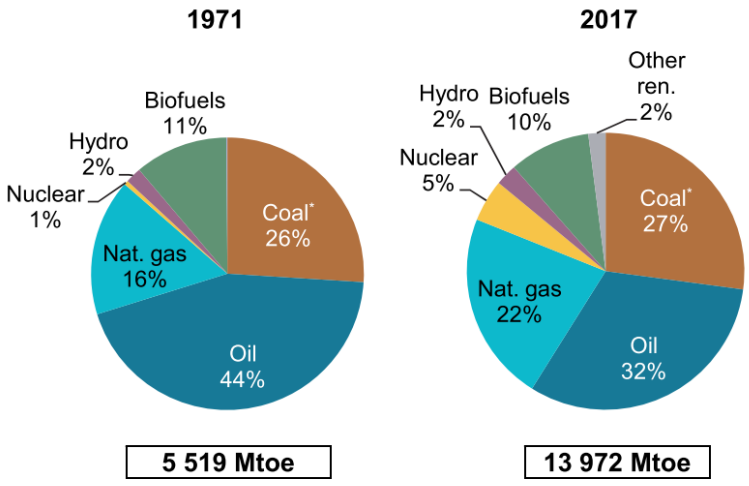

Figure 1.1: Total worldwide primary energy supply by fuel [1].

Furthermore, energy consumption has passed from the simplicity of lighting a house to the present complex electric grid. Overall energy demand has increased (figure 1.2, [2]) and transport has taken an important role in the sense that electrical energy demand from electric transportation has risen dramatically in the last years. In addition, many grid services [3] related to electricity distribution has taken importance due to the new energetic scenario.

To meet the rising energy demand, global reliance on fossil fuels over the last centuries

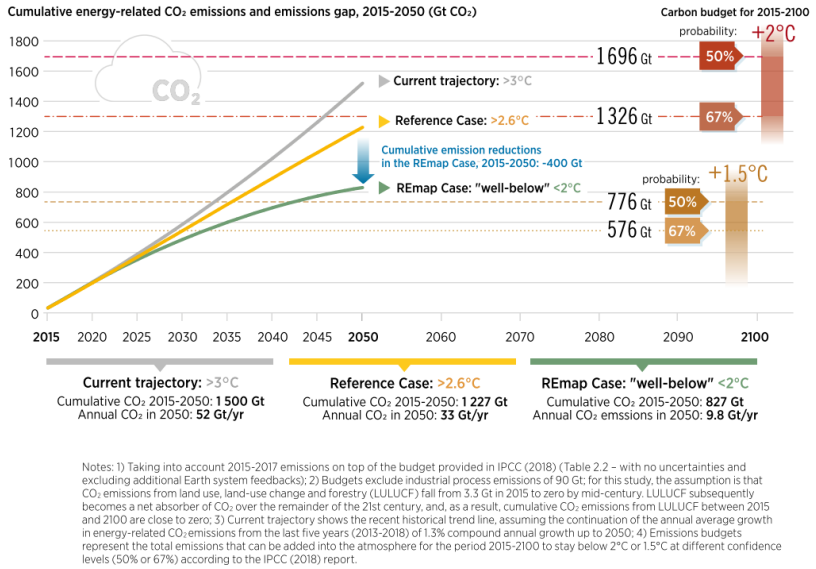

Figure 1.2: Cumulative energy-related CO_2 emissions and emissions gap, 2015-2050 (Gt CO_2) [2].

has caused severe consequences. CO_2 emissions are primary contributors to the greenhouse effect that is causing climate change. This is a problem that can not be ignored any longer and which is constantly growing (figure 1.3).

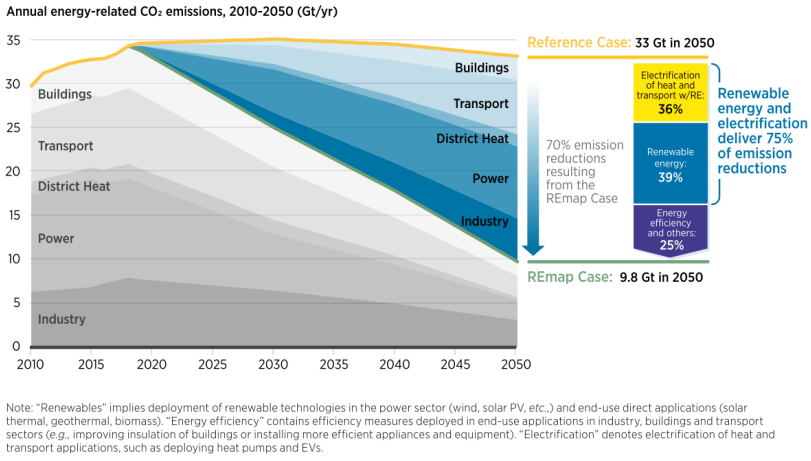

Figure 1.3: Annual energy-related CO_2 emissions, 2010-2050 (Gt/yr) [2].

Other emissions such as chlorofluorocarbons(CFC) have caused nontrivial damage to the ozone layer [4]. Human health is also affected due to air pollution, and related deaths are not isolated events, as shown in figure 1.4.

The energetic scenario described above is not sustainable any longer and renewable-energy

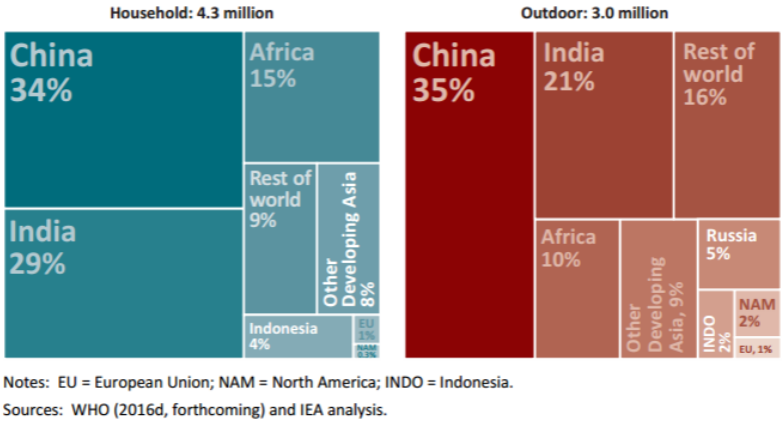

Figure 1.4: Deaths attributable to household and outdoor air pollution, 2012 [5].

sources appear to be the most plausible alternative to fossil fuels. These sources do not themselves generate contamination, even though their CO_2 footprint is not completely erased because of the production and maintenance of the associated infrastructure. Nevertheless, the intermittent nature of these energy sources (such as wind or solar) introduce technical challenges that need to be solved. Energy needs to be delivered to different loads whenever consumption is demanded from those loads, and the timing of this demand is independent of the timing of energy generation. Energy storage is therefore a real and actual need, permitting the storage of energy when there is an excess of generation capability and delivering energy when it is needed by a consumer.

Due to the above mentioned systemic challenges some politic initiatives have been pushed. *Horizon 2020* is a one of the best examples in Europe together with the future *Horizon Europe*, and other similar attempts have been boosted around the rest of the world.

In the future it is believed that demand tendencies are going to continue increasing as the population is growing. Due to the actual scenario and the oil availability decrease, other generation alternatives as nuclear fusion are being studied. Nevertheless those technologies can only be considered in the long term due to their immaturity. For these reasons renewable generation technologies are key in the near future. This highlights the strategical importance of the energy storage research. Different storage technologies as beyond post-lithium batteries [7] are being developed, but those technologies can neither be considered as short term approaches.

In figure 1.6 a classification of energy storage systems (ESS) used nowadays can be ob-

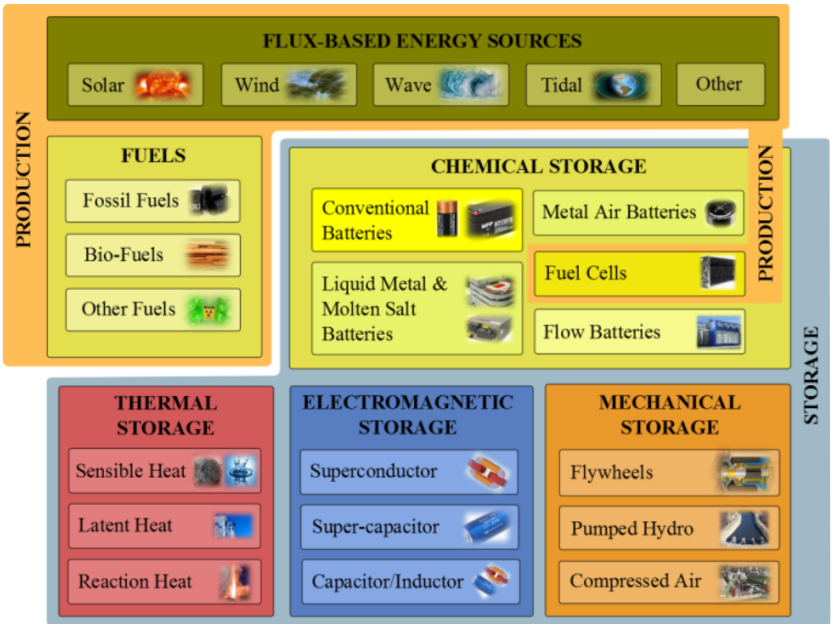

Figure 1.5: The landscape of energy/electricity generation and storage solutions (representative sample). It should be noted that fuel cells are a production technology but have been categorized as storage to adhere to common convention [6].

served. Electromagnetic storage (figure 1.5) as superconductors are still an immature technology. On the contrary supercapacitors are already in use, and mainly used for power quality, figure 1.6. For energy management purposes flywheels pumped hydro and compressed air storage (CAES) are used to store high amounts of energy applied to grid management purposes. The working range of the batteries makes them the best solution for most of the applications considered up to date and improving this ESS (energy storage system) is therefore crucial. Batteries are the most used devices in transportation, grid services, industrial and residential applications. More specifically the highest volumetric energy density of Li-ion technology makes it the best mature solution for most of energy storage applications.

As explained along the above paragraphs lithium ion batteries are the most promising batteries in the market. Figure 1.7 shows a classification of the different cathodes for Li-ion batteries (normally the battery cell is defined by the cathode as graphite anodes are generally used). Each of it has its own benefits and drawbacks, and the most appropriate one need to be chosen for each case.

Li-ion batteries are more dangerous (due to the leak, fire or even explosion risk) than Lead-acid batteries used on industry for years. It is therefore necessary to adopt some security measurements. Batteries are also normally used within battery packs, allowing the designer

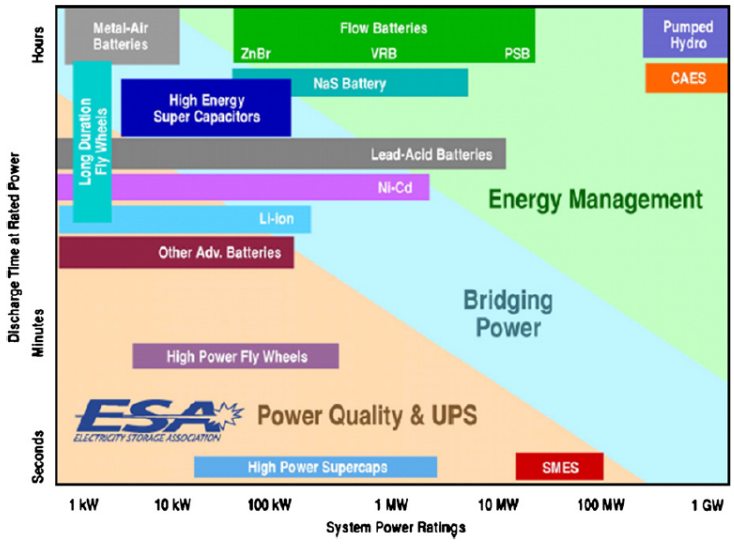

Figure 1.6: Distribution of storage techniques as a function of their field of application [8].

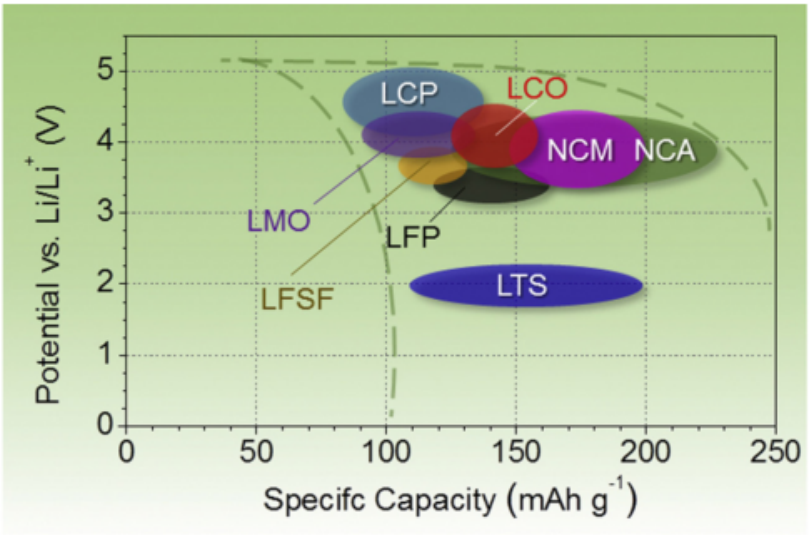

Figure 1.7: Approximate range of average discharge potentials and specific capacity of some of the most common intercalation-type cathodes [9].

to adapt the capacity and the power capability of the full ESS. In conclusion, a battery pack (to adapt capacity and power) and a battery management system (BMS), to ensure safe operation need to be considered for a battery-based ESS solution.

The purpose of a BMS is to monitor and equalize the batteries composing the battery pack. In addition it has to decide if the battery pack is under suitable working conditions or not to disconnect it if necessary, or even to manage a cooling system. A battery pack composed by cells, the BMS and the cooling system is shown in figure 1.8.

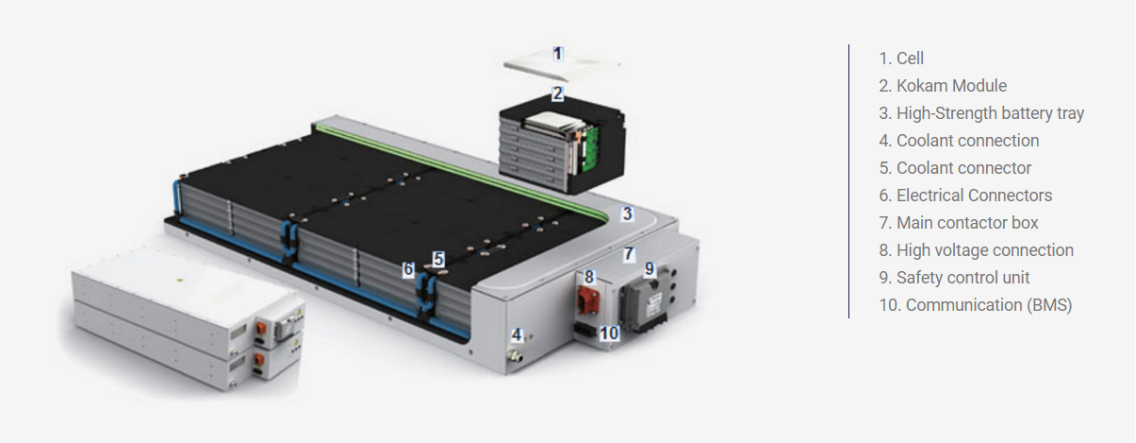

Figure 1.8: Kokam battery pack [10].

There are still some challenges that need to be faced to achieve better battery-based ESS. As exposed previously due to the penetration of renewable energies and the electric transportation market growth, the demand of battery systems is increasing. Nevertheless lithium resources are finite and alternatives to obtain lithium are key. Furthermore the price of batteries has been high up to date, this fact is evident when considering that the payback of those systems is in the range of years. Future trends says that the price will drop as the market is growing, an evident sign of this fact is the cell manufacturing gigafactory that *Tesla Motors* built [11]. Despite, the return range will not be negligible if that price does not drop much lower than expected.

Two considerations need to be taken into account at this point: the price per Wh and the aging of batteries (even if batteries lifetime is being extended, aging is still a key factor). Up to date, it is considered that the aging of a battery cell is only application dependent. Working temperature, charge/discharge rate and depth of discharge (DOD) affect directly the battery cell aging evolution (oversizing is used to overcome the aging nowadays). It is also considered that the capacity of the cells is used completely. Those thoughts are being revised and it is believed that with the correct managing of the batteries under/over utilization can be avoided. This way should be possible to store more energy than the addressed by manufacturers. Furthermore, aging is believed to be reduced by correct current management, based on voltage and temperature values (since all this values are linked with battery aging). It is therefore necessary to develop an adequate control strategy to properly limit the utilization window of batteries. This control need to be based on the internal variables of the cell, that if

predicted can be used to define the state at which the battery is operating, and to model the ongoing aging mechanisms. For this reason electrochemical models are a key point within this future improvements, making possible to control the operation window of the battery, when modifying the current based on model predictions. The reason behind this is that lumped parameter behavioral models or electrical equivalent models do not give information about the internal ongoings of the cell, they only emulate the voltage and temperature response.

To overcome this challenge, on the one hand specific hardware need to be designed or adapted, and on the other hand the correct control need to be designed and applied by the use of electrochemical models.

1.2 Objectives

The scope of this thesis is oriented to the **development and validation of an online physics-based battery control system**. The system has to avoid lithium plating as a first step towards the development of these type of systems full potential. Figure 1.9 shows the general overview and structure of the proposed system. The main parts of the system are the battery cell, the converter and the control implemented in a dedicated embedded system. Figure 1.9 also illustrates the main processes needed to achieve the main objective (electrochemical model parameter identification, reduced order model development, converter and cell assembly and control constraints generation) that will be treated along this thesis.

To reach this general objective the below partial objectives have been defined:

- **[O1]** Reduced order electrochemical model developement: Generate a functional reduced order model (ROM) without battery cells internal ongoings information loss. This means that model simplifications need to be avoided in order to preserve the models potential.

- **[O2]** Electrochemical model paramter identification: Identify the parameters required for the tuning of an electrochemical model, whether physico-chemically or using non invasive methods.

- **[O3]** Develop a lithium plating oriented functional control system: Develop a system able to prevent lithium plating, based on a ROM running in a low cost microprocessor and the needed hardware to control the lithium plating affecting variables.

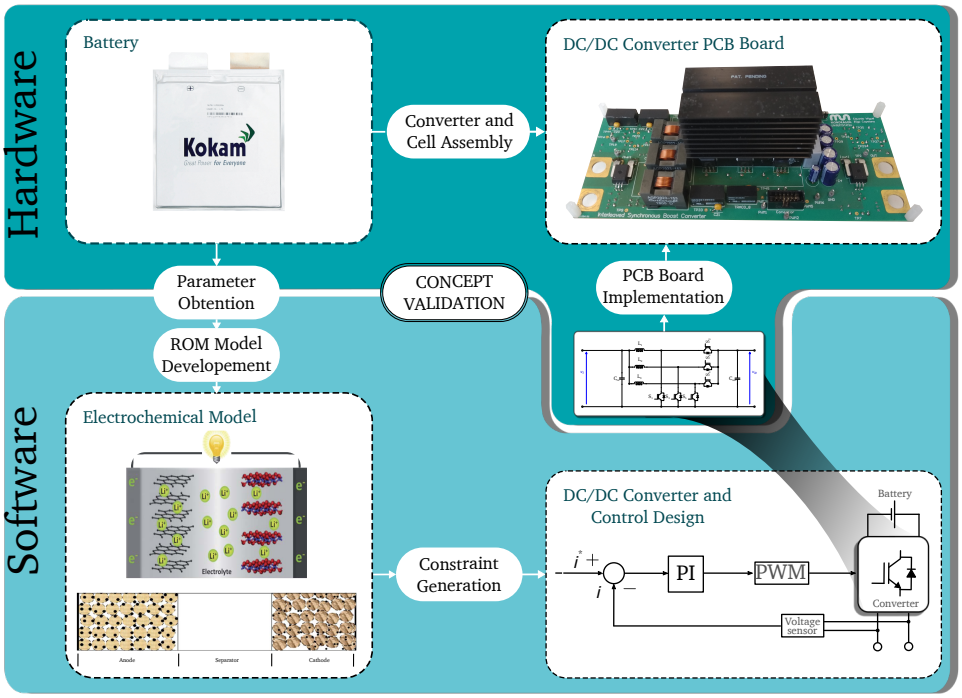

Figure 1.9: General scope of the proposed system.

1.3 Outline of the thesis

The document is divided in 6 chapters, the partial objectives described along this chapter are faced in the chapters shown in figure 1.10, where also titles can be observed. In the following paragraphs a brief description of each chapter is given.

After the introduction and motivation of the work, chapter 3 reviews the state of the art related to electrochemical models and reduction methods used by the different authors. After, the selected approach is explained in detail and the developed ROM model results are presented. To continue towards the general objective, chapter 4 treats the parameter identification for the previously developed ROM and the state of the art related to this topic. Both invasive physico-chemical and non-invasive parameter identification techniques are reviewed, and following the implemented identification and model tuning are explained in detail. With the already parameterized and tuned ROM, chapter 5 treats the implementation of a hardware system able to manage the battery cell current, governed by the ROM model running in a low cost embedded system. Finally the results obtained with the lithium plating prevention system

are gathered also in chapter 5, followed by conclusions and future lines in chapter 6.

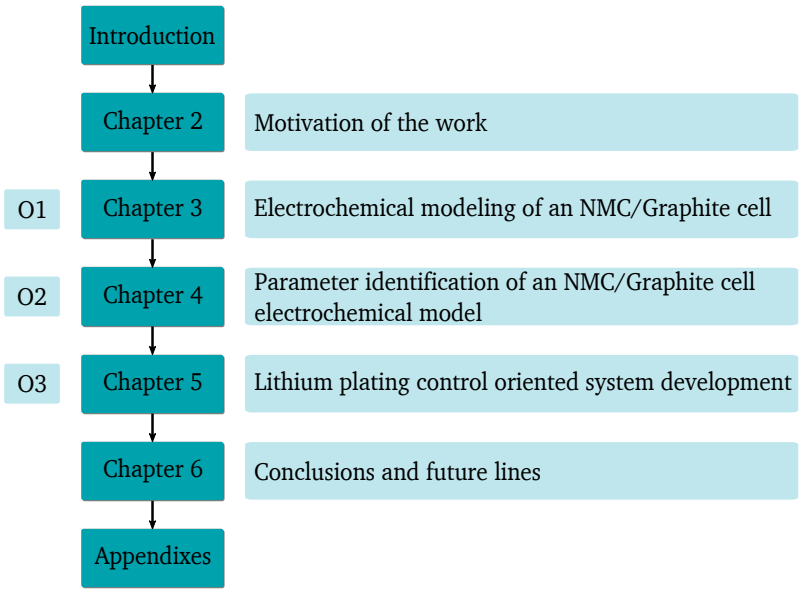

Figure 1.10: Thesis outline.

1.4 Scientific contributions

During this thesis a functional lithium plating control system has been developed. The conclusions are detailed at the end of each chapter, while the final conclusions gathered in chapter 6. In the following, a schematic view of the main contributions is presented, so a brief overview of the proposed advances can be clearly seen.

- A reduced order electrochemical battery model has been developed. Based on Plett *et al.* a more advanced reduced order model is developed. This model keeps all the P2D (pseudo two dimensional) model information, while the reduction process makes it light enough to run in a microprocessor. A sigma point Kalman filter and the required model structure to implement it is also developed. The model is able to represent the battery cells internal variables along all state of charge (SOC) range, for different temperatures. Finally the accuracy of this model is maintained, considering the error to be negligible.

- Physics-based models parameter identification is presented as a complex task. After identifying computational and physics-based procedures, a physics-based methodology is implemented. This job highlights the benefits and drawbacks of this methodology,

identifying ease and accuracy in the specific parameters identification. This evaluation provides the perfect scenario to further develop mixed optimum parameter identification procedures. These procedures will be developed after the initial phase presented in this thesis by L. Oca within her PhD work entitled "Optimization of the fabrication process of pouch cells for industrial applications through advanced electrochemical models", developed in the Energy Storage research line at Mondragon Unibertsitatea Faculty of Engineering.

- The implementation of a lithium plating control platform, evidenced the validity of electrochemical models in online systems. Different works reported evidence of lithium plating avoidance controlling the overvoltage, this fact together with a system suitable for an online implementation demonstrates the validity of advanced state of function (SOF) control.

1.5 Publications

Conference papers

[1] L. Oca, E. Miguel, L. Otaegui, A. Villaverde, and U. Iraola, "Methodology to assess the impact of electrochemical model parameters based on design of experiments," Comsol conference 2018, Lausanne, Switzerland, 2018.

[2] E. Miguel, E. Gucciardi, L. Oca, E. Bekaert, and U. Iraola, "Model identification through parameter estimation of a commercial LiFePO4 / graphite cylindrical battery," ISE Annual Meeting conference, Bolognia, Italy, 2018.

[3] L. Oca, E. Bekaert, E. Miguel, J. Ajuria, and J. M. Campillo-Robles, "Lithium-ion capacitor characterization for implementing in simulations," Materialen Zientzia eta Teknologia Kongresua, 2016.

Journal papers

[1] E. Miguel , Gregory L. Plett, M. Scott Trimboli, L. Oca, U. Iraola, "On electrochemical models parameter identification methods," (sent to *Journal of Renewable & Sustainable Energy Reviews*)

[2] E. Miguel , Gregory L. Plett, M. Scott Trimboli, L. Oca, U. Iraola, "Sigma point kalman filter corrected phisycs-based reduced-order model implementation for online applications," (in preparation, will be sent to *Journal of Power Sources*)

[3] L.Oca, E. Miguel, A. Herran, E. Gucciardi, L. Otaegui, E. Bekaert, A. Villaverde, U. Iraola, "Full parameter obtention methodology of a commercial lithium-ion battery for a pseudo-two-dimensional model," (in preparation, will be sent to *Journal of Electrochimica Acta*)

Chapter 2

Motivation of the work

This chapter describes the background of Li-ion batteries aging management, gathering the different tendencies found in literature. Benefits and drawbacks are analyzed, and the potential of electrochemical model-based battery control systems is explained. Finally the methodology followed during the thesis is presented, detailing the proposed system implementation and validation overview.

2.1 Background

Battery aging has been presented as the main factor affecting batteries profitability (since price is considered to be market dependent). Lithium plating is generated when operating at low temperatures (below 5 °C to 0 °C, shown in figure 2.1 and reported in [12]). Solid electrolyte interphase (SEI) growth is specially generated at high working temperatures (higher than approximately 45 °C); also low working temperatures enhance this reaction, figure 2.2. These aging mechanisms are considered the more significant among other aging mechanisms [13, 14].

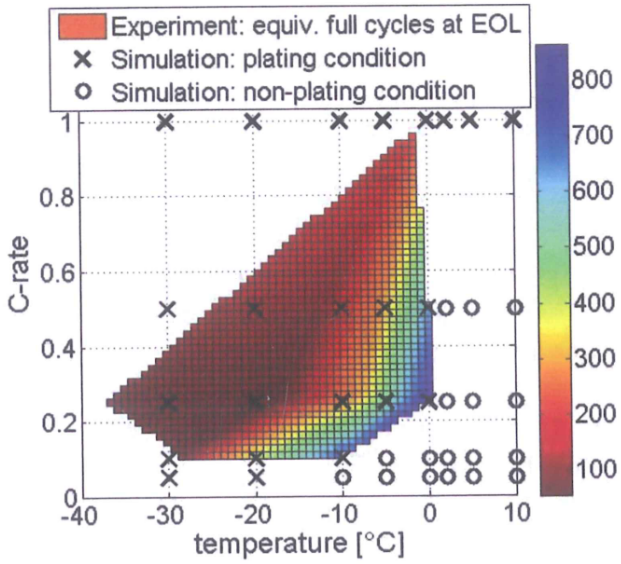

Figure 2.1: Lithium plating conditions reported by Ecker *et al.*[12].

In addition, applications are demanding higher energy densities and longer lifetime ESS systems, such as electric vehicle battery packs. It is therefore important to review the different approaches found in the literature to minimize aging, what would improve the battery systems making the Wh cost lower.

Cooling systems can be used to lower battery working temperature, so the aging rate is reduced and oversizing is avoided to some extent. These systems comprises fans, cold-plates or PCMs among others [16, 17], making the cost of the ESS rise. The most common practice otherwise, specially when looking at industry, is to oversize batteries to deal with the aging (also increasing the battery pack cost). When a battery pack is oversized, operating conditions related with battery aging [18] are modified, being the main factors the following:

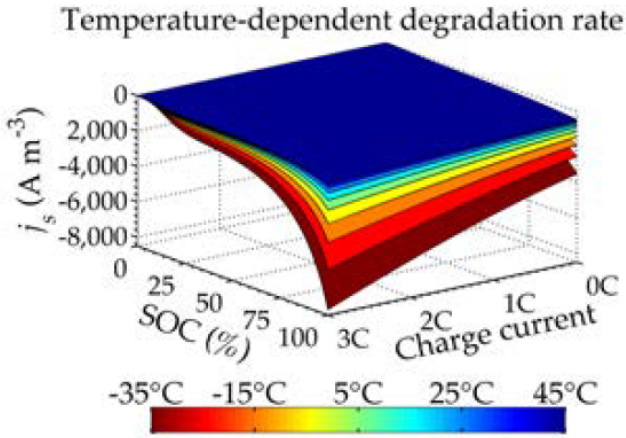

Figure 2.2: Instantaneous SEI degradation rate as computed by the ROM. (Adapted from Fig. 1 in Randall *et al.*, Journal of Power Sources, 209, 2012, pp. 282-288.) and extracted from [15].

- DOD
- Battery lifetime (maximum life cycles)
- Temperature
- Charge and discharge current

For a certain demand, if the battery pack capacity is augmented (over the needed amount), the current delivered by each battery cell is decreased (C-rate). This will also cause the DOD to be smaller, as well as the temperature to be lower, due to a smaller C-rate (since temperature increases with the C-rate). As a consequence, if the variables affecting aging are softened the aging rate will decrease. The concept of oversizing a battery is then simple, introduce more capacity than strictly needed to reach the battery pack specifications. This process is done during the pack design phase, and can be addressed differently. Model-based oversizing [19] is the most common method, pseudo empirical aging model [20], or adaptive aging model-based [21] pack optimizations tools are a good example.

Hybrid ESS systems are other alternative, with the use of different energy storage devices the demand can be satisfied avoiding batteries aging to some extent. For example, if supecapacitors are integrated into a battery pack (or even if not integrated in the pack and externally connected, what is known as external hybridization), the C-rate of the batteries can be limited (since the supercapacitors will feed power pulses, also known as peak saving) [22, 23]. Even

supercapacitors does not add a a lot of capacity (compared to batteries), this method can lead to a decrease in battery pack capacity requirement. The aging of batteries will still decrease, since their operation window will be more favorable, avoiding to oversize the pack in terms of battery capacity.

Second life of batteries is also a technique that can be used to mitigate the cost of batteries [24, 25]. When a battery or battery pack is considered to be no longer valid for its application, could be transferred to another application [26, 27]. Whether disassembling the battery pack and using the cells to build a different pack, or using the battery pack directly. The second life of the batteries mitigates the cost, since their use is extended over the first life. Incomings from that second life will reduce the overall Wh cost of batteries. As an example, electric vehicle batteries are considered to be useless when the state of health (SOH) is under 70-80% of the nominal capacity; these cells when recycled are often used to build battery packs for stationary ESS [28, 29, 30].

The methods presented above are all valid to mitigate the aging of batteries, being oversizing the main method. On the one hand, this method has been demonstrated to be effective. On the other hand, the efficiency of the whole battery pack (economically) is subjected to the method that is used to define how much a pack is oversized. As an example, if very accurate models are used to predict the aging of the battery pack (aging models), this method can lead in a very effective aging management. There are however some drawbacks inherent to the method, this pack design should be done for the worst case scenario (the demand profiles and working temperature should be known then). Not only this, as this aging management is done offline no changes can be applied when the battery pack has been assembled, and the design will not be optimum for every case.

More advanced methods to manage aging of batteries are based on SOF control techniques. These methods allow to change the aging management on demand (taking into account that aging can be controlled only by derating batteries maximum electric characteristics). These SOF controls are normally based on electrochemical models, and designed for an specific battery cell. This means that the system can be used for different applications avoiding an specific design. Electrochemical models describe the internal processes of battery cells, what allow to model any profile independently from the application.

Some authors pointed out the advantages of these methods, whether to monitor batteries SOF, create more flexible aging models or implement advanced control strategies, such as fast

charging or enhancing battery capacity. These authors posed electrochemical models use as a key tool to develop their advanced battery monitoring and control systems. A good example are the fast charging algorithms developed by Chu *et al.* [31, 32]. The proposed fast charging algorithm used a physics-based model to limit the overvoltage above 0 V , what was supposed to prevent lithium plating. The current applied to the battery was risen until the overvoltage prediction went below 0 V, and then the SOF control system managed it to keep the overvoltage at the desired constraint, as shown in figure 2.3.

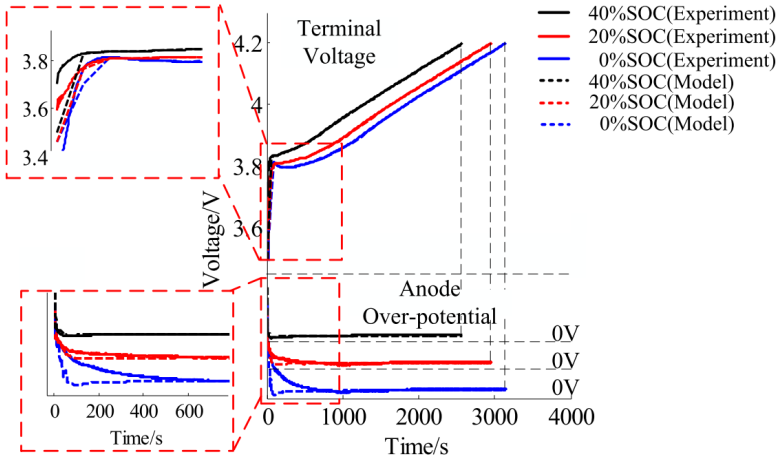

Figure 2.3: Battery charge profiles and overvoltage evolution during charge [31].

The authors did use a laptop to run the model and the control loops, what is not suitable for an online application. On the contrary, they reported physical evidence of the lithium plating prevention. A battery cell charged with a constant current profile was compared with a cell charged with the developed charging strategy, and the cell lithium plating was found only in the cell cycled with a constant current profile (figure 2.4).

Moura *et al.* [33, 34] developed physics-based SOF control oriented to optimal charging strategies. They reported that different compromises between charging time and battery aging were possible while using these systems, figure 2.5. This type of control could be used to manage the battery on demand, even considering market conditions to evaluate the cost of aging the batteries opposed to the benefit that is obtained [35]. Other good example of potential use of this type of battery modeling is to use these models to design battery packs, knowing more accurately how much the pack is oversized.

Trimboli *et al.* [36, 37, 38] reported the validity of electrochemical models to estimate the power limits of batteries, reporting that accurate calculation of these limits can lead to more

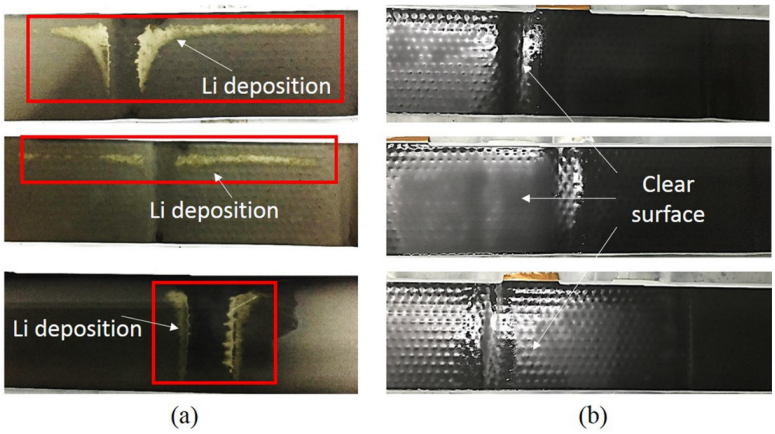

Figure 2.4: Battery post-mortem analysis of cell charged with a constant current profile (a), and with a physics-based fast charging control system (b), [31].

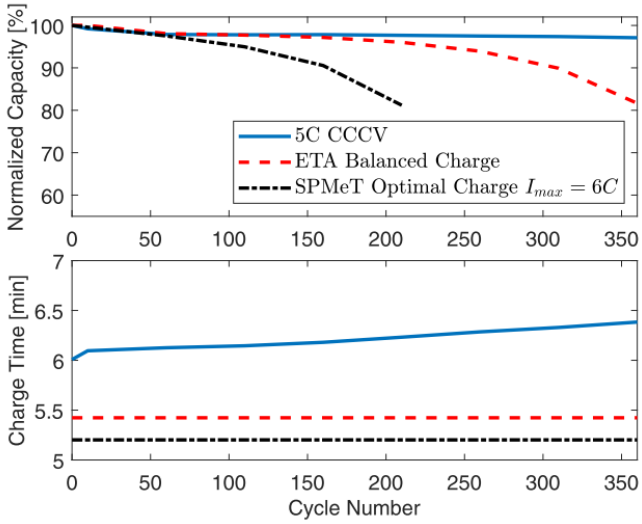

Figure 2.5: Physics-based battery charge strategies, showing different balance between charging time and aging [33].

efficient battery utilization, figure 2.6.

Plett et al. [15, 39] used algorithms based on sigma point kalman filters (SPKFs) able to adapt, choosing precomputed battery models. These models were generated according to the battery aging, using electrochemical aging models to build those already computed models. The algorithm could be used to monitor batteries, to design SOF controls or even to identify aging states of batteries (as the system also accounted for different aging states), as shown in figure 2.7.

It is also worth to mention that all these authors made a big effort to make electrochem-

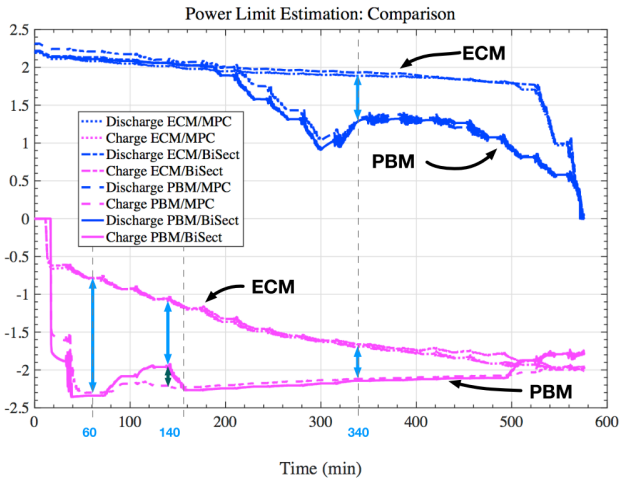

Figure 2.6: Power limit estimation comparison, using electric circuit models (ECM) and physics-based models (PCM) [36].

Aging mechanism (ψ) ↓ Side reaction...Material loss →	Capacity retained (α) 1.000	0.925	0.850	0.775	0.700
0.00	100%	90%	93%	100%	100%
0.25		95%	100%	100%	100%
0.50		95%	100%	100%	100%
0.75		65%	100%	100%	100%
1.00		93%	100%	100%	100%

Figure 2.7: Estimation probabilities of different ROM models related to different aging states [40].

ical models computationally efficient so they could be affordable for and embedded system [41, 42, 43, 44, 32]. This works illustrate that a correct monitoring of a battery SOF would allow to redefine the concept of safety operation area (SOA), leading to a dynamic SOA approach. Looking at the described research, is then **the hypothesis of this PhD thesis that the aging of batteries can be controlled using physics-based SOF control embedded systems**. Something that if proven, would confirm the concept of a dynamic SOA.

2.2 Work methodology

When looking at a SOF system implementation different parts are needed as found in the literature and shown in figure 1.9. Within this thesis the following topics have been addressed, resulting in a complete lithium plating control platform:

- Reduced order model development; a reduced order electrochemical model is developed and implemented in a low cost micropocessor. The use of this type of model is justified since other models such as electric ones does not account for battery internal variables. These variables are later used to control the lithium plating (the overvoltage more precisely), as a demonstration of the potential of this type of SOF control systems. The fact of running the model in a microprocessor will illustrate the viability of the system itself for online applications. Braking the old assumption stating that electrochemical models are out of the scope of online systems due to their computational expense.

- Electrochemical model parameter identification; electrochemical models are feed by a big set of parameters, and the identification process is not trivial, specially when experimental work is addressed.

- Converter and cell assembly; as a method to validate the full potential of physics-based SOF a converter is designed and connected to every tested battery cell. This structure assures the control of each cell current and voltage, exploding the control cappabilities to the maximum.

- Control system development; a control loop to control the lithium plating is designed and implemented. The overvoltage prediction is then used as the control loop feedback, maintaining overvoltage values positive. This positive values of overvoltage over the whole operation time will avoid lithium plating, as stated in literature [12, 15].

With the lithium plating control platform the concept of physics-based control system will be validated; prove of the whole system working in an embedded platform, and also prove of the whole concept of being able to control batteries SOF (based on electrochemical models predictions).

In this specific case, after the platform is developed a lithium plating control will be implemented (by limiting the battery solid-electrolyte interface to positive values, [34, 36, 15]).

This is only one of the potential benefits of this technique, as described above, but still enough to prove the concept of managing the aging of batteries using a physics-based SOF control. Not only this, the fact of centering the validation in controlling the lithium plating allowed to isolate this aging mechanism. For this reason the validation test were performed at a -10 ^{o}C temperature, were no SEI growth or other mechanisms are expected to be relevant. The tested device was a SLPB 7.5 Ah high power NMC Kokam cell (SLPB75106100) , this cell was chosen as a representative NMC device, commonly used in electric transportation.

Chapter 3

Electrochemical modeling of an NMC/Graphite cell

This chapter is dedicated to the development of an electrochemical ROM. This model will fulfill the partial objective of developing an electrochemical ROM, that will be suitable for an online system. For this purpose, the state of the art will be reviewed and after the developed solution presented. This model will be used in the validation platform (chapter 5), embedded in a low cost microprocessor, so it needs to be computationally light enough while maintaining accurate predictions. To fulfill this requirements, a state space form ROM will be employed, avoiding simplifications in the reduction process (in order to avoid loosing information). Finally the ROM results will be compared with a FOM reference data.

3.1 State of the art

Within this section the state of the art related to electrochemical models will be reviewed. First the know how of electrochemical models is presented and the different types and characteristics are reported. Following the reduction process of electrochemical models is treated and the conclusions of the state of the art are discussed.

3.1.1 Electrochemical models

Electrochemical battery models are those describing the behavior of batteries based on the internal physical phenomena. As a consequence complex sets of equations describing the physico-chemical processes inside the cell need to be solved. Nevertheless, the accuracy of the output and the amount of information related to the cells internal ongoings has no point of comparison, making electrochemical models of great interest to control or monitor internal battery cell processes.

3.1.1.1 Physical mechanisms and scales

When describing a battery cell different scales are found, related to the materials composing the cell. At least four different physical scales can be clearly defined, this is important as different physical phenomena take place at each scale, figure 3.1.

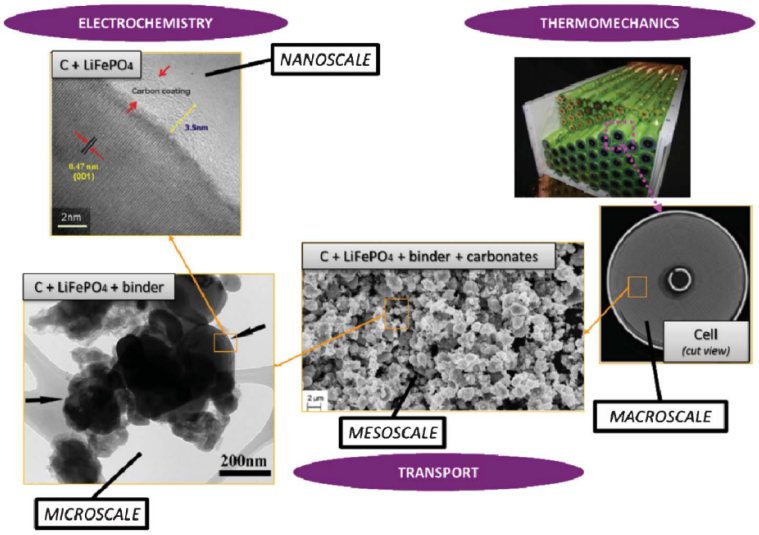

Figure 3.1: Scales in a $LiFePO_4$ electrode and physico-chemical mechanisms [45].

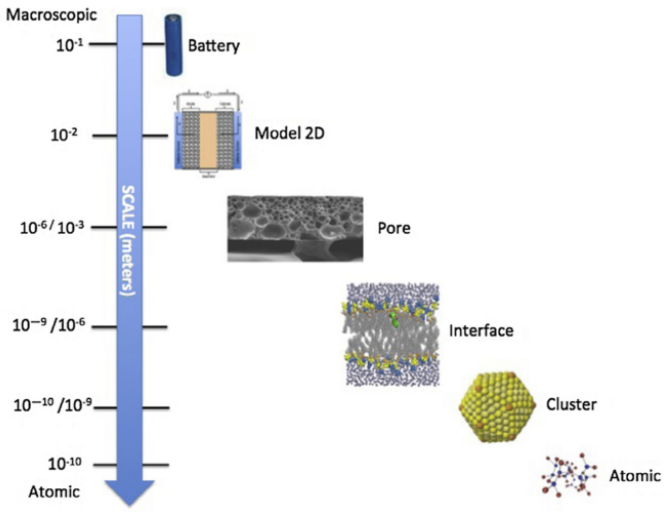

Figure 3.2: Schematic representation of the different physical and chemical scales influencing battery cell operation [46].

Nanoscale

In the order of 10^{-10} meters atoms can be found (figure 3.1 and 3.2) and models at this scale are used by physicists to study the insights of the materials structures, using density functional theory (DFT) calculations.

Microscale

Between $10^{-10}/10^{-6}$ meters [46] clusters and interfaces can be found, figures 3.1 and 3.2. Electrochemical reactions (redox and intercalation/deintercalation processes) occur between this scale and the nanoscale. Models formulated within this two scales can be defined as molecular-atomistic models [47]. molecular-atomistic models are out of scope of this thesis as they are not suitable for battery control, nevertheless this studies provide some input to larger scale models in form of parameters, used to describe electrochemical reactions.

Mesoscale

In the range of $10^{-6}/10^{-2}$ the mesoscale is defined [46]. Pores of the electrodes and the separator can be seen, as well as the interfaces between them, figure 3.1. The transport mechanisms inside electrochemical cells are modeled at this level with parametrized formulas and parameters representing lower scale characteristics. The comportamental electrochemical models are defined within this scope.

Macroscale

The macroscale can be defined from 10^{-1} meters [46] and above. At this level is where full electrochemical cells are defined, figure 3.1. Multyphysic models are used involving equations and data from the other scales (parametrized formulas that represent lower scale phenomena are used). The multiphysic models are able to model the distribution of all the variables precisely along the whole cell geometry. The full cell is considered the lowest complexity system [48], while battery packs the most complex [49]. Generally finite element method (FEM) simulations are used to design cells and battery packs. Nevertheless nowadays big efforts are being made to use this type of models in online system such as advanced BMSs [50].

3.1.1.2 Modeling scope

An electrochemical cell model (as it is normally refereed to) needs to describe different physical phenomena occurring at different scales. The mechanisms that enable an electrochemical cell to work and need to be modeled are Electrochemical processes, mass transport and thermodynamics [51]. In figure 3.1 can be observed that electrochemical reactions take place within the nanoscale and microscale, and mass transport as thermodynamics are observed between the mesoscale and the macroscale.

This means that information or equations coming from different scales are coupled to reach results at the macroscale (for engineering purposes mesoscale or macroscale models are used, for battery cell design or control). Nevertheles this coupling is problematic as the computational cost is an inverse function of the lengthscale, figure 3.5. Very different approaches have been made related to how many processes are modeled and how accurate, as will be explained in subsection 3.1.1.3.

Figure 3.3 shows the hierarchy between multiphysics and multiscale concepts. A multiphysics model need to be multiscale (in the case of actual batteries). Battery models (electrochemical models) need to use equations describing the processes running inside it as has been stated. Therefore the key issue when formulating a multiphysics model is how this different equations are linked, since parameter-based equations are used to avoid the smaller scales rigorous calculation and lighten the computational load.

Electrochemical models used for engineering purposes are defined between mesoscale and

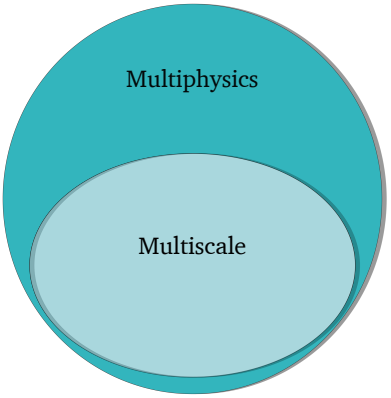

Figure 3.3: Interdependencies between multyphysics and multiscale terminologies, adapted from [45].

macroscale as explained before, and lower scale phenomena as the electrochemical reactions are represented with parameter-based formulas (the Butler-Volmer equation is a good example). Figure 3.4 shown a general overview of the mechanisms and the formulas used in electrochemical modeling. In addition different timescales are involved in the description of an electrochemical cell. Solving them is not cumbersome as will be explained in subsection 3.1.2.

3.1.1.3 Model classification

Figure 3.5 shows a classification of the most used electrochemical models, going from empirical or electrical models to molecular-atomistic ones, passing through meso-macro scale models. As mentioned before molecular-atomistic models are out of the scope of this thesis. Furthermore empirical models are also discarded as they do not provide information of the internal ongoing of the cells, which is crucial for SOF evaluation and control.

The first electrochemical models developed were created for Lead-Acid and NIMH batteries. Nernst theory and Butler-Volmer equation where used while assuming homogeneous spatial distribution of chemical products [53]. Nevertheless the set of differential algebraic equations(DAEs) composing those models was insufficient to describe newer cell technologies like Li-ion [52]. With the evolution of the Li-ion cells and the need of distributed models Doyle Fuller and Newman developed the P2D model [54, 55] based on the porous electrode and concentrated solution theories [56, 57]. This model described the complex processes inside a Li-ion cell and was generic enough to incorporate further advances as 3D or aging

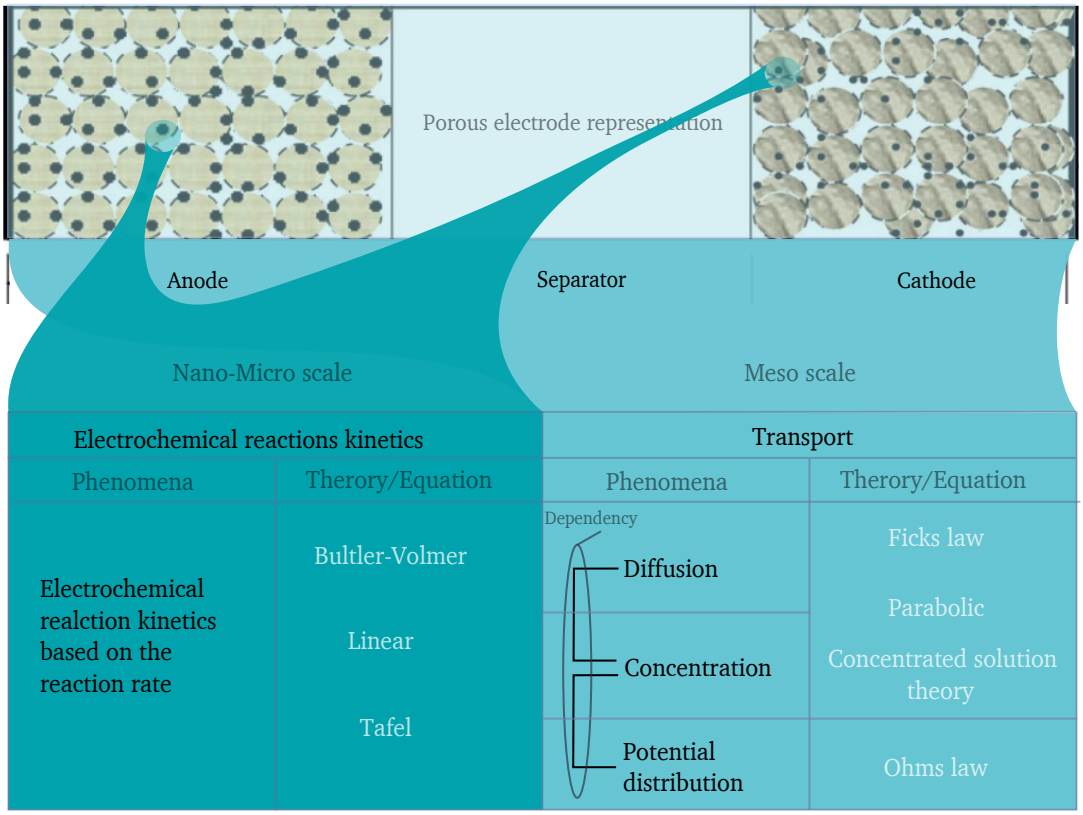

Figure 3.4: Simulated electrochemical phenomena with electrochemical models and used equations classified by scale, adapted form [52].

models, most of the actual electrochemical models are based on it. It is therefore important to understand the characteristics of this model in contrast to others. In the following paragraphs the porous electrode and P2D models will be explained, in addition the single particle model is also going to be considered as it has represented a very successful attempt for computationally cheap approaches.

Porous electrode model

The porous electrode theory [56] developed by Newman and Tiedemann states the needed PDAEs (partial differential algebraic equation) and boundary conditions to model a cell represented by three different areas, the two electrodes and the separator (figure 3.6). The transport and charge transfer phenomena are considered to happen in the x axis and the other two are neglected. As the x axis is in the order of 100 μrmm and y and z axes around 1 000 000 μrmm this assumption can be applied to nearly every battery system, leading in a generic 1D model [53], figure 3.6. The particularity of this repre-

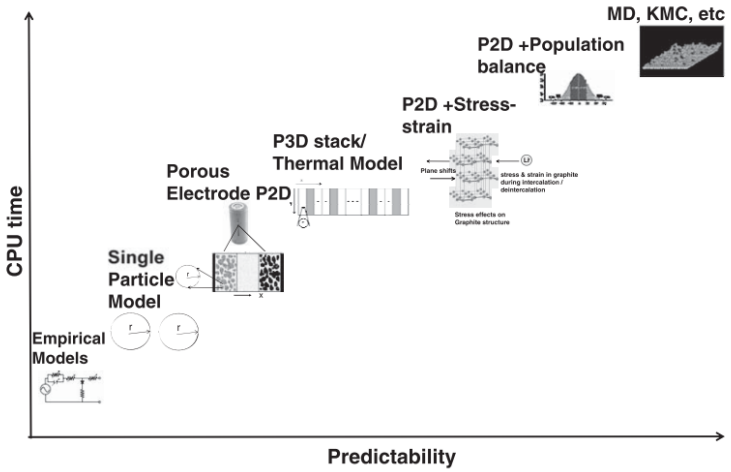

Figure 3.5: Classification of battery cell model types [47].

sentation compared to previous attempts is that the electrodes are defined as a porous composite soaked with electrolyte. This is particularly important because since the late 90's and in the 21st century the commercially avaliable cells have been "rocking chair batteries" manufactured with porous electrodes that improved the capabilities of the previous polymer ones (due to the higher surface area generated in porous electrodes).

The porous electrode model considers all the major electrochemical processes, table 3.1. Electrochemical reaction kinetics can be modeled either with linear, "Tafel" or exponential expressions (Butler-Volmer equation). The transport in both, the solid and the electrolyte is modeled with the "Ohms law" based on the conductivities of each phase, which are affected by the porosity of the electrodes. Nevertheless transport phenomena is not treated rigorously, using averaged values, and therefore the distribution of concentration and voltage drop are not obtained. As a consequence accuracy is lost and the information regarding to distribution within the phases is not predicted.

This model was the beginning of the research in the field of Li-ion electrochemical modeling and nowadays is obsolete, nevertheless it is important to understand it as more modern attempts framework.

Pseudo two dimensional porous electrode model (P2D model)

The Pseudo two dimensional model is an evolution of the previously explained porous electrode model, figure 3.6. While making the same assumptions as the porous electrode model it makes a description of the transport phenomena and it is able to obtain con-

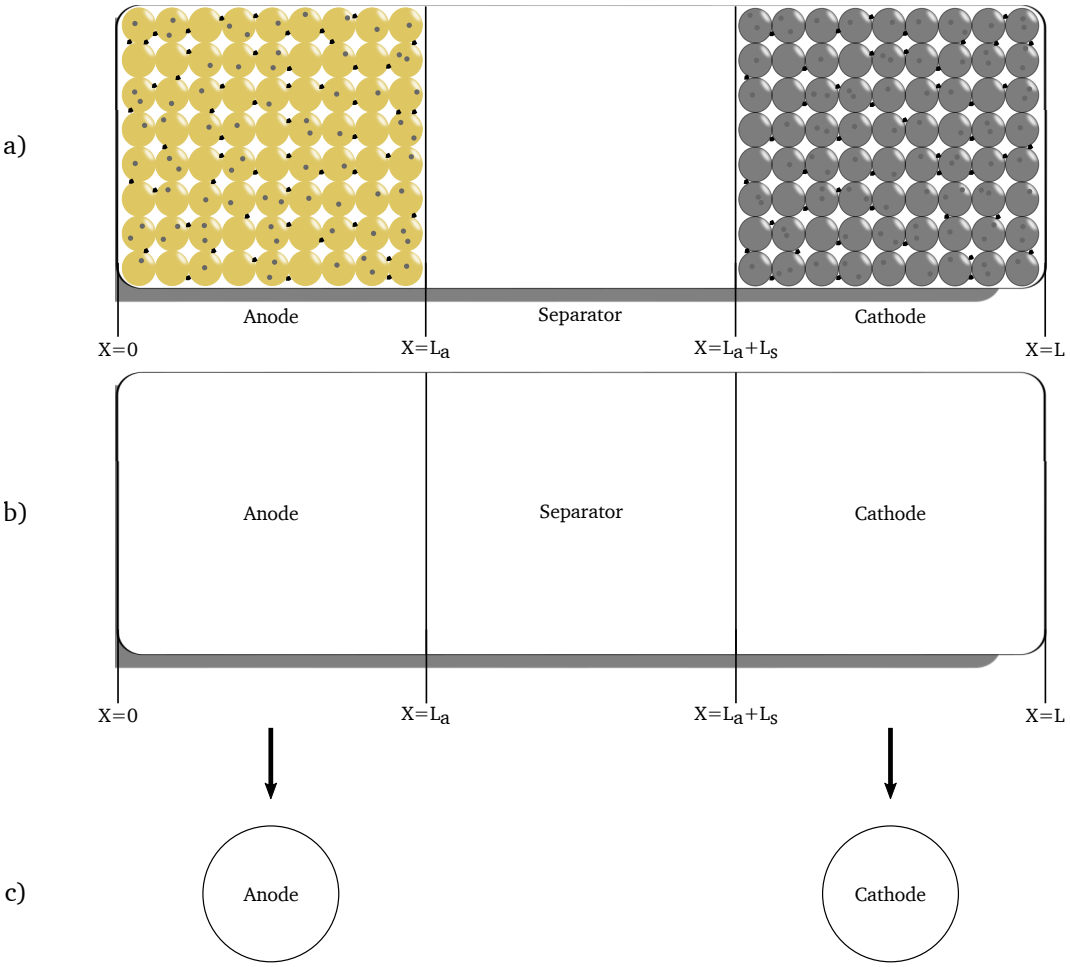

Figure 3.6: Simplification of the rigorous two-dimensional model (a) to the P2D model (b) and the single particle (SP) model (c).

centration and potential distributions in the whole x axis of the cell [54, 55, 58], fixing the handicaps of the porous electrode model. Diffusion is assumed as the only driving process of species transport, as it is the predominant mechanism. The concentrated solution theory [57] describes the spices transport in the electrolyte, being general enough to be modified and account for multiple salts electrolytes. Regarding the diffusion in the solid the "Ficks law" and superposition [55, 58] are used. The active material in a porous electrode is composed of different particles and this is why a second pseudo dimension representing the radial diffusion on the particles is used, giving the name to the model.

The model was developed by Marc Doyle, Thomas F. Fuller and Jhon Newman in the early 90s reason why is sometimes called DFN model. Many modifications have been

made to the standard DFN model over time to describe cell degradation mechanisms. For example, the lithium plating process [59], SEI layer growth [60, 61, 62, 63], manganese dissolution in the positive-electrode [64] or a particle fracture description [65]. All these degradation models augment the basic DFN framework, so to predict degradation one must first have to be able to implement the DFN model.

In addition, many computational simplifications have been made to the standard DFN model to make it more suitable for BMS. These include SP models [66, 67, 68] and parabolic approximations of solid concentrations to reduce complexity of PDEs (partial differential equation) resolution [69, 70]. Other approaches such as Padé approximations, residue grouping [71, 72] or the discrete-time realization algorithm [73, 74] have been considered.

Single particle model (SP)

The single particle model [67, 68] is the most computationally efficient model presented in this document. It considers the cell structure as two spherical particles equivalent to the active surface area of the whole cell, as shown in figure 3.6. The transport in the solid is modeled taking the diffusion as the only mechanism as in the previously presented attempts. Concentration is obtained using the "Ficks law" or even a parabolic approximation [52] and the potential distribution for the solid phase can be obtained as the transport in the solid is taken into account. The drawback of this model is that as the lumped models or the porous electrode model does not consider the transport phenomena in the electrolyte phase, and this is why it is only valid for certain conditions as low charge-discharge rates or thin electrodes [52].

Next the temperature of evolution of a battery cell and the aging of it can be considered within a model. This predictions are normally considered as separated models because both are linked to one of the previously explained models.

Thermal modeling

Ones the models insights are known thermal modeling can be faced. The thermal models are intimately linked with the behavioral models presented in the above paragraphs. Lumped thermal models are normally employed in order to represent the temperatures macroscale effect [75].

Table 3.1: Different models capabilities.

	Scale				
	Nonoscale	Microscale	Mesoscale/Macroscale		
	Electrochemical reactions kinetics		Transport (Diffusion and Concentration)		Potential Distribution
	-		Solid phase	Electrolyte	-
Lumped	Butler-Volmer		✗	✗	✗
SP	Butler-Volmer		Parabolic/Ficks law	✗	Solid phase
Porous electrode	Liner/Tafel/Butler-Volmer		✗	✗	✗
P2D	Butler-Volmer		Ficks law	Concentrated solution theory	Solid phase+electrolyte

Other important consideration is the treatment of the temperature, that can be an input for the model or an output depending on the aim of the model. If temperature is an input a reference temperature need to be introduced to the model so the model parameters temperature dependency is contemplated. A thermal model itself it not used then, as the parameters temperature dependency is only modeled and there is not temperature prediction. Furthermore a temperature sensor is needed to feed the model. On the contrary if the temperature is not considered as an input to the model and a prediction is wanted a thermal model is needed. The whole system becomes more complex but a temperature prediction is obtained.It is therefore important to define if a temperature prediction is needed for each specific application of the electrochemical model. Within this thesis the temperature will be treated as an input for the sake of simplicity and thermal modeling left for future investigations.

Aging models

There can be found different aging model types in the literature as empirical or pseudo empirical models considering different aging mechanisms [76, 13, 14]. Nevertheless when considering an electrochemical battery behavioral model the most natural evolution is to use electrochemical aging models.

The advantage of electrochemical aging models is the insight on the specific aging phenomena that is being modelled. This is, if for example SEI growth is considered the model is going to be able to predict when and how much the SEI has grown. Furthermore as the aging mechanism driving reaction itself is simulated there is no need to

differentiate between aging and cycling live. In addition the interaction between different aging mechanisms is intrinsically considered through the cell internal variables (assuming that the aging mechanism reaction is correctly described). All this facts make this type of models the most appropriate for battery design, and SOF control or battery pack sizing are starting to be more and more visible within the literature as the electrochemical battery models evolve.

In general most of the aging of a battery cell is associated to the side reactions occurring in the anode (depending on the used materials this can change). Modeling the side reactions driving the SEI growth and lithium plating is the base of most of the electrochemical aging models and the correctness of this approximation can be seen in the accuracy of this models [77]. Battery cell internal variables predictions are used in order to estimate the aging of the battery so the link between models is straightforward. The Butler-Volmer equation is normally used to model the side reactions the same way it is used in the electrochemical behavioral models to predict the intercalation, deintercalation, reduction or oxidation processes. The difference then is that the parameters representing the nanoscale elements properties are different.

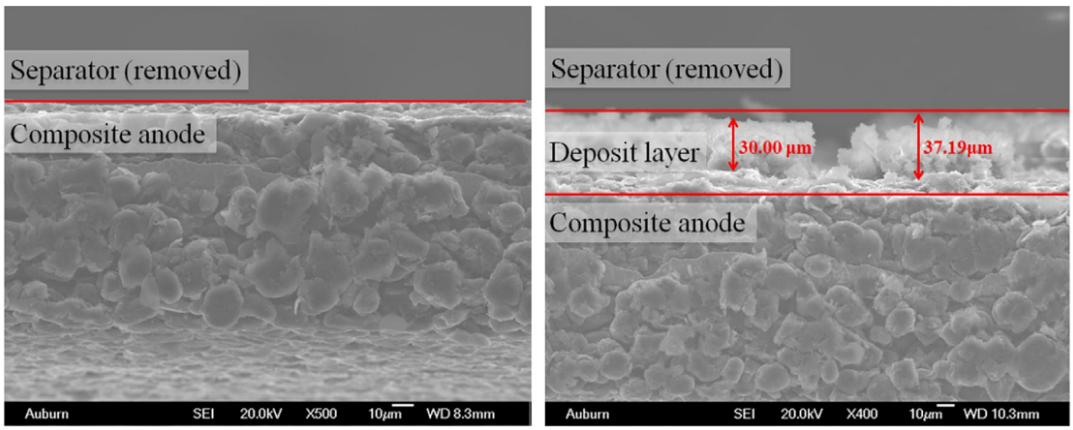

Figure 3.7: Side reaction deposit layer growth validation via post mortem analysis [77].

There are several literature references modeling the side reactions as a cause of battery aging [59, 78, 77, 79, 80, 81, 82, 62, 83, 84, 85]. The work of Fu*et al.* [77] stands out as they experimentally validated their results with post mortem analysis (figure 3.7) and electric tests (figure 3.8).

Aging models are out of the scope of this thesis, and will be treated in following works, as

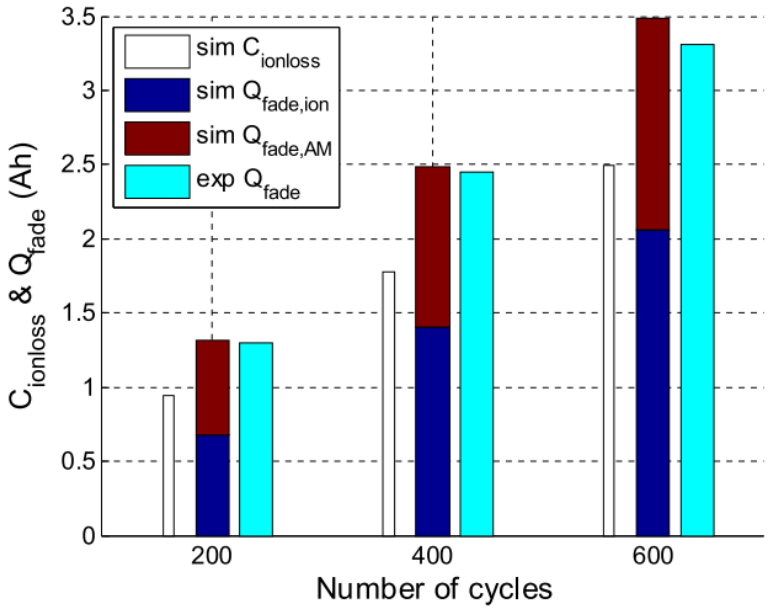

Figure 3.8: Capacity loss validation [77].

they are the next logical step once a functional SOF control system have been developed.

3.1.1.4 Solving methods

PDAEs (used in electrochemical models) are normally solved using numerical methods as analytic solutions are not possible. Discretization is therefore a procedure to overcome. The first steps in battery cell simulation used a simple technique called finite difference. Continuous quantities are assumed to be constant in finite space and time intervals and derivatives approximated by Taylor series expansions, Eulers rule or similar [73]. Although this method is simple a big number of finite spaces along the x axes of the cell need to be solved to avoid loosing accuracy and time. This fact leads in a excessive computational load for an online system. Nevertheless this methods and similar ones (figure 3.9) that are going to be briefly explained in the next paragraphs are important as are intensively used.

Other method used for offline simulation is the finite volume method. This technique divides the time in small segments the same way as in finite difference and the space is discretized in volumes. "Flux terms at volume boundaries are evaluated, and concentrations are updated to reflect material fluxes" [73]. After the discretization linear algebra solvers are used as in the finite difference method again. The division of space in volumes enforces mass conservation as the flux entering a volume is the same going out to the adjacent volume. This method is

particularly recommendable for unstructured mesh systems.

The last offline method presented in this document is the finite element method. The particularity of this method in comparison to the other two presented here is that the spatial variables are discretized over a summation of N linear or quadratic terms, finite element functions F. Then as one dimensional equations have been defined PDEs are solved as vectors, equation 3.1. The form and spacing of the finite element functions can be changed as far as at every spatial location the summation is 1 (as the representation of the variable is a summation of functions this summation need to be normalized, thus a weighted summation of finite element functions is applied) [73]. Finite elements method is very popular for a large amount of applications such as electric machines design [86] or fluid dynamics [87] for example.

$$Z(x,t) = \sum_{m=1}^{N} Z_m(t) F_m(x) \tag{3.1}$$

Later researches have being focused on the improvement of the simulation time to make general purpose simulations more affordable and also to move towards the online implementation of complex models. Two directions have been followed in this sense; the first alternative is based on a different solving method of the equations for a better handling and consequent faster solving [88, 83, 74, 48, 89, 90]; the second alternative is to reformulate the models equations assuming a loss of information due to a simpler formulation [91] (normally this approach is normally applied to electrochemical models solving when moderated rates or cell working points are modeled). Both alternatives have been deeply studied and a lot of literature can be found, nevertheless the reformulation of models is out of the scope of this document as one of the objectives of this document is to avoid loss of information.

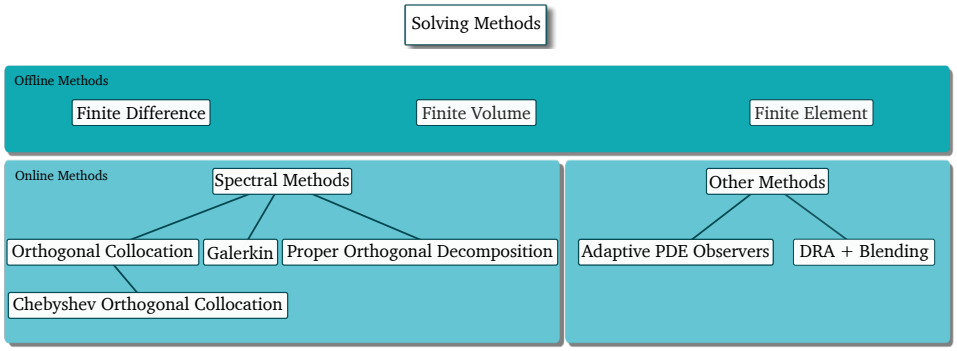

Figure 3.9: Parameter solving methods.

Figure 3.9 shows a classification of methods designed to speed up the models resolution. The online term in the classification can be misleading because there is not a clear barrier defining the time limit, neither clear resolution times associated to each method. Nevertheless these are the methods that provide potential solutions for real time applications.

Spectral methods have been deeply studied in order to make faster simulations [90, 89, 92]. The main concept behind spectral methods is to approximate the solutions of the PDEs using orthogonal basis functions. PDEs are represented therefore as a set of coupled ODEs (ordinary differential equation). In a similar way to the previous methods time and space are discretized, BS different resolution of the equations within the discrete time and space make the difference regarding solving time. Other attempts as the Padé approximation and residue grouping method are also significant in the literature [46].

All this methods made a big difference in models viability, making the simulations affordable for many researches. Even so, due to the nature of control systems a state space representation is highly recommended if not necessary. In addition the solving of state space models is straightforward, and this makes that the most promising approaches for online methods have adopted other philosophies. Analytical discretization methods [73, 93, 92] are used as a simpler way to obtain transfer functions in the Laplace domain, since state space models are developed more naturally from those equations. One of the most advanced work in this field was developed by Ecker *et al.*. This work will be explained in section 3.1.2.

3.1.1.5 Modeling software and implementation

The software contemplated within this subsection is based on the presented previous models (normally the P2D model) or modifications of them [94, 95, 96]. The particularity is that the models are solved rigorously and without making any assumption (model reductions) that rest accuracy. To solve the models in such a rigorous manner the FEM method is normally applied. The y and z axes are not neglected and accurate current and thermal distributions [97] can be obtained. Furthermore 3D representations of the electrodes shape (microscale shape) can be used to increase even more the accuracy [98, 97]. It is worth to mention that simulation time is not a so crucial characteristic when considering this type of modeling, as they are used for cell and battery pack validation and design, being online systems out of the application field of this type of software. This software is still crucial for the present work, as

it is used to validate parts of the work.

The first dedicated toolbox was developed by John Newman in FORTRAN when the first electrochemical models where developed. This code is still in use and updated with several improvements [99]. This is despite a basic toolbox and no interface was designed being not straightforward to modify the model. in order to obtain spatial distributions for example. On the other hand it is a useful tool as integration with other softwares is fast and easy.

COMSOL Multiphysics Ⓡ and CD-adapco Ⓡ are two other dedicated and newer programs. In the case of COMSOL Multiphysics it is not only valid for battery modeling, but the quality of the battery simulation package makes it a very useful software, figure 3.10. This software is specially valid for research purposes as it is designed to model physical phenomena in general, and this makes easy to modify and extend the models. CD-adapco is in this sense a software opposite to COMSOL Multiphysics as it is specifically designed to integrate electrochemical and thermal modeling, oriented to industrial battery pack design and validation. Within this software the newly acquired HEEDS optimization software is worth of mention because increases the power of this tool for battery pack design purposes.

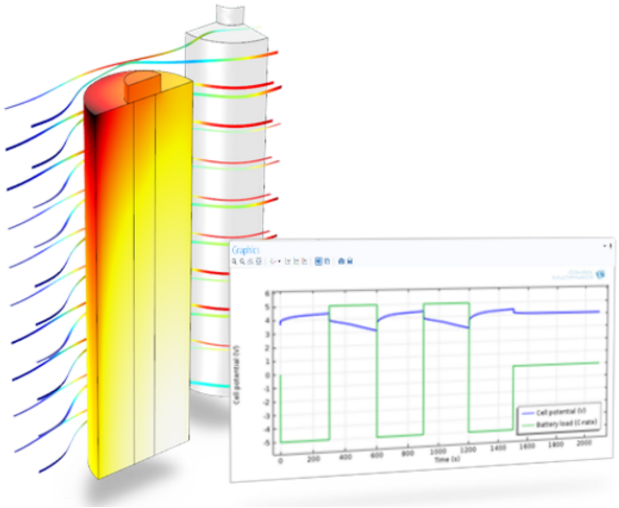

Figure 3.10: COMSOL Multiphysics implementation example [100].

3.1.2 Reduced order models for online systems

Equations composing electrochemical models are many and complex. The description of the cell mechanisms lead to the formulation of 4 PDAEs and one algebraic equation [73], these are stated for cathode, anode and for the separator region (not all of them are formulated for

all the regions). All these PDAEs are coupled with the boundary conditions [46, 73] to enable the continuity of the whole micro scale model leading in a set of 14 coupled PDAEs with 14 unknowns [53]. Furthermore not only the amount of equations but the intrinsic complexity of a partial differential algebraic equation (PDAE) make the resolution of these models a non trivial issue that has maintained electrochemical models out of the scope of online systems for years.

Electrochemical models complexity and the weak penetration of advanced technologies as lithium ion together with a considerable computational expense used to make them simply out of scope. Li-ion batteries have experienced a significant advance in industrial utilization (which is traduced in a emerging market) and consequently a high research effort have been made, which can be clearly seen if we consider that post-lithium-ion batteries concept is already in use [7]. Furthermore the computational power of the actual microprocessors has increased, creating the appropriate environment to overcome online implementation of electrochemical models.

In this scenario the reduced order models become crucial. Even the computational power of actual microprocessors has increased reduced order models make not only possible but cheaper to implement this type of models as simpler microprocessors can be used. Model reduction therefore, is a technique that makes a certain model lighter to solve. This can be achieved on the one hand simplifying the equations and loosing information and possibly accuracy. On the other hand there are some methods that achieve this objective reformulating the equations or transforming them in some way without loosing accuracy, as stated before. The main approaches for the electrochemical model reduction process will be reviewed along this section.

The selection of the model is a key step, some models require lighter computational resources offering less or more inaccurate data and vice versa, as explained in subsection 3.1.1.3. Therefore not only the model reduction process but the selected model itself are important in terms of accuracy and computational expense.

Finally is mandatory to take into account that the parameters of a cell change with aging [101, 75] and a method to update those parameters is necessary.

Within this research fields four different groups stand out, table 3.2. Through the next subsections the approaches developed by these groups will be explained taking as common thread the challenges explained in the paragraph above.

Table 3.2: Authors working in the field of electrochemical models for online systems.

Group	Author	References
G1	Scott Moura Hector Perez	[34, 44, 102, 33, 42, 41, 33, 103, 104]
G2	Gregory L. Plett M. Scott Trimboli	[88, 83, 48, 73, 74, 105, 36, 38, 37, 43, 40, 39]
G3	Ramadesigan Venkat R. Subramanian Shriram Santhanagopalan PaulW. C. Northrop Richard D. Braatz Bharatkumar Suthar	[49, 47, 106, 107, 108, 109, 110]
G4	A.M. Bizeray S.R. Duncan D.A. Howey	[92, 89, 111, 112, 109, 113, 114]

3.1.2.1 Model selection

All the contemplated groups work with the P2D model. G1 and G3 also has some relevant work with the SP models. G1 authors [103] used the SP model as the mathematics involved in this model were more convenient to develop observers which were used in this work, also G3 authors used it due to its lower computational cost and accuracy for low battery cycling currents [106]. The P2D model is the simplest model that define all the desired insights of a battery cell at every working conditions (without taking into account models working at other scales as 3D models or more advanced modifications of the P2D model, figure 3.5) and this is why it is the most used accurate model up to the date.

3.1.2.2 Model reduction and solving

All the authors focused their resolution methods into state space models, which are specially valuable for control purposes. The main difference between them is how they developed that model. All the models passed through a model reformulation due to the complex mathematics involved and the way to solve the equations was the key issue (even some slight assumption can be taken to reach the objective and still succeed to preserve the whole information without loosing accuracy).

G1, G3 and G4 developed a state space model-based on the linearization of the model.

When this step was done they differed in the solving method. G3 made a comparison between finite difference and orthogonal collocation methods. They also introduced in the comparison a single particle model to illustrate the meaningful difference in time and accuracy, as shown in figure 3.11 [115]. Feasible times to implement the model in real microprocessors were reported, figure 3.12.

Simulation Scheme	Number of DAEs	Error (mV)	Simulation Time (PC) (ms)
1,1,1 Finite Difference	33	93.3	172
16,8,16 Finite Difference	197	1.55	515
75,50,75 Finite Difference	871	N/A	16645
1,1,1 Collocation	21	11.8	125
7,3,7 Collocation	72	0.539	250
15,15 Single-Particle Model	34	311	47

Figure 3.11: Simulation times and errors for various levels of refinement for collocation and finite difference methods. The (M, N, P) nomenclature refers to the number of interior node points or terms in the cathode, separator, and anode, respectively, for the finite difference approach or collocation solution. For the single-particle model (M, N) refers to the number of points considered in the single particle of the cathode and anode, respectively [115].

Number of DAEs	Finite Difference 33		Reformulation 21		SPM 34	
	Numerical Jacobian	Analytical Jacobian	Numerical Jacobian	Analytical Jacobian	Numerical Jacobian	Analytical Jacobian
Time to solve in platform 1 (s)	0.553	0.132	0.129	0.083	0.095	0.011
Time to solve in platform 2 (s)	12.864	3.902	4.522	2.269	2.955	0.499
Time to solve in platform 3 (s)	570	165	190	120	185	35

Figure 3.12: Comparison of the lowest order finite difference and reformulation simulations in the microcontroller platforms. Note the general improvement in speed for the reformulated models for all cases, as well as improved computational speed achieved when using an analytical Jacobian [115].

Group G4 used the chebyshev orthogonal collocation method to solve the model. They also developed a modified extended Kalman filter in order to achieve a precise estimation despite small measurement errors, incorrect initializations or inhomogeneities in the cells [89]. The benefit of this two approaches was that after the model development, it was not needed to regenerate it. This strategy was opposite to the other attempts as is explained in the parameter update subsection. In contrast the accuracy of the predictions was in function of the number of discrete spatial points that could make the resolution more time consuming.

An alternative approach went one step beyond and was proposed by G1, which use an adaptive partial differential equation (PDE) observer to solve the model, figure 3.13. They developed in addition a feedback to update the system while the cell ages or even for initialization [41]. This method was highly oriented to online systems. Nevertheless not much

information about the accuracy of the internal variables estimation was shown.

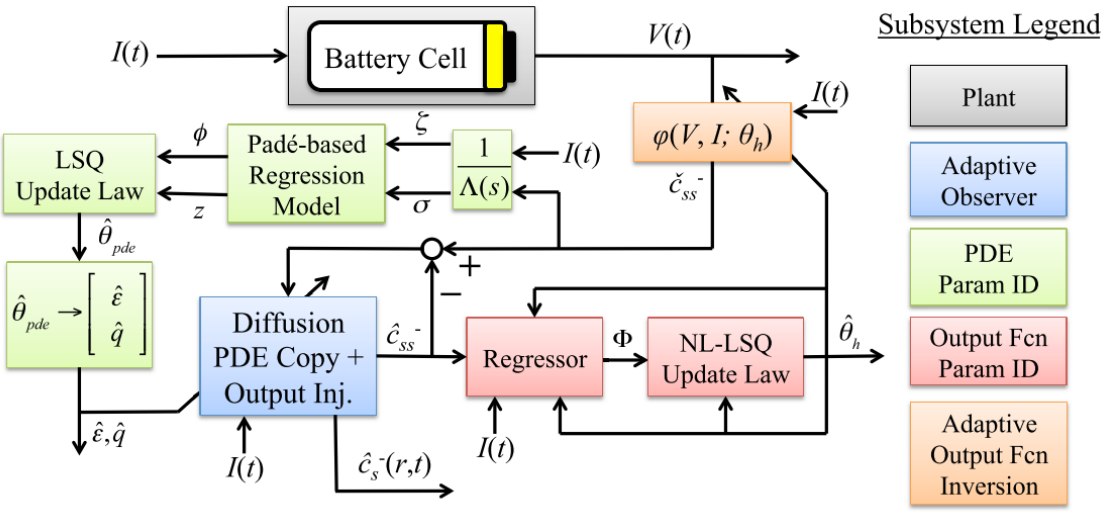

Figure 3.13: Block diagram of the adaptive observer [103].

The last method was a different strategy developed by G2 [105]. They developed a state space representation based on their own method, the discrete time realization algorithm (DRA) [74]. First they linearized the original model in order to derive the transfer functions of the system. Physical parameters did not play a role and this step was only required to be done once. Parameters of the cell were obtained by parameter obtention methods [116] and together with transfer functions the DRA method was used to generate a linear state space model, figure 3.14.

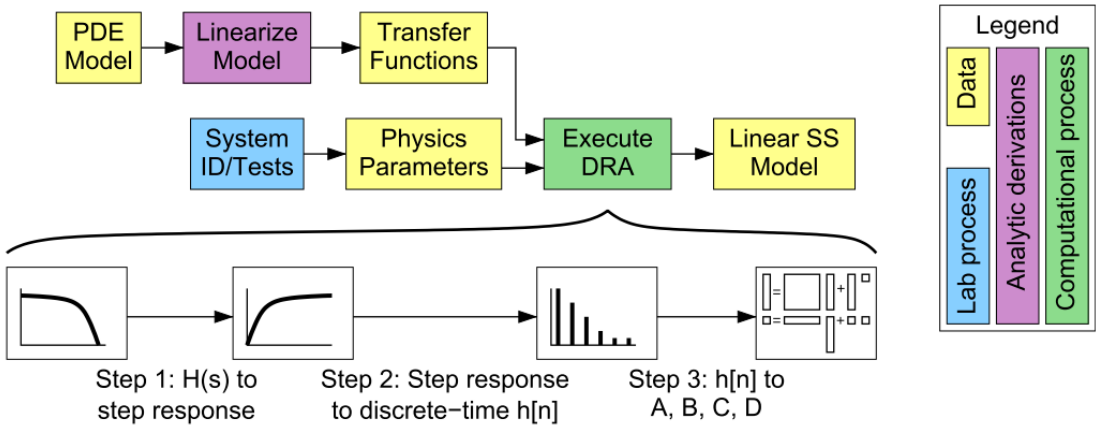

Figure 3.14: Approach to generating the linear state-space model [105].

Once a linear state space was obtained some corrections to describe the nonlinearity of the model were performed, figure 3.15.

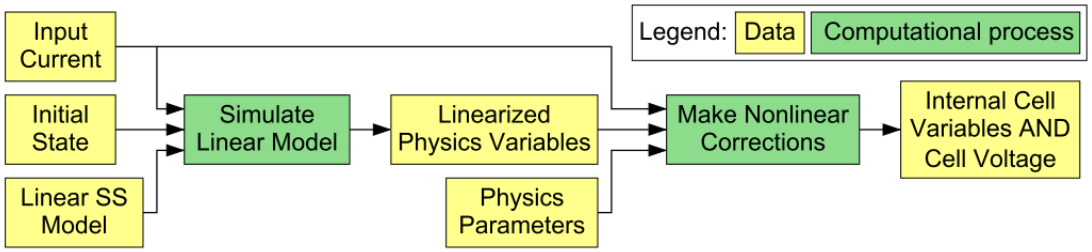

Figure 3.15: Simulating a reduced-order-model [105].

To model the influence of the temperature and SOC this authors implemented a model blending as shown in figure 3.16 [105], demonstrating its accuracy. Even multiple linear state space models needed to be stored in the memory of the microprocessor allowed maintaining the simplicity of the model and the fast solving. A diagram of the full approach implemented in MATLAB Simulink ® is shown in figure 3.17.

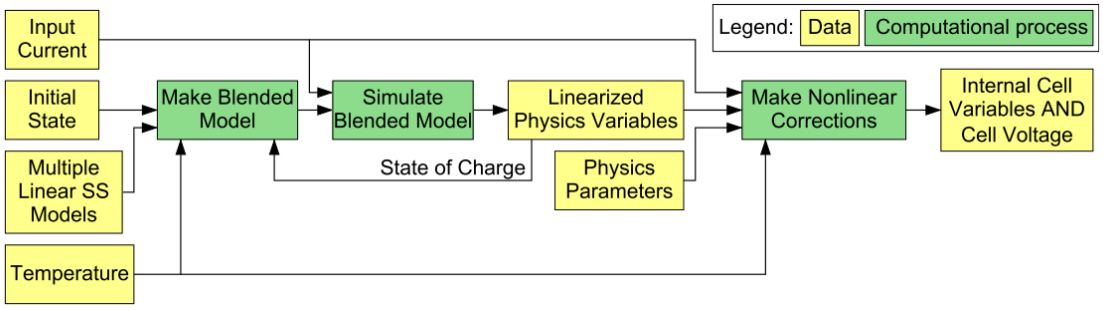

Figure 3.16: Simulating a cell using model-blending approach [105].

They also implemented an extended Kalman filter and gave proof of the good cells internal variables estimation [88].

3.1.2.3 Parameters update

It is well known that cells parameters change while aging. Even this is not the case for the whole set of parameters some of them were demonstrated to follow a defined progression in function of the SOH [75]. The direct consequence of this variation is the necessity to update the parameters values so an accurate prediction is maintained over the whole life of the battery.

Depending on the model solving method, or the way the model is reduced, this update implies different approaches. G1 authors used a closed loop to update their observer, and therefore the system did not need to be stopped or externally updated, figure 3.13.

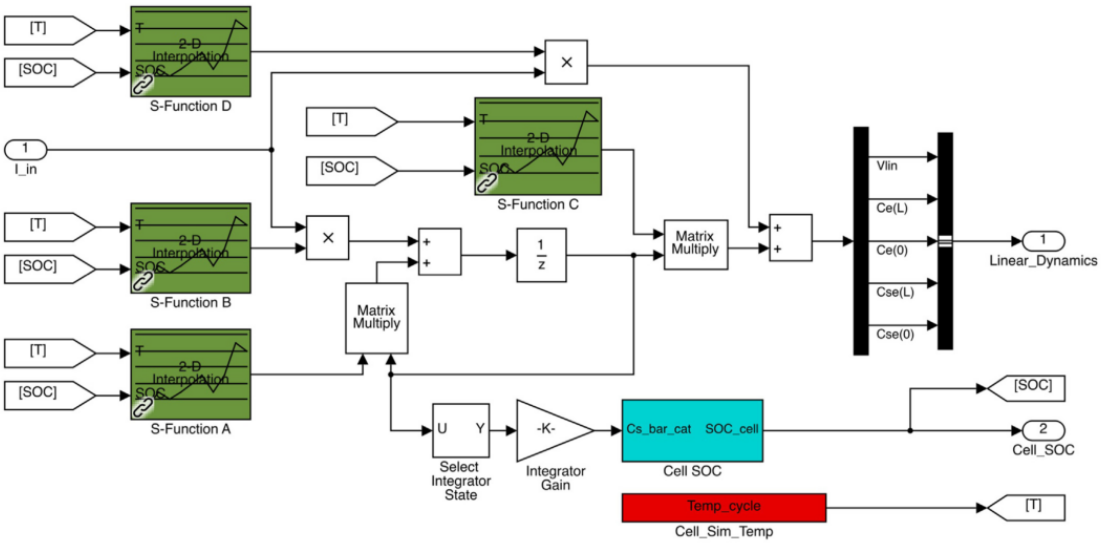

Figure 3.17: An implementation of the model-blending approach using MATLAB Simulink [105].

G2 authors also studied this problem, in this case as their ROM had a an offline computation step so some parameters could not be updated online. This is, when the parameters were determined to change significantly a different ROM was needed. In addition they also published relevant work using Kalman filters to use their model in real case scenarios [117] what could mitigate the experimental errors up to some level. This system was able to adapt the state vector of the state space model in order to improve the prediction as a function of a measured variable (cell voltage in this case). Nevertheless, this solution was not enough to mitigate the parameters evolution during aging and they further developed interacting multiple model Kalman filters-based methodologies [39, 40].

3.1.2.4 Validation

Validation is always a crucial step to demonstrate the validity of any systems. However, there are some issues that make the validation of these type of systems difficult. First of all when considering a system that controls a battery cell, several steps need to be fulfilled as explained along this document. Nowadays this is not trivial since most of the authors work only in specific topics, table 3.3, what makes very difficult to have a complete system that could be validated. In addition, cells internal variables can not be easily measured, so there is no data to compare the predicted values.

All this facts forced researchers working in this field to pseudo empirical data-based validation. This data is generated using higher order models (normally with dedicated software as COMSOL Multiphysics). It is therefore a big challenge to validate rigorously the proper functioning of both, models and online systems.

Table 3.3: Overview of the working fields for the considered groups.

Group	Model selection	Model resolution	Paramters update	Validation
G1	P2D/SP	Adaptative PDE observer	YES	Pseudo empirical data
G2	P2D	State space (DRA)	YES	Pseudo empirical data
G3	P2D	State space (finite difference/orthogonal collocation)	NO	Pseudo empirical data
G4	P2D	State space (orthogonal collocation)	NO	Pseudo empirical data

Table 3.3 shows an overview of the gathered different approaches. The most robust one is proposed by G2, giving internal variables prediction errors (compared to FOM data). The easy implementation and fast resolution without loss of accuracy provides a perfect scenario to advance in the field of battery control. Furthermore the parameter update system proposed by G1 and G2 are also of great interest as parameters values can be estimated without interrupting the system operation.

3.1.3 State of the art conclusions

Along the state of the art the conception of electrochemical models, description, types and characteristics have been presented as well as the solving methods and available software. The P2D model stand out as it is the more accurate and complete approach to model a battery cell. In the following this model will be used on the one hand as a reference or full order model and as the starting point to create a reduced order model.

Reduced order model approaches has also been presented identifying four standing out work groups. The approach of the second work group (G2) will be adopted as a base due to its simplicity, versatility and prove of accuracy in their reduced order model. Along the rest of the chapter then, this work will be continued in order to develop a functional online system.

3.2 Electrochemical model implementation

This section gathers the reduced order model implementation process. An augmented state space model was created based on the reduced order model developed by Plett *et al.* [73], so this augmented state space model form was suitable for a sigma point Kalman filter structure. The sigma point Kalman filter was also designed and implemented based on Plett *et al.* [73] and applied to the augmented state space model for the whole SOC range, taking also into account the temperature variation. This implied to deal with the filter update when the SOC or temperature variation forced to change the reduced order model composition. This filter was used to palliate the inaccuracies that could be generated throughout the model reduction process and the experimental error.

The implementation of a thermal model is out of the scope of this thesis. The temperature prediction is not a mandatory variable in order to evaluate the validity of electrochemical models for control purposes. So temperature will be treated as an input to the model and this topic will be treated in following works.

3.2.1 Reduced order model

The reduced order model was implemented in MATLAB Simulink. The algorithm was developed in MATLAB code and finally inserted in MATLAB Simulink as a "Matlab function block". The reason to this type of hybrid implementation was that this model will be linked with a Texas Instruments "TMS320F28379D" board in order to manage the measurements and send the control signals to a power converter as is explained in chapter 5.

The structure of the whole implementation is shown in figure 3.18. Initial State of the battery, applied current and temperature were considered as inputs for the model and the internal cell variables, SOC and voltage as outputs.

Looking deeper into the model three differentiated parts were identified. The first one is the augmented state space model that will be described in subsection 3.2.1.1. The second section corresponds to the main simulation loop in which the state space vector and the linear outputs of the model are calculated [73]. Finally nonlinear corrections needed due to the equations linearization process are done (subsection 3.2.1.3).

Also the previously generated linear state space models and the physic parameters of the cell (chapter 4) needed to be used, as shown in figure 3.18. The linear state space models

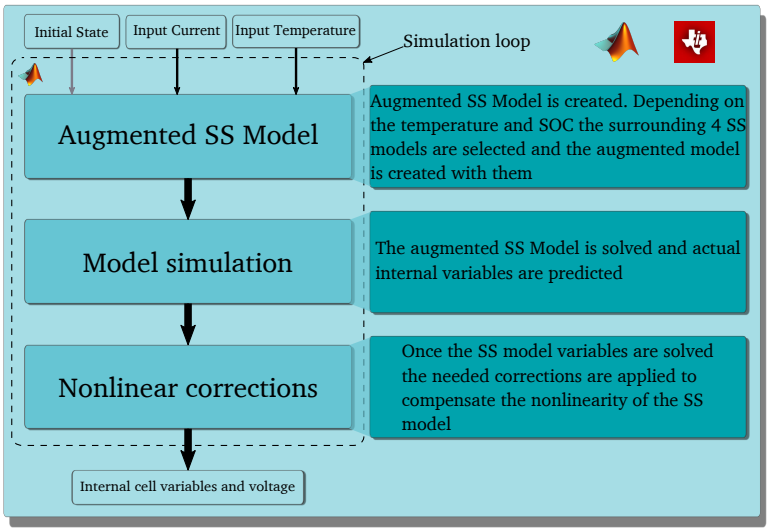

Figure 3.18: Scheme of the ROM model implementation.

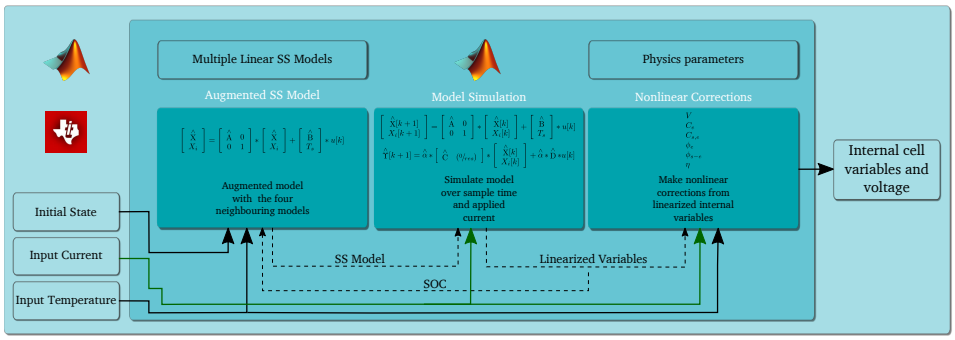

Figure 3.19: Scheme of the ROM model implementation.

used when blending the model were generated following the process in [73].

3.2.1.1 Augmented state space model

The augmented state space model followed the general state space form, shown in equations 3.2 and 3.3, where X is the state vector, u is the input, Y is the output and A, B, C, D were the matrices describing the battery. Also, the model need to be slightly modified as will be

explained along the next paragraphs.

$$\mathrm{X}[k+1] = \mathrm{A} * \mathrm{X}[k] + \mathrm{B} * u[k] \tag{3.2}$$

$$\mathrm{Y}[k+1] = \mathrm{C} * \mathrm{X}[k] + \mathrm{D} * u[k] \tag{3.3}$$

The whole model developed in this chapter was corrected with an SPKF (sigma point Kalman filter) explained in subsection 3.2.2. The SPKF and in general the Kalman filters are designed to modify the state vector of a model so the predictions match closer the reference measurement, therefore a single state space model is needed. This was a problem since a model blending is required to mitigate the fact that the ROMs are discrete (a set of ROMs linearized along SOC and temperature points was used), so in a real case scenario instead of a single ROM a set of ROMs was used.

The blending of the models was performed between the closest ROMs (the ROMs corresponding to the closest temperature and SOC points). Once these models were selected a bilinear interpolation was used minimizing the influence of using linearized ROMs (at least two different type of blendings can be used and will be addressed in the next paragraphs, once the augmented model have been created), figure 3.20.

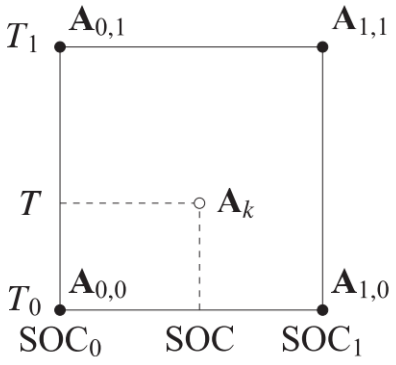

$$x = \frac{\mathrm{SOC} - \mathrm{SOC}_0}{\mathrm{SOC}_1 - \mathrm{SOC}_0}$$

$$y = \frac{T - T_0}{T_1 - T_0}$$

$$\mathbf{A}_k = (1-y)\big((1-x)\mathbf{A}_{0,0} + x\mathbf{A}_{1,0}\big) + y\big((1-x)\mathbf{A}_{0,1} + x\mathbf{A}_{1,1}\big)$$

Figure 3.20: Bilinear interpolation of the A matrix for "model" blending, adapted from [105].

As a single model was needed due to the use of a SPKF a possible solution was to build an augmented model. This model would then contain the selected four ROMs while still maintain

the form and properties of a state space model.

$$\hat{\mathrm{X}}[k+1] = \hat{\mathrm{A}} * \hat{\mathrm{X}}[k] + \hat{\mathrm{B}} * u[k] \tag{3.4}$$

$$\hat{\mathrm{Y}}[k+1] = \hat{\mathrm{C}} * \hat{\mathrm{X}}[k] + * \hat{\mathrm{D}} * u[k] \tag{3.5}$$

Equations 3.4 and 3.5 show the augmented model description. Looking deeper into this formulation is shown that this model contained the four ROMs used for the blending, equations 3.6 and 3.7.

$$\hat{\mathrm{X}}[k+1] = \begin{bmatrix} A_1 & 0 & 0 & 0 \\ 0 & A_2 & 0 & 0 \\ 0 & 0 & A_3 & 0 \\ 0 & 0 & 0 & A_4 \end{bmatrix} * \begin{bmatrix} X_1[k] \\ X_2[k] \\ X_3[k] \\ X_4[k] \end{bmatrix} + \begin{bmatrix} B_1 \\ B_2 \\ B_3 \\ B_4 \end{bmatrix} * u[k] \tag{3.6}$$

$$\hat{\mathrm{Y}}[k+1] = \begin{bmatrix} C_1 & 0 & 0 & 0 \\ 0 & C_2 & 0 & 0 \\ 0 & 0 & C_3 & 0 \\ 0 & 0 & 0 & C_4 \end{bmatrix} * \begin{bmatrix} X_1[k] \\ X_2[k] \\ X_3[k] \\ X_4[k] \end{bmatrix} * \begin{bmatrix} D_1 \\ D_2 \\ D_3 \\ D_4 \end{bmatrix} * u[k] \tag{3.7}$$

Where the elements in the matrices for a 5th order model (the order of the model was decided while the DRA method was applied [73]) are:

- $X_n[k]$ is a $1X5$ matrix
- A_n is a $5X5$ matrix
- B_n is a $1X5$ matrix
- C_n is a $NX5$ matrix, depending N in the number of outputs of the model
- D_n is a $NX1$ matrix, depending N in the number of outputs of the model

At this point there was still an issue to deal with before finishing the augmented model. All the ROMs contained an extra state responsible of integrating the time [73]. This state was used to add a residue generated while the linearization of the FOM equations and dependant on the time integral. This issue could be ignored as each integrator state should be the same

(except for numerical calculation inaccuracies and without paying attention to the extra computational effort). Nevertheless as a SPKF needed to be implemented and the filter modified this integrator states it was conceptually wrong to make a different correction to every integrator state. For this reason and to avoid unnecessary operations in the developed augmented state space model a single integrator state was used, as shown in equations 3.8 and 3.9.

$$\hat{\mathbf{X}}[k+1] = \begin{bmatrix} A_1 & 0 & 0 & 0 & 0 \\ 0 & A_2 & 0 & 0 & 0 \\ 0 & 0 & A_3 & 0 & 0 \\ 0 & 0 & 0 & A_4 & 0 \\ 0 & 0 & 0 & 0 & 1 \end{bmatrix} * \begin{bmatrix} X_1[k] \\ X_2[k] \\ X_3[k] \\ X_4[k] \\ X_i[k] \end{bmatrix} + \begin{bmatrix} B_1 \\ B_2 \\ B_3 \\ B_4 \\ T_s \end{bmatrix} * u[k] \tag{3.8}$$

$$\hat{\mathbf{Y}}[k+1] = \begin{bmatrix} C_1 & 0 & 0 & 0 & (0/_{res})_1 \\ 0 & C_2 & 0 & 0 & (0/_{res})_2 \\ 0 & 0 & C_3 & 0 & (0/_{res})_3 \\ 0 & 0 & 0 & C_4 & (0/_{res})_4 \end{bmatrix} * \begin{bmatrix} X_1[k] \\ X_2[k] \\ X_3[k] \\ X_4[k] \\ X_i[k] \end{bmatrix} + \begin{bmatrix} D_1 \\ D_2 \\ D_3 \\ D_4 \end{bmatrix} * u[k] \tag{3.9}$$

Where the elements in the matrices were as follows (note that elements are smaller as the individual integrator states were removed):

- $X_n[k]$ is a $1X4$ matrix
- A_n is a $4X4$ matrix
- B_n is a $1X4$ matrix
- C_n is a $NX4$ matrix, depending N in the number of outputs of the model
- $(0/_{res})_n$ is a $NX1$ matrix, depending N in the number of outputs of the model. The symbol represented the residue that might be added to the adequate position depending on the output, for example if $(0/_{res})_n$ was a $1X1$ matrix and the output needed to be corrected the value would be res and on the contrary 0
- D_n is a $NX1$ matrix, depending N in the number of outputs of the model

What could also be represented in a compact form, equations 3.10 and 3.11.

$$\begin{bmatrix} \hat{\mathrm{X}}[k+1] \\ \mathrm{x}_i[k+1] \end{bmatrix} = \begin{bmatrix} \hat{\mathrm{A}} & 0 \\ 0 & 1 \end{bmatrix} * \begin{bmatrix} \hat{\mathrm{X}}[k] \\ \mathrm{x}_i[k] \end{bmatrix} + \begin{bmatrix} \hat{\mathrm{B}} \\ T_s \end{bmatrix} * u[k] \tag{3.10}$$

$$\hat{\mathrm{Y}}[k+1] = \begin{bmatrix} \hat{\mathrm{C}} & (0/_{res}) \end{bmatrix} * \begin{bmatrix} \hat{\mathrm{X}}[k] \\ \mathrm{X}_i[k] \end{bmatrix} + \hat{\mathrm{D}} * u[k] \tag{3.11}$$

3.2.1.2 Blending the model

The ROM implemented along this document was composed of a set of ROMs due to the discrete nature of the linearization process. Each ROM composing the set was linearized around an specific SOC and temperature point thus, when the battery SOC and temperature evolved an appropriately linearized ROM was used. In the previous subsection an augmented ROM composed of 4 ROMs was developed in order to allow the use of a Kalman filter. However, there was still pending to manage on the one hand the selection of the ROMs composing the augmented model (as the SOC and temperature of the battery evolve) and on the other hand the relation between the obtained four subsets of predictions (which in this case were embedded in the output vector of the augmented model).

First the selection of the ROMs composing the augmented state space model was done. This selection was SOC and temperature dependant. The implementation was straightforward when these values were known as the nearest four models were used. The temperature was an input of the model so it was not needed to be calculated. On the contrary the SOC was a variable that needed to be estimated using the model. Therefore, the actual SOC value (what was the same as the previous step SOC prediction value) was used, figure 3.19. For the first time step the SOC was initialized and the predictions for the next steps were used in the following. The initial SOC value could be set estimating it be means of the open circuit voltage (OCV) relation to the state of charge. Nevertheless the accuracy of this estimation was not so crucial as a Kalman filter was used (subsection 3.2.2).

Once the ROMs were selected and the augmented model explained in the previous subsection, the blending was the next step. The model authors at UCCS reported in literature the "model blending", as mentioned in the state of the art of this chapter. This method was based on the interpolation of the A matrix of the system and transferring this influence of the four

models to the output equation, figure 3.20. This interpolation method was demonstrated to work properly as shown in [105].

There was however another attempt published by these authors called "Output blending" [118]. This approach was found to work better during constant current cycles, when the model evolves along the whole SOC range. Because of this reason, this blending technique was used and it is explained along the next paragraphs.

The "output blending" still maintained the conception of interpolating the influence of the four neighboring models, but the implementation was however completely different. The models outputs were computed individually opposite to the previous approach and was at the end, after all the predictions were calculated when the blending action was done.

To implement this approach in the augmented state space model a compact form was developed. Note that the blending action was taken when the outputs were computed, what means that the state equation remained unmodified and the action was introduced in the output equation.

Equation 3.12 shows the compact form of the state equation with the "Output blending". An $\hat{\alpha}$ matrix (equation 3.13) was introduced in the output equation being responsible of describing the relation between the four sets of predictions.

$$\hat{Y}[k+1] = \hat{\alpha} * \begin{bmatrix} \hat{C} & (0/_{res}) \end{bmatrix} * \begin{bmatrix} \hat{X}[k] \\ X_i[k] \end{bmatrix} + \hat{\alpha} * \hat{D} * u[k] \tag{3.12}$$

$$\hat{\alpha} = \begin{bmatrix} \alpha_1 & 0 & \cdots & 0 & \alpha_2 & 0 & \cdots & 0 & \alpha_3 & 0 & \cdots & 0 & \alpha_4 & 0 & \cdots & 0 \\ \cdots & \alpha_1 & 0 & \cdots & 0 & \alpha_2 & 0 & \cdots & 0 & \alpha_3 & 0 & \cdots & 0 & \alpha_4 & 0 & \cdots \\ \cdots & 0 & \ddots & 0 & \cdots & 0 & \ddots & 0 & \cdots & 0 & \ddots & 0 & \cdots & 0 & \ddots & 0 \end{bmatrix} \tag{3.13}$$

The $\hat{\alpha}$ matrix was a $5X4N$ size matrix, formed with the α_n components responsible of giving a certain weight to each set of predictions. This means that each prediction set corresponding to each ROM was multiplied by an α_n coefficient, bring the summation of all of them as follows ($\alpha_1 + \alpha_2 + \alpha_3 + \alpha_4 = 1$). More details about the construction of the $\hat{\alpha}$ matrix are given in appendix 7.1.

Calculation of the α_n coefficients was similar to the interpolation used in the "model blending". The coefficients were calculated as a function of the SOC and temperature, as shown in

figure 3.21 and equations 3.14-3.19.

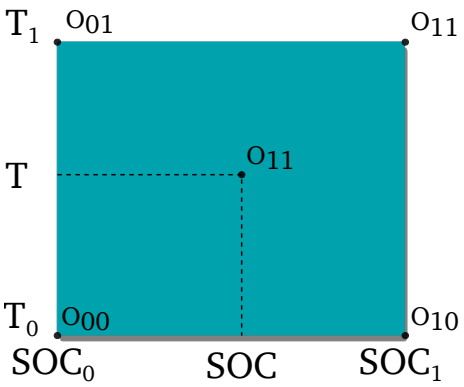

Figure 3.21: Bilinear interpolation for the ROMs output sets "O".

$$x = \frac{SOC - SOC_0}{SOC_1 - SOC_0} \tag{3.14}$$

$$y = \frac{T - T_0}{T_1 - T_0} \tag{3.15}$$

$$\alpha_1 = (1-y)(1-x) \tag{3.16}$$

$$\alpha_2 = (1-y)x \tag{3.17}$$

$$\alpha_3 = (1-x)y \tag{3.18}$$

$$\alpha_4 = yx \tag{3.19}$$

3.2.1.3 Outputs and nonlinear corrections

The reduced order model implemented in [73] was composed of nine outputs including the cell voltage V_{cell}, the concentration of the electrolyte (at the anode and cathode current collector) C_e, the solid surface concentration (at the solid-electrolyte interphase) C_s, the reaction flux j, the potential of the electrolyte (at the anode and cathode current collector) ϕ_e, the solid-electrolyte potential difference ϕ_{s-e} and the overpotential η. Due to the conception of the ROM the nonlinear components of the FOM equations were isolated and subtracted so the linearization step was possible. Consequently the linear outputs of the ROM needed to be corrected in order to model the nonlinearity of the real battery cell. In [73] and [48] the linear variables were noted with $\sim$ sign so the same notation was adopted throughout this document, more details about the symbols used in these corrections can be found in appendix

7.6. The needed corrections are enumerated and explained above.

1. Cell voltage

   The cell voltage can be calculated as follows.

$$\begin{aligned} v_{cell} &= {\phi_s}^{pos}(0,t) - {\phi_s}^{neg}(0,t) = \\ &= \eta^{pos}(0,t) + {\phi_e}^{pos}(L^{tot},t) + U_{ocp}^{pos}\left(C_{s,e}^{pos}(0,t)\right) + FR_f^{pos} j^{pos}(0,t) - \eta^{neg}(0,t) - \\ &\quad - {\phi_e}^{neg}(0,t) - U_{ocp}^{neg}\left(C_{s,e}^{neg}(0,t)\right) - FR_f^{neg} j^{neg}(0,t) \\ &= (\eta^{pos}(0,t) - \eta^{neg}(0,t)) + \tilde{\phi}_e(L^{tot},t) + \left(U_{ocp}^{pos}\left(C_{s,e}^{pos}(0,t)\right) - U_{ocp}^{neg}\left(C_{s,e}^{neg}(0,t)\right)\right) + \\ &\quad + F\left(R_f^{pos} j^{pos}(0,t) - R_f^{neg} j^{neg}(0,t)\right) \end{aligned} \tag{3.20}$$

   The linear voltage calculated with the state space model included the $\tilde{\phi}_e(L^{tot},t)$ and $F\left(R_f^{pos} j^{pos}(0,t) - R_f^{neg} j^{neg}(0,t)\right)$ terms. It was therefore necessary to add the rest of the terms as a nonlinear correction.

$$v_{cell} = v_{linear} + (\eta^{pos}(0,t) - \eta^{neg}(0,t)) + \left(U_{ocp}^{pos}\left(C_{s,e}^{pos}(0,t)\right) - U_{ocp}^{neg}\left(C_{s,e}^{neg}(0,t)\right)\right) \tag{3.21}$$

   Furthermore if the α coefficient was 0.5 the overvoltage could be simplified as follows.

$$\eta^d(z,t) = \frac{2RT}{F} asinh\left(\frac{j^d(z,t)}{2k_0^d\sqrt{C_e(z,t)\left(C_{s,\max}^d - C_{s,e}^d(z,t)\right)C_{s,e}^d(z,t)}}\right) \tag{3.22}$$

2. Concentration in Electrolyte

   The equilibrium concentration of the electrolyte value was subtracted during the linearization of the transfer function. Therefore to obtain the corrected nonliear value this term was manually added, as shown in equation 3.23.

$$C_e(x,t) = \tilde{C}_e(x,t) + C_{e,0} \tag{3.23}$$

3. Solid Surface Concentration

   The same way as with the concentration of the electrolyte the equilibrium concentration

of the solid was added to obtain the nonlinear variable, equation 3.24.

$$C_{s,e}(z,t) = \tilde{C}_{s,e}(z,t) + C_{s,0} \tag{3.24}$$

4. Potential of Electrolyte

   Following, the correction needed for the ROM prediction of the potential of the electrolyte is shown in, equation 3.25. More details about the correction can be found in [48].

$$\phi_e(x,t) = \tilde{\phi}_e(x,t) - \phi_{s-e}(0,t) \tag{3.25}$$

5. Solid-Electrolyte Potential Difference

   The correction applied to the solid-electrolyte potential difference is shown in 3.26. The reason behind this correction is the same as in the rest of variables, the removal of a pole in the original transfer function. The correction was not straightforward in this case and was modified for better performance. The derivation of this correction is explained in [48].

$$\phi_{s-e}(z,t) = \overset{\sim}{\phi}^{*}_{s-e}(z,t) + U_{ocp}(C_{s,avg}(t)) \tag{3.26}$$

6. Overpotential

   This thesis was specifically focused on the detection of lithium plating in the anode, the overpotential prediction was therefore essential. This variable could be calculated as in the cell voltage nonlinear correction. On the contrary if α was different than 0.5 the overpotential should have been calculated as follows.

$$\eta = \phi_s - \phi_e - U_{ocp} - FR_f j \tag{3.27}$$

3.2.2 Sigma point Kalman filter

Until this point of the chapter, a reduced order model able to predict the internal variables of the cell and the voltage was developed. This model was suitable in terms of memory size, and computational requirements for its implementation in a microcontroller. However the models were designed with some assumptions that were not realistic, and in the other hand

some considerations related to the conception of the system itself needed to be revised.

- Every single battery cell is different

  All the battery cells even from the same brand or the same model are slightly different. The manufacturing processes even if accurate are not perfect and therefore inhomogeneities related to the materials and assembly appear in the final product. This could be considered as a minor effect but if for example the initial capacity dispersion between cells is considered can be seen that meaningful differences appear. The model created for a certain sample cell (the one used for the parametrization of the model) does not necessarily need to be accurate for other very similar cells. Furthermore the error in the internal variables predicted by this model could not be considered accurate for any cell, as this inhomogeneities could not be considered negligible.

- The cell current and temperature were not be accurately measured

  The current applied to the cell and the temperature were the inputs of the model. In a theoretical conception this was data introduced in the model in a straightforward manner. When thinking about a real case scenario on the contrary, this step carried an intrinsic error, as any sensor carries a certain error.

- The reduced order model had a prediction error

  The used ROM had an error compared with the data obtained from the FOM. This error was caused by the reduction process and the discrete nature of the reduced order model (even this fact was mitigated blending the models). Not only this even the FOM had an intrinsic error due the taken assumptions and the formulation of the equations (that are only a representation of the reality).

All these facts made necessary to take a solution in order to reduce the amount of error in the predictions and make the system valid for any cell (cells that are the same model of the same brand). As mentioned in the state of the art of this chapter, Kalman filters were a possible solution to this problem.

Kalman filters are based on a framework named "sequential probabilistic inference" [15]. Using a model of the described system and a feedback of the real response of this system, the filters made the predictions converge to more accurate results. In the specific case of a battery cell the more evident response of the system was the output voltage which was used as feed-

back (figure 3.22). It is worth to mention at this point that the voltage sensor also introduced an error the same way the current sensor did it, this error as the ones itemized above were taken into account when the filter was developed. The filter was not able to make a perfect prediction as the errors coming from the sensors or the model itself were not deterministic (the errors explained in the list above), it used probability to give a mean prediction, and more important, confidence bounds. This meant that the filter would accurately give a prediction and confidence bounds where the true value was contained. The theory behind the "sequential probabilistic inference" and Kalman filters is complicated and out of the scope of this thesis, for the interested readear a detailed explanation can be found in [15].

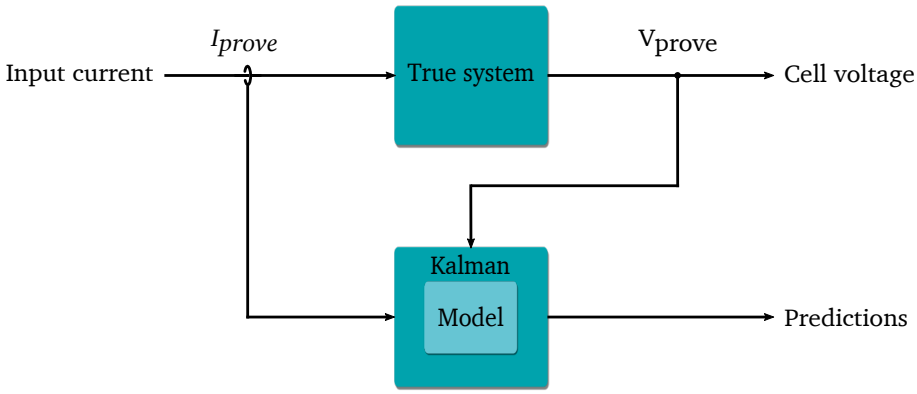

Figure 3.22: Structure of the model with a Kalman filter.

Different Kalman filters can be found in literature. The linear Kalman filter for example, is a very well known approach demonstrated to have a very good response when applied to linear systems, while the extended Kalman filter or nonlinear Kalman filter is an evolution of the linear Kalman filter specifically designed for nonlinear systems. Moreover more advanced versions have also been developed as adaptive Kalman filters. A thorough study of this types of filters applied to the ROM developed at UCCS was carried out by [117]. The main conclusion of this work was that due to the nonlinear nature of the battery a nonlinear filter was required, being the SPKF the one showing the best performance. In addition to this the SPKF had several advantages when comparing it with the extended Kalman filter (the most popular form of nonlinear Kalman filter), these differences are explained below and summarized from [15].

- Derivatives did not need to be computed

  When using a SPKF some points (sigma points) were used to define the variation of

the output response. Those input points or sigma points were selected using a normal distribution around the working point. This approach made that derivatives were not needed, as they are in the extended Kalman filter. This step is the most common source of errors when implementing Kalman filters, what makes this property even more desirable.

- No need of differentiable functions

  As the derivatives of the equations were not necessary those equations did not have to be differentiable, what made the filter valid for a wider range of systems.

- Better covariance approximations

  Typically better covariance approximations were found to be achieved, leading to better state estimations and error bounds

- Comparable computational complexity

  Even sigma points needed to be computed, meaning that the model was executed more times, the computational complexity remained similar in addition to the advantages described above.

3.2.2.1 Sigma point Kalman filter implementation

Since Kalman filters are based on the "sequential probabilistic inference", a six step process was followed. There were three steps to calculate the prediction and another three to correct that prediction. In the following lines the six steps will be briefly explained (more detailed information can be found in [117, 15] and a summary of the equations in appendix 7.2).

Before explaining the six steps process it was necessary to define the model used with the Kalman filter. This nonliear state space model has been explained in subsection 3.2.1.1 and will be represented with the following notation.

$$x_k = f(x_{k-1}, u_{k-1}, w_{k-1}) \tag{3.28}$$

$$y_k = h(x_k, u_k, v_{k-1}, w_{k-1}) \tag{3.29}$$

Equations 3.28 and 3.29 represent the state equation and output equation. This means that f is equivalent to equation 3.10 and h to equation 3.12.

An augmented random vector x_k^a that gathered the randomness of the state, process and sensor noises was also needed. The process randomness was related to the current sensor noises and the sensor randomness to the voltage sensor for the feedback. This was an adopted assumption as it was assumed the process randomness to be caused by the current sensor.

$$x_k^a = \left[x_k^T, w_k^T, v_k^T\right]^T \tag{3.30}$$

Moreover, the state estimation error covariance matrix $\Sigma_{\tilde{x},k}^a$ was needed.

$$\Sigma_{\tilde{x},k}^a = diag\left(\Sigma_{\tilde{x},k}, \Sigma_{\tilde{w}}, \Sigma_{\tilde{v}}\right) \tag{3.31}$$

The SPKF filter was based on propagating the sigma points through the state and output equations, being this sigma points created as a function of the augmented random vector x_k^a . Certain p sigma points were then used to create the χ_k^a matrix.

$$\chi_k^a = \left[\left(\chi_k^x\right)^T, \left(\chi_k^w\right)^T, \left(\chi_k^v\right)^T\right]^T \tag{3.32}$$

$$p = 2\dim(x_k^a) \tag{3.33}$$

- Step 1a. State estimate time update:

  To start Step 1a the augmented posteriori state estimate $\hat{x}_{k-1}^{a,+}$ and augmented state estimation error covariance matrix $\Sigma_{\tilde{x},k-1}^{a,+}$ were generated (this values were representing the previous time interval values as denoted with + and organized as in equations 3.30 and 3.31). Next the p sigma points were generated as shown in equation 3.34 (note that {} signs denoted a group instead of a vector [15]).

$$\chi_{k-1}^{a,+} = \left\{\hat{x}_{k-1}^{a,+}, \hat{x}_{k-1}^{a,+} + \gamma\sqrt{\Sigma_{\tilde{x},k-1}^{a,+}}, \hat{x}_{k-1}^{a,+} - \gamma\sqrt{\Sigma_{\tilde{x},k-1}^{a,+}}\right\} \tag{3.34}$$

  The part of the generated $\chi_{k-1}^{a,+}$ matrix related to the state vector (excluding the process and sensor noise positions) was extracted to generate $\chi_{k,i}^{x,-}$. All the sigma points together with the mean were then propagated through the state equation f as shown in equation 3.35.

$$\chi_{k,i}^{x,-} = f\left(\chi_{k-1}^{x,+}, u_{k-1}, \chi_{k-1,i}^{w,+}\right) \tag{3.35}$$

Finally a weighted mean of the sigma points was performed with the $\alpha_i^{(m)}$ column to calculate the predicted mean state vector $\hat{x}_k^-$.

$$\hat{x}_k^- = \sum_{i=0}^{p} \alpha_i^{(m)} \chi_{k,i}^{x,-} \tag{3.36}$$

- Step 1b. Error covariance time update

  In step 1b the error covariance was calculated as shown in equation 3.37. This operation subtracted the mean value from each sigma point.

$$\widetilde{\chi}_{k,i}^{x,-} = \chi_{k,i}^{x,-} - \hat{x}_k^- \tag{3.37}$$

  To calculate the error covariance a weighted mean was again applied with the column $\alpha_i^{(c)}$.

$$\Sigma_{\tilde{x},k}^- = \sum_{i=0}^{p} \alpha_i^{(c)} \left(\widetilde{\chi}_{k,i}^{x,-}\right)\left(\widetilde{\chi}_{k,i}^{x,-}\right)^T \tag{3.38}$$

  A simpler computation could be done by this modification.

$$\Sigma_{\tilde{x},k}^- = \left(\widetilde{\chi}_{k}^{x,-}\right) diag\left(\alpha^{(c)}\right)\left(\widetilde{\chi}_{k}^{x,-}\right)^T \tag{3.39}$$

- Step 1c. Output estimate

  To finish with the prediction steps the output estimate was calculated. The sigma points representing the randomness of the state prediction computed in step 1a, as the ones for process and sensor noise, were propagated through the output equation h.

$$\mathrm{y}_{k,i} = h\left(\chi_{k,i}^{x,-}, u_k, \chi_{k-1,i}^{v,+}, \chi_{k-1,i}^{w,+}\right) \tag{3.40}$$

  Furthermore as it was done with the mean state vector prediction a weighted mean output prediction $\hat{y}_k$ was calculated.

$$\hat{y}_k = \sum_{i=0}^{p} \alpha_i^{(m)} \mathrm{y}_{k,i} \tag{3.41}$$

- Step 2a. Estimator gain matrix

To start with the correction steps, the required covariance matrices were computed with the results from the previous prediction states (equations 3.42 to 3.44).

$$\tilde{\mathrm{y}}_{k,i} = \mathrm{y}_{k,i} - \hat{y}_k \tag{3.42}$$

$$\Sigma_{\tilde{y},k} = \sum_{i=0}^{p} \alpha_i^{(c)} \left(\tilde{\mathrm{y}}_{k,i}\right)\left(\tilde{\mathrm{y}}_{k,i}\right)^T \tag{3.43}$$

$$\Sigma_{\tilde{x}\tilde{y},k}^{-} = \sum_{i=0}^{p} \alpha_i^{(c)} \left(\widetilde{\mathcal{X}}_{k,i}^{x,-}\right)\left(\tilde{\mathrm{y}}_{k,i}\right)^T \tag{3.44}$$

After, the state estimator gain matrix L_k was computed.

$$L_k = \Sigma_{\tilde{x}\tilde{y},k}^{-} \Sigma_{\tilde{y},k}^{-1} \tag{3.45}$$

- Step 2b. State estimate measurement update

  When the estimator gain matrix was calculated the state measurement was updated using the y_k value from the feedback (the reference value obtained with the voltage sensor).

$$\hat{x}_k^{+} = \hat{x}_k^{-} + L_k\left(y_k - \hat{y}_k\right) \tag{3.46}$$

- Step 2c. Error covariance measurement update

  To finish with the process, the error covariance measurement was updated so all the necessary values for the next iteration were computed.

$$\Sigma_{\tilde{x},k}^{+} = \Sigma_{\tilde{x},k}^{-} - L_k \Sigma_{\tilde{y},k} L_k^T \tag{3.47}$$

In the particular case of the reduced order model that has been created during this thesis nonlinear corrections were contemplated as shown in figure 3.19. This corrections were also needed when implementing the Kalman filter, and applied when the sigma points were propagated through the output equation h.

Another issue that needed to be taken into account was that even the state vector was corrected the model predicted more outputs than the cell voltage. It was necessary then to recalculate this electrochemical variables again, after the estate vector was corrected in step 2b. This corrections were applied right after step 2c and referred as the 3a step.

- Step 3a. Calculation of updated electrochemical variables

The electrochemical states predicted by the model were calculated as shown in equations 3.48 to 3.50.

$$\chi 2_k = \left\{ \hat{x}_k^+, \hat{x}_k^+ + \gamma\sqrt{\Sigma_{\tilde{x},k}^+}, \hat{x}_k^+ - \gamma\sqrt{\Sigma_{\tilde{x},k}^+} \right\} \tag{3.48}$$

$$\mathrm{y}2_{k,i} = h_2\left(\chi 2_{k,i}, u_k, \chi_{k-1,i}^{v,+}, \chi_{k-1,i}^{w,+}\right) \tag{3.49}$$

$$\hat{y}2_k = \sum_{i=0}^{p} \alpha_i^{(m)} \mathrm{y}2_i \tag{3.50}$$

To finish, nonlinear corrections were applied to the electrochemical states, obtaining the values of the electrochemical variables. To gather all the steps and their implementation, the whole system structure whit the SPKF is shown in figure 3.23.

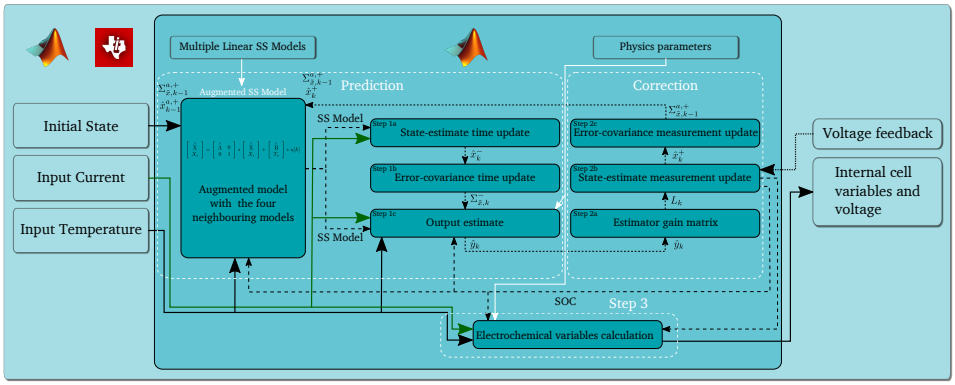

Figure 3.23: Scheme of SPKF and ROM model implementation.

It is worth to mention at this point that during the design of the SPKF some assumptions were taken. On the one hand, during the design of the SPKF filter the process noise was assumed to be caused only by the current sensor. Furthermore, the sensor noise was assumed to be independent from the current sensor noise and attributed to the voltage sensor. On the other hand the temperature was measured and introduced in the model as an input, this value was measured but no error was considered. Despite this assumptions were taken, the results were proven to be in a very good agreement with the reality (not experimental but virtual data) as will be demonstrated in section 3.3.

3.2.2.2 Sigma point Kalman filter initialization

The initialization of Kalman filters was a nontrivial and key step. State vector and error covariance needed to be initialized, being this initialization of great influence in the filter immediate response. Moreover, a very bad initialization could cause that the filter got lost. In addition, the covariances of the process noise and the sensor noise also needed to be initialized. This is an extensive field out of the scope of this thesis, and the used values were obtained based on an iterative trial and error process [117], proven to work properly can be seen in chapter 5. The used values are the following.

$$\hat{x}_0^{a,+} = [0,0,0,0,0,0,0,0,0,0,0,0,0,0,0,0,0,0,0,0,0] \tag{3.51}$$

$$\begin{aligned} \Sigma_{\tilde{x},0}^{a,+} &= diag\left(\Sigma_{\tilde{x},0}^{+}, \Sigma_{\tilde{w}}, \Sigma_{\tilde{v}}\right) = \\ &= diag(10,10,10,10,10,10,10,10,10,10,10,10,10,10,10,10,10,10^6,0.4,0.1) \end{aligned} \tag{3.52}$$

In addition, the ROM model used in this thesis had a particularity that specially affected the initialization of the filter. The augmented model was composed of four ROM models, selected in function of the temperature and SOC. The problem arised when the ROMs composing the augmented model were changed (when the cell entered a different temperature or SOC section) and consequently the augmented model changed as well. On the other hand the covariance values did not necessarily make sense when the model was changed.

To solve this problem, the part of the state vector corresponding to the changed ROMs was introduced in it when the augmented model was created (this state vectors were updated since the state equation was executed in every step for all the ROMs maintaining them updated) as it would be done even if the SPKF was not used. Regarding the covariance values, it was assumed that the covariance would not change significantly for the new augmented model. In addition the part of the augmented model that was changed would not affect in the right after time steps, due to the blending (for those new ROMS the blending factor will start as 0) and consequently the covariance values would evolve smoothly, adapting without accuracy loss in the prediction. It is worth to mention that to take this assumption it was key to use a single integrator state for all the models so the corrections applied to that state would keep sense even if the augmented model was modified. The result obtained with this assumption will be discussed in section 3.3.

3.3 Experimental results and validation

This section is dedicated to the evaluation of the ROM and the SPKF.

Whether full order models implemented in FEM simulations or reduced order models need to make an estimation error when looking to real cells variables prediction. It is important therefore to evaluate this error in order to verify and quantify the accuracy of a model. Due to the need of specific equipment and lack of validated techniques it is very difficult to measure the internal variables of batteries. Up to the date the estimation of those variables is one of the main benefits of this type of battery models, being temperature and terminal voltage the only easily accessible variables. In the model developed along this chapter temperature was treated as an input and therefore could not be used for validation purposes. Remained the cell terminal voltage then to validate the model. This variable can be a good indicator of the overall model accuracy, but it was not necessarily enough prove of the correct internal variables prediction due to the low impact of some of them in the voltage response (note further than the OCV defines the DC component of the voltage response, having normally most of the weight of the prediction).

Within this section data from a FOM developed in COMSOL Multiphysics was used as virtual data. This data was enough to validate the ROM development (as the intrinsic errors coming from the model definition itself, the parameterization and measurements were isolated) and a very close approximation to the SPKF working scenario. The internal variables ($C_e, C_{s,e}, \phi_{s-e}, j$), voltage and SOC values for the case where only the ROM was used and with the corrections of the SPKF are going to be presented compared to the FOM.

3.3.1 Electrochemical variables evaluation

Once virtual data is obtained from the FOM a method to quantify the error faithfully was needed. In this document, an analysis of the error based on the variability of the FOM predictions was adopted. This approach allowed a more standard view of the error and the effect on latter steps as capacity fade or SOF management. Maximum and minimum values of each internal cell variable were identified , so a direct image of the maximum variability of each prediction was obtained.

Two types of profiles were used to evaluate the maximum variability of the battery variables, constant current charge and discharges at the different C-rates, and high current pulses

(5C discharge and 1C charge as it was the current limit of the battery according to its datasheet) at different SOC values (figure 3.24 shows the applied current at 1,0.9,0.8,0.7,0.6,0.5,0.4,0.3,0.2 and 0.1 SOC).

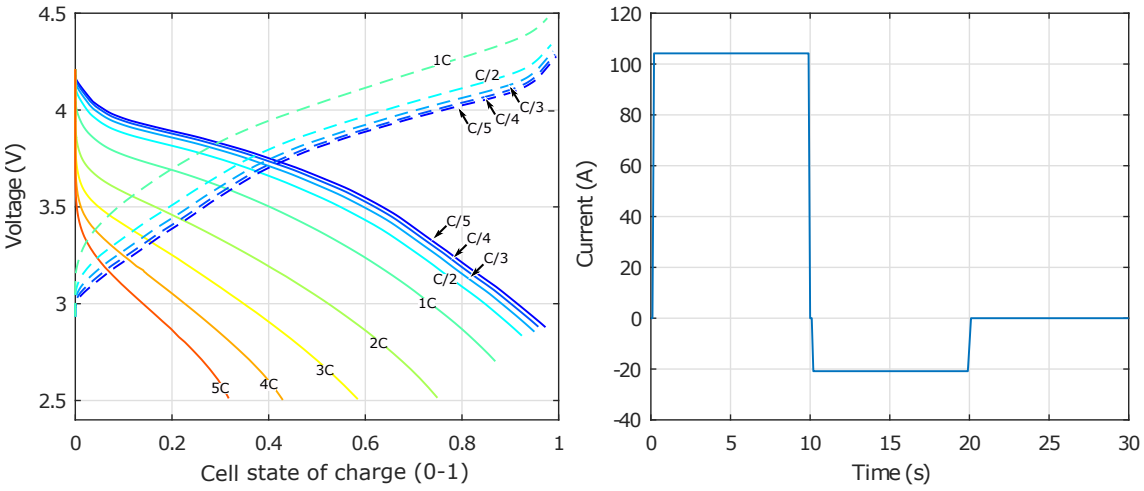

Figure 3.24: Cell voltage at different charge and discharge rates and maximum current pulses.

These profiles were selected in order to achieve the maximum and minimum values of the variables inside the cell. DC limit conditions were achieved with the full galvanostatic charge and discharges and maximum and minimum polarization effects were considered with the current pulses. According to the performed simulations the variability values that will be used for the error evaluation are shown in table 3.4. These values gave an overall and meaningful image of the amount of error made in the predictions.

Table 3.4: Variability of FOM electrochemical variables predictions.

Variables	Maximum	Minimum	Variability
C_e	2.7520e+03	1.2534e+03	1.4986e+03
$C_{s,e}$	2.0729e+04	1.1075e+03	1.9622e+04
ϕ_{s-e}	4.4058	-0.0329	4.4387
j	4.1380e-04	-2.8386e-04	6.9765e-04

3.3.2 Model evaluation without aging

Whit a proper error evaluation system it was necessary to evaluate the performance of the ROM and the SPKF corrected predictions. In a first case scenario and for the sake of simplicity a single charge and discharge cycle was used, without considering that the cell would age during its lifetime. Figure 3.25 shows the voltage and state of charge predictions.

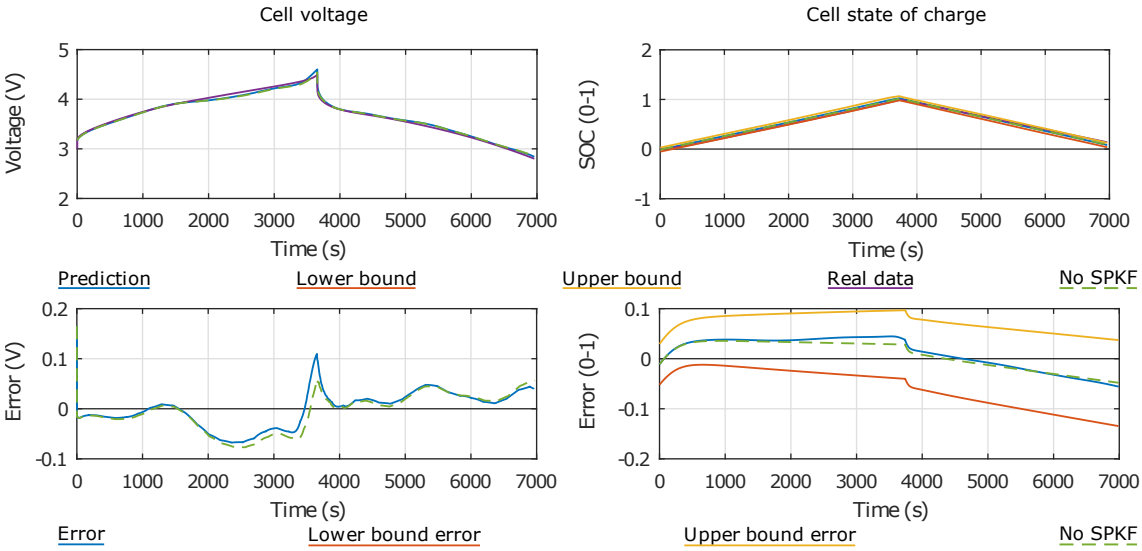

Figure 3.25: Voltage and state of charge predictions without aging influence.

As stated before even if voltage was not an enough correctness prove, together with the SOC gave a good image of the models performance. In this charge and discharge cycle the voltage error was kept under ± 0.1V and the SOC error under ±0.05 in the worst case. Furthermore when using the SPKF, the SOC prediction was kept all the time between the upper and lower boundaries assuring a realistic state of charge prediction.

Figures 3.26 to 3.29 show the ROM and SPKF results for C_e, $C_{s,e}$, ϕ_{s-e} and j in the negative electrode. All the ROM predictions estimated accurately the true data with a negligible error. SPKF predictions were similar and what it is more important, the true data remained inside the error boundaries.

Taking a deeper look into the results could be seen that there were some small peaks or jumps in the SPKF predictions (this phenomena can be seen clearly in figure 3.26).The reason behind this SPKF behavior was due to the SPKF update, explained in section 3.2.2.2. The ROM model did not present peaks like the ones of the SPKF what meant that the model update due to a change of the SOC region and the model blending was working correctly. Consequently this phenomena was explained with the covariance values update (it was assumed that covariance values did not change from one set of models to the next). Despite these peaks the SPKF was correctly tracking the variables and it was recovered from those perturbations very fast (take into account that a constant discharge profile is one of the most severe working scenarios for the model blending as passes through all the SOC ranges). Could be considered then that

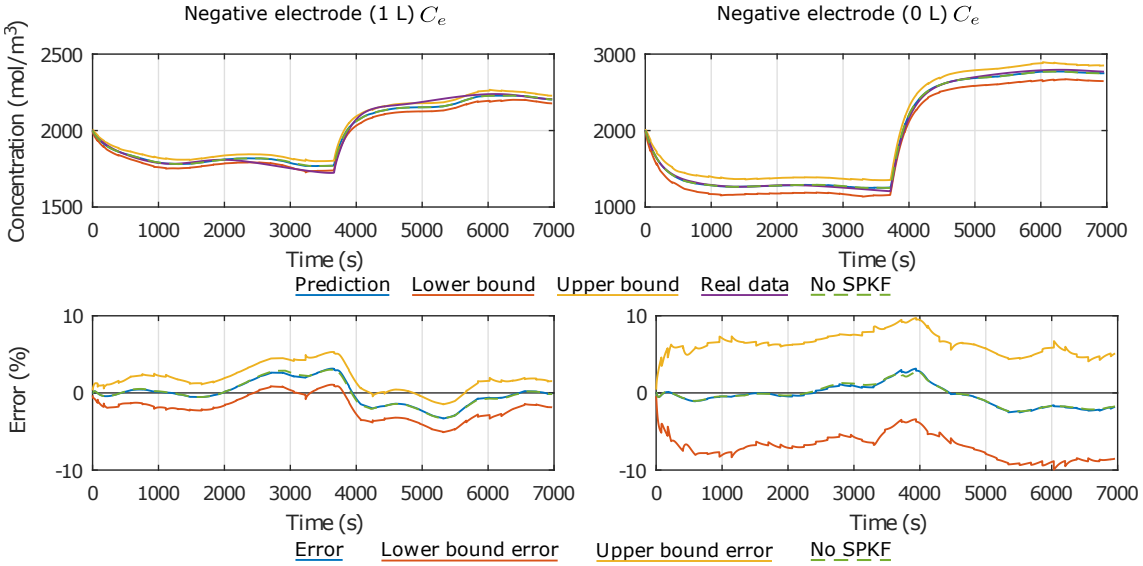

Figure 3.26: ROM, FOM and SPKF predictions and errors for C_e.

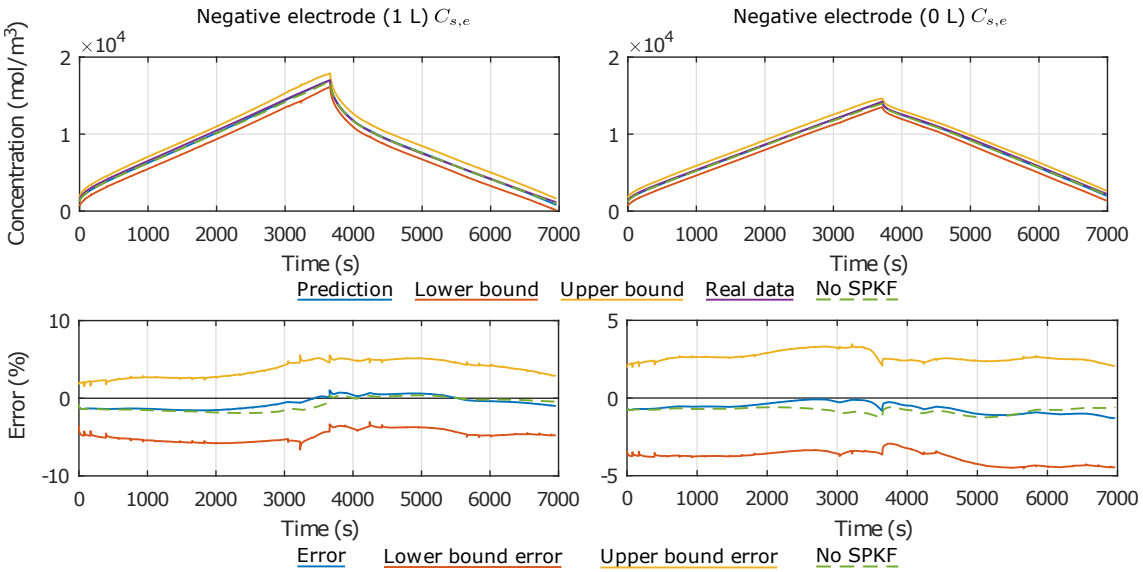

Figure 3.27: ROM, FOM and SPKF predictions and errors for $C_{s,e}$.

the taken assumption was working correctly and those peaks could be treated in following investigations to improve the system.

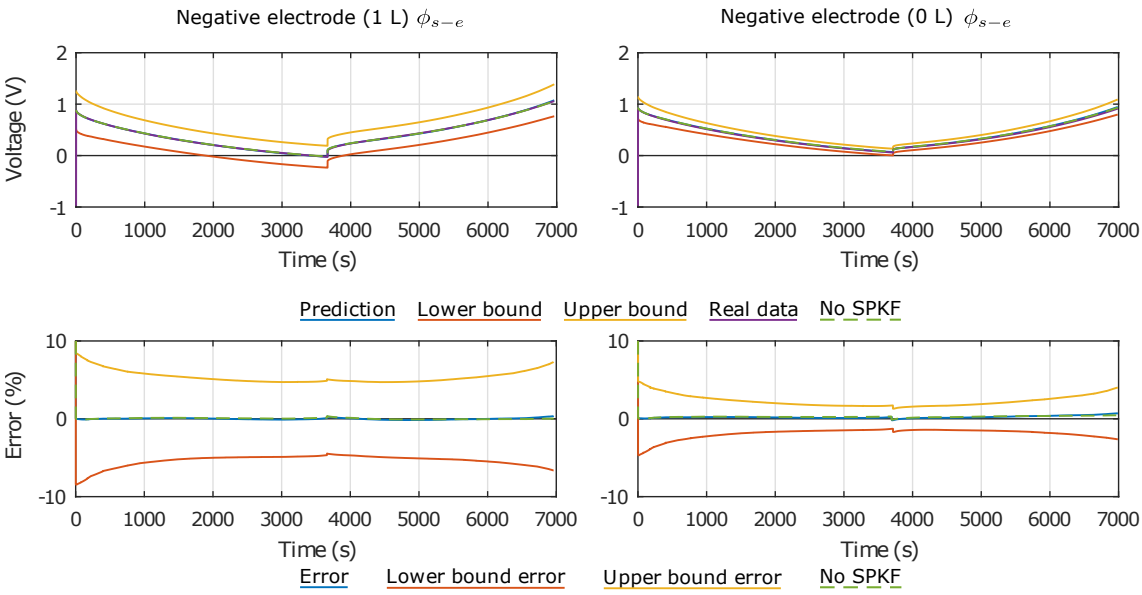

Figure 3.28: ROM, FOM and SPKF predictions and errors for ϕ_{s-e}.

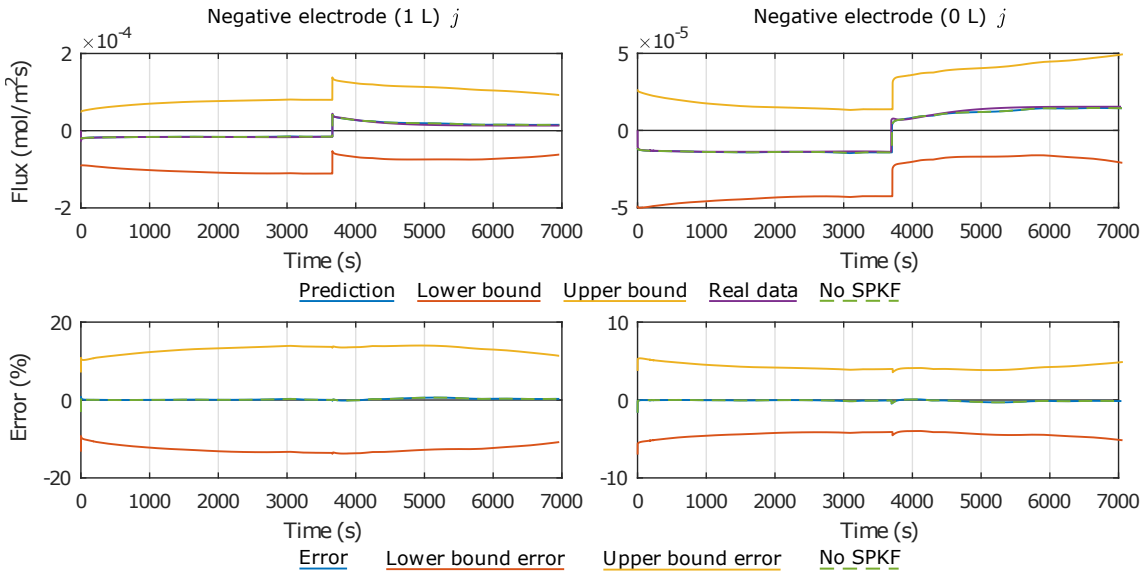

Figure 3.29: ROM, FOM and SPKF predictions and errors for j.

In the case of the positive electrode the ROM model predictions for C_e, $C_{s,e}$ and j were not so precise as can be seen in figures 3.30 and 3.31. Furthermore FOM data was significantly out of the boundaries when using the SPKF. The boundaries were affected by the tuning of the SPKF being a possible reason for this phenomena. Nevertheless, the fact that the error of the

ROM was higher in the area where the true data got out of boundaries showed that it was not only a matter of how the filter was tuned, but a local decrease on the ROM model predictions. This decrease in the ROM accuracy could be due to a less precise linearization of the FOM equations in that specific working range. The described tendency was seen for all positive electrode variables predictions, but this phenomena is not longer studied and assumed as a negligible and localized error. The main reasons to assume this error as negligible was that not the SOC nor the negative electrode predictions were affected, as the motivation of the model is to monitor and limit an aging mechanisms occurring in the anode made sense to leave this issue for further investigations.

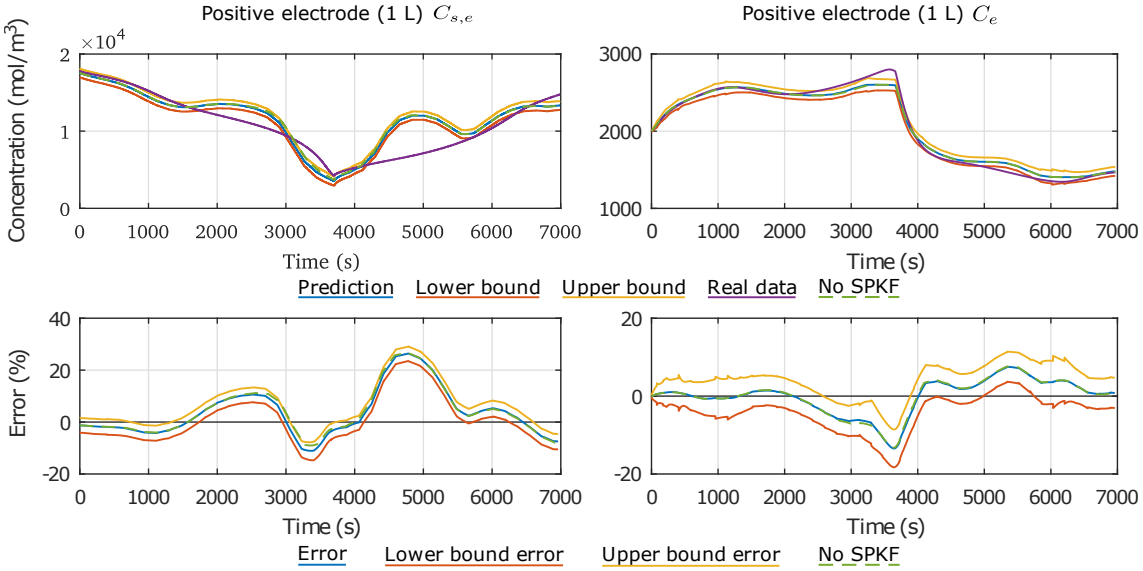

Figure 3.30: ROM, FOM and SPKF predictions and errors for C_e and $C_{s,e}$.

These results showed a very good overall response of both, the ROM and the SPKF. Prediction errors were kept very low in all the negative electrode areas and the true data between the error boundaries. At this point it was necessary to validate the behavior if the SPKF on the one hand with longer cycles to check its evolution in time, and on the other hand when the cell ages.

Figure 3.32 shows the voltage and SOC responses during 20 cycles. Both, voltage and SOC errors were greater when using the SPKF during the first one or two cycles, and similar to the ones reported in the previous single cycle analysis. Nevertheless, the SPKF started to improve the prediction as time advanced. The voltage error without the SPKF increased from the first time steps on, while the prediction with SPKF kept the error constant. In the case of

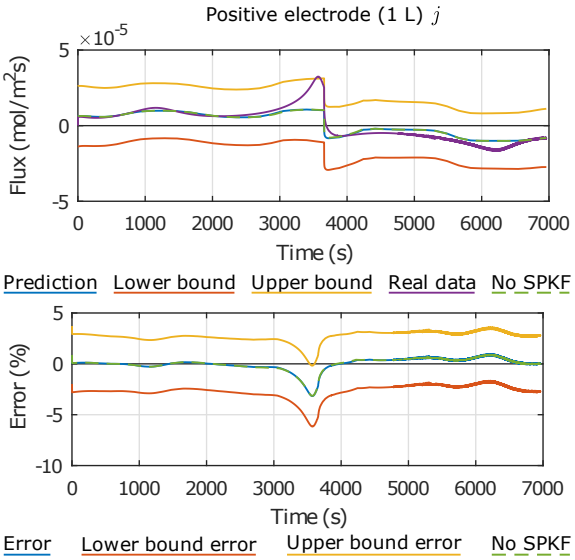

Figure 3.31: ROM, FOM and SPKF predictions and errors for j.

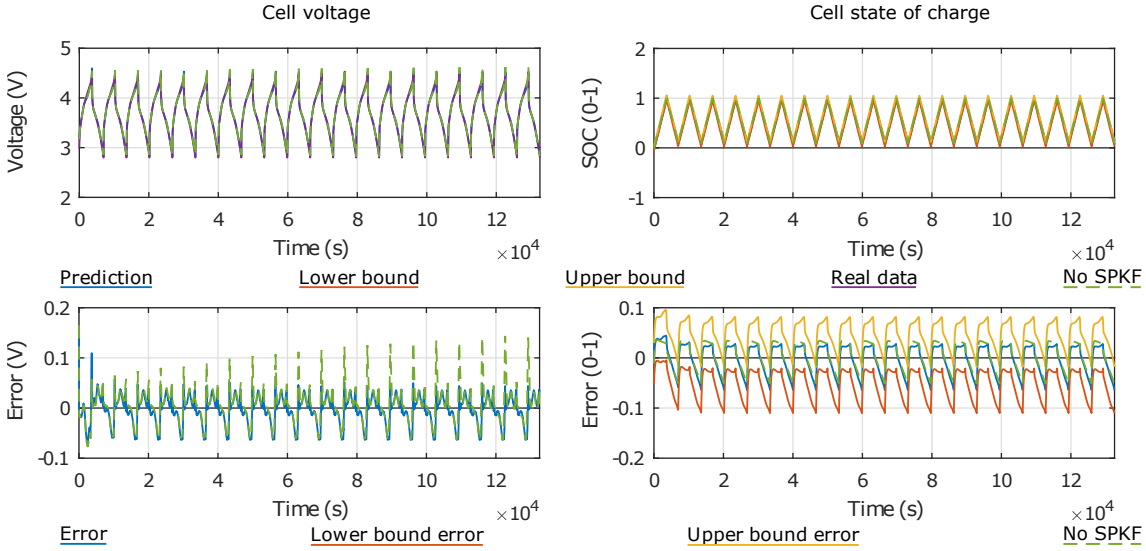

Figure 3.32: Voltage and state of charge predictions without aging influence for 20 cycles.

the SOC the error, without the SPKF did not increase while the SPKF prediction errors were still similar or lower from the first cycles on. These results showed the SPKF proper behavior and the validity of it since made the ROM a more accurate tool. The tendency shown in figure 3.32 was maintained for the rest of the cells internal variables analogously.

3.3.3 Model evaluation with aging

The last step to validate the ROM and SPKF system was to analyze the error evolution when the cell aged. Because when the battery starts to age some internal parameters values change. When using an aging model parameters such as the range of electrode utilization are predicted and could be directly corrected in the ROM. Nevertheless the volume fractions of the electrolyte and anode (if we consider Li plating and SEI growth as aging mechanisms occurring in the cell) could not be varied in the ROM. This was because these parameters introduced in the models equations were fixed during the linearization process, and as this operation was precomputed offline could not be updated easily. This fact is already known and treated in [39]. Nonetheless, and assuming that this update would be possible in the future it was worth to evaluate how the variation of the electrolyte and anode volume fractions change affected the system predictions. This could give a hint about when would be an update needed, and how much would affect not to do so.

Table 3.5: Aging parameters variation.

Variables	Maximum	Minimum	variation
$\varepsilon_{\mathrm{s}}^{\mathrm{n}}$	0.357	0.311	12.88%
$\varepsilon_{\mathrm{e}}^{\mathrm{n}}$	0.471	0.411	12.73%

Volume fractions of the solid and electrolyte at the negative region ($\varepsilon_{\mathrm{s}}^{\mathrm{n}}$ and $\varepsilon_{\mathrm{e}}^{\mathrm{n}}$) were varied along a 40 cycles simulation of 1C charge and discharges. Table 3.5 shows the initial and final values that changed around a 12%.

The voltage and SOC errors tended to increase as the cell aged, and the model predictions were consequently further than the modeled system. The SPKF mitigates that error and kept the true data inside the boundaries as they evolved in time.

The predictions for $C_e, C_{s,e}$ and ϕ_{s-e} in figures 3.34 to 3.36 showed a similar tendency. Starting with the same amount of error shown in the previous section and increasing along the cycles.

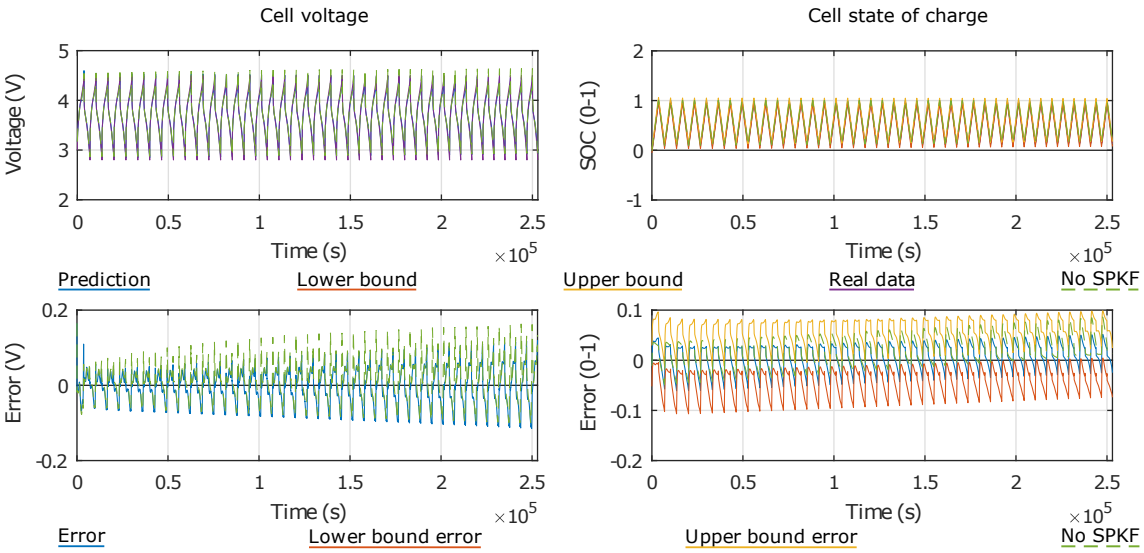

Figure 3.33: Voltage and state of charge predictions with aging influence for 40 cycles.

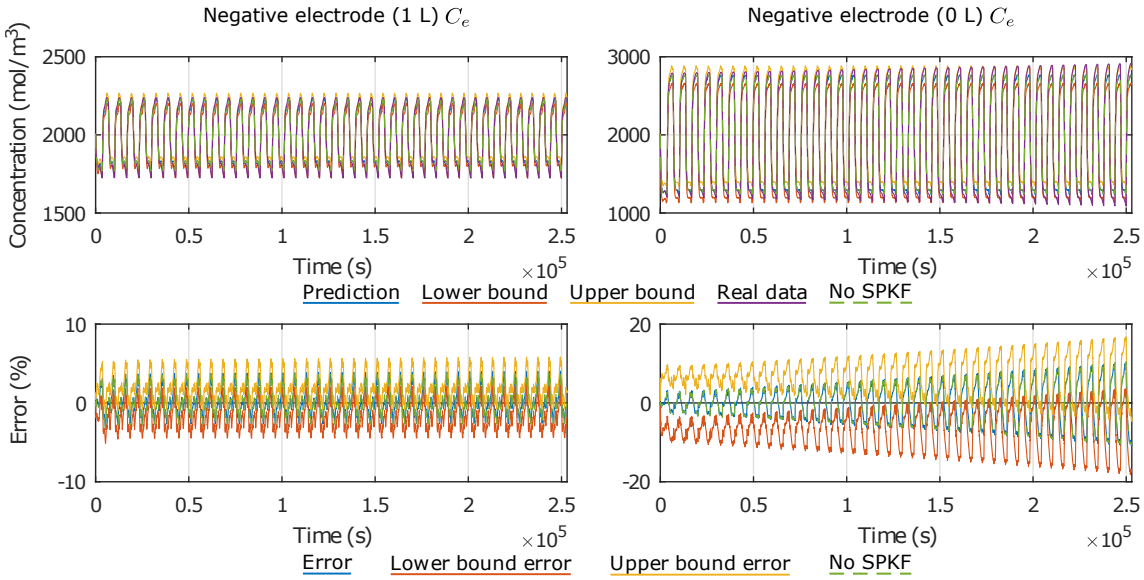

Figure 3.34: ROM, FOM and SPKF predictions and errors for C_e.

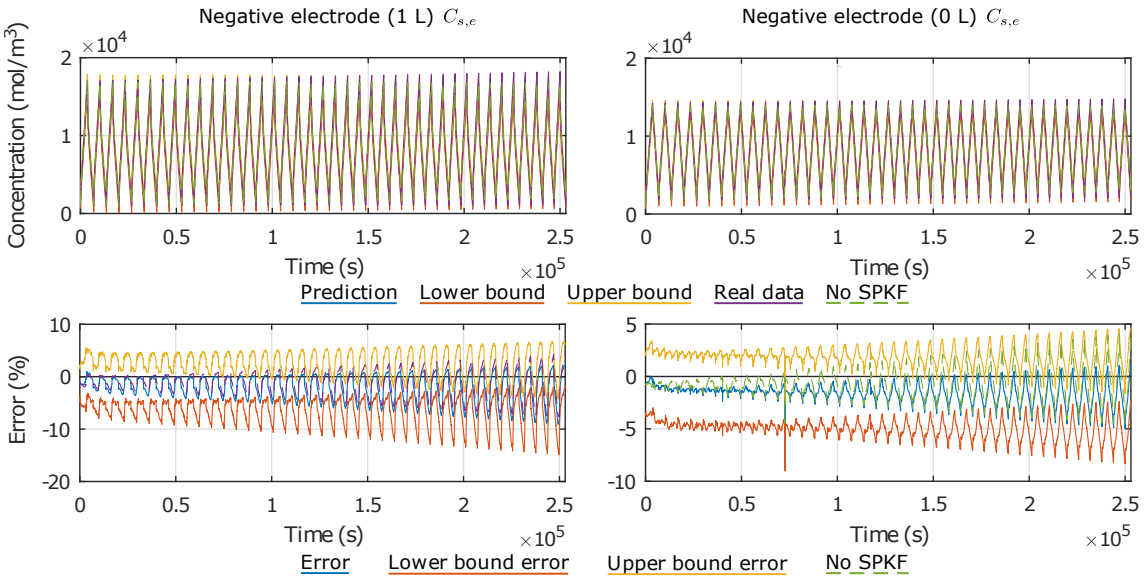

Figure 3.35: ROM, FOM and SPKF predictions and errors for $C_{s,e}$.

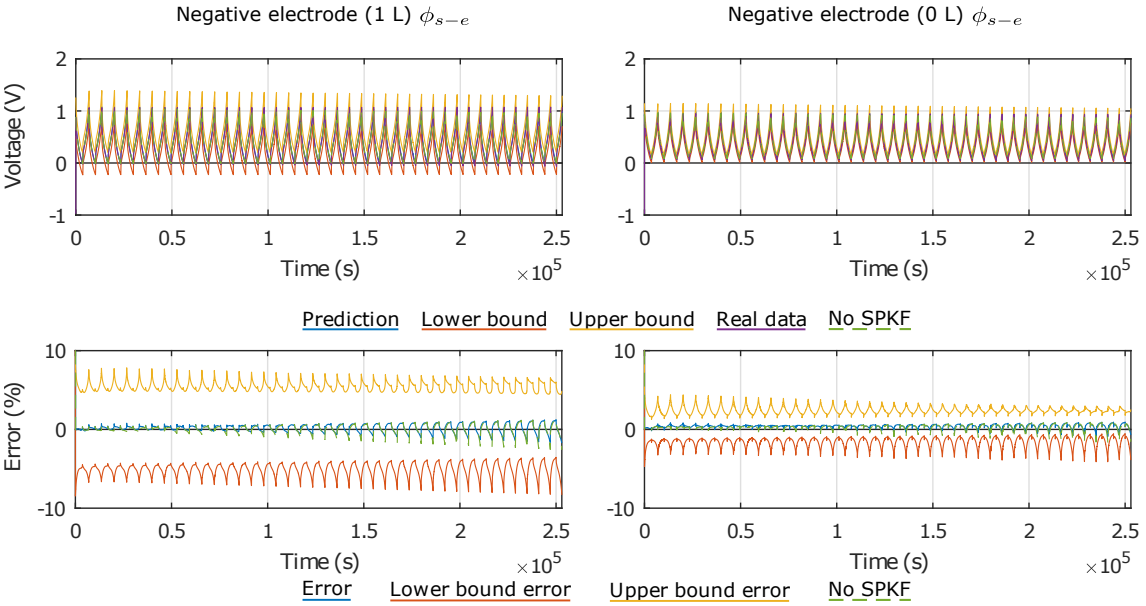

Figure 3.36: ROM, FOM and SPKF predictions and errors for ϕ_{s-e}.

Oppositely figures 3.37 and 3.38 demonstrated that the flux along the negative and positive electrodes were not significantly affected. This gave consistency to the model as the flux should not to be significantly affected, being a direct image of the applied current (which was not changed as the cycles were identical).

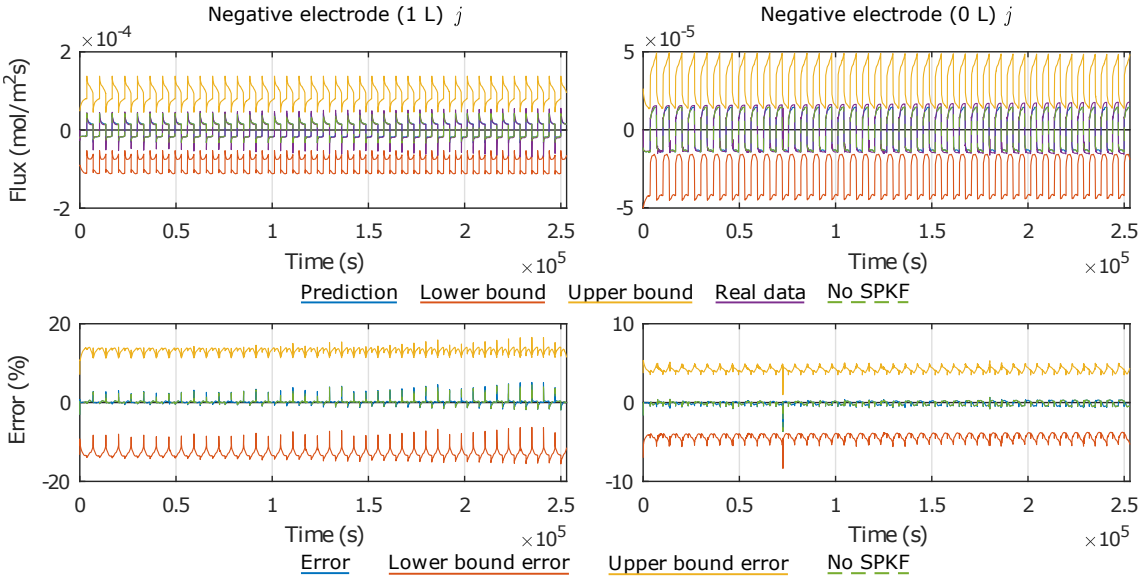

Figure 3.37: ROM, FOM and SPKF predictions and errors for j.

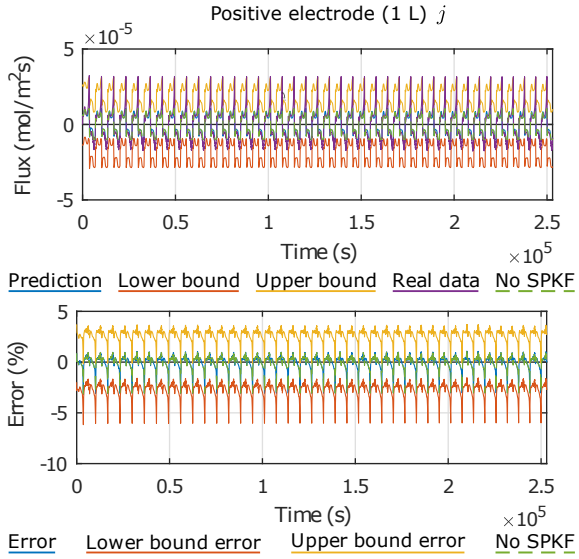

Figure 3.38: ROM, FOM and SPKF predictions and errors for j.

In the positive electrode the modeled aging did not make a meaningful change, as the volume fraction of this electrode was not modified (figure 3.39).

The results shown within this section demonstrated that the model update was a real need

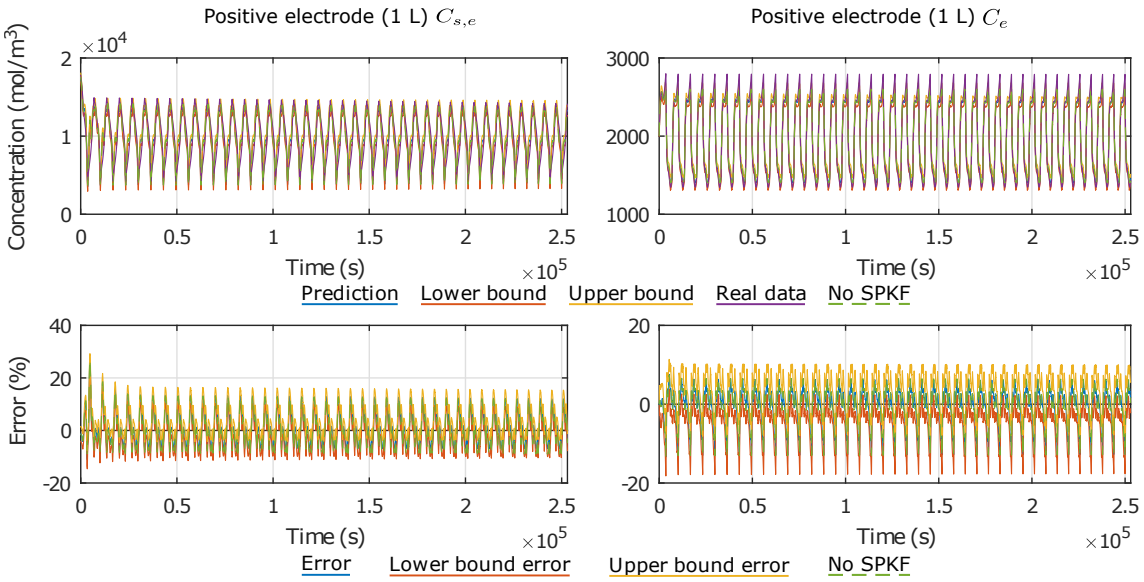

Figure 3.39: ROM, FOM and SPKF predictions and errors for C_e and $C_{s,e}$.

in order to maintain the accuracy of the ROM, while the errors and error boundaries were kept low enough to use this system to check the viability of this type of advanced BMS.

Conclusions

During this chapter a P2D model ROM was developed. This model predictions were compared with a FOM-based cell response, demonstrating the accuracy of the reduction process. This process, assured no loss of information, remaining all the predictions of the P2D model highly accurate. In addition, a SPKF filter was implemented to compensate experimental inaccuracies, and validated its benefit. There were found on the contrary some points to improve in further research works:

- The predictions at the positive electrode were less accurate than in the negative. This performance reason is still unclear and need to be investigated, so future model uses are not affected.

- During the design of the SPKF filter the process noise was assumed to be caused only by the current sensor. Furthermore, the sensor noise was assumed to be independent from the current sensor noise and attributed to the voltage sensor. This two assumptions did not affect significantly the SPKF performance, but should be solved in future investigations to reach higher filter efficiencies.

- The SPKF covariance values were not changed when not updated when the augmented model was regenerated (when changing from one SOC or temperature range to another). This caused small noises in the predictions, that even if did not affect the filter performance should be eliminated or mitigated as much as possible, to get smoother predictions.

- This model was proven to works very well when a cell parameters are known, but aging is and added problem in a real case scenario. Through the life of the battery internal side reactions occur, changing the physics inside. This will lead into a parameter change that is not updated in the model. This is a line already addressed by some authors as explained in the state of the art of this chapter, but it is important to further refine and experimentally test this aging management strategies, so the models are able to keep accurate predictions along battery life. Not only this, but a clear image of how the battery is evolving (identifying the aging mechanisms) could be done. The importance of this techniques also relies on the difficulty of isolating aging mechanisms ongoing since the exact moment when the cell is assembled. The importance of this techniques also relies on the difficulty of isolating aging mechanisms ongoing since the exact moment when the cell is assembled.

All in all both, ROM and SPKF were proven to predict battery cell internal variables accurately when running in a low cost microprocessor what satisfied the partial objective of developing an electrochemical ROM, that will be suitable for an online system. This model parameters will be identified along the next chapter, to finally integrate the a complete system (chapter 5).

Chapter 4

Parameter identification of an NMC/Graphite cell electrochemical model

This chapter presents a review of different parameter identification techniques; based on computational methods and based on physico-chemical analysis. The parameters that are identified are not few and the identification problem itself difficult. An efficient methodology for the identification is still a key challenge (both, in terms of cost and time). The state of the art presents some works that accurately identify groups of lumped parameters accurately, this is an efficient procedure, but the parameters still remain lumped. Physico-chemical parameter identification techniques otherwise, are still inmature and a big research niche is found. A phyisico-chemical parameter identification procedure was then implemented, in order to gain insights on this techniques. Understanding this procedures complexity and accuracy level will be the base to further develop optimum parameter identifications, a topic that will be continued in a PhD developed by L. Oca that collaborated within this chapter. A FOM was used to compare voltage and SOC predictions as a sign of adequate parameterization (even if not necesarilly enough). Later the ROM developed in chapter 3 will be feed with the resulting parameters in chapter 5 .

When an electrochemical model has been defined there is still a intrinsic step to overcome, the model parameters identification. Every battery cell is unique, due to the materials in the phase composing the electrodes, the electrolyte, the separator and the design. Furthermore as manufacturing of electrochemical cells is not a simple process the reproducibility is not ideal. Even if the batteries are suposed to be equal (the same model of a defined manufacturer, and build in the same batch) they are never exactly equal. Kalman filters can mitigate moderate deviations, but if to sensitive parameters are not accurately identified, significant errors can appear. Taking this into consideration the need of identifying adequate sets of parameters is evident.

Depending on the used electrochemical model that is considered the number of parameters involved changes (more exhaustive models need more parameters as they describe more mechanisms inside the battery cell). Also different arrangement of the algebraic equations can lead to different sets of parameters as will be explained in the following paragraphs. From here, on if not stated the contrary, the reference set of parameters used for the P2D model will be adopted from [73] and are summarized in table 4.1. As the different arrangement of the model equations make the set of parameters different, classifying them by their conceptual use can be clarifying, giving an overview of which parameters compose the whole set and what characteristics represent. Table 4.2 shows the parameters classified in four different categories; geometry related parameters, parameters related to the material properties, the ones related to the electrochemical reaction kinetics and transport related parameters.

Table 4.1: List of parameter summarized from [73].

Negative electrode	Separator	Positive electrode
σ^{n}_{eff}		σ^{p}_{eff}
a^{n}_{s}		a^{p}_{s}
L^{n}	L^{s}	L^{p}
κ^{n}_{eff}	κ^{s}_{eff}	κ^{p}_{eff}
D^{n}_{s}		D^{p}_{s}
R^{n}_{s}		R^{p}_{s}
ε^{n}_{e}	ε^{s}_{e}	ε^{p}_{e}
$D^{n}_{e,eff}$	$D^{s}_{e,eff}$	$D^{p}_{e,eff}$
k^{n}_{0}		k^{p}_{0}
$c^{n}_{s,max}$		$c^{p}_{s,max}$
α^{n}		α^{p}
R^{n}_{f}		R^{p}_{f}
θ^{n}_{0}		θ^{p}_{0}
θ^{n}_{100}		θ^{p}_{100}
A, t^{0}_{+}, $\partial \ln f_{\pm}/\partial \ln c_{e}$, $c_{e,0}$ span all cell regions		

Table 4.2: Parameters classification. M, E and S represent Material (or solid phase), Electrolyte phase and Separator related parameters respectively.

Geometry	
Electrode plate area	M
Thickness of the electrode	M
Material properties	
Particle radius	M
Tortuosity	M
Electric conductivity	M
OCV curve	M
Electrolyte activity coefficient ln derivative	E
Cationic transference number	E
Electrolyte conductivity	E
Activation energies	M/E
Bruggeman constants	M/E
Porosity/volume fraction	M/E/S
Electrochemical reaction kinetics	
Charge transfer coefficient	M
Reaction rate coefficient	M
Transport	
Diffusion coefficient	M/E

Geometric parameters

Within this category we can find the values related to the geometric sizes of the battery cell. As a typical variation in some model formulations, the electrode plate area is directly given instead of the length and height.

Material related parameters

Most of the parameters used in a model fall into this category. They represent the characteristics of the electrode material and electrolyte phases, the separator and also some particularities of the electrode development as the porosity or tortuosity for example. In the following lines some differences regarding which parameters are included are reported.

The particle radius together with the solid phase volume fraction is generally used to calculate the specific surface area of the solid, nevertheless the volume fraction is sometimes represented by means of porosity.

Activation energies are used to describe the dependency between solid diffusion and conductivity coefficients with the temperature. Reaction rate coefficient, ionic conductivity and diffusivity of the electrolyte are also corrected using the activation energies, if the temperature is different from the reference (temperature at which parameters are measured or estimated). This correction is done applying the Arrhenius equation.

Species transport in a porous media is not equal than in a liquid. To model this phenomena caused by the porous structure the Bruggeman constant is used. Electrolyte diffusivity and ionic conductivity plus electrode electric conductivities are corrected obtaining effective values. The Bruggeman constant and the tortuosity are intimately linked and both values can be found as model parameters representing this issue.

Other types of variations are also found in the literature. In the description presented in [73] the junction potential coefficient is calculated using the activity factor and the transference number, to describe the overpotential of the electrolyte out of equilibrium. Nevertheless the electrolytes electrical conductivity could also be addressed.

Finally in this group of parameters the thermodynamic properties (OCV curves, balancing and maximum lithium concentrarion in the solid), the electrolyte diffusivity and ionic conductivity are introduced as experimental data to be interpolated/extrapolated

latter, or a mathematical expression of a previously done fitting is given.

Transport related parameters

Despite, in this document only the diffusion coefficient was classified in this section, this is controversial. Some parameters classified as material parameters affect directly to the transport phenomena, and those parameters could also be contemplated within transport related parameters. The electrodes electric conductivity and electrolyte ionic conductivity, as well as the tortuosity or the electrolyte diffusivity parameters are a good example.

Electrode kinetics related parameters

Electrode kinetic parameters represent the charge transfer between the electrodes active material and the electrolyte. Butler-Volmer equation is used in the most rigorous models to describe this phenomena using as a consequence a reaction rate or exchange current density term. The usual variations within this section fall back in the exchange current density term that can be directly given or the reaction rate constant provided in order to calculate it.

Moreover some data representing the initial state and maximum absolute values of the cell need to be provided, table 4.3. Without this values the model could not converge to a solution. Not only this, the initialization values define the initial state of the cell at the beginning of the simulation and define the upper and lower limits (maximum and minimum state of charge).

Table 4.3: Initial and absolute maximum values.

Parameter
Reference temperature
Simulation temperature
Initial solid phase concentration
Maximum solid phase concentration
Minimum solid phase concentration
Initial SOC
Electrolyte salt concentration
Initial electrolyte salt concentration
Maximum electrolyte salt concentration
Minimum electrolyte salt concentration

Finally it has to be taken into account that also some universal constants are needed in

the models as well as boundary conditions to ensure the cohesion of the model formulation. [46, 55, 58, 73].

4.1 State of the art

In the lines above the obtention of a specific set of parameters for every cell is presented as crucial, and consequently a procedure to overcome the extensive and complicated parameterization is necessary. All the methods proposed in the literature could be classified within two very different approaches, figure 4.1.

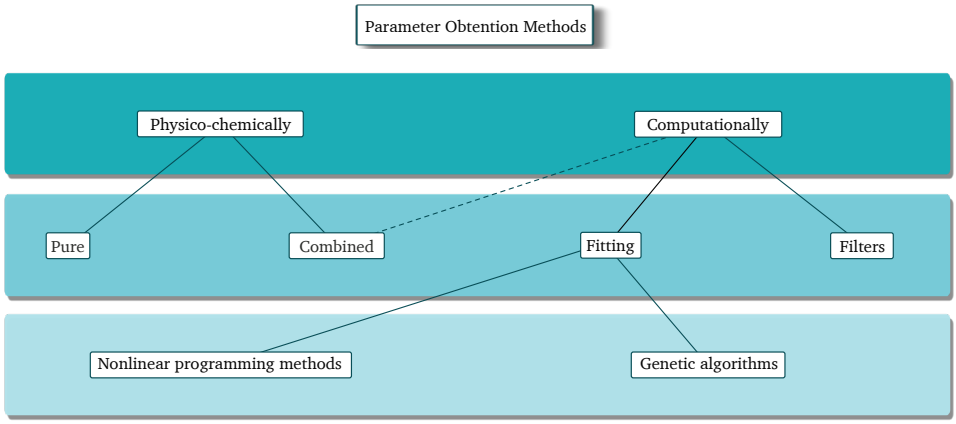

Figure 4.1: Parameter obtention methods.

The first approach was based on the physico-chemical analysis of representative samples of the cell. This method was believed to be the most precise as the parameters were measured directly through different electrochemical techniques such as galvanostatic intermittent titration technique (GITT), Hg porosimetry and others [119, 120]. Research in this type of parameterizations was still immature so it was not a fair comparison, note that the accuracy of the method relied in the used specific techniques own accuracy. The disassembly of a cell and the following physico-chemical analysis is not a trivial process due to the complexity of the required experiments. In addition, the required infrastructure is not accessible to all the researchers; glove boxes, electron microscopes, nuclear magnetic resonance (NMR) platforms and X-ray diffractometers are only a part of the required devices, found in advanced material research laboratories but far from industrial applications developers.

The other alternative approach consisted in obtaining the values of the parameters using computational methods. This approach was less infrastructure requiring even if computation

resources were needed [121]. The experiments that needed to be carried out were also more simple as only cycling data was needed. Nevertheless this methods coud fall into a lack of precision, the identifiablility of the parameters was not always optimum as is explained in the following ,and this could make impossible to determine the whole set of parameter with a perfect accuracy [122].

Within the computational methods filters, and fitting methods could be found. Kalman filters were the most used in SOC and SOH algorithms [88, 50]. This systems were able to fit a models predictions such that they continuously followed the behaviour of the considered plant. These kind of filters were applied when the plant was represented as a state-space model [123] (normally filters modify models state variables so it is not a direct way of obtaining parameters). The drawback of this method relied on the state-space representation of an electrochemical model, because during that process the physical meaning of the parameters was lost [123]. Consequently this kind of approach was not normally used as a specific method to obtain the parameters itself, but to adjust some of the model predictions when the model was running continuously.

The remaining group within computational methods, fitting methods, was the most used procedure when obtaining the parameters of a cell. The experimental data of the cell (cycling data) was used to adjust the model. The general idea was to find the combination of parameters that fitted best with the original data. To do so, nonlinear programming methods or genetic algorithms were the typical approaches.

Nonlinear-programming methods for optimization tried to find solutions to a system of equalities and inequalities over a set of unknown real variables (constrained or unconstrained). Within this system, an objective function was maximized or minimized. In the case of finding parameter values for the nonlinear DFN model, nonlinear solvers must be used (e.g, [124]). These solvers were often based on calculus approaches such as gradient descent or different approximations to Newtons method. When the problem could be posed in a nonlinear least-squares form, approaches such as the Levenberg-Marquardt or Gauss-Newton methods could be used [125, 126].

Genetic algorithms defined several candidate parameter sets (depending on the exact method, these sets might be randomly or deterministically generated). After performing a simulation with each of the candidate parameter sets, the parameters of the simulation reaching the results closest to the experimental dataset were selected and the remaining parameter

sets discarded. The selected parameters were then randomly mutated to form a new population (as they were called in the method) of candidate parameter sets. This process was repeated continuously until the difference between experimental data and simulation data were admissible; the process could be done in series or in parallel (Figures 4.2 and 4.3) as stated before [127, 128, 129]. A variation of this method was the multi objective genetic algorithms (MOGA) [75] that could optimize more than one objective variable within the same process.

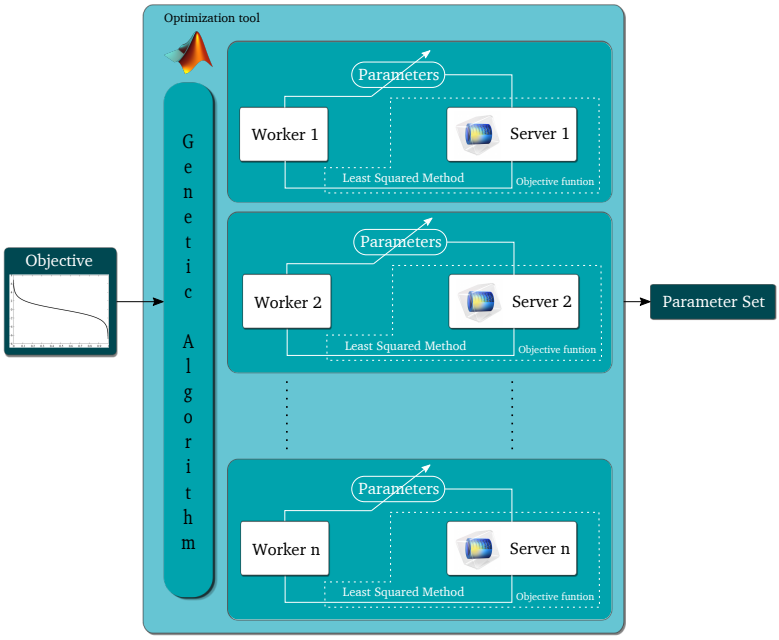

Figure 4.2: Genetic algorithm optimization with parallel computing structure example.

Root-mean-squared (rms) prediction error was contemplated generally as a way to evaluate the accuracy of the results.

$$\text{rms} = \sqrt{\frac{1}{N}\sum_{n=1}^{N}[y_{\text{simulation}}(t_n) - y_{\text{experimental}}(t_n)]^2}. \tag{4.1}$$

The minimization of Eq. (4.1) with respect to model parameter values optimized a relationship between simulated and experimental data. In this case $y_{\text{simulation}}$ is the output voltage from the simulation of the model that is being adjusted, and $y_{\text{experimental}}$ is the set of voltage data

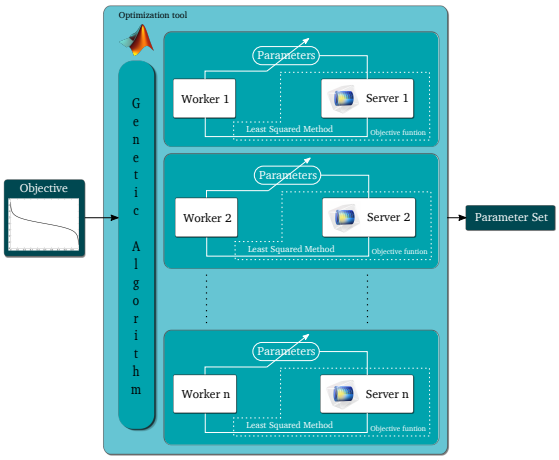

Figure 4.3: Genetic algorithm optimization with parallel computing structure example.

measured when cycling the real cell.

It is important to understand nevertheless that the selection of an optimization method was significant only once the optimization problem itself was well stated. This meant that the choice of solver would important to improve the accuracy of results and the time consumed by the optimization, but if the optimization problem itself was not well stated or excessively complicated then all the solvers would struggle with it. The solver could be chosen and tuned for each case once an optimization problem was correctly defined and the specific model equations fixed.

4.1.1 Computational parameterization methods

Computational parameter obtention methods estimated battery cell parameters based on measured cycling data, whether simple constant current discharges or more specifically dedicated profiles. The general idea was to find the combination of parameters that fitted best the true data with the models voltage and/or temperature prediction. Computer-based optimization tools were used to optimize the parameters so the model response was equal to the real cell data. Different optimization methods could be used (linear, nonlinear or genetic algorithms) and solved differently (series or parallel computing) are typical approaches.

4.1.1.1 Grouping parameters

Before analyzing the computational parameter-identification methods, it was noticed that there was a common drawback to all. The electrochemical models were composed of coupled PDAEs, and some of the parameters in these equations were therefore coupled together such that not all parameter values could be determined uniquely from input-output data (they are not all "observable") [116, 32]. Thus, many different combinations of parameter values could lead to the same model output. Even if an optimized set of parameter values fitted the experimental input-output data perfectly, the model may not gave acceptable results in terms of its predictions of cell internal variables.

As a simple analogy to this problem, consider the equation $y = (A*B)x+C$. The parameters of this equation are A, B, and C. If we collect a set of input–output data pairs (x, y), we might attempt to find values for the parameters to fit the equation to the data. But, the problem is that A and B are not independently observable. Only the product $M = A*B$ is observable. Many different combinations of A and B arrive at the same product (but perhaps only one of these combinations is physically correct).

To solve this problem, two different solution approaches could be found in the literature. Some authors opted to reformulate the models so new lumped parameters were used as will be explained more extensively in the following [116, 32]. (In the simple example, the model would be reformulated as $y = Mx + C$ and the data pairs would be used to determine M and C uniquely; no attempt would be made to determine A and B). The second alternative grouped parameters based on the sensitivity of the measured voltage or voltage and temperature to their values. Parameters to which the voltage was very sensitive were called "sensitive" parameters and the remaining were called "insensitive" parameters. The authors chose to identify the sensitive parameters (or group parameters creating "sensitive" groups) and either use nominal values for the insensitive parameters or delete portions of the model equations in which the insensitive parameters occurred (an example was SP model, which often completely discards electrolyte dynamics from the cell model since the parameters that describe electrolyte potential and concentration were relatively insensitive).

There was however a drawback to both of these solutions that remain unsolved. Aging models were often linked with electrochemical cell models so the most benefit of electrochemical models was obtained. These aging models used some parameters included in the

electrochemical model which were lumped together or even discarded during the optimization process. This involves some difficulties. If the model was lumped there could be two solutions, the aging model could be reformulated accordingly or the set of lumped parameters could be freed using additional tests (whether cycling or physico-chemical). On the other hand if some parameters were discarded or even if nominal values were used because voltage was insensitive to the parameters, it was possible that those parameters were crucial to the aging model. Errors in or omission of these "insensitive" parameters could lead therefore to an important lack of accuracy in an aging model. To the knowledge of the author, there was no published research giving solution to this topic, being a research gap still uncovered.

4.1.1.2 Comparison of computational methods

All the computational parameter obtention methods could be classified in two groups based on the definition of the optimization problem, single-optimization analysis (SOA) and multi-optimization analysis (MOA). Single optimization methods used data obtained experimentally (charges, discharges or different types of cycles) and optimized the whole set of parameters so the model output fitted the data. Multi-optimization methods used also data sets or differentiated sections of them; then differing from SOA methods, single parameters or groups of parameters were optimized independently to fit experimental data.

In the following subsections, SOA and MOA approaches from the literature were identified. Since most authors presented their own different reformulations of the P2D or SP models, there was not room in this thesis to present each reformulation and to explore all the differences between every reformulation. Instead, it was wanted to compare the ability of each method to determine the values required to parameterize the models used by those methods. The interested reader is referred to the references presented in the following subsections for more details.

4.1.1.3 Single optimization analysis (SOA)

To implement a single-optimization analysis, normally a single set of experimental data was used (typical profiles includes constant-current discharges). Either a single discharge, discharges at different rates or other cycles could be used. The shared characteristic of these methods was that the load profiles were not specifically designed to isolate the effect of spe-

Table 4.4: Summary of the literature references.

Reference	Model	Parameters		Validation data			Profiles	
		Full	Partial	Voltage	Temp.	Param.	SOA	MOA
[126]	$P2D^{s}$		X				X	
[130, 131, 132, 133]	P2D		X	X			X	
[134]	$P2D^{s}$		X	X			X	
[125, 135, 136]	P2D		X	X	X		X	
[122]	SPM^{e}		X	X		X	X	
[137]	SPM		X	X		X	X	
[138]	$SPM^{ve,v,r}/P2D^{v}$		X^{LS}	X		X	X	
[129]	P2D	X		X				X
[139]	P2D		X	X				X
[140]	$P2D^{ve}$		X	X				X
[123]	SS	X^{R}		X				X
[141]	P2D	X^{LS}		X				X
[91]	$P2D^{r}$	X^{R}		X	X			X
[142]	SPM^{e}	X^{LS}		X	X			X
[143]	P2D		X	X	X			X
[144]	SPM^{e}	X		X	X			X
[145]	P2D	X^{LS}				X		X
[146]	$SPM^{re}/P2D^{v}$	X^{L}		X		X		X
[147]	$P2D^{ve,r,re}$	X^{L}		X	X	X		X
[116]	$P2D^{re}$	X^{L}		X	X	X		X
[121, 127, 148, 149]	P2D	X^{LS}		X	X	X		X

s: state space; r: reduced order; re: reformulated; e: extended; v: used for voltage observation ; ve: own version or similar; L: lumped parameters; LS: parameters lumped using sensitivity analysis; R: ROM parameters (without physical meaning).

cific parameters or sets of parameters in the input–output data. All parameter values were jointly optimized to fit the experimental data. After the data was collected, each author used a specific model and/or model-reduction in addition to a solving method. Nevertheless, this approach could lead to an accuracy loss due to a highly complex optimization scheme. For this reason was important to discriminate the accuracy of the obtained results even if the model parameters were lumped.

All the authors using SOA choose whether to use the P2D or SP model (sometimes small variations or reformulations were made, Table 4.4). These models led to different sets of parameters that must be identified; for example, since SP models predicted fewer phenomena occurring inside the cell than P2D models, they required fewer parameters to do so. Nevertheless this aspect was not crucial at this point as all the authors using SOA methods obtained a partial set of parameters.

Results could be validated using three different approaches, based on voltage, temperature and parameter values themselves. Voltage validation referred to evaluating the voltage response of the cell versus the parameterized cell model (this could be done with the same cycles used for the validation or with different ones such as UDDS cycles for example). Additionally temperature could also be taken into account as it had significant influence on battery behavior. These two methods could be implemented with real cycling data or with virtual data coming from a full order electrochemical model [138]. The last validation strategy compared the identified parameter values directly to the true parameter values. To implement this strategy, the true values must be known, which was not generally the case. However, this strategy was still useful when initially determining whether the parameter-identification methods were able to produce reasonable results by generating synthetic simulated cell-test data from a cell model (e.g., simulating the P2D model for some input-current profile), then using the simulated cell-test data to determine parameter values, and finally comparing the identified parameter values to the true values used in the simulation.

It was therefore necessary to think about these validation methods and their viability. Some authors demonstrated that cell voltage was not sensitive to some of the model parameters [138, 150]. This was a key conclusion as it invalidated the concept that voltage validation was sufficient to assure a good model parameterization. (This could be true because the parameters were fundamentally not observable, as discussed in Sect. 4.1.1.1, which could be solved by grouping parameters together into "lumped parameters". It could also be true because the

parameters were observable in principle but the signal-to-noise ratio available in the measured data was not sufficient to allow accurate parameter estimates. This might be solved using enormous data sets, but the nonlinear optimization methods required to find the parameter values were not guaranteed to find the uniquely correct values in that case). Furthermore Zhang *et al.* [121, 127, 148, 149] reported the same conclusion when implementing a MOA method based on different temperature and rates constant current cycles (this method is presented in section 4.1.1.4). Because of this reason this section was focused on the references that report reliable proofs of proper parameter identification, this is, based on parameter values (reporting the error of the estimated parameters towards virtual data). Rajabloo *et al.*, Masoudi *et al.* and Deng *et al.* [122, 137, 138] work was be studied therefore within this section.

Rajabloo *et al.*used a SP model that was improved with an state of charge linear dependency (for which they also found parameter values) that was solved in COMSOL Multiphysics. The selected parameter values were after identified linking COMSOL Multiphysics with MATLAB trough the COMSOL Multiphysics LiveLink for MATLAB. MATLAB Optimization toolbox was utilized to run the optimization routine, and more specifically, a solver dedicated to constrained nonlinear multivariable problems based on the Newtons method.

Masoudi *et al.* also used the SP model, but employed Maplesim to solve the equations. For parameter identification, the "Homotopy optimization method" was used to avoid inaccurate results due to local minima solutions.

Deng *et al.* used their own version of the SP model to generate a reduced order model and after identify parameters, in addition P2D and SP models were used for voltage response observation.

The models that were used nevertheless were not so trivial since all of these authors identified partial sets of parameters, this is, few parameters values were identified in order to validate the identification method itself (Figure 4.5).

The results obtained by these authors are presented in Figures 4.4 and 4.5. The error of the estimated parameters varied widely (between 0% and 42.8%). This is a sign of the difference in sensitivity among the individual parameters. Not only this, in the case of Deng *et al.* even when using different cycles the results were different due to the parametric sensitivity (Figure 4.4a).

Reduced order, P2D and SP models were studied using different optimization methods with different experimental cycling profiles intending to identify various sets of parameters.

Table 4.5: Parameters identified by authors using SOA. r:Rajabloo *et al.*, m:Masoudi *et al.*, d:Deng *et al.*.

Negative electrode		Separator		Positive electrode	
σ^{n}_{eff}	m			σ^{p}_{eff}	
a^{n}_{s}				a^{p}_{s}	
L^{n}		L^{s}		L^{p}	
κ^{n}_{eff}		κ^{s}_{eff}		κ^{p}_{eff}	
D^{n}_{s}	d/r			D^{p}_{s}	d/r
R^{n}_{s}				R^{p}_{s}	
ε^{n}_{e}	d/r	ε^{s}_{e}	m	ε^{p}_{e}	d/r
$D^{n}_{e,eff}$		$D^{s}_{e,eff}$		$D^{p}_{e,eff}$	
k^{n}_{0}	d			k^{p}_{0}	d
$c^{n}_{s,max}$	d			$c^{p}_{s,max}$	d
α^{n}				α^{p}	
R^{n}_{f}				R^{p}_{f}	
θ^{n}_{0}	r			θ^{p}_{0}	r
θ^{n}_{100}				θ^{p}_{100}	
A, t^{0}_{+}[m], $\partial \ln f_{\pm}/\partial \ln c_{e}$, $c_{e,0}$ [d/m] span all cell regions					

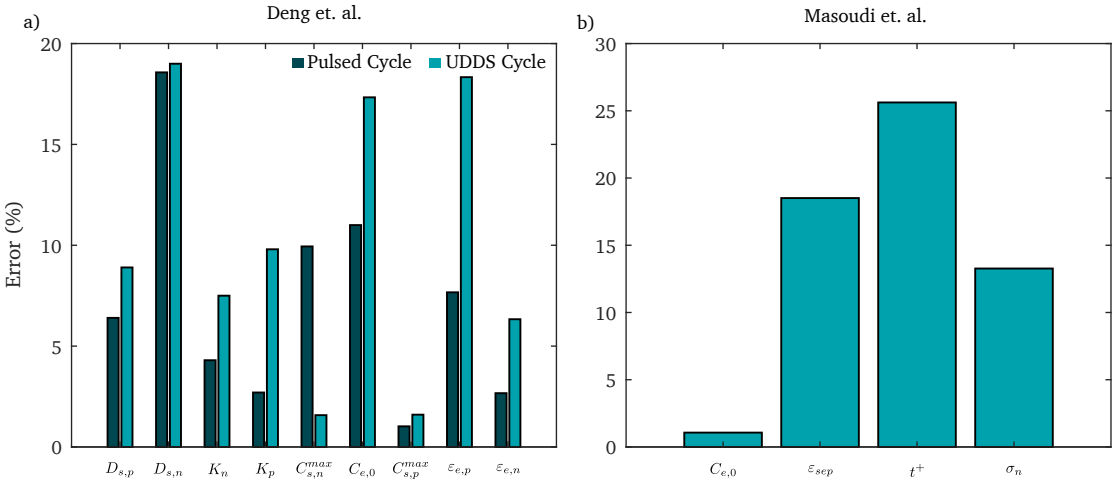

Figure 4.4: Parametric errors adapted from [138](a) and [137](b).

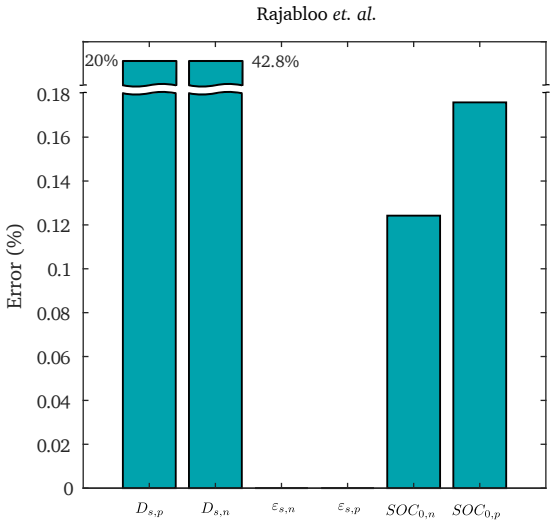

Figure 4.5: Parametric errors adapted from [122].

The parametric errors obtained in these works were not negligible nevertheless. The reason behind could poor parameter observability as explained before, which could be addressed in MOA methods by lumping parameters. Furthermore the necessity of dedicated input profiles or specific fitting procedures designed for each parameter or parameter group could be an alternative to improve the identification accuracy as will be presented in the next section.

4.1.1.4 Multi optimization analysis (MOA)

Similar to the single-optimization analysis, the idea behind the multi-optimization analysis was to fit the model parameters using optimization routines to obtain output variables similar to experimental data. However, instead of using generic input-current profiles to collect a data set, the MOAs made a more advanced attempt to design profiles to isolate specific parameters or groups of parameters. Electrochemical impedance spectroscopy (EIS) tests, charge and discharge tests conducted at different rates, pulse tests, tests at different temperatures, tests around different cell states of charge, sensitivity analysis or any combination of these could be used [116, 146, 147, 121, 127, 148, 149, 145].

Most of the authors using MOA (shown in table 4.4) used P2D, SP or similar models. There were however some exceptions that reduced the models leading in a state-space or equation-based simpler model [91, 123]. Nevertheless the validation methods used for these reductions were based on voltage and temperature because the set of parameters that was used in those models was related to the specific model, discarding parameters that were not

used due to the reduction or losing the physical meaning in the case of a state-space model. This validation therefore could not be taken as proof of a good parameterization because the parameters could not be compared to those of a full-order model. The validity of this type of model should be oriented to online system implementation and could be developed once a reliable set of parameters was previously obtained.

At this point it is important to take a look at the validation results reported by authors using P2D or SP models as was done in section 4.1.1.3 for SOA. The rest of the subsection will be then focused in the publications showing reliable proofs of parameterization (reporting the error of the estimated parameters towards virtual data). In the table 4.6 an overview of the parameter groups and experimental profiles or sequences that were proposed in the studied works for the parameter identification are presented.

Zhang *et al.* [121, 148, 149, 50] reported an identification methodology for the full set of parameters of a thermal-electrochemical P2D model. The used methodology was based on three steps, which were introduced in [149]. First of all, the maximum voltage sensitivity point for each parameter was searched based on benchmark parameter values best condition for identification (BCI). Then the results were normalized and weighted in order to be comparable. Finally, the Fuzzy-C-Means method for parameter clustering was used. The parameters that were identified by this methodology were collected in table 4.6 in which two different parameter clusterings are proposed by the authors [149, 121]. [149] studied 28 parameter from which five parameter were considered insensitive to the voltage, three parameter could not be clustered as the degree of membership was less than 0.6 and the remaining parameters were clustered into four groups. Authors claim that other parameters were changeless during cycling or can be obtained directly (geometric or material characteristics) therefore those were not included in the analysis. They grouped the parameters as a function of their sensitivity towards constant-current discharges at different temperatures. Among the studied experimental profiles the authors concluded that three profiles could be used as the best practicable conditions (BPC) for parameter identification: very low temperature/very high rate, room temperature/medium rate and very high temperature/very high rate. In order to reduce the computation time parallelized genetic identification was proposed by the authors [149, 50]. [121] was based on [149], but several improvements in the methodology and the model were included. The thermal-electrochemical model (P2D model) was coupled to a thermal impedance model so as to simulate the thermal distribution in the radial direction of the

Table 4.6: MOA: Parameter groups and experimental sequences.

Reference	Grouped parameters	Experimental profiles
Zhang2013	4 clusters: (A) σ^{p}, c_{e}, κ, k_0^{p}, $E_{act}^{\mathrm{n}}k_0$, $E_{act}^{\mathrm{p}}k_0$, $E_{act}^{\mathrm{n}}D_e$, $E_{act}^{\mathrm{n}}\kappa_e$; (B) $\varepsilon_{\mathrm{e}}^{\mathrm{n}}$, $\varepsilon_{\mathrm{s}}^{\mathrm{n}}$; (C) $R_{\mathrm{s}}^{\mathrm{n}}$, $R_{\mathrm{s}}^{\mathrm{p}}$, $D_{\mathrm{s}}^{\mathrm{n}}$, $D_{\mathrm{s}}^{\mathrm{p}}$, $\varepsilon_{\mathrm{s}}^{\mathrm{p}}$, D_e, $\varepsilon_{\mathrm{e}}^{\mathrm{p}}$, $E_{act}^{\mathrm{n}}D_s$; (D) $R_{\mathrm{f}}^{\mathrm{n}}$, R_{ext}; (NC) θ_0^{n}, θ_0^{p}, k_0^{n}; (IS) σ^{n}, $R_{\mathrm{f}}^{\mathrm{p}}$, ρ_e, $\varepsilon_{\mathrm{e}}^{\mathrm{s}}$, $E_{act}^{\mathrm{p}}D_s$	Five different temperatures (-5, 10, 25, 40, 55) °C and five different discharge rates (0.2, 0.5, 1, 2, 4) C.
Zhang2014	3 clusters: (A) $R_{\mathrm{s}}^{\mathrm{p}}$, $D_{\mathrm{s}}^{\mathrm{p}}$, c_{e}, R_{ext}, $\varepsilon_{\mathrm{e}}^{\mathrm{p}}$, k_0^{n}, k_0^{p}, $E_{act}^{\mathrm{n}}k_0$, $E_{act}^{\mathrm{p}}k_0$, $E_{act}^{\mathrm{n}}D_s$, $E_{act}^{\mathrm{p}}D_s$, λ; (B) $R_{\mathrm{s}}^{\mathrm{n}}$, $D_{\mathrm{s}}^{\mathrm{n}}$, σ^{p}, θ_0^{n}, $\varepsilon_{\mathrm{s}}^{\mathrm{n}}$, κ, $E_{act}^{\mathrm{n}}D_e$, h; (C) $\varepsilon_{\mathrm{s}}^{\mathrm{p}}$, $R_{\mathrm{f}}^{\mathrm{n}}$, D_e, $\varepsilon_{\mathrm{e}}^{\mathrm{n}}$, $\varepsilon_{\mathrm{e}}^{\mathrm{s}}$; (NC) θ_0^{p}, $E_{act}^{\mathrm{n}}\kappa_e$; (IS) σ^{n}, $R_{\mathrm{f}}^{\mathrm{p}}$, ρ_e	Five different temperatures (-5, 10, 25, 40, 55) °C and five different discharge rates (0.2, 0.5, 1, 2, 4) C.
Jobman2016	Non-lumped parameters grouped according to the optimization groups (*1): (A) Related to OCV testing: $\theta_{0,coin}^{\mathrm{n}}$, $\theta_{100,coin}^{\mathrm{n}}$, $\theta_{0,coin}^{\mathrm{p}}$, $\theta_{100,coin}^{\mathrm{p}}$; (B) Related to pulse testing: $\kappa_{\mathrm{eff}}^{\mathrm{n}}$, $\kappa_{\mathrm{eff}}^{\mathrm{s}}$, $\kappa_{\mathrm{eff}}^{\mathrm{p}}$, $\sigma_{\mathrm{eff}}^{\mathrm{n}}$, $\sigma_{\mathrm{eff}}^{\mathrm{p}}$, k_0^{n}, k_0^{p}, $R_{\mathrm{f}}^{\mathrm{n}}$, $R_{\mathrm{f}}^{\mathrm{p}}$, θ_0^{n}, θ_0^{p}, $\theta_{100}^{\mathrm{n}}$, $\theta_{100}^{\mathrm{p}}$; (C) Related to frequency testing: $c_{\mathrm{e},0}^{n}$, $c_{\mathrm{e},0}^{s}$, $c_{\mathrm{e},0}^{p}$, $D_{\mathrm{e,eff}}^{\mathrm{n}}$, $D_{\mathrm{e,eff}}^{\mathrm{s}}$, $D_{\mathrm{e,eff}}^{\mathrm{p}}$, $D_{\mathrm{s}}^{\mathrm{n}}$, $D_{\mathrm{s}}^{\mathrm{p}}$, t_+^0	Experimental procedure (i) Half Cell OCP data (coin cells) C/30 CC process; (ii) OCV/Rss data (full cell) C/30 CC process; (iii) Full cell frequency data; (iv) Full cell R0 data (0.1 s pulses at different Crates). At different temperatures (0, 10, 25, 30, 40) °C.
Namor2017	SPM grouped parameters (*2): (A) Related to low-rate testing: Q^n, Q^p; (B) Related to pulse testing: $k_0^{*,\mathrm{n}}$, $k_0^{*,\mathrm{p}}$, R_{cell}; (C) Related to GITT testing: $D_{\mathrm{s}}^{*,\mathrm{n}}$, $D_{\mathrm{s}}^{*,\mathrm{p}}$	(i) Low rate tests; (ii) Pulse tests; (iii) Galvanostatic Intermittent Titration Technique (GITT) tests.
Li2018	Grouped parameters: (A) Related to OCV testing:θ_0^{n}, θ_0^{p}, $\theta_{100}^{\mathrm{n}}$, $\theta_{100}^{\mathrm{p}}$, Q^n, Q^p; (B) Related to ohmic resistance and reaction polarization: P_{act}; (C) Related to diffusion processes: P_{con}, τ_s	Special operating condition with constant current charge/discharge of 6 minutes and 15 minute rest.
Park2018	Grouped parameters: (A) $R_{\mathrm{s}}^{\mathrm{n}}$, $R_{\mathrm{s}}^{\mathrm{p}}$; (B) $D_{\mathrm{s}}^{\mathrm{n}}$, $D_{\mathrm{s}}^{\mathrm{p}}$, $\varepsilon_{\mathrm{e}}^{\mathrm{n}}$, κ, D_e, $\partial \ln f_{\pm}/\partial \ln c_{\mathrm{e}}$; (C) $R_{\mathrm{f}}^{\mathrm{n}}$, $R_{\mathrm{f}}^{\mathrm{p}}$, k_0^{n}, $\varepsilon_{\mathrm{e}}^{\mathrm{p}}$, $c_{\mathrm{e},0}$; (D) k_0^{p}, σ^{n}, σ^{p}, $\varepsilon_{\mathrm{e}}^{\mathrm{s}}$, t_+^0; Fixed parameters: L^{n}, L^{s}, L^{p}, A	738 different profiles: pulses, sinusoids and driving cycles.

R_{ext}: extra resistance; E_{act}: activation energy; ρ_e: electrolyte density; λ: thermal conductivity; h: heat transfer coefficient; (NC): Not clustered, (IS): insensitive; (*1) For better comprehension of the studied works, the original non-lumped parameters are presented in the table. However, in order to apply Jobman's methodology, parameter should be lumped as specify in (*2) $Q = FR_s a_s c_{s,max}$; $k_0^* = (k_0 c_e^{0.5})/R_s$; $D_s^* = D_s/R_s$; R_{cell}: cell resistance. P_{act}: coefficient of anode reaction polarization; P_{con}: proportional coefficient of liquid-phase diffusion; τ_s: solid-phase diffusion time constant.

cylindrical battery. The sensitivity analysis was performed in both voltage and temperature and two additional parameters (related to thermal properties) were added to the analysis. Zhang et al. [121] grouped 30 parameters into three clusters as specified in table 4.6. In this case, the degree of membership of non-clustered parameters was less than 0.5. They did a further step making a MOA, implementing a stepwise identification process based on the results of the sensitivity analysis in order to decrease the computational time and overcome difficulties of low sensitivity parameter identification. The stepwise experimental design consisted of three steps and the start point of the parameters was also from literature values. In the first step, highly sensitive parameters were identified based on the BPC, which corresponded to the condition that made a cluster of parameters most sensitive (based on BCI results). The second step identified the sensitive parameters within another BPC point, while highly sensitive parameters were taken from step 1 and low sensitivity parameters were assigned benchmark values. Finally, in the third step, low sensitivity parameters were identified. They obtain the best optimization results with this method. Except for two parameters with a maximum error of 20.86%, the remaining parameter identification error was 10% or lower. Authors reported a comparison of the relative errors using different experimental profiles (shown in Figure 4.6). Furthermore, in [148] a multi-objective optimization approach based on genetic algorithms was proposed. DST profile at 15 and 30 ^{o}C was used for identification without parameter grouping or sequencing.

Jobman *et al.* [116] and Chu et al. [32] proposes an identification process that was performed on a P2D model reformulated using lumped parameters. This made parameter identification possible and reduced the number of independent parameters to the minimum. The lumped parameters were obtained including the influence of design adjustable parameters (L, A, a_s, ε_e, ε_s, R_s) into the remaining parameters so as to avoid their crosslinked interactions in the parameter identification process. The parameters were sequentially identified using four steps, which used only cell voltage and current relationships. The sequenced experimental profiles used in this methodology are described in table 4.6. The first set of tests collected slow C/30 charge and discharge data from the electrodes and full cell to determine open-circuit-potential and open-circuit-voltage relationships. The second set of tests collected pulse responses from the cell at different initial SOC setpoints and pulse magnitudes, exploiting the nonlinearity of the instantaneous voltage response predicted by the cell model to determine 15 of the model parameter values. The third set of tests collected frequency-response data

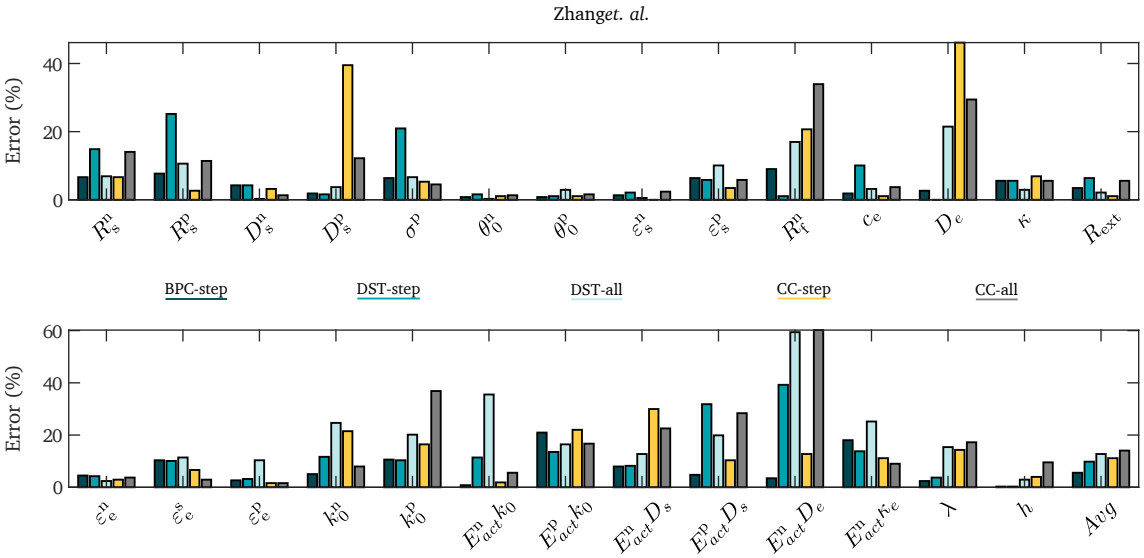

Figure 4.6: Comparison of relative errors in parameter identification from [121] using best practicable condition (BPC), dynamic stress test (DST) or constant current (CC) experimental profiles and stepwise (step) or non-stepwise identification (all) sequences.

from the cell around different SOC setpoints using EIS to determine the remaining model parameter values. A final set of tests collected constant-current charge and discharge data from the cell at different (slow) rates to exploit the nonlinearity of steady-state response to refine the parameter values (especially those describing the electrolyte dynamics, which were technically observable but which in practice were quite insensitive). These tests were repeated for several temperatures and Arrhenius relationships were fit to parameter values to make a model that described the cell over the entire operating range. The reported errors for the full parameterization are reported in Figure 4.7. All of the parameters were kept below 10.1% of error except the $n_{e,0}$ terms (the lumped initial electrolyte concentration term). The author reported that this error could be refined further with a better optimization method.

Namor *et al.* [146] performed a parameter identification in a single-particle model using non-invasive testing (see table 4.6). The SP model parameters were normalized and grouped reducing from 14 to 7 the parameters to be identified. Three parameter groups were then defined and each group was identified separately based on experimental test on table 4.6. The maximum error was kept below 22% as is presented in the Figure 4.8.

Li *et al.* [147] adopted in the paper a simplified model with regrouped and reduced parameters based on the SP model and their previous work. They grouped the parameters as presented in table 4.6, according to the proposed parameter identification process. Three

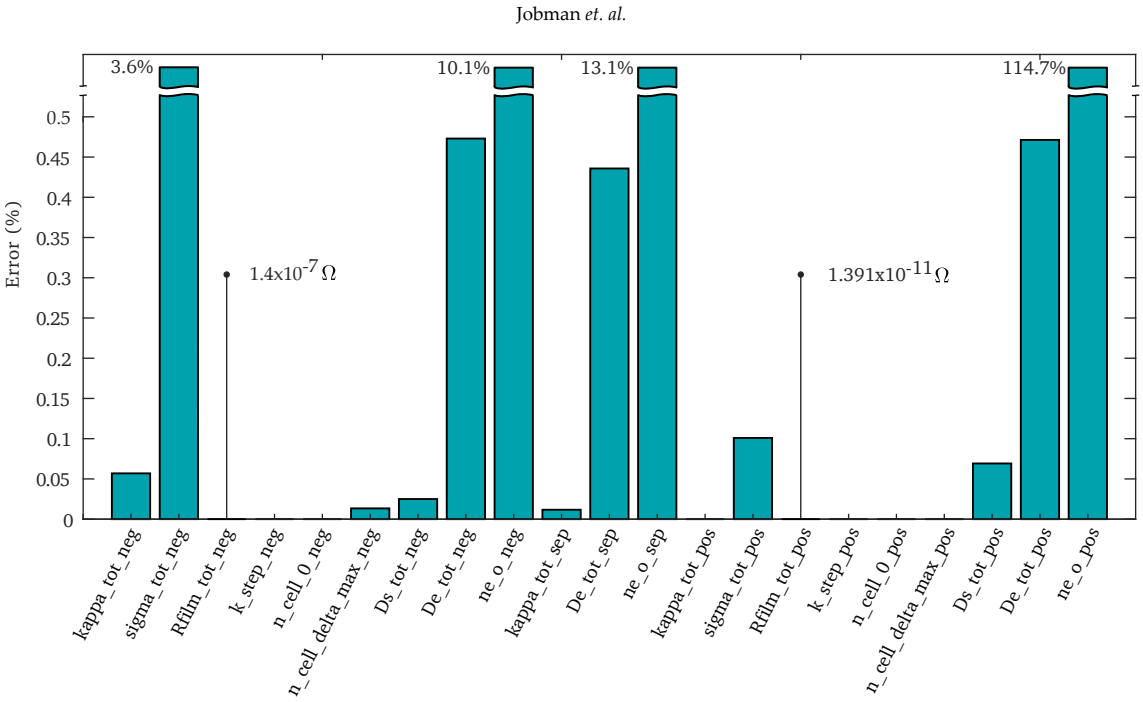

Figure 4.7: Parametric errors adapted from [116]. Note that parameters are labeled according to reference.

steps were defined in the methodology in which 9 parameters were identified with an specific pulsed profile. The stepwise procedure consisted on identification of parameters related to the open-circuit potential, the ohmic resistance and reaction polarization and related to diffusion processes. The fitting errors (shown in Figure 4.9a) were kept below 20% for the worst case, and most parameter errors were negligible. The reduction of the model made the optimization problem easier (due to a smaller number of parameters and a simpler model itself) while losing some information (note that already the SP model was less rigorous than the P2D model).

Park *et al.* [145] used a similar methodology than [149, 121] in which the general P2D model was used [54]. First, sensitivity analysis was performed across a variety of profiles including pulses, sinusoids and driving cycles. They generated a library gathering different input profiles oriented to maximize the sensitivity of model parameters. Then, a normalization was applied and the linear dependence and sensitivity ranking was calculated. The parameter grouping was shown in table 4.6. Finally, parameter fitting was done with a gradient-based algorithm. Figure 4.9b shows the error percentage using two different cycles (a dedicated one and a typical 1C constant current one [145]) with similar results. This work only reported the validation of parameterization for four parameters where some of the errors were non trivial.

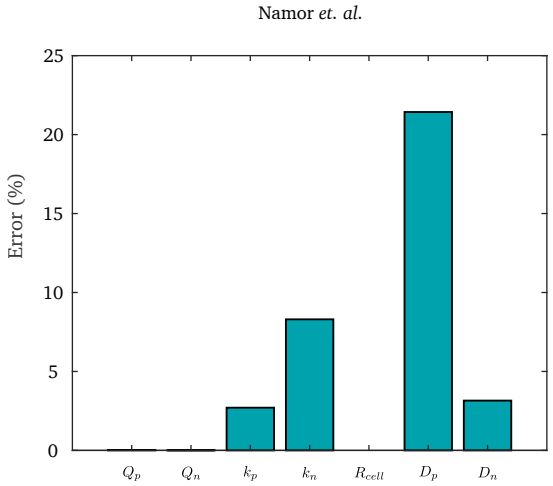

Figure 4.8: Parametric errors adapted from [146].

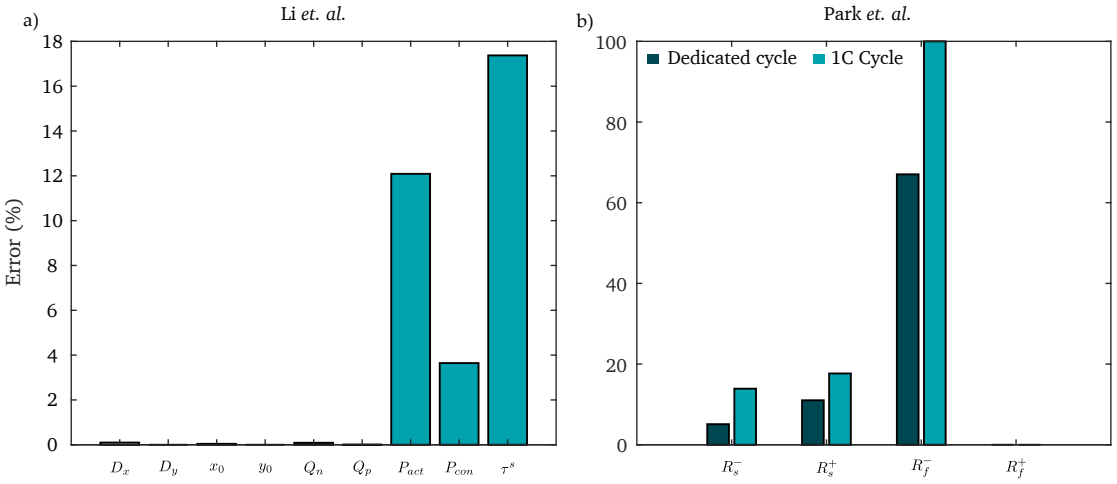

Figure 4.9: Parametric errors adapted from [147] (a) and [145] (b).

4.1.2 Physico-chemical parameterization methods

As mentioned before other alternative to identify battery cell parameters were physico-chemical procedures. Some specific parameters were normally measured, these parameters are shown in figure 4.10 classified as a function of the components of the battery that was analyzed. The reason behind that specific parameter set was to ease the needed test that are implemented. Note that once obtained, they could be easily recalculated in the desired form (as the variations between parameter sets of the same model were only a slightly different mathematical representation of the same parameter set, some examples have been described at the beginning of the chapter).

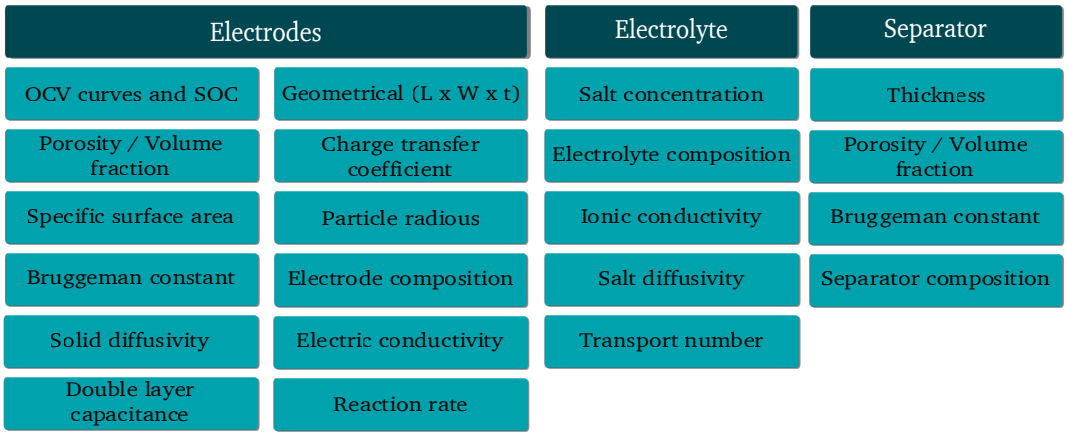

Figure 4.10: Model parameters clasified by components (electrodes, electrolyte and separator).

Methodologies in which the full or partial set of parameters were obtained experimentally are considered in the following paragraphs. In order to give an overview of the work developed in the literature authors that were focused on an specific technique or not oriented to implement those parameters into an electrochemical model have not been taken into account. It has been specified for each reference whether model parameters were measured, fitted or assumed from literature. To the authors knowledge, the only review of physico-chemical characterizations techniques applied to electrochemical models was performed by Falconi *et al.* [151]. This author provided a comparison between 31 references specifying whether parameters were measured, fitted, taken from another author or it was not reported the source.

Two groups could be distinguished when considering the amount of measured parameters, partial and full parameter obtention methodologies. On the one hand, partial charac-

terizations were commonly found in literature, and could be implemented in less time and consuming fewer resources [152, 153, 154, 155, 151]. In general this methods imply opening a battery cell and performing a basic physico-chemical characterization (geometric parameters measurement, electrode OCV curve extraction and scanning electron microscopy (SEM)/ energy-dispersive X-ray spectroscopy (EDX) techniques to estimate the active material composition and particle radius). However, transport and kinetic parameters were usually estimated or taken from literature. In this case model variables predictions could not be accurate enough despite the voltage response fitted closely the experimental data as explained before. In table 4.7 the parameters that each author measured are presented. It is possible to conclude then that parameters such as conductivities, diffusivities or reaction rates among others were not frequently measured within literature. Probably due to the complexity, time consumption or the needed specific equipment. As an example PITT/GITT techniques can be used to determine the solid diffusivity, nevertheless the test would take approximately one month long for each temperature (the test is normally repeated at different temperatures so activation energies can be calculated).

On the other hand, only few articles performed a complete physico-chemical characterization [156, 119, 120, 157, 158]. Table 4.7 show which parameters were measured (note that even if not all the possible parameters were measured some of them are intimately related and could be assumed to be measured, as an example it can be accepted that if the electrolyte ionic conductivity is measured and the diffusivity derived using the Einstein relation both were measured parameters, even if diffusivity was indirectly measured). The required infrastructure can be not accessible to most of the researchers. Glove boxes, electron microscopes NMR platforms and X-ray diffractometers are common equipments that makes this process expensive and sometimes inaccessible. Doyle *et al.* [159, 156] explained the parameter obtention procedure and used techniques. Nevertheless these authors stated that further work needed to be accomplished to study the suitability of different techniques to obtain the same parameters increasing the overall accuracy. Ecker *et.al.* obtained the model parameters [120] and then validated the model predictions towards experimental data [119].

The techniques that are generally used within literature have been collected in figure 4.11. Those techniques were classified into physico-chemical, structural and electrical or electrochemical characterization techniques. Furthermore the specific technique that could be used for the measurement of each specific parameter gathered in figure 4.10 is summarized in figure

Table 4.7: Overview of the measured physico-chemical parameters for electrochemical models.

	[152]	[153]	[154]	[155]	[156]	[151]	[12, 119, 120]
Full cell							
Capacity	X	X	X	X	X	X	X
OCV				X		X	X
Resistance							X
Electrodes							
OCV			X	X	X	X	X
Electrode area		X	X	X	X	X	X
Specific surface area							
Thickness	X	X	X	X	X	X	X
Porosity		X					X
Volume fraction	X			X			
Solid diffusion	X	X		X			X
Particle radius	X	X	X	X		X	
Reaction rate/Exchange current density	X	X					X
Electronic conductivity	X	X			X		X
Bruggeman constant/-Tortuosity		X					X
Charge transfer coefficient	X	X					
SEI film resistance	X	X					
Current collector resistance		X					
Electrolyte							
Ionic conductivity					X		X
Transport number	X						
Diffusion	X	X					
Initial salt concetration		X			X		
Separator							
Thickness	X				X	X	X
Bruggeman constant/-Tortuosity		X					X
Porosity	X	X					X
Volume fraction							

4.12.

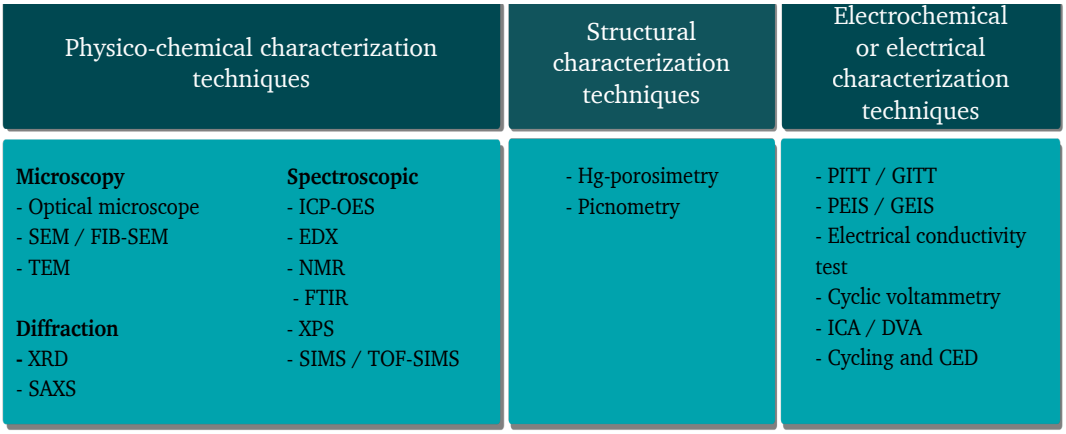

Figure 4.11: Electrode characterization techniques [160, 161].

4.1.3 State of the art conclusions

Along this section the need of a proper parameterization of electrochemical models as a crucial step to achieve accurate predictions has been presented.

Parameterization approaches based on computational methods have been classified within two different groups: single-optimization analysis and multi-optimization analysis (SOA and MOA). The results of authors showing reliable proof of parameterization have been presented for both of the approaches showing significant differences depending on the used method. Some of the SOA methods reported good accuracy, but did not fully parameterize a P2D model (only partial sets of parameter values were identified). On the other hand, authors using MOA have reported accurate parameterizations of both SP and P2D models. These MOA works either reformulating the models using analytic parameter lumping or using optimization routines to group parameters based on sensitivity tests. The analytic method appears to give more accurate result than the sensitivity-based method but is able only to find values for groups of parameters and not for every individual parameter. It remains to be seen which of these approaches gives the best inputs to models of cell aging.

An interesting future avenue of investigation would be to develop methods to de-group lumped sets of parameters. This might involve introducing physico-chemical tests, introducing different sensors (e.g., magnetic in the case of iron-phosphate cells, reference electrodes in a commercial cell [76] or stress/strain in a more general setting) to give a richer dataset,

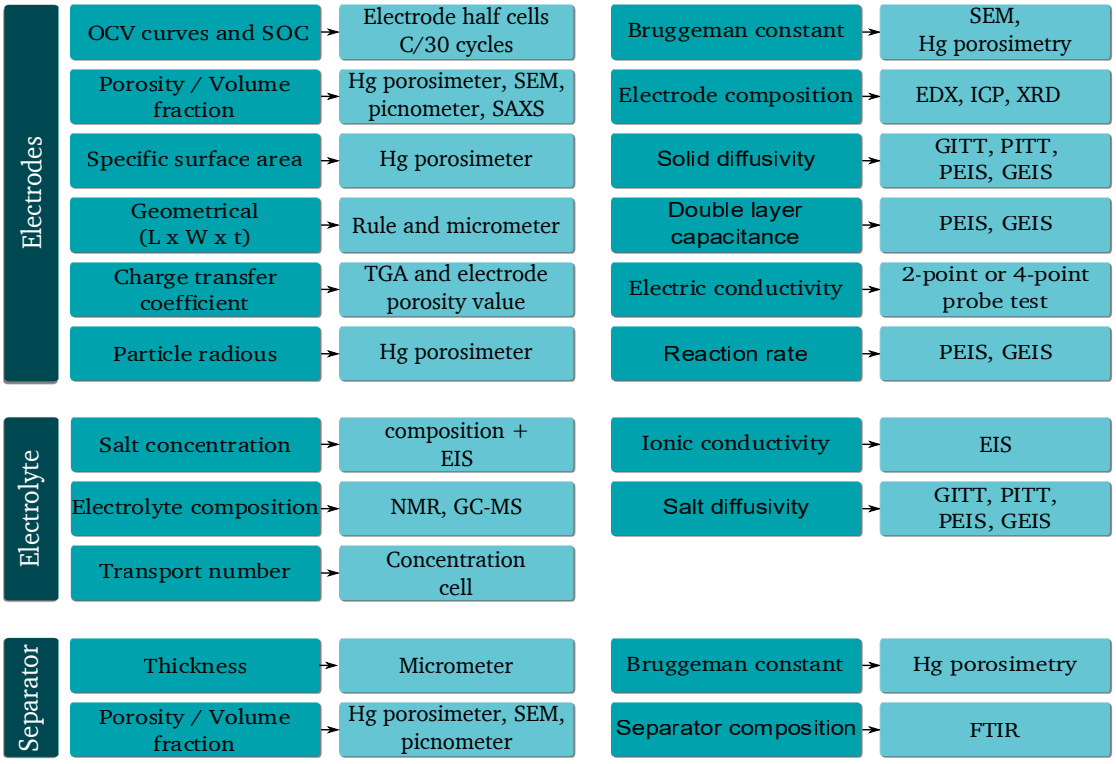

Figure 4.12: Physico-chemical obtention method: parameters and techniques.

or designing more specific identification tests (perhaps based on observed rates of aging) to identify key parameters that can be used to free the full set. Furthermore the definition of mixed methods comprising physico-chemical tests and model-based fitting identification could be a good approach. Not only to de-group lumped parameter models but to define efficient, reducing the time and cost of the identification procedure while increasing the accuracy.

Rergarding physico-chemical cell characterization there is still a big research niche in order to get all the potential accuracy of these techniques and methodologies as well as standardize them. Taking again into account that mixed methods can boost the potential of both methodologies.

4.2 Experimental parameterization

Within this section a parameterization of an SLPB 7.5 Ah high power NMC Kokam cell (SLPB75106100) was done. For this, physico-chemical tests and literature references of the specific cell model were used. This section will give results showing the accuracy and difficulties when employing this type of system identification procedure, creating a better context to propose future and more accurate and/or efficient mixed system identification methods if necessary.

The parameters of the P2D model have already been presented, nevertheless a more detailed list can be seen in table 4.8 (each parameter definition can be found in appendix 7.3). These parameters are therefore going to be identified along the next subsections.

4.2.1 Cell opening, geometric parameters and porous matrix characterization

First, a sample cell was opened inside a glove-box. The argon atmosphere inside the glove-box prevents reactions of the battery components with the ambient which could be a safety hazard, not only this, the samples are also preserved until the needed tests are done.

Figure 4.13 shows the cell after being disassembled. It was found to be composed of 23 double coted anode electrodes and 22 cathodes of the same type in addition to 2 single side coated cathode electrodes (table 4.9). Those electrodes were piled up while a separator was intercalated in a z-fold type configuration as shown in figure 4.13.

Table 4.8: List P2D model parameters.

Negative electrode	Separator	Positive electrode
σ^{n}_{eff}		σ^{p}_{eff}
$brug_{\sigma^n}$		$brug_{\sigma^p}$
$E^{n}_{act,\sigma}$		$E^{p}_{act,\sigma}$
a^{n}_{s}		a^{p}_{s}
L^{n}	L^{s}	L^{p}
κ^{n}_{eff}	κ^{s}_{eff}	κ^{p}_{eff}
$brug_{\kappa^n}$	$brug_{\kappa^s}$	$brug_{\kappa^p}$
D^{n}_{s}		D^{p}_{s}
E^{n}_{act,D_s}		E^{p}_{act,D_s}
R^{n}_{s}		R^{p}_{s}
ε^{n}_{e}	ε^{s}_{e}	ε^{p}_{e}
ε^{n}_{s}		ε^{p}_{s}
$D^{n}_{e,eff}$	$D^{s}_{e,eff}$	$D^{p}_{e,eff}$
$brug_{D^n_e}$	$brug_{D^s_e}$	$brug_{D^p_e}$
k^{n}_{0}		k^{p}_{0}
$E^{n}_{act,k}$		$E^{p}_{act,k}$
$C^{n}_{s,max}$		$C^{p}_{s,max}$
α^{n}		α^{p}
R^{n}_{f}		R^{p}_{f}
θ^{n}_{0}		θ^{p}_{0}
θ^{n}_{100}		θ^{p}_{100}
A, t^{0}_{+}, $\partial \ln f_{\pm}/\partial \ln c_e$, $c_{e,0}$, E_{act,D_e},$E_{act,\kappa}$ span all cell regions		

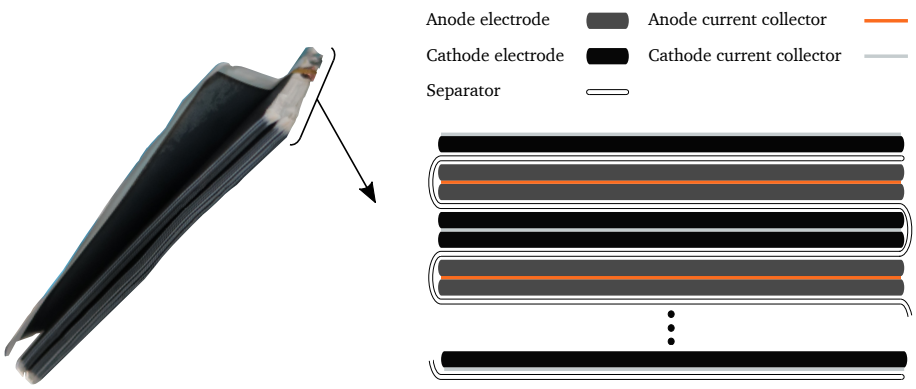

Figure 4.13: Cell structure.

4.2.1.1 Geometric measurements

Table 4.9: Measured cell geometric values; dsce: double side coating electrode, ssce: single side coating electrode.

			Anode	Separator	Cathode	Anode CC	Cathode CC
Layers	-	[-]	23	1	22 dsce 2 osce	23	22 ssce 2 ssce
Width	-	$[m]$	0.086	0.089	0.084	0.084	0.086
Length	-	$[m]$	0.102	4.557	0.1	0.1	0.102
Thickness	L^{n}	$[m]$	$63.8 \cdot 10^{-6}$	$1.33 \cdot 10^{-5}$	$34 \cdot 10^{-6}$	$1.57 \cdot 10^{-5}$	$2.00 \cdot 10^{-5}$
Area	A	$[m^2]$	$0.88 \cdot 10^{-2}$	0.406	$0.84 \cdot 10^{-2}$	$0.84 \cdot 10^{-2}$	$0.88 \cdot 10^{-2}$

With the cell opened a sample electrode was selected (excluding the single coated cathodes in the top and bottom of the cell). In order to measure the dimensions of the electrode components, pieces were cleaned three times in one minute dimethyl carbonate (DMC) baths, so the remaining salt coming from the electrolyte was removed. The electrodes including current collector and two coatings were measured with a micrometer, after the coatings were removed using n-methyl pyrrolidone (NMP) that dissolved the binder in the electrode and also measured the current collectors. The current collector coatings were calculated finally as the current collector thicknesses were known. All the values are summarized in table 4.9. Note that all thickness values were measured at least in three different samples or sample points to ensure homogeneity, and the presented value is the mean one.

The obtained geometric values were in the range of the values reported by Ecker *et al.*[12]. Those values were gathered in table 4.12 and used in the final set of parameters to maintain consistency with other parameters taken from this reference. Nevertheless the geometric values mainly affect the capacity of the cell ,that was fitted in subsection 4.2.3, and therefore the difference can be considered negligible. It is important to have good geometric values to maintain the consistency in the OCV fitting, but small differences will not affect the final model result.

4.2.1.2 Active material identification

The next step was to identify active material composing the anode and cathode electrodes. This was used to define the molecular weight (M) of the active material phases and its density (ρ), used in section 4.2.3.

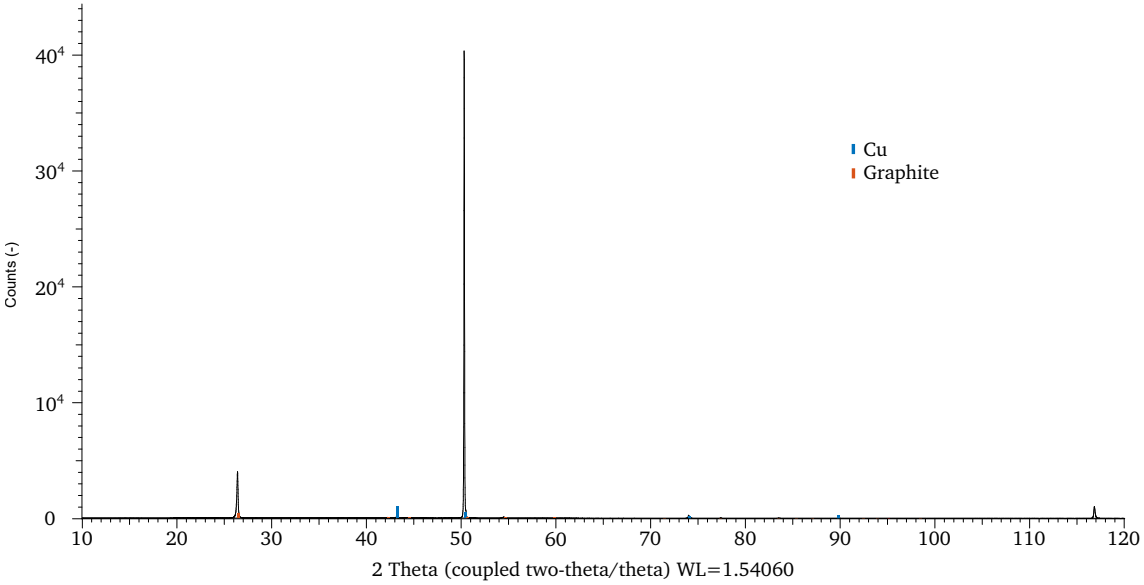

Figure 4.14: Anode X-ray diffractogram processed with crystallography open database and PDF-2 database.

The anode diffractogram in figure 4.14 shows the identification of Cu (from the current collector) and graphite phases (a *Bruker D8 Discover* diffractometer was used). On the contrary the cathode material was found to be a material blend composed of two different phases and the Al current collector, figure 4.15 shows the identification of $CoLiO_2$, and two more suitable phases $Li(Ni_{0.8}Co_{0.2})O_2$ and $Li(Ni_{0.6}Co_{0.4})O_2$. $CoLiO_2$ was clearly identified, while the matching difference between $Li(Ni_{0.8}Co_{0.2})O_2$ and $Li(Ni_{0.6}Co_{0.4})O_2$ were very small. This results were in line with the material identification that Ecker *et al.*[12] reported using ICP (graphite and $Li(Ni_{0.4}Co_{0.6})O_2$, being the last one a mean measurement of $CoLiO_2$ and $Li(Ni_{0.8}Co_{0.2})O_2$/$Li(Ni_{0.6}Co_{0.4})O_2$). The cell materials were considered to be graphite for the anode and a blend of $CoLiO_2$ and $Li(Ni_{0.8}Co_{0.2})O_2$ (since it is slightly closer) for the cathode. The fact that cathode material was composed of a blend was additionally observed with SEM and particle size analyzer (PSA) as will be shown in the following, while its influence is discussed.

4.2.2 Porous matrix characterization

After disassembling the cell and identifying electrodes composition the porous matrix was analyzed. SEM/EDX (*FEI - QUANTA 200 Field Emission Gun (FEG)*) and ion-milling (*Hitachi Ion Milling 4000Plus*) cross sections were employed to check the electrode particles shapes,

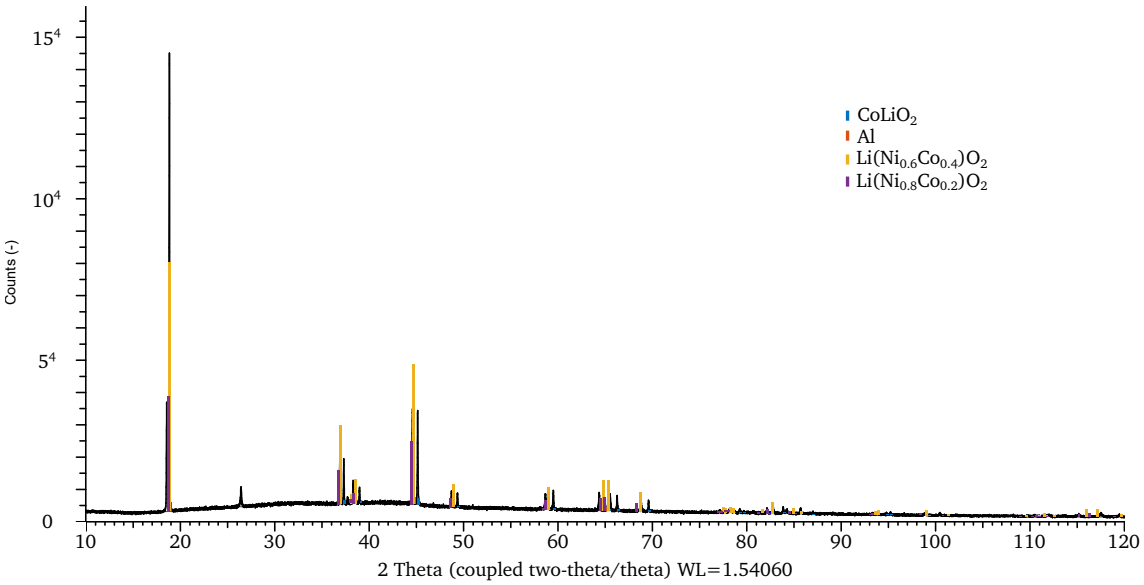

Figure 4.15: Cathode X-ray diffractogram processed with crystallography open database and PDF-2 database.

sizes, homogeneity and confirmation of electrodes composition.

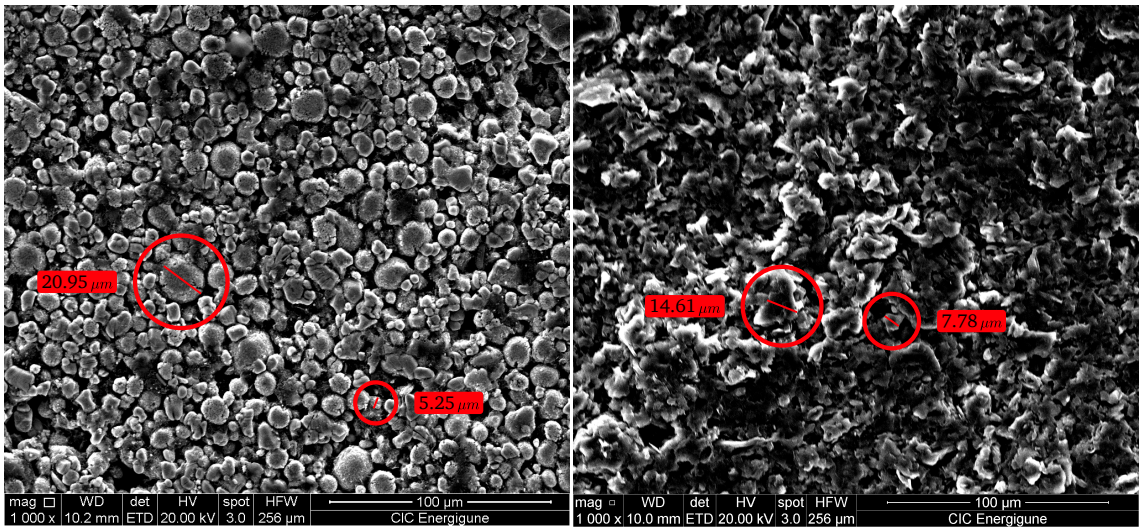

Figure 4.16: Cathode (left) and anode (right) SEM images.

The anode electrode is composed of "flakes" as can be seen in figure 4.16 (left). The flakes in the anode were identified to be graphite with the XRD test, nevertheless the EDAX data (table 4.10) confirmed that no other elements were present in the electrode. Cathode particles found to be spherical (figure 4.16 right) and also the XRD phase identification was confirmed with EDAX results (table 4.10).

Table 4.10: Anode and cathode electrodes EDAX data.

Cathode		Anode	
Element	Wt%	Element	Wt%
C	27.87	C	100.00
O	12.24		
Co	39.68		
Ni	20.21		

When measuring electrodes thickness the values obtained in the cross sections were in the same range of values obtained measuring with the micrometer. It can be seen looking at the cross section images (figures 4.17 and 4.18) the reason why all the measured values were in the same range with variations up to tens of micrometers, the electrodes surface was not completely homogeneous and therefore depending on the measured area the result differed. This dispersion could be considered admissible since the geometric parameters are only affecting the capacity and that can be compensated during the OCV fitting and cell balancing process.

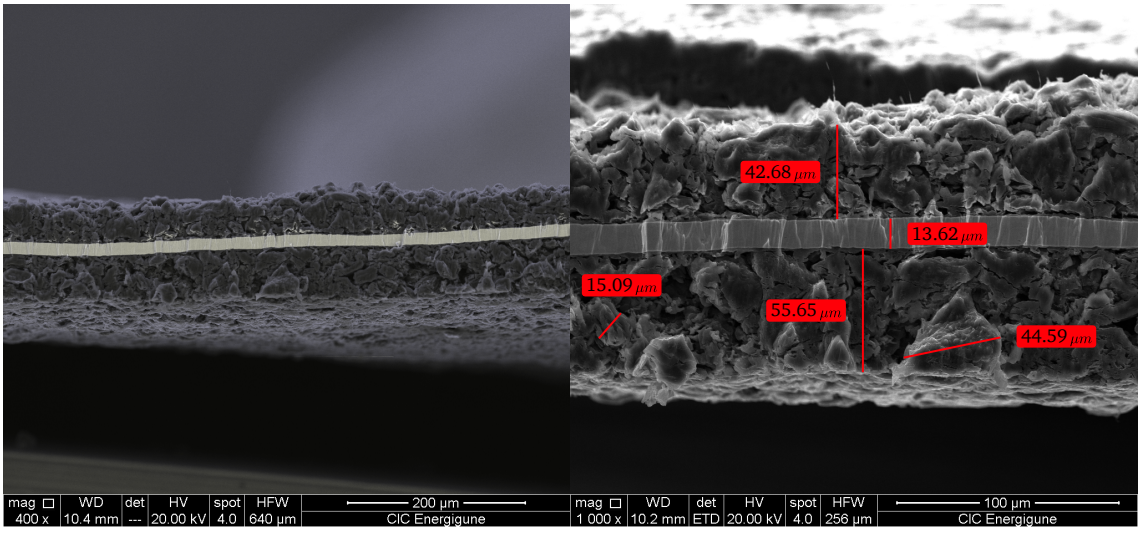

Figure 4.17: Anode cross section.

4.2.2.1 Volume fraction, Bruggeman exponent and specific surface area

Electrodes volume fraction is typically measured with "Hg-porosimetry". This technique measures the pores in the electrode (porosity δ) by filling them with mercury, it is why can be considered as a direct measure of the electrolyte volume fraction (equation 4.2). Nevertheless in the case of the solid phase volume fraction it only can be considered as an approximation

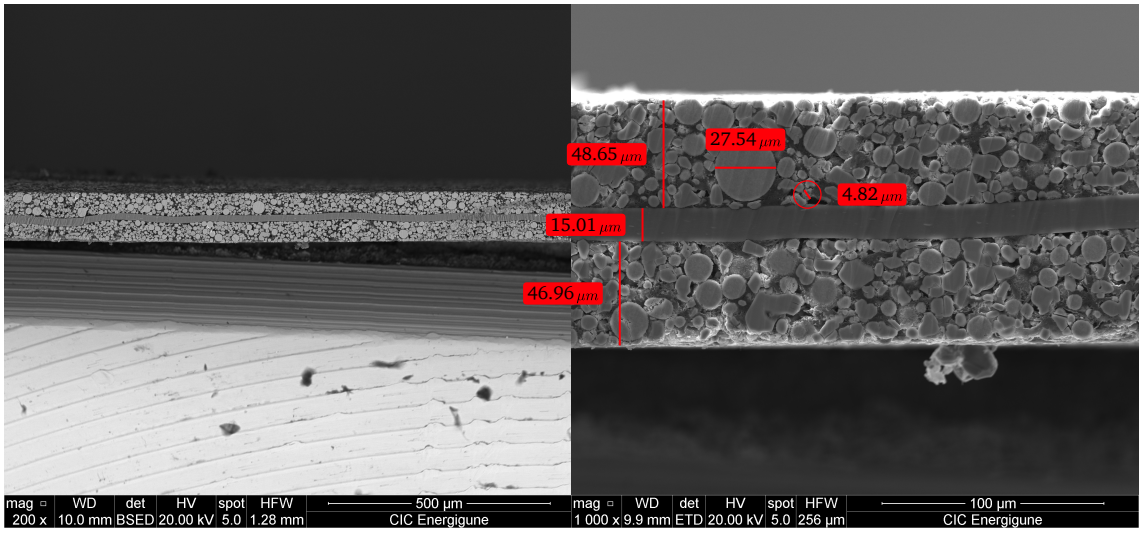

Figure 4.18: Cathode cross section.

to the real value. Conductive aid (δ_C^x) and binder (δ_B^x) are added to the electrodes to improve the battery performance and maintain the porous matrix together on top of inactive parts unintentionally generated during the production of the electrodes. This means that the volume fraction of the solid that is measured by a porosimeter corresponds to the active material, conductive aid and binder together (equation 4.3).

$$\varepsilon_e^x = \delta^x \tag{4.2}$$

$$\varepsilon_s^x = 1 - \delta_A^x - \delta_B^x - \delta_C^x - \delta_{IN}^x \approx 1 - \delta^x \tag{4.3}$$

The porosity value reported by Ecker *et al.*[12] for the same battery model was used as reference. In the case of the electrolyte volume fraction, this value can be considered a good approximation. Otherwise in the case of the solid phase volume fractions the term was corrected with an inactive part (δ_{IN}^x) within section 4.2.3. It is also important to note that the solid phase volume fraction is only used for the calculation of the effective solid phase ohmic resistance in the model, and to calculate the particle radius of the solid phase. Taking into account that the ohmic resistance in the active material has little influence in the model polarization (Zavalis *et al.* [162] reported a cell polarization analysis where active material polarization influence was demonstrated to be negligible, figure 4.19) using this approximation seemed to be logical. The calculation of the particle radius will be addressed in the following. Final values can be found in table 4.13.

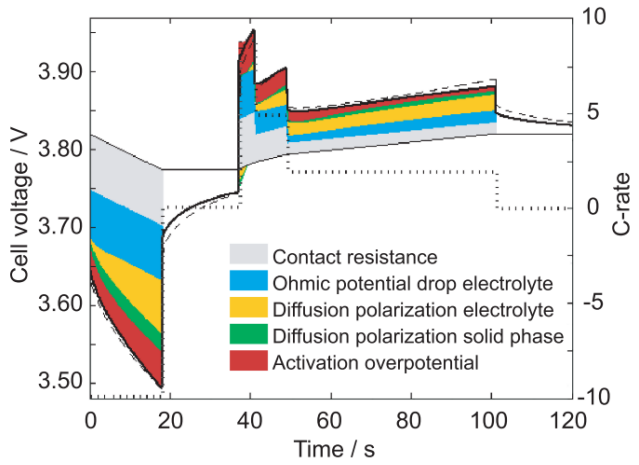

Figure 4.19: Cell polarization analysis [162].

Bruggeman exponents (*brug*) used to calculate effective porous matrix parameters where derived from porosity (δ) and tortuosity (τ) values as follows.

$$\tau^x = \delta^{x^{-brug_x^x}} \tag{4.4}$$

$$brug_x^x = -\log_\delta(\tau^x) \tag{4.5}$$

The same way as the volume fractions this is an approximation since the porosity and tortuosity are measured with the porosimetry test, but it was still a more accurate approach than assuming $brug = 1.5$ as it is commonly done. Calculated values are shown in table 4.12 and 4.13.

Finally to characterize the porous matrix the specific surface area was calculated as a function of the electrode thickness and volume fraction [163] (equation 4.6).

$$a_s^x = 3\frac{\varepsilon_s^x}{R_s^x} \tag{4.6}$$

4.2.2.2 Particle radius

The radius of the particles conforming the anode and the cathode is contemplated in the model as a single value, but in the reality particles has a notable deviation. Not only this but it is possible that two different active materials are used (even same material composition but different particle radius) to improve performance. Figures 4.16, 4.17 and 4.18 show that

different particles were found in the electrodes under study, as well as the cathode XRD data 4.15. Additionally a PSA test was used to confirm two different particle radius in the cathode electrode (figure 4.20, obatined with a *Mastersizer 3000 Malvern* PSA). Both electrodes show two different particle size distributions, being more significant in the cathode. Together with XRD results (figure 4.15) can be confirmed that two different material phases where used in the cathode, and that residual smaller flakes are found in the anode. To model the particle radius in this work the average value reported by Ecker *et al.*[12] (calculated from the porosity measurements and in line with the obtained results) was used as a first approximation and modified latter to fit the experimental voltage response (since the model formulation assumes a single active material phase per electrode). This process was done after the OCV was correctly adjusted since the particle radius is a dynamic parameter itself (the final value can be found in table 4.12).

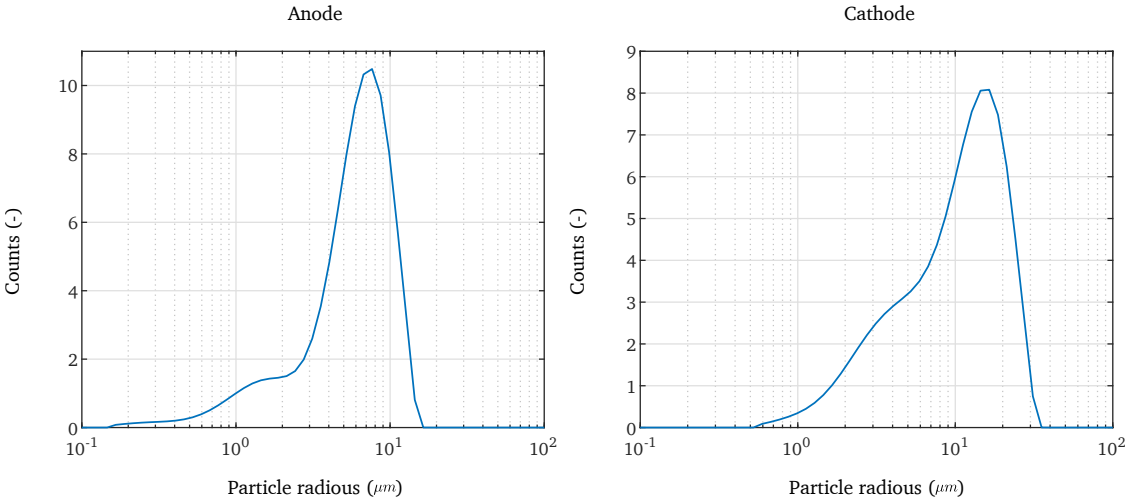

Figure 4.20: Anode (left) and cathode (right) electrode PSA results.

4.2.3 OCV fitting, cell balancing and capacity related parameters

The following step in the model parameterization was the OCV fitting, where anode and cathode experimental OCV curves were processed so they could be introduced in the model, after the balancing of the cell was defined.

First, parameters in table 4.11 were fixed defining basic properties of the electrodes materials. The molecular weight (M) was calculated from the X-ray experiments performed previously as the material phases components and its ratios were measured. These tests were also

used to define the density of the active material (ρ) that was extracted from the inorganic crystal structure database (ICSD). Finally the volume fraction was assumed as explained in section 4.2.2.1.

Table 4.11: OCV fitting process parameters.

Parameter	Anode	Cathode
Molecular mass M $[g/mol]$	72.0669	90.84
Density of the material ρ $[g/m^3]$	$2.2 \cdot 10^6$	$4.94 \cdot 10^6$
Porosities ε_s [-]	0.329	0.296
Coin cell radius r $[m]$	$\frac{12 \cdot 10^{-3}}{2}$	$\frac{12 \cdot 10^{-3}}{2}$

After fixing the values in table 4.11 the theoretical maximum lithium concentration of anode and cathode was calculated as follows:

$$C^x_{s,\max} = \frac{\rho^x}{M^x} \tag{4.7}$$

Each material OCV curve was experimentally obtained. To do this right after disassembling the cell under an argon atmosphere, coin cells composed of each electrodes samples and a lithium counter electrode were built. These cells were then cycled at a current lower than $C/30$ to avoid polarization effects. Current corresponding to $C/30$ was calculated based on the theoretical capacity (equations 4.8).

$$\begin{aligned} C^x_{theoretical,coin} &= \frac{C^x_{\mathrm{s,max}} V^x_{coin} (1-\varepsilon^x_s)(1-0)F}{3600} \\ V^x_{coin} &= \pi {r_x}^2 L^x \end{aligned} \tag{4.8}$$

Figure 4.21 shows the anode and cathode coin half cells voltage response and voltage limits. These curves needed to be represented as a function of lithium content $\left({C^x_s}/{C^x_{\mathrm{s,max}}} \right)$ so they could be used in the model. Looking at the anode coin cell voltage response it can be seen at the beginning and end of cycle the voltage had an asymptotic behavior. This behavior indicates a electrochemical reaction transition, what is important since can be considered then that the electrode is fully lithiated and delithiated.

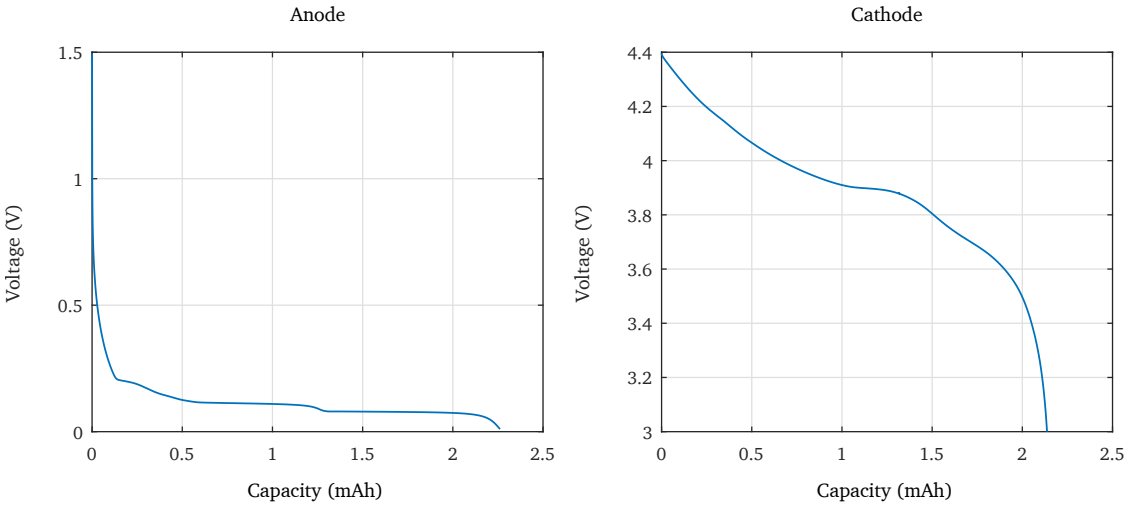

Figure 4.21: Coin half cells experimental OCV.

The inactive part of the electrode can be then calculated as follows:

$$inactive^n = 1 - \frac{C^n_{coin}}{C^n_{theoretical,coin}} \tag{4.9}$$

On the contrary, the cathode electrode could not be fully delithiated since the electrolyte would be deteriorated at the voltage where the cathode is completely discharged. To maintain coherent lithium content values then, the cathode inactive part was fixed (with a value of $inactive^p = 0.45$ the cathode lithium content was maintained around $C^x_s / C^x_{s,max} \approx 0.3$ as can be usually found within literature [151]).

This calculations above were based on the values fixed in table 4.11. Volume fraction (ε_s) and coin cell radius (r) values were however only approximate thus, the lithium content values were also approximated. In both cases the measurements rely on one or few samples, what is not necessarily an average representation of the full cell. Not only this the volume of the full cell is also relaying on representative electrodes and measuring points. To solve this, a correction factor was introduced as shown in equation 4.10 and used during the cell balancing process.

$$V^x_{coin} = \pi {r_x}^2 L^x f^x \tag{4.10}$$

Figure 4.22 shows the half coin cells voltage as a function of lithium content after using $f^n = 0.8$ and $f^p = 0.82$ corrections factors.

With the OCV curve of each electrode, the cell balancing was fitted. Based on the method

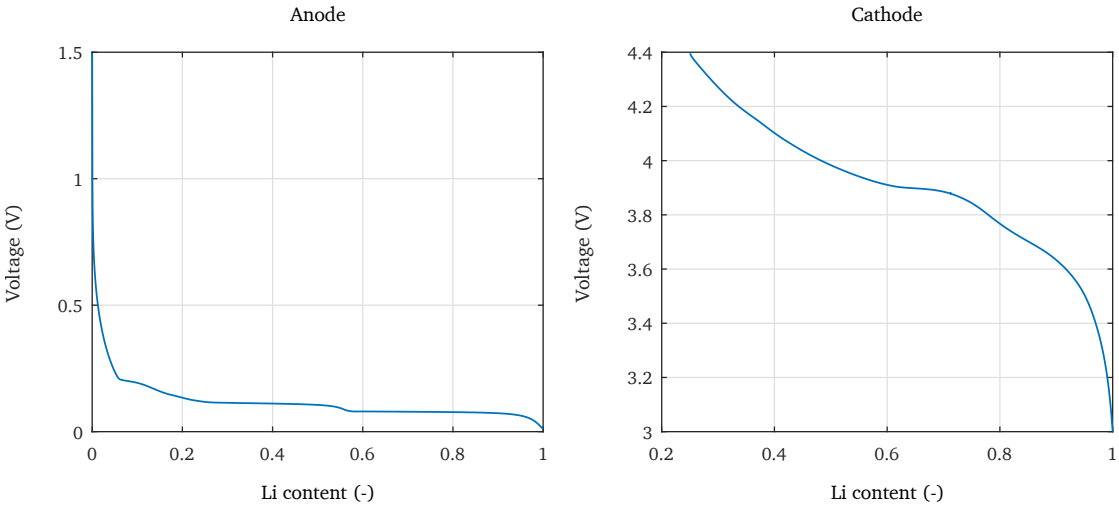

Figure 4.22: Coin half cells OCV lithium content.

proposed by *Ecker et al.*[12] the initial and final stoichiometric points $C_s^x / C_{s,max}^x$ were fitted. This method considered the cell electrodes lithium content starting before the formation cycles, and defined the needed formulation to describe this lithium content after SEI formation and electrodes balancing stabilization.

A diagram of the maximum and minimum lithium concentrations at each stoichiometric point (C_s^x) after the formation cycles, when the cell is charged and when the cell is discharged can be found in figure 4.23. Those lithium concentrations at each point could be calculated as shown in equations 4.12 to 4.15. After adjusting C_{SEI} and utilization terms the stoichiometric points can be found in table 4.12. In addition figure 4.24 shows the ranges of OCV that were used in the case of each electrode.

$$C_{s,charged}^{p} = (1 - \text{utilization}) C_{s,max}^{p} \tag{4.11}$$

$$C_{s,charged}^{n} = (\text{utilization} - C_{SEI}) C_{s,max}^{p} \frac{V^p (1 - \varepsilon_s^p)(1 - inactive^p)}{V^n (1 - \varepsilon_e^n)(1 - inactive^n)} \; ; \; V^x = L^x A^x \tag{4.12}$$

$$C_{s,discharged}^{p} = (1 - C_{SEI}) C_{s,max}^{p} \tag{4.13}$$

$$C_{s,discharged}^{n} = 0 + offset \tag{4.14}$$

$$\tag{4.15}$$

In order to properly adjust f^n, f^p, utilization and C_{SEI} correction and balancing factors respectively, differential voltage analysis were also used. Differential voltage curves aided to show materials phase transitions so not only the local or average voltage error was taken into

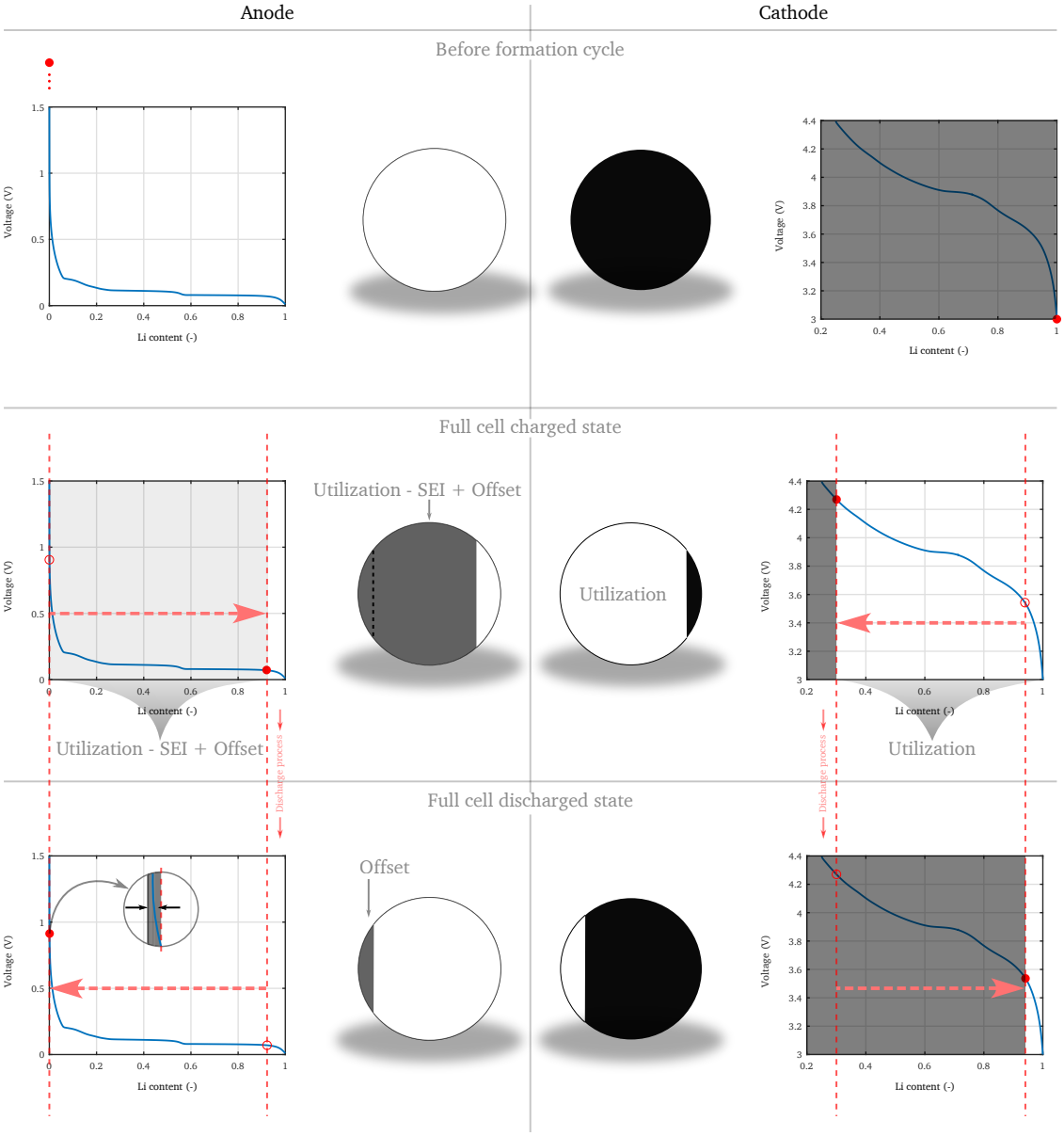

Figure 4.23: Battery balancing before formation, at charged and discharged state.

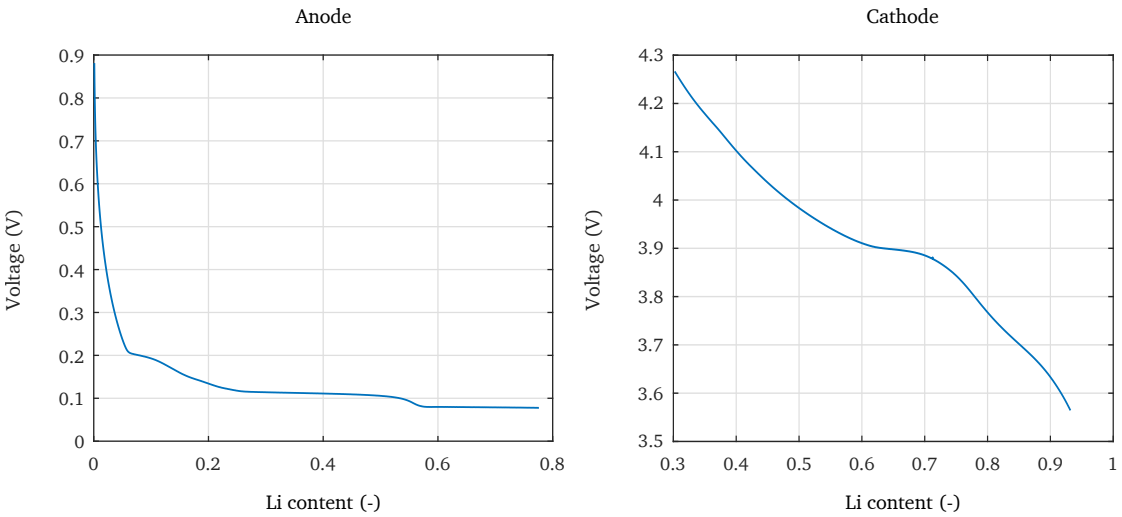

Figure 4.24: Coin half cells OCV lithium content operation range.

account, but also the lithiation phase of each electrode (half cell reconstructed OCVs and their differential voltage vs lithium content curve can be seen in figure 4.25).

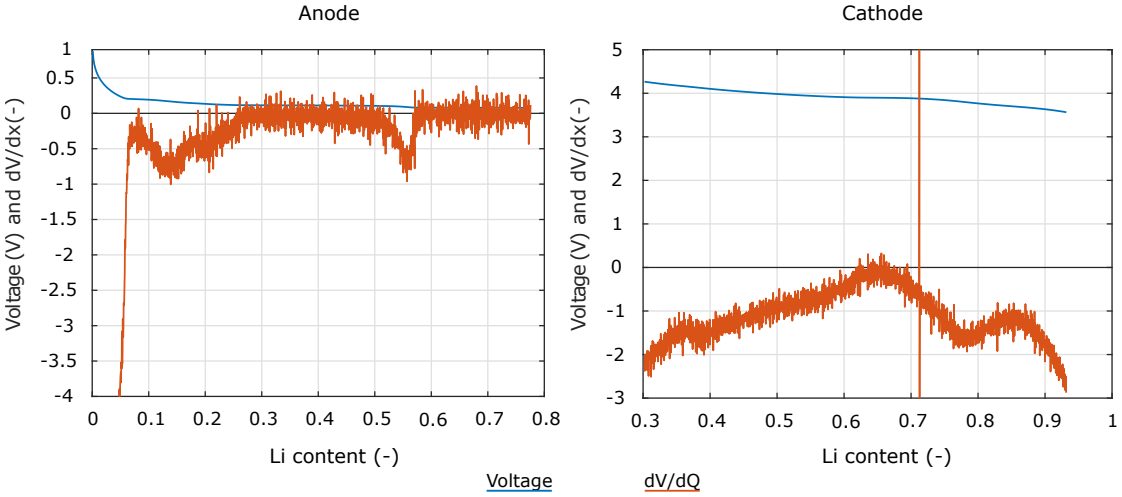

Figure 4.25: Coin half cells OCV vs lithium content operation section, and dV vs lithium content operation range.

The result of the OCV fit and cell balancing are shown in figure 4.26 together with the differential voltage curves of the real cell (cycled at $C/30$) and reconstructed OCV. The OCV reconstruction has an accurate phase transition fit with a maximum voltage error below 30 mV or 2% (figure 4.27).

Finally as a proof of proper parameterization of the cell DC response, a discharge of the real cell at $C/30$ (in order to avoid polarization effects) was compared with a FOM simulated with

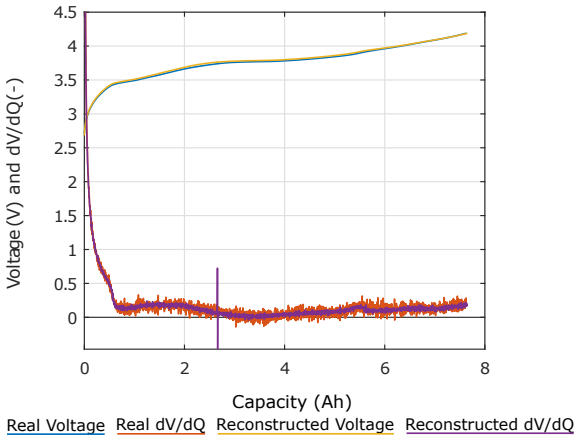

Figure 4.26: OCV reconstruction.

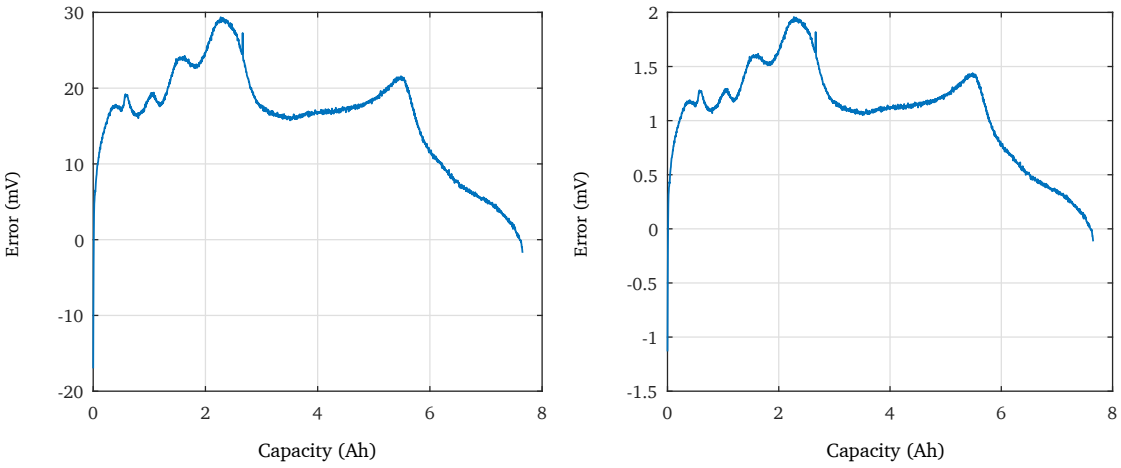

Figure 4.27: OCV reconstruction error.

COMSOL Multiphysics (figure 4.28) showing even a lower voltage error (below 15 mV). This can be understood as a sign that lower current rates to obtain experimental OCV data would give more accurate results, nevertheless the results can be considered as accurate enough since the model is not designed to predict voltage but the states of the battery (lithiation states and internal variables) and this issue will be improved in future investigations.

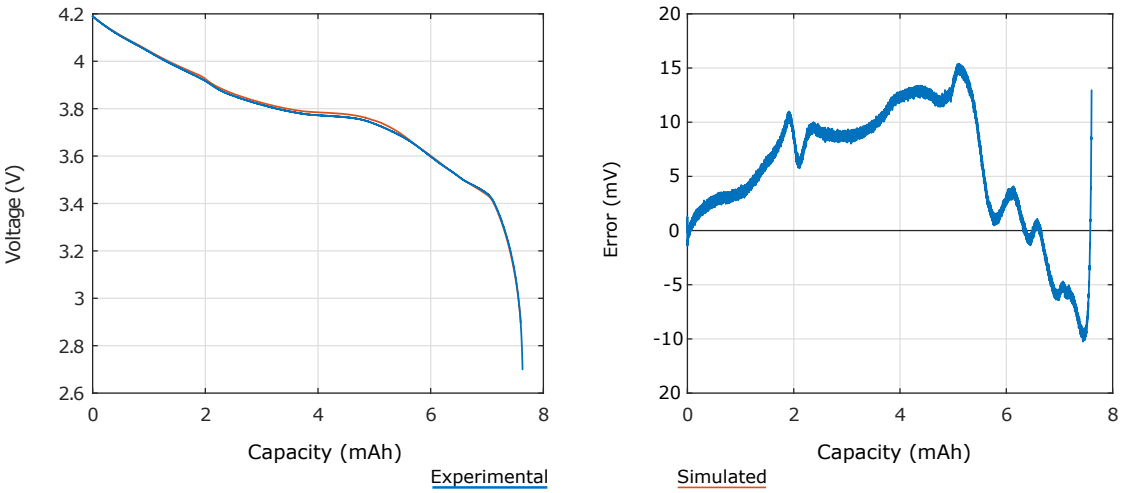

Figure 4.28: Model voltage response and error at $C/30$.

4.2.4 Electrolyte

Ecker et al.[12] reported an electrolyte parameterization (κ^{x}_{eff}, $D^{x}_{e,eff}$ and t^{0}_{+} used for the electrolyte phases in all the model regions) based on a LP50 electrolyte. These authors measured the ionic conductivity of the electrolyte κ as a function of lithium concentration and derived the diffusion coefficient D_e using the Einstein relation, while this relation is only true for diluted solutions is still considered a fair enough approximation. The cationic transference number t^{0}_{+} was otherwise extracted from literature.

However they did not provide proof of the electrolyte identification, it is why this section is focused on identifying the electrolyte composition to consider the parameterization presented by Ecker *et al.*. The used identification process was based in two different steps, the first one is the electrolyte solvent identification and the second the salt detection.

In order to identify the solvent of the electrolyte when the cell was disassembled a sample including negative and positive electrodes as well as separator (all impregnated in electrolyte) were rapidly submerged in dichloromethane. Right after the whole solution was processed by

GC-MS so the solvents could be analyzed.

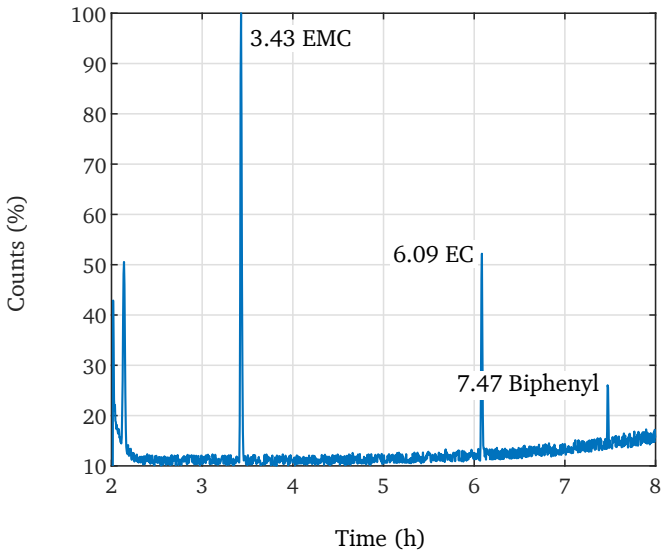

Figure 4.29: GC-MS chromatogram.

Figure 4.29 shows the chromatograph corresponding to the GC-MS (*Perkin Elmer Mass Spectrometer Clarus SQ8T*) test. Ethylmethylcarbonate (EMC), ethylene carbonate (EC) and biphenyl were found. EMC and EC are part of the solvent expected in the LP50 electrolyte and biphenyl is a commonly used additive to protect the battery in overcharge events. It is also important to notice that the ratios in this case can not be taken as a quantitative value, the solvents were evaporated at different rates when the cell was disassembled thus, the GC-MS test it is only accurate identifying the presence of the mentioned solvents.

Next the salt composition was identified. NMR *Bruker Avance III 500 MHZ* was used, after dissolving the salt contained in the electrodes into deuterated acetone, fluor and phosphorous were found.

The identified solvent components and salt were then EMC/EC/$LiPF_6$, it was assumed then that the electrolyte used for this specific cell is LP50, and therefore the values reported by Ecker *et al.*[12] were used.

Finally the initial concentration of electrolyte was assumed to be $c_{e,0} = 1000$, as no liquid electrolyte is recovered. Furthermore the total amount of electrolyte is unknown being a complex parameter to measure. The simulations nevertheless show a good initial prediction (figure 4.34) supporting the assumption.

4.2.5 Dynamic parameters

Next the parameters related to the dynamic behavior of the cell were characterized, as will be explained in the next sections.

4.2.5.1 Solid phase electric conductivity

Solid phase electric conductivity was reported to be a highly variable value (orders of magnitude variations were reported in literature [164]). Even when measuring electrodes with 4-point prove setups variations up to 60% were reported as a common phenomena [12, 165, 166]. Ecker *et al.* [12] measured the electrodes with a four point prove setup in order to at least define the order of magnitude of the parameter. In this work and assuming that the influence on cell polarization of the solid phase electric conductivity was negligible as explained in section 4.2.2.1, values reported by Ecker *et al.* were used (4.12).

4.2.5.2 Film resistance

Film resistance R_f^x in the electrodes parameter is responsible of describing the ohmic resistance in the battery cell. This parameter is used to model the voltage drop due to the current collectors and contact resistances proportional to the cycling current. Furthermore when considering an experimental scenario where the voltage measuring setup has its own voltage drop, film resistance can also be used to compensate it. Film resistance was therefore adjusted within section 5.3.2.

4.2.5.3 Reaction rate coefficient, charge transfer coefficient and solid phase diffusivity

The reaction rate coefficient j^x, charge transfer coefficient α^x and solid phase diffusivity D_s^x are three model parameters intimately linked. They are used to parameterize the Butler-Volmer equation (appendix 7.4) responsible of modeling the electrochemical reaction kinetics. Typically is fitted using FOM models or measured using electrochemical techniques as PITT/GITT or PITT/GITT+PEIS/GEIS. It is important to understand that there are four parameters involved in the equation that models the GITT or PITT experiment and it is therefore necessary to measure/assume three of them to calculate the fourth. Ecker *et al.*[12] used PITT experiments to obtain these parameters (table 4.13 and [12]). Based on that work the normalized reaction rate coefficient k_0^x and the charge transfer coefficients α^x were derived. In the case

of the diffusion coefficient D_s^x the parameter as a function of lithium content (proportional to the SOC) used by Ecker *et al.* was initially introduced (figure 4.30), with the voltage response and error shown in figure 4.31.

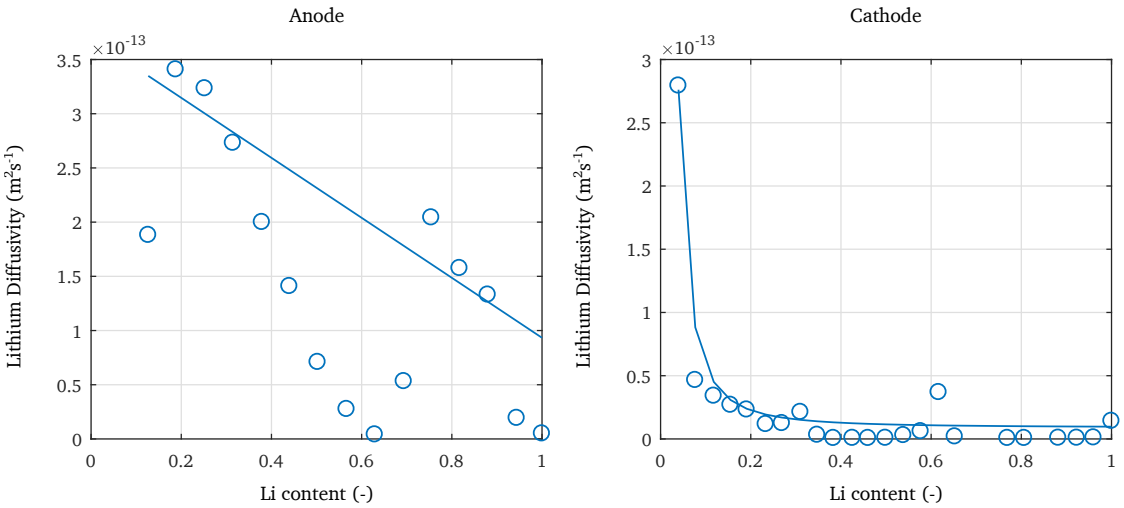

Figure 4.30: Lithium diffusivity experimental data from [119, 12] (dots) and fit used in the model (solid).

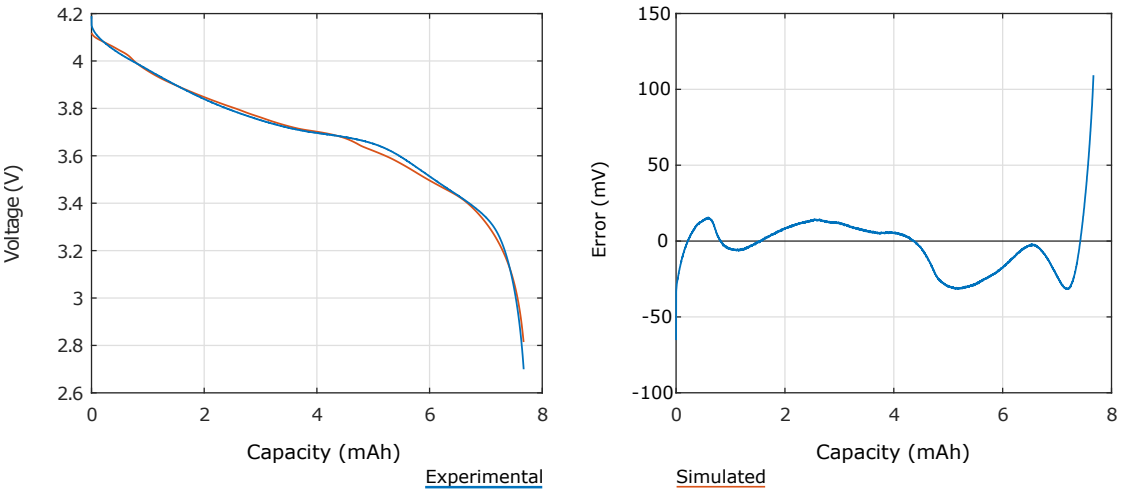

Figure 4.31: 1C rate FOM model simulation with D_s^x reported by Ecker *et al.*.

The voltage prediction was in line with the literature [120] in terms of form and tendency as well as in absolute error in mV. Oppositely when looking at the anode lithium concentration $\left(C_s^x / C_{s,max}^x\right)$ the curve showed increasing values at some ranges as can be seen in figure 4.32. This effect was not consistent since the cell was discharged during the whole cycling time, in addition the derivatives of that curve change from negative to positive what can generate

problems while the reduction process used to create the ROM (section 3.2).

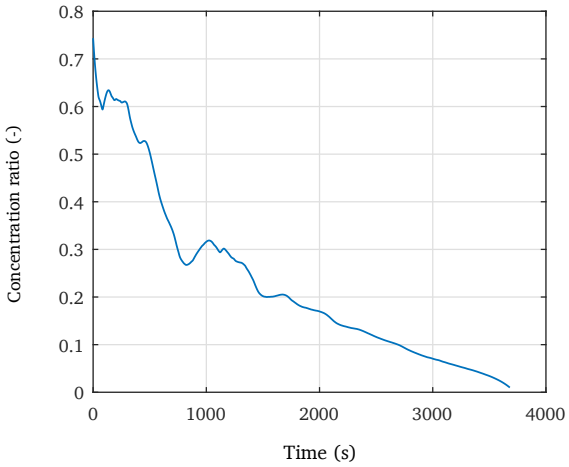

Figure 4.32: Anode lithium concentration FOM prediction at 1C rate with D_s^x reported by Ecker *et al.*.

To solve this issue the diffusivity was fitted with a polynomial approximation (solid lines in figure 4.30). After simulating again with those fits the problem was solved as can be seen in figure 4.33.

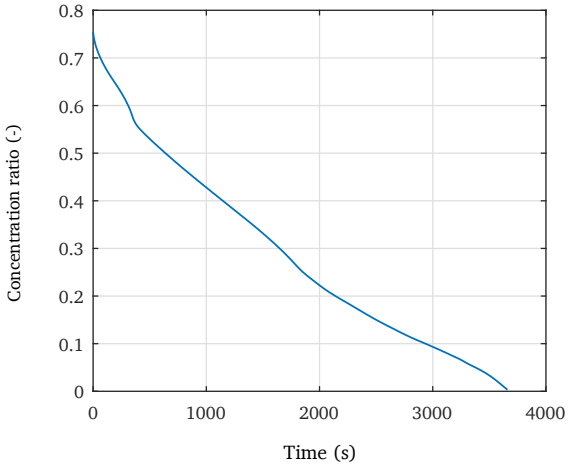

Figure 4.33: Anode lithium concentration FOM prediction at 1C rate with D_s^x fitted from data reported by Ecker *et al.*.

Looking again to the voltage response can be seen that the error shifted (the maximum value was found in a different SOC range, figure 4.34), but in this case with a constantly decreasing lithium content evolution in the anode (figure 4.33) and constantly increasing in the cathode (when discharging the cell). The diffusivity in the solid material changes the voltage response due to the diffusivity related polarization, and this is the reason why changing

this parameter shifted the maximum error and the voltage response itself. It is also important to note that Ecker *et.al.* used GITT to derive the diffusivity what it is correct when the electrode is composed of a single active material phase, on the contrary if the electrode is a blend of materials (it was the case as demonstrated in section 4.2.1.2 and 4.2.2.2) this technique need to be modified. Authors reported fittings similar to the ones implemented in this work [157] as an assumption, even so dedicated techniques will be developed and adopted in future investigations.

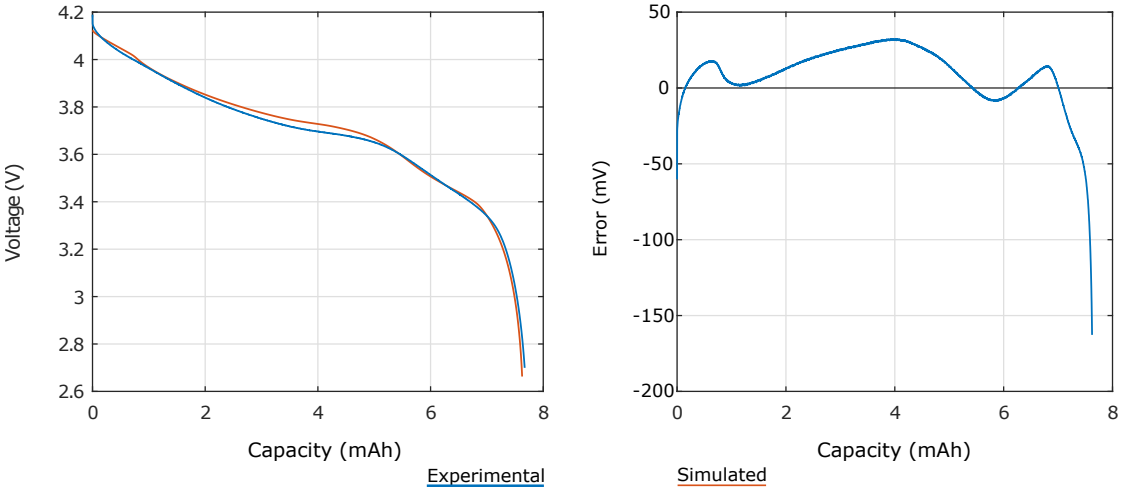

Figure 4.34: 1C rate FOM model simulation with D_s^x fitted from data reported by Ecker *et al.*.

Table 4.12: P2D model parameters.

Geometry			
Electrode plate area	A	$[m^2]$	0.41208
Thickness of the anode electrode	L^{n}	$[m]$	$7.37 \cdot 10^{-5}$
Thickness of the separator	L^{s}	$[m]$	$1.9 \cdot 10^{-5}$
Thickness of the cathode electrode	L^{p}	$[m]$	$5.45 \cdot 10^{-5}$
Material properties			
Anode particle radius	$R_{\mathrm{s}}^{\mathrm{n}}$	$[m]$	$1.38 \cdot 10^{-5}$
Cathode particle radius	$R_{\mathrm{s}}^{\mathrm{p}}$	$[m]$	$6.49 \cdot 10^{-6}$
Anode solid phase electric conductivity	$\sigma_{\mathrm{eff}}^{\mathrm{n}}$	$[S/m]$	14
Cathode solid phase electric conductivity	$\sigma_{\mathrm{eff}}^{\mathrm{p}}$	$[S/m]$	68.1
Anode solid phase electric conductivity activation energy	$E_{act,\sigma}^{\mathrm{n}}$	$[J/mol]$	0
Cathode solid phase electric conductivity activation energy	$E_{act,\sigma}^{\mathrm{p}}$	$[J/mol]$	0
Anode solid phase electric conductivity Bruggeman coefficient	$brug_{\sigma^{\mathrm{n}}}$	$[-]$	1.57
Cathode solid phase electric conductivity Bruggeman coefficient	$brug_{\sigma^{\mathrm{p}}}$	$[-]$	1.9
Anode electrode film resistance	$R_{\mathrm{f}}^{\mathrm{n}}$	$[\Omega/m^2]$	0.1
Cathode electrode film resistance	$R_{\mathrm{f}}^{\mathrm{p}}$	$[\Omega/m^2]$	0.1
Anode solid phase initial lithium concentration	$\theta_{100}^{\mathrm{n}}$	$[\%]$	0.78
Cathode solid phase initial lithium concentration	$\theta_{100}^{\mathrm{p}}$	$[\%]$	0.3
Anode solid phase final lithium concentration	θ_{0}^{n}	$[\%]$	0.001
Cathode solid phase final lithium concentration	θ_{0}^{p}	$[\%]$	0.932
Electrolyte activity coefficient ln derivative	$\partial \ln f_{\pm} / \partial \ln c_{\mathrm{e}}$	$[-]$	0
Cationic transference number	t_{+}^{0}	$[u/l]$	0.26
Electrolyte conductivity in the anode region	$\kappa_{\mathrm{eff}}^{\mathrm{n}}$	$[S/m]$	ref. [119]
Electrolyte conductivity in the separator region	$\kappa_{\mathrm{eff}}^{\mathrm{s}}$	$[S/m]$	ref. [119]
Electrolyte conductivity in the cathode region	$\kappa_{\mathrm{eff}}^{\mathrm{p}}$	$[S/m]$	ref. [119]
Electrolyte conductivity activation energy	$E_{act,\kappa}$	$[J/mol]$	17100
Electrolyte conductivity Bruggeman coefficient in the anode region	$brug_{\kappa^{\mathrm{n}}}$	$[-]$	1.57
Electrolyte conductivity Bruggeman coefficient in the separator region	$brug_{\kappa^{\mathrm{s}}}$	$[-]$	1.32
Electrolyte conductivity Bruggeman coefficient in the cathode region	$brug_{\kappa^{\mathrm{p}}}$	$[-]$	1.9
Maximum anode lithium concentration in the solid	$c_{\mathrm{s,max}}^{\mathrm{n}}$	$[mol/m^3]$	$3.05 \cdot 10^4$
Maximum cathode lithium concentration in the solid	$c_{\mathrm{s,max}}^{\mathrm{p}}$	$[mol/m^3]$	$5.44 \cdot 10^4$
Initial lithium concentration in the electrolyte	$c_{\mathrm{e},0}$	$[mol/m^3]$	1000

Table 4.13: P2D model parameters.

Electrolyte volume fraction in the anode electrode	ε_e^n	$[1-0]$	0.329
Electrolyte volume fraction in the separator	ε_e^s	$[1-0]$	0.492
Electrolyte volume fraction in the cathode electrode	ε_e^p	$[1-0]$	0.296
Solid volume fraction in the anode electrode	ε_s^n	$[1-0]$	0.4145
Solid volume fraction in the cathode electrode	ε_s^p	$[1-0]$	0.3872
Specific surface area of the anode electrode	a_s^n	$[1/m]$	$9.01 \cdot 10^4$
Specific surface area of the cathode electrode	a_s^p	$[1/m]$	$1.79 \cdot 10^5$
Electrochemical reaction kinetics			
Anode solid charge transfer coefficient	α^n	$[u/l]$	0.49
Cathode solid charge transfer coefficient	α^p	$[u/l]$	0.53
Anode reaction rate coefficient	k_0^n	$[mol/m^2s]$	$1.2 \cdot 10^{-4}$
Cathode reaction rate coefficient	k_0^p	$[mol/m^2s]$	$5.19 \cdot 10^{-5}$
Anode reaction rate coefficient activation energy	$E_{act,k}^n$	$[J/mol]$	53400
Cathode reaction rate coefficient activation energy	$E_{act,k}^p$	$[J/mol]$	43600
Transport			
Diffusion coefficient in the anode solid	D_s^n	$[m^2/s]$	ref. [119]
Diffusion coefficient in the cathode solid	D_s^p	$[m^2/s]$	ref. [119]
Diffusion coefficient in the anode solid activation energy	E_{act,D_s}^n	$[J/mol]$	40800
Diffusion coefficient in the cathode solid activation energy	E_{act,D_s}^p	$[J/mol]$	80600
Effective diffusion coefficient in the anode region electrolyte	$D_{e,\text{eff}}^n$	$[m^2/s]$	ref. [119]
Effective diffusion coefficient in the separator region electrolyte	$D_{e,\text{eff}}^s$	$[m^2/s]$	ref. [119]
Effective diffusion coefficient in the cathode region electrolyte	$D_{e,\text{eff}}^p$	$[m^2/s]$	ref. [119]
Diffusion coefficient in the electrolyte activation energy	E_{act,D_e}	$[J/mol]$	17100
Diffusion coefficient in the anode region electrolyte Bruggeman coefficient	$brug_{D_e^n}$	$[-]$	1.57
Diffusion coefficient in the separator region electrolyte Bruggeman coefficient	$brug_{D_e^s}$	$[-]$	1.32
Diffusion coefficient in the cathode region electrolyte Bruggeman coefficient	$brug_{D_e^p}$	$[-]$	1.9

Conclusions

Along this chapter, the state of the art related to electrochemical models parameter identification was revised. As a result of this revision, it was decided to use physico-chemical characterization techniques to compare experimental data with a FOM model predictions (SOC and voltage in a first stage, as aging results should give prove of parameter identification accuracy). This procedure was important to gain knowledge about the difficulty and accuracy of the process, so further mixed parameter identification techniques could improve the lacks of computational parameterization methods.

The diffusion coefficients were found to be controversial, since a fitting process was needed in order to eliminate measurement noises. Optimizations were also used to adjust the balancing of the electrodes since the porous matrix was difficult to characterize based on cell samples (one weak point of physico-chemical techniques was found to be the reliance in representative samples). Finally the electrolyte parameters identification was found to be complex, as electrolyte extraction can be difficult (especially when considering pouch type cells). Not only this, but the use of NMR and the need of reproducing the electrolyte made this analysis expensive and long. Moreover, it is unclear how to measure the initial lithium content in the electrolyte. In general the characterization of the porous matrix of the electrodes was found to be the more challenging task (reason behind the use of tuning parameters). The porous matrix also influence the results of other tests, being crucial to correctly identify its parameters. A proper identification of this matrix would enable to increase the amount of optimizations that could be used without loosing accuracy and avoiding some physico-chemical tests. The OCV curves where measured, but no hysteresis effects where taken into account, this fact is known to introduce some error and will be treated in future investigations.

On the one hand, all this considerations will be used in future investigations to design more efficient parameter identification methodologies. On the other hand, as the voltage and SOC predictions were in line with experimental data, the parameters will be used to feed the ROM in chapter 5 and further explore the validity and accuracy of the model predictions.

Chapter 5

Lithium plating control oriented system development

While different methods to model and parameterize battery cells have been reviewed in chapters 3 and 4 respectively, battery cells are normally used within battery packs and not isolated. To the date it is unclear what would be the best way to implement this type of advanced controls as different approaches can be considered.

The model itself can be used to predict the SOF of each cell or as an statistic representation of a full pack, and used for monitoring purposes or for SOF management. Not only this, the hardware that would need to be used is still not defined as each cell current could be controlled independently, per each branch, per module or only the battery pack output current (these options in addition lead to the use of several converters for each battery pack as it is gathered within chapter). The architecture of the battery pack is then a key element when considering how to apply and advanced SOF control or monitoring system. All this issues are reviewed within this chapter.

Finally, a converter is designed to control each battery cell with the model previously developed. Doing so, the full potential of the techniques gathered in this thesis wanted to be explored. Not only this, but the parameter identification process implemented in the previous chapter will be evaluated.

5.1 State of the art

Battery control systems proposed along this state of the art are based on voltage and current control. Voltage can be limited to enhance battery cell lifetime by limiting aging favorable operation areas (this is normally done indirectly by oversizing the battery pack to operate at certain DOD margins), nevertheless the control of each cell current in a typical battery pack configuration (figure 5.1) is not possible. This would not pose a problem if a SOF monitoring system is the objective, on the contrary if the SOF of the cells composing the battery pack need to be managed, then controlling the current of each cell becomes a significant issue.

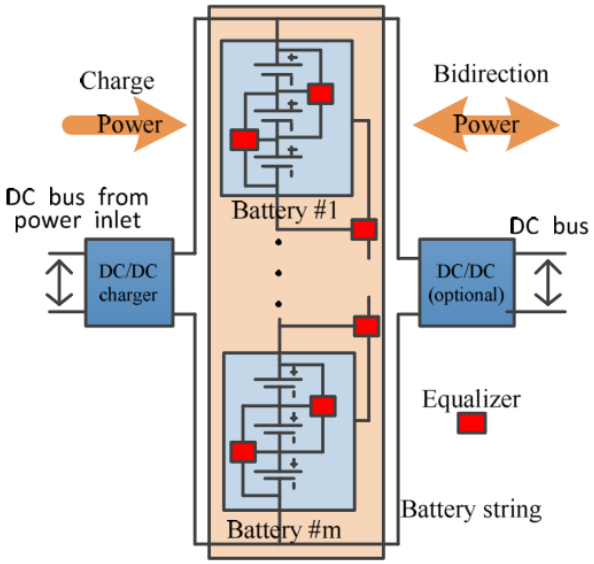

Figure 5.1: Classic battery pack topology [167].

Considering SOF control, individual current control through each cell in a battery pack is not a possibility in a typical battery pack architecture as stated before. At this point then, it is important to define if the SOF control is going to be oriented to the whole battery pack (with statistical deviations and average predictions for example) or individually for each cell. Nowadays the experimental validity of a SOF control in these two different scenarios has not been investigated to the known of the author, and it is then a natural step to start evaluating the benefits that can be extracted from a rigorous per cell SOF control. Later, when this potential is explored, further considerations about the most appropriate SOF control implementation culd be dilucidated. To evaluate the full potential of a rigorous SOF control then, the need of

one converter for each single battery cell stands out, leading to a modular converters system (figure 5.2). This fact makes also a difference when configuring the battery pack due to the flexibility that modular converters can give (figure 5.2).

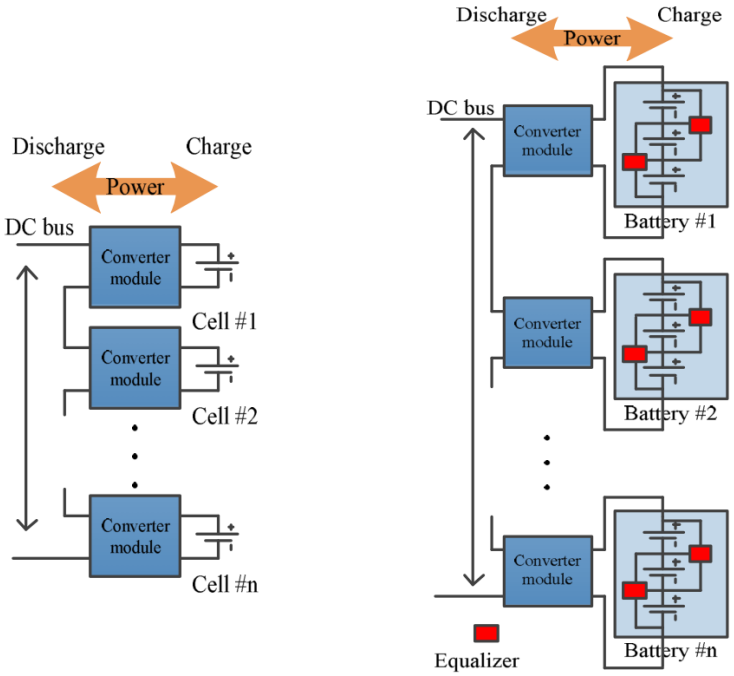

(a) Proposed cell-level integration (b) Two-stage structure

Figure 5.2: Modular (a) and mixed (b) battery pack topologies [167].

The pack can be topologically designed in a classic manner even when using those converters, or a parallel topology can be proposed [168] as shown in figure 5.3. Mixed topologies are also a further alternative, as seen in figure 5.2 b.

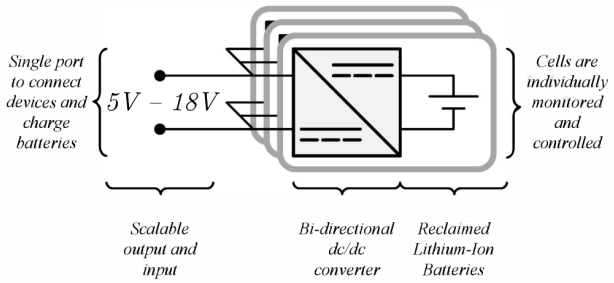

Figure 5.3: Parallel pack topology [168].

The topological design of the pack is highly dependent on the application and it is a step that the designer does normally have to face. Distributed converters can be used for cell balancing purposes for example [169]. The benefits of active battery cells equalizataion have also been reported [170], and even taking into account that this type of equalization is more expensive (than passive equalization), could be an added benefit when considering distributed converter systems. This active equalization is a big benefit of those hardware systems, because the SOC control of the cells can be done independently and in a coordinated manner, using all the energy stored in the battery pack. Tipically the series connected cells strings need to be stopped when each strings cell with the least capacity is discharged, in order to avoid damaging it, meaning that the remaining energy in the rest of the cells can not be used. Even in the case of cells coming from the same device (same model cells) the difference in capacity can still result in a pack underutilization, as the capacity of each string is limited to the weakest cell. This capability is specially important when second life cells are used [168, 171], as different chemistry and capacity cells are considered. In this case, the dispersion in aging behavior increases this problem making even more profitable the use of modular converters. Hybridization is also a field that can take benefits of modular converters due to the individual control of the devices [171, 172], that can have different capacities falling into the above explained case. In addition the devices voltage difference generates design difficulties that are mitigated with this architectures. Other kind of structures, such as configurable battery packs [173] are also a good proof of the flexibility that modular converters give, and that are an excellent path for new research lines in the energy storage area. Looking at the design process, the electronics used for specific cells can be designed only once and further treated as plug and play. This way, the electronics design process will only be carried out once.

There is some research regarding modular converters for distributed ESS, nevertheless few of them are focused on modular converters connected for individual cells. Following this philosophy the work of Ye Li *et al.* [174, 175] was found to be the most advanced. They proposed a modular converter system based on a buck converter. They also introduced bypass and pass-through modes that gave operation flexibility to the system in case of failure or complete discharge of an specific cell. They designed, implemented and validated a functional converter (figure 5.4) that covered the function of charger equalizer and BMS, what implies some benefits and some drawbacks or challenges as well:

- ✔ Better capacity utilization due to individual SOC management
- ✔ Individualized cell protection due to individual monitoring and actuation ability
- ✔ Enhanced system reliability and redundancy due to the bypass mode
- ✔ Easier installation due to the modularity and the lack of additional BMS system. In this case the system could also be optimized for a certain cell and the design process that design engineers need to face can be limited
- ✔ More flexibility as the hybrid systems did not present added complexity and the expansion of the battery pack could easily be faced
- ✔ Higher equalization speed and efficiency as the equalization was intrinsic
- ✗ The efficiency of the system could be affected due to the increase of power switches number, nevertheless as utilization of energy in the cells is higher deeper studies would be needed
- ✗ The cost of the full system was expected to be higher due to the amount electronics involved, nevertheless the integration of the BMS, mass production, on-chip solutions and a better energy utilization are issues that could make the system affordable

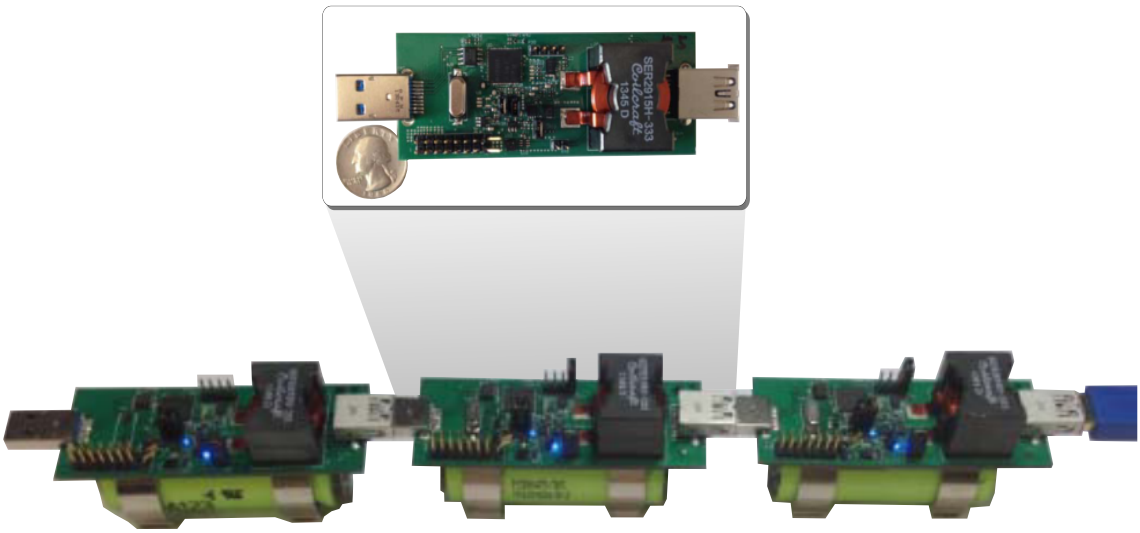

Figure 5.4: Prototype (adapted from [174]).

Their work included in addition, a proposal for the control of the converters that had to be coordinated in order to ensure the battery pack correct functioning. Their control approach

was based on a second level control, communicated by CAN (controller area network). And a local control, implemented on a local microcontroller. This two level control proposal could lead in failure due to communication and other self working techniques and the mean time to failure (MTTF) could be increased. Many research could be found related to control of distributed systems, being one of the most promising ones the droop control. With this control scheme the equalizing would be automatic, as the power would balanced between the systems, and it could work with negligible information about the global system (it could need some initial information for configuring or tuning).

5.1.1 Conclusions

Along this section different pack architectures were analyzed, taking into account their use for SOF monitoring or control systems. Battery packs based on modular converters stand out because of their capability to control battery cells current independently and added functionalities. On the contrary, their expected cost is higher. Finally it is important to note that the experimental profitability of SOF control systems has not been deeply studied. Further research is then needed to evaluate the extent of SOF control potential benefits, before specific architectures can be evaluated.

Few or none authors treat the online experimental implementation of reduced order electrochemical models. This is a great challenge as well as of great interest, since would give proof of the viability of the full concept of using physics-based models for SOF control. In this chapter then, an experimental platform used to validate this concept is going to be presented.

5.2 Platform development

The objective of this thesis was to validate the concept of a system able to prevent lithium plating. This system needed to be proven suitable for a real application, so it was then necessary to run the ROM model (developed and parameterized within chapters 3 and 4 respectively) inside a low cost microprocessor. Within this work a system composed of a single battery cell was studied as a first approach and as a proof of concept before further investigations as stated before. To do so, each cell was controlled using a ROM + Kalman filter. In order to be able to prevent the lithium plating, cells current was controlled using a power converter. Moreover, the use of a converter for each battery cell will explore the advantages of a SOF

control to its maximum, giving valuable information about the real validity of the concept. This converter was designed and implemented due to the lack of dedicated converters in the market, and the design details can be found in appendix 7.5. A scheme of the whole system can be seen in figure 5.5.

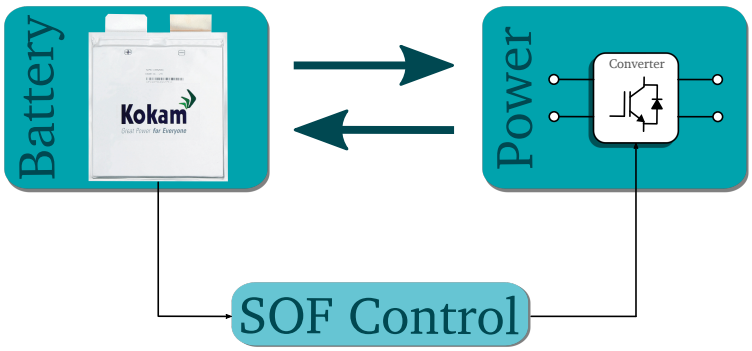

Figure 5.5: Platform general concept.

To implement this scheme platform, software and hardware devices were designed. Figure 5.6 shows all the hardware involved in the platform implementation, divided into power and control sections. On one hand, the battery cell itself and a power converter used to control the current can be seen. On the other hand, two low cost microprocessor prototyping boards were used for high (ROM, SPKF and lithium plating control) and low level (current control, voltage and current measurements) control loops. These two sections composing the whole platform will be explained more deeply in the following lines.

5.2.1 Power management

With the objective of controlling the charge and discharge currents of the battery cell, a power converter (synchronous boost) was designed as explained above (appendix 7.5), and this converter was connected to a power supply and to an electronic load as shown in figure 5.7. The load absorbed the energy stored in the cell when it was discharged, and the source would deliver it when charging. The electronic source was also responsible of maintaining a fixed voltage so the power converter could oscillate around and regulate the cell current.

The power converter also integrated the input current, voltage and temperature measurement hardware. This hardware included the sensors (dedicated integrated circuits for current and voltage, and a thermistor for the temperature) and the needed conditioning of sensors signals (more details can be found in appendix 7.5). These signals were connected then to the

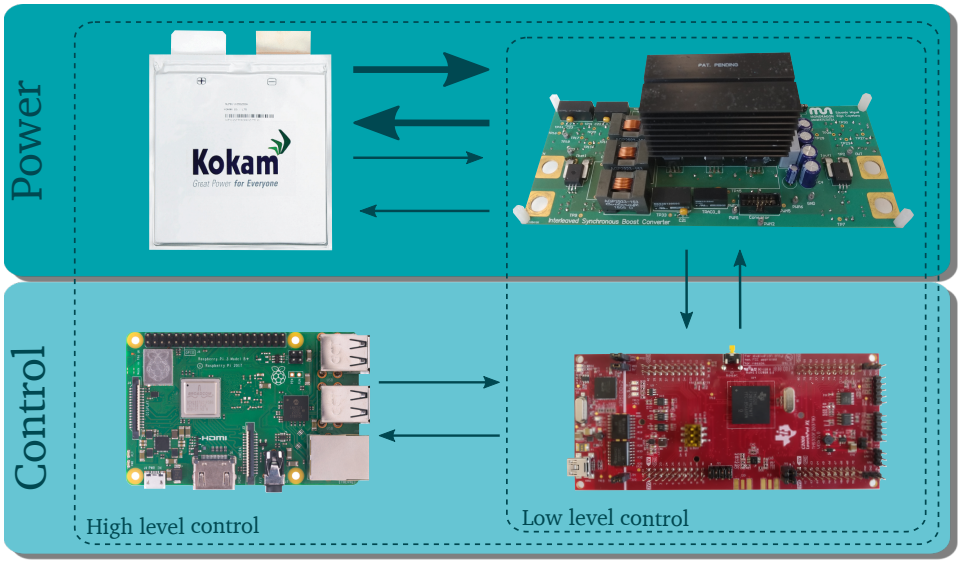

Figure 5.6: Platform general scheme.

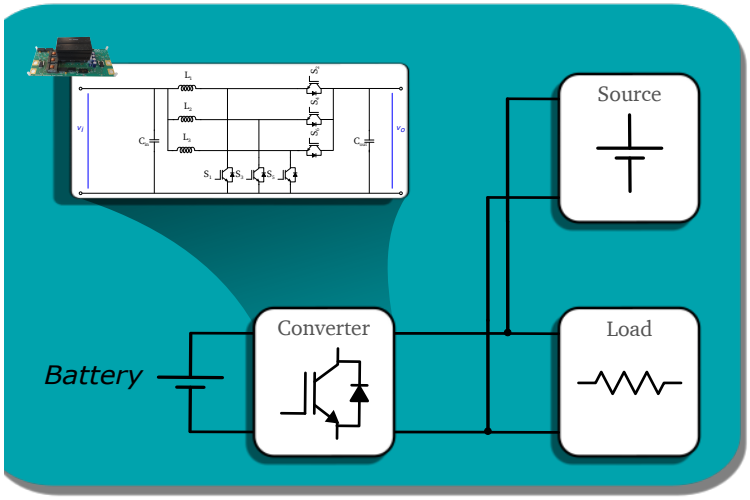

Figure 5.7: Power management scheme.

low level control board as shown in figure 5.8.

5.2.2 ROM, Kalman filter and control loops

in order to manage the power converter, a control oriented prototyping board including a microprocessor and the needed peripherals were used ("TMS320F28379D" developed by Texas instruments). This boards main task was the low level control (control of the power converter),

that was implemented to manage the current flowing through the converter (whether positive or negative when discharging or charging the battery). The current was fixed as a function of the constraints fixed by the high level control loop. To do so a proportional integral (PI) controller was programmed, using the real current measurement as the feedback of the loop, as shown in figure 5.8. This microprocessor was then used to generate the pulse width modulation (PWM) signals that drove the converter switches. In addition to the current control, the analog to digital converter (ADC) of the board was used to convert analog measurement signals to digital so they could be used in both control loops. The mentioned microprocessor had two cores; one of them was used for the control and measurement signals treatment, what enabled a sampling rate of 25 KHz. The second core otherwise was employed to communicate the low level control with the high level control (the "TMS320F28379D" board used for low level control with the "Raspberry Pi 3 Model B+" used for high level control) via the I2C (inter integrated circuits) communication protocol.

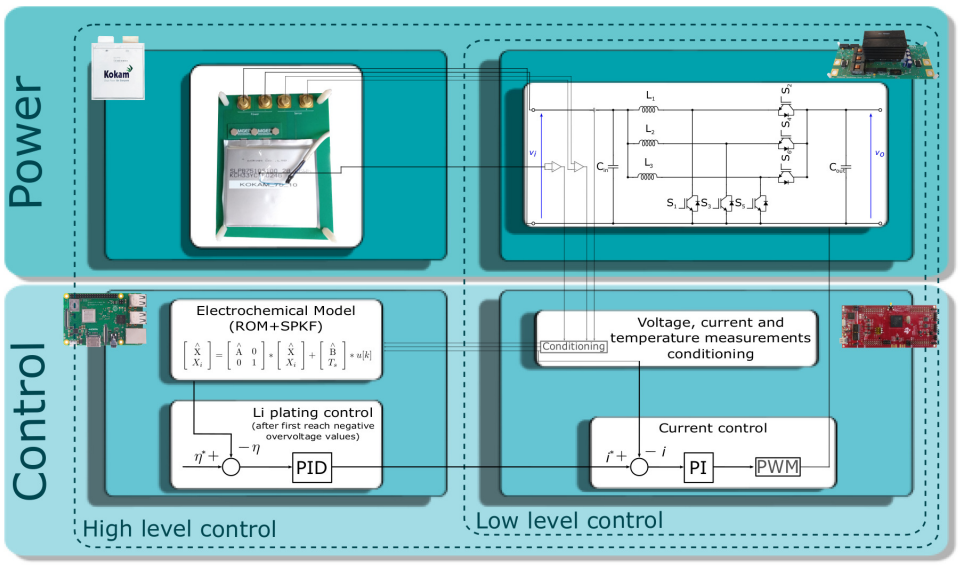

Figure 5.8: Platform general scheme. Note that the Li plating control shown in within the high level control is activated once the overvoltage first reaches a negative value during a charge process.

As mentioned above a Raspberry Pi was used for the high level control. This level integrated the ROM model, the Kalman filter and the lithium plating control loop, as shown in figure 5.8. The ROM model and Kalman filter code developed in chapter 3 was implemented together with the lithium plating control loop in MATLAB Simulink, so they could be charged

in the Raspberry Pi board using the "*code generator*" of this software. The inputs of this board came from the low level control as explained above, and were the converter input current and voltage (the input is defined as the battery side). These inputs fed the ROM model and Kalman filter, that predicted the overvoltage, used as the feedback of the lithium plating loop as can be seen in figure 5.8. The overvoltage constraint otherwise, was treated as a predefined constant, keeping the overvoltage above 0 V as was be explained within chapter 2. The sampling rate of the model was designed to be of one second, a rate that the low lever control board would be able to handle easily, nevertheless this second high level control board was needed due to the limited memory resources of the low level control board ("TMS320F28379D").

5.3 Experimental validation

After assembling the platform it was validated at two different conditions, room temperature as a first approach, and -10 ^{o}C used for the validation of the proposed system (the reasons behind using this temperature are explained within chapter 2). Finally the lithium plating control was tested at the proposed validation conditions (chapter 2).

5.3.1 Room temperature

First, the platform was validated at room temperature, what approximately was 22 ^{o}C, as can be seen in figure 5.9 (this figure shows the surface temperature of the cell during cycling, what was obviously higher than the room temperature). After constant current symmetrical $1C$ cycles where done to see the platform response. In addition, during the first discharge cycle the current was set to $0.5C$ in order to check the capacity of changing the cycling rate during operation (during a few minutes short pulse).

Temperature, voltage and current measurements can be seen in figures 5.9 and 5.10 as well as the model prediction for voltage and SOC, corrected by the Kalman filter. The current regulation was proven to be inside the design specifications (%10 current ripple was fixed during the power converter design. The control performance was demonstrated to work properly when the current is set to $0.5C$ as the setpoint is correct and the time elapsed until the value was stabilized can be considered negligible with not an excessive transient over or under current. The voltage prediction otherwise, was found to be excessively high according to the results obtained in chapter 4. The reason behind was deduced to be ohmic polarization

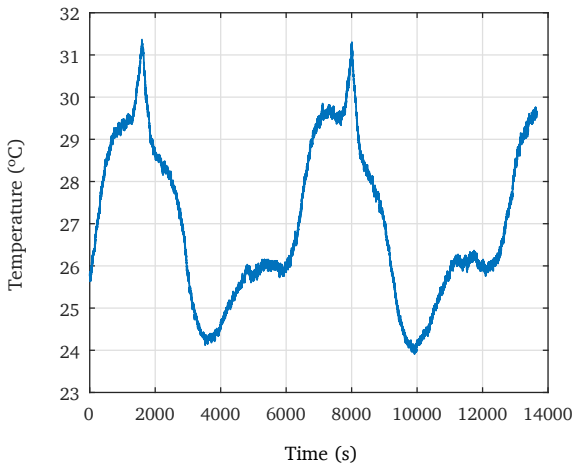

Figure 5.9: Cell surface temperature at room temperature.

effects that were not contemplated during the parameter identification of the cell. On the one hand the voltage drop when the battery switch from charge to discharge (and the opposite) was significantly larger than expected. On the other hand, a continuous voltage offset was observed.

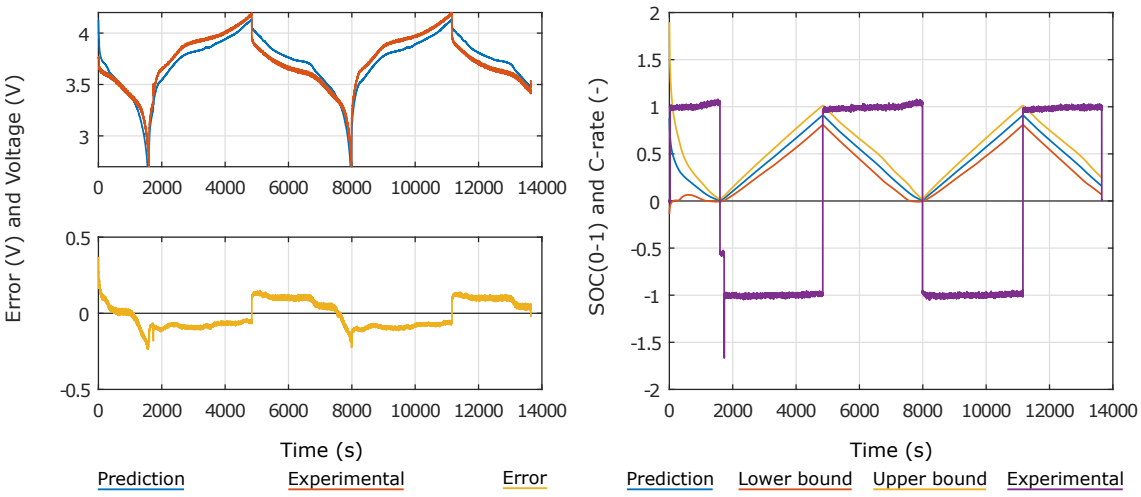

Figure 5.10: Platform experimental validation waveforms at room temperature.

Looking into the model there are two effects that cause this polarization, contact resistance and ohmic potential drop in the electrolyte (as reported by Zavalis *et al.* [162] and presented in chapter 4 (figure 4.19)). Jobman *et al.* [116] also presented mathematical prove of it. The electrolyte was identified within chapter 4 and the characterization presented by Ecker *et al.*[12] was proven to be plausible. Not only this, but the platform measurement hardware could not be considered ideal and some amount of error was expected, something that would

introduce an additional voltage offset in the measurement. The voltage offset found in the experimental validation, then was assumed to be caused by contact resistant (neglected until this point). After fitting this value (R_f^x) by a trial error process results were found to be in line with the predictions in chapter 4, as can be seen in figure 5.11.

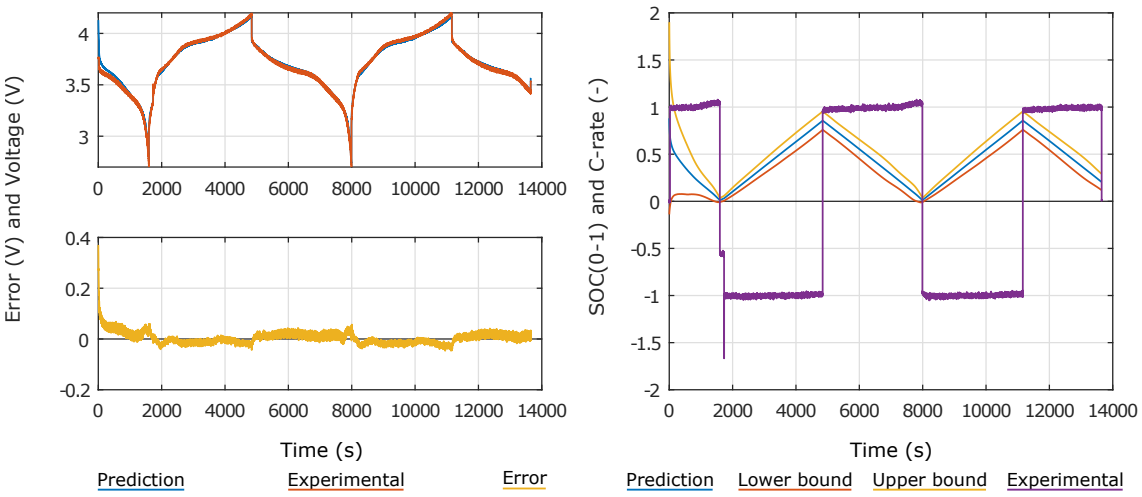

Figure 5.11: Platform experimental validation waveforms at room temperature after film resistance fit.

5.3.2 Negative temperature (−10 °C)

Following, the system validation test were done at −10 °C. A battery cell was introduced inside a climatic chamber that maintained the ambient temperature at −10 °C. In the case of this test scenario the cycles were shorter in time due to the high polarization thus, the cells surface temperature was measured to be closer to the ambient temperature, as the rise caused by cycling was lower (figure 5.12).

The contact resistance (R_f^x, found in table 4.12) was again fitted to compensate the issue described in the section above, as it was a temperature dependent value. Model predictions were found to be close to measurements after an stabilization time. This stabilization time was higher than at room temperature, and this effect was assumed to be caused by a higher inaccuracy in the model prediction at the beginning (an inaccuracy that was corrected by the SPKF). The electrochemical model was parameterized at positive reference temperatures, and even activation energies were measured and implemented to compensate the temperature variations, the operation temperature was significantly further. It is plausible then that the model had a higher deviation due to an operation point located far from the parameterization

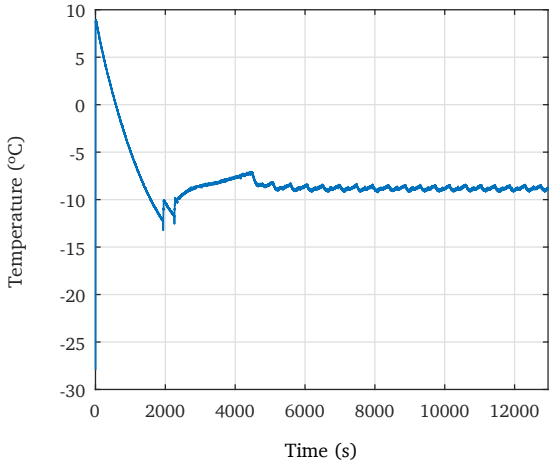

Figure 5.12: Cell surface temperature at −10 °C.

temperature. All in all, the Kalman filter compensated the voltage error. This is a future line to be tested by the research group in the near future, the possibility of doing the parameterization reaching these low temperatures.

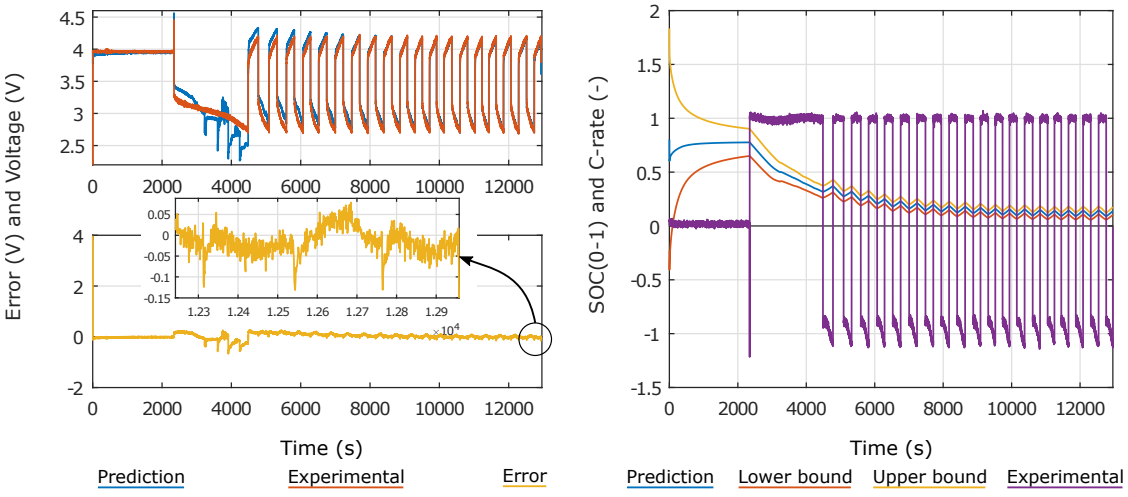

Figure 5.13: Platform experimental validation waveforms at −10 °C after film resistance fit.

5.3.3 Lithium plating control

Finally the lithium plating control was tested at −10 °C with the same constant current symmetrical 1C cycles (limiting the charge current due to the lithium plating control). Cell surface temperature reached higher values as shown in figure 5.14, as an effect of lowering the charge current to prevent the lithium plating (as the charging time increased, the temperature

had a longer period to increase).

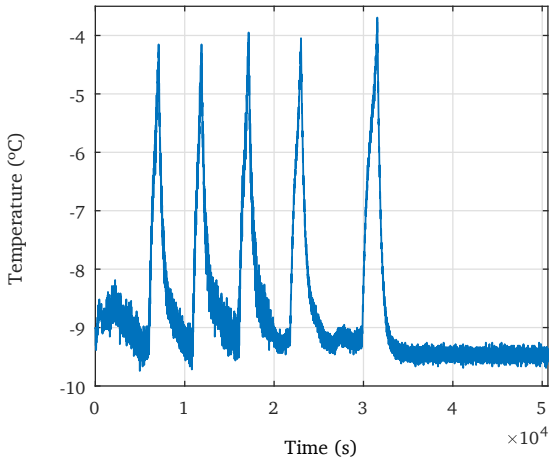

Figure 5.14: Cell surface temperature at −10 °C after lithium plating control implementation.

Measured and predicted values are shown in figure 5.15, where can be seen clearly that the charging time was increased due to the lowering of the cycling rate. The prediction accuracy was in line with the validation presented previously at −10 °C, were the error was compensated gradually up to approximately the fifth cycle. The current was the same way controlled with a lower ripple due to this error compensation. Not only this, but the charging time increased slightly when the predictions matched better the measured voltage.

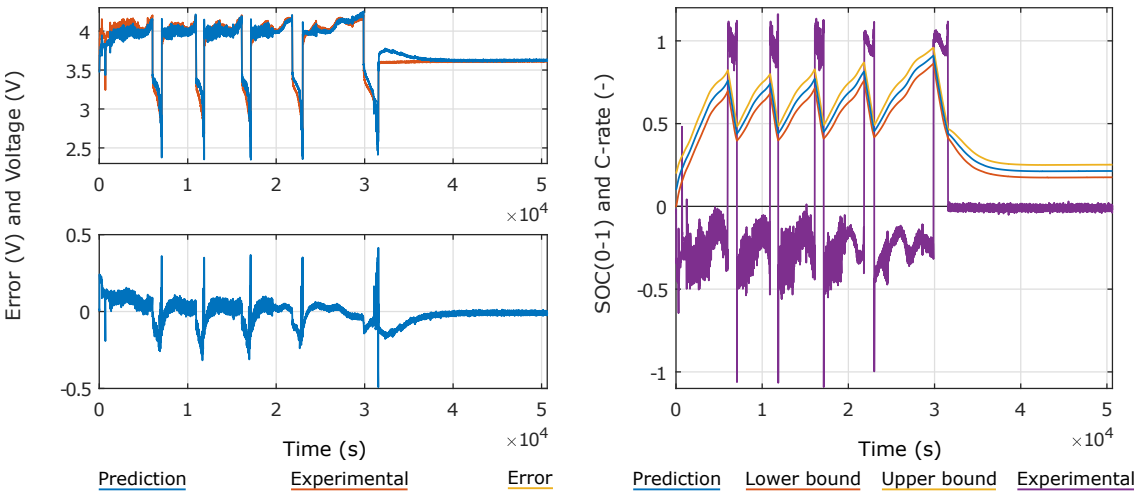

Figure 5.15: Platform experimental validation waveforms at −10 °C after lithium control implementation.

The evolution of the current ripple and charging time due to the model gradual compensation were further seen when looking at the overvoltage (figure 5.16), as the overvoltage ripple

was the same way reduced gradually.

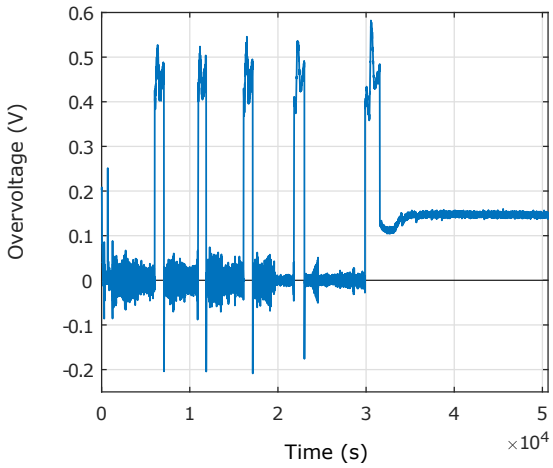

Figure 5.16: Platform experimental validation overvoltage at −10 °C after lithium control implementation.

The platform was then proved to control the overvoltage at the defined constraint (0 V) increasing the accuracy over time as the Kalman filter compensated the error (due to the intrinsic ROM model error and to a extreme operation area as the cell was cycled at −10 °C).

5.3.4 Lithium plating evolution in real cells

At this point the whole platform and the lithium plating control system where developed, but still the effect of this control was unproven. To evaluate the mentioned effect, cells where cycled using the developed platform. Applying the lithium plating control, and with no lithium plating control. When using the platform lithium plating was expected to be completely or partially prevented (due to inaccuracies), while in the case of the reference cells (cells cycled with no lithium plating control) lithium plating should be found.

The cells under test where cycled with symmetrical 1C cycles at −10 °C. The definition of temperature and cycling rate was set based on Ecker *et al.* [12] investigations, where these conditions where reported to generate lithium plating (figure 5.22). In addition, low temperature makes cells age faster due to high lithium plating generation, what should minimize the SEI growth caused aging (as a limited amount of cycles are done). This will isolate the desired aging mechanism to the maximum. The Checkups where done at 25 °C and the same cycling rate (without applying lithium plating control). Also a constant voltage phase was done at the end of the charge (this phase was implemented so polarization effect will not reduce the

charged capacity).

Figure 5.17 shows the aging evolution in terms of capacity of two representative samples coming from each group. Two checkups where done in the cell were the lithium plating control was applied, and three in the cell without any control. The initial capacity was assumed to be the nominal reported by the manufacturer (capacity used to normalize the SOH), this initial capacity was not coherent with the measured data, and a variation between approximately 104% and 105.55% was measured in other fresh cells (initial SOH points in figure 5.17 are not real, and they were assumed to be in the limits of the typical initial capacity variation, only to illustrate the aging evolution). This variation range helped to illustrate why a similar aging evolution of both cells was assumed, with a small initial capacity offset of around 0.5% (deviation found when comparing the SOH at similar FCE (full equivalent cycles)).

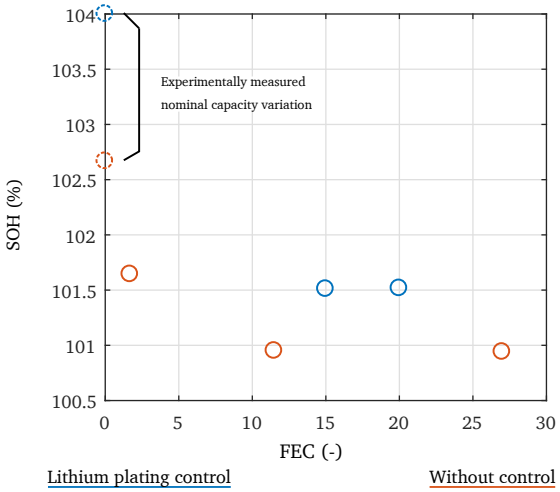

Figure 5.17: Representative samples of tested cells aging evolution.

The results above showed a similar aging evolution of all the cells, what was opposed to the hypothesis that the developed system was able to totally or partially prevent the lithium plating. Whit this results a deeper study of the system behavior was needed, what will be divided in four as follows.

- Model predictions analysis

  Voltage prediction showed a good performance tracking the voltage as shown along this chapter, thus the internal variables predictions were checked looking for anomalous behaviors that could explain the aging difference in the group of cells cycled while using lithium plating control (the results presented above where obtained without lithium

plating control to analyze model behavior). All the internal variables values where inside logical values and tendencies, but the boundaries of the solid-electrolyte interface voltage prediction (ϕ_{s-e}) where too far from predictions, compared to the experimental results at 25 °C. Figure 5.18 shows voltage and SOC predictions and figure 5.19 shows the spread of (ϕ_{s-e}) boundaries at a −10 °C.

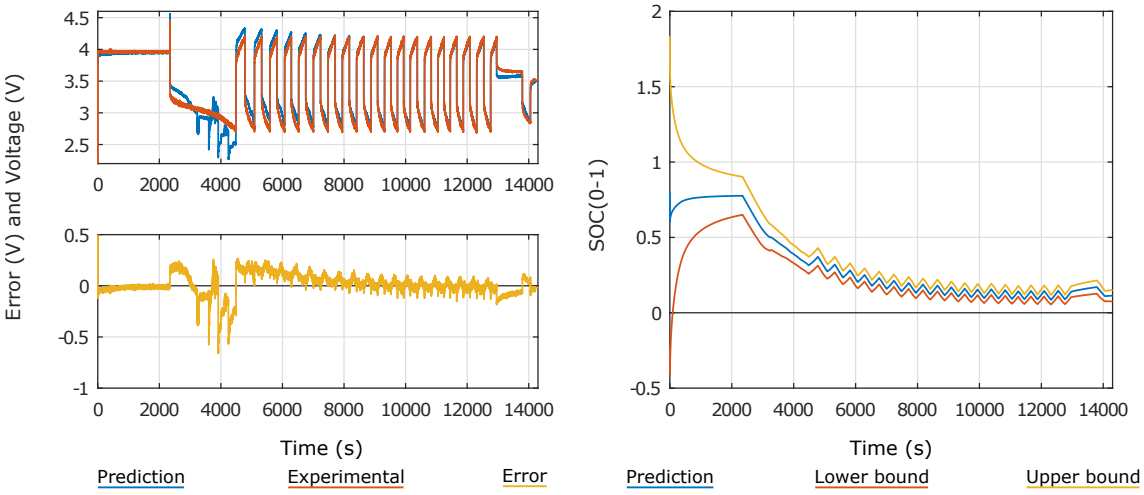

Figure 5.18: Voltage and SOC predictions at −10 °C.

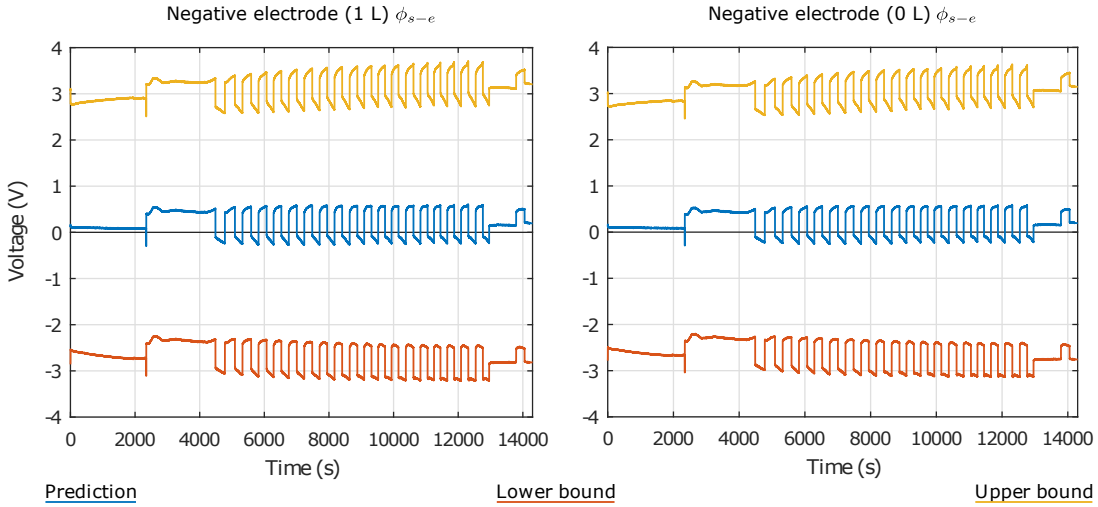

Figure 5.19: ϕ_{s-e} predictions at at −10 °C.

Looking at the same predictions at 25 °C (figures 5.20 and 5.21) voltage and SOC predictions looked similar (despite a faster convergence time) while the (ϕ_{s-e}) prediction boundaries are in good agreement with the data obtained during the model validation (chapter 3 figure 3.28).

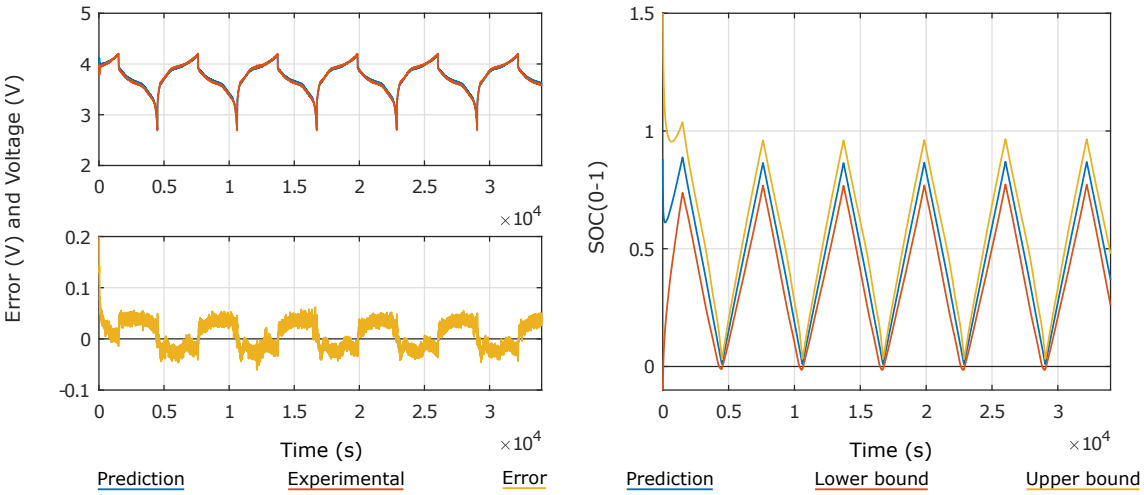

Figure 5.20: Voltage and SOC predictions at 25 °C.

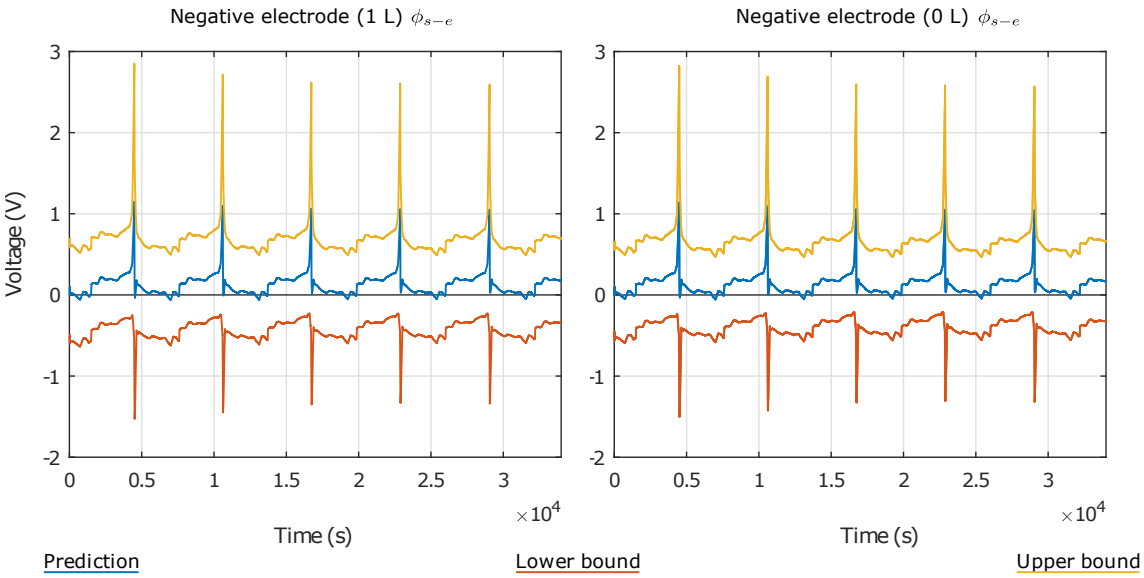

Figure 5.21: ϕ_{s-e} predictions at at 25 °C.

The fact that boundaries were further from the predictions is attributed to more inexact model predictions. The SPKF corrected the variable in order to track the measured voltage, while the boundaries were increased. Looking deeper, the points where the model predictions were further from the measured data, were at transitions between charge and discharge. This potential drop was considered during the model fitting process (subsection 5.3.1), and was exposed that there are two effects that cause this polarization, contact resistance (film resistance in the model) and ohmic potential drop in the electrolyte. The contact resistance was fitted for the specific setup and cell, so could be

discarded. Electrolyte parameterization then was considered the main root of the explained inaccuracy. It is also important to note that the working temperature (−10 °C) was significantly low, what could influence in the electrolyte properties. The electrolyte is liquid and phase changes can occur increasing property changes.

In addition, the current was lowered in order to prevent the lithium plating when charging the cell. This current reduction could affect the proper fitting of the contact resistance (since it is a temperature and current sensitive parameter).

- Test conditions analysis

  The inaccuracies of the model explained above could lead to a deviation in the lithium plating limitation, but it could not be enough explanation to the fact that the aging tendencies were very similar (specially looking at the current derating applied by the lithium plating control, figure 5.15, that was a $0.25C$ mean value). Ecker *et al.*[12] reported lithium plating free operation conditions at test temperature for very low cycling rates (figure 5.22), that were in line with the lithium plating control current limitation.

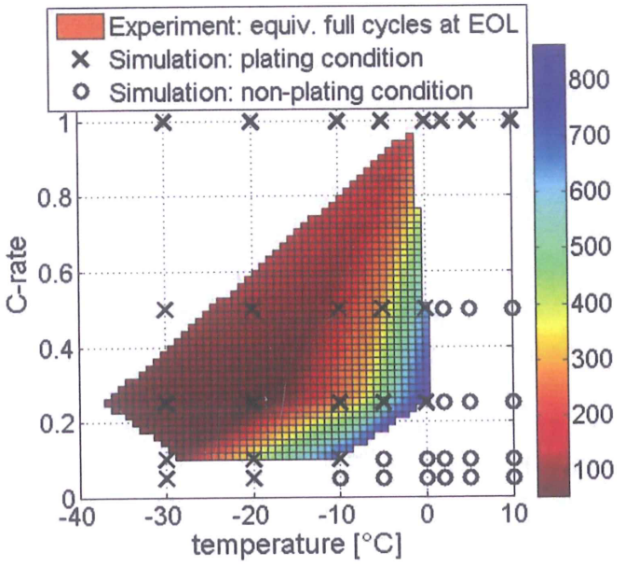

Figure 5.22: Lithium plating conditions and cycling results reported by Ecker *et al.*[12].

The study presented by Ecker *et al.* was experimentally validated based on maximum cycles achieved by the cells at different conditions. The lithium plating generation boundary was theoretically binary, but different aging rates were reported (associated with more or less lithium plating generation). This can mean that in the test conditions used

for this thesis validation, lithium plating was still not significant in terms of aging (specially when looking at the aging results, figure 5.17), and more cycles were needed to test the lithium prevention. This is, since the generated lithium plating was low (due to a few number of cycles), the difference in aging tendency was still not evident. Furthermore, as the model was not completely accurate and the lithium plating generation boundary not binary the aging was not completely eliminated.

More cycles should be necessary to evaluate if the aging evolution of the tested cells would differ, but the model inaccuracy made the tests to stop since the kalman filter could not keep working with such a voltage difference. All in all the post-mortem analysis presented above will give of the lithium plating presence.

- Current regulation

  The converter used in this thesis had a certain amount of current ripple (figure 5.16), forcing the charge current higher than desired transiently (as can also be seen in the overvoltage prediction ripple).

- Use of an average model

  Finally the use of an average model and the fact that the anode was really a blend of two different phases can lead to local plating generation. To further investigate this effect the cells where disassembled and analyzed.

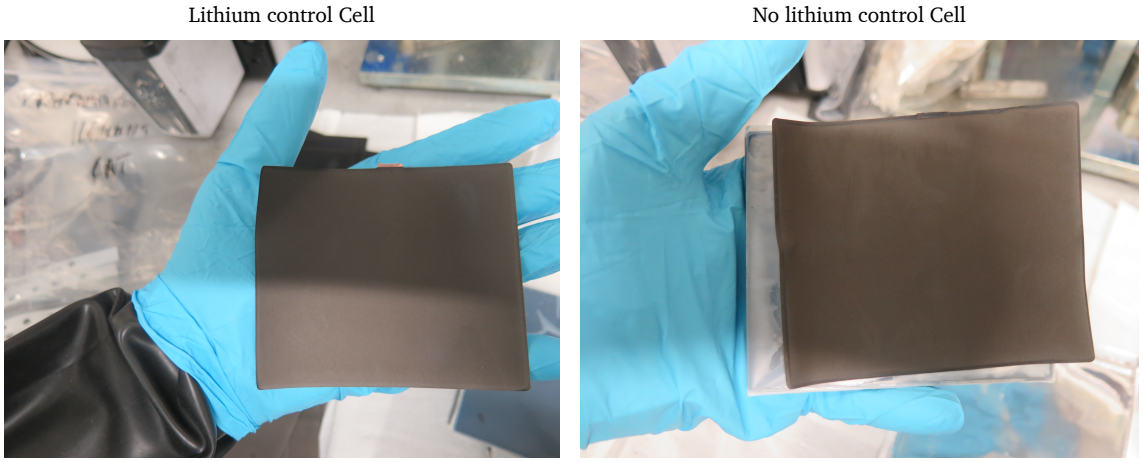

Figure 5.23: Studied cells anodes after aging.

- Post-mortem analysis

The cells discussed within this subsection (one cell cycled with the lithium plating control and other cell with no lithium plating control), were disassembled to investigate the aging of each one. Figure 5.23 shows both cell anodes, where no aging signs were found, whether lithium plating or any other.

The lack of lithium plating signs (that normally appear visually as different color, white in general, shapes) indicates the amount of full equivalent cycles applied were insufficient in order to generate significant lithium plating, not only in the cell where lithium plating was controlled but in the other one. These result corroborates what explained previously about the test conditions. Not only this, but the influence of not homogeneous lithium plating could not be analyzed.

Conclusions

This chapter describes the development of a platform for the Li plating control. This system was implemented using low cost microprocessors, proving an image of its suitability for and industrial application. The lithium plating control included the a ROM and SPKF combination in the control loop, that was developed and parameterized in the previous chapters. Different structures for this hardware were considered, analysing their different potential benefits. Finally a structure where one converter controlled a single cell was selected and implemented, in order to explore the full potential of the advanced SOF control systems itself. The implementation of this system and the needed hardware was not trivial, and highlights the potential for industrial applications. To the known of the author there have not been developed systems of this characteristics, and it is important to underline the considerations and future improvements that are extracted from this validation.

The platforms showed good performance in general predicting SOC and voltage values as well as limiting lithium plating related internal variables, in line with the experimental data at room temperature. Nevertheless some aspects were found that need to be solved to achieve good performance at low temperatures. The use of low temperature test conditions was chosen to isolate the lithium plating mechanism, allowing to control it and give proof of proper parameter identification.

- The internal resistance of the electrodes was needed to adjust during the experimental validation, but this adjust is not enough, since resistance is SOC, current, and temperature dependant. The proper identification of this parameter and its activation energies will make the predictions more accurate and enhance the SPKF benefits.

- The electrolyte parameterization appear not to be accurate at the low test temperature, something that affected the predictions. Also when considering a real case scenario, this conditions are possible, what makes necessary to improve it.

- The power converter current ripple was excessively high at very low currents, what introduced ripple in the controlled internal variable, something that will affect the accuracy of the lithium plating control.

Despite the lacks described above the system drove the cell to lithium plating free operation points reported in the literature. Inaccuracies at low temperature made impossible to age the cells more extensively, and deeper research is needed to improve the parameter identification procedure, as well as to improve the used hardware to reach the maximum control accuracy.

Chapter 6

Conclusions and future lines

Within this thesis batteries, lithium-ion batteries more precisely, have been presented as one of the more promising technological solution towards a cleaner and more sustainable energetic scenario. Also, the importance of correctly and efficiently managing these devices, in order to ensure safety and explode their capabilities to the maximum. Different battery modeling tendencies focused on battery aging prevention found in literature, benefits and drawbacks are analyzed, and the potential of electrochemical model-based battery control systems explained.

The hypothesis of this PhD document has been enunciated; aging of batteries can be controlled using physics-based SOF control embedded systems. To validate this hypothesis a reduced order model enhanced with a SPKF has been developed and implemented in a low cost microprocessor. In addition, the model parameters have been identified, and a platform dedicated to control lithium plating as proof of the whole concept has been developed.

The presented reduced order model was based on a P2D model. This model predictions were compared with a FOM-based cell response, demonstrating the accuracy of the reduction process. This reduction process, assured no loss of information, remaining all the predictions of the P2D model highly accurate in general. On the contrary the predictions for the positive electrode where found to be less accurate, and even for the development of this thesis this fact was negligible, in the future poistive electrode predictions should be imporved. The SPKF filter demonstrated to compensate experimental inaccuracies improving the whole system capabilities.

The parameter identification problem has been studied, and a physico-chemical method implemented. This method have been useful to identify cell parameters on the one hand, and

to evaluate the potential of the method on the other hand. This is important since parameter identification is found to be the most inefficient task when using electrochemical models. The cost and time needed nowadays to identify cell parameters with a physico-chemical method are excessively high to consider it industrially. On the contrary, the lumping of parameters when solving the identification problem by means of computational methods, poses a difficulty for further integration of the models. These investigation identified the insights of physico-chemical methods, what will be used in future works to enhance computational methods-based identification procedures leading to new mixed methodologies, achieving the best balance between cost and development time while the accuracy is maintained. For this purpose a proper characterization of the electrodes porous matrix is found to be crucial, since these characteristics impact in most of the other parameters identifications (when optimizing or when indirectly measuring them). A fast, accurate and cheap method to characterize a porous matrix could be the key for industrially usable parameter identification procedures.

The lithium plating platform included the a ROM and SPKF combination in the control loop, that was developed and parameterized in the previous chapters. In order to experimentally validate this control different hardware structures were considered. To the date it is unclear what would be the best way to implement this type of advanced controls, and it was found crucial to first explore the full potential of the method. A converter per each battery cell have been then used, as it assures a rigorous SOF control (in terms of hardware). Later, the benefits and drawbacks of each hardware structure could be studied in detail, comparing the benefits that each of these structures maintains or looses from rigorous control.

The platforms showed good performance in general predicting SOC and voltage values as well as limiting lithium plating related internal variables, in line with the experimental data at room temperature. Nevertheless some aspects were found that need to be solved to achieve good performance at low temperatures. The use of low temperature test conditions was chosen to isolate the lithium plating mechanism, allowing to control it and give proof of proper parameter identification. The system drove the cell to lithium plating free operation points reported in the literature, but inaccuracies at low temperature made impossible to age the cells more extensively. Deeper research is needed to improve the parameter identification procedure, as well as to improve the used hardware to reach the maximum control accuracy. All in all, the whole platform was integrated and validated to be suitable for and industrial applications. The performance was also found to be as expected and the improvements needed

were not structural, what drives the whole method much closer to a industrial application use case scenario. The developed system makes a step forward to fully explode the potential of physics-based SOF control.

Once proven that ROM models are suitable for online applications, how to manage battery aging is still a big question. Different approaches were found in literature, but all of them still presented important flaws. It is therefore, the managing of aging, the missing chain link towards a complete and online physics-based battery management system.

Chapter 7

Appendixes

7.1 Appenidx A - Derivation of the blending matrix

Within this appendix the derivation of the blending matrix for the output equation will be explained. A bilinear interpolation was used to interpolate 4 models created at two SOC and two temperature points. Figure 7.1 shows the bilinear interpolation concept with four outputs named O_{xx}.

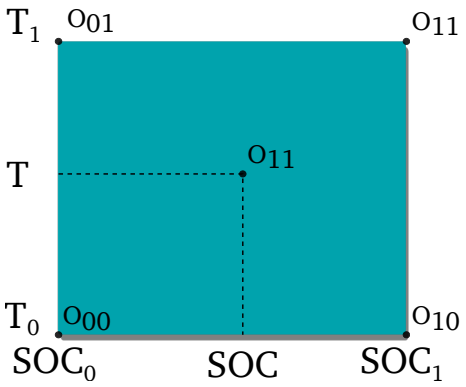

Figure 7.1: Bilinear interpolation for the ROMs output sets "O".

The interpolated output value was defined by the equation 7.1 according to the four outputs in figure 7.1.

$$O = (1-Y)((1-X)O_{00} + XO_{10}) + Y((1-X)O_{01} + XO_{11}) \tag{7.1}$$

Being the X and Y terms defined as follows.

$$\begin{aligned} x &= \frac{SOC - SOC_0}{SOC_1 - SOC_0} \\ y &= \frac{T - T_0}{T_1 - T_0} \end{aligned} \tag{7.2}$$

Further simplifying could be found four α_x coefficients multiplying the O_{xx} outputs.

$$\begin{aligned} O &= (1-Y)(1-X)O_{00} + (1-Y)XO_{10} + (1-X)YO_{01} + YXO_{11} \\ O &= \alpha_1 O_{00} + \alpha_2 O_{10} + \alpha_3 O_{01} + \alpha_4 O_{11} \end{aligned} \tag{7.3}$$

The α_x coefficients were calculated (equations 7.4) so in function of the actual SOC and temperature each O_{xx} output had a bigger or smaller influence in the blended output.

$$\begin{aligned} \alpha_1 &= (1-y)(1-x) \\ \alpha_2 &= (1-y)x \\ \alpha_3 &= (1-x)y \end{aligned} \tag{7.4}$$

Once the α_x coefficients were calculated it was needed to create the blending matrices so each models output is multiplied by the concerning coefficient. Starting from the compact output equation (equation 7.5) the outputs were computed to check the validity of the defined blending matrices (introduced in the equation 7.7).

$$\hat{\mathrm{Y}}[k+1] = \hat{\alpha} * \begin{bmatrix} \hat{\mathrm{C}} & (\%_{res}) \end{bmatrix} * \begin{bmatrix} \hat{\mathrm{X}}[k] \\ X_i[k] \end{bmatrix} + \hat{\alpha} * \hat{\mathrm{D}} * u[k] \tag{7.5}$$

$$\hat{\mathrm{Y}}[k+1] = \hat{\alpha} * \begin{bmatrix} C_1 & 0 & 0 & 0 & (\%_{res})_1 \\ 0 & C_2 & 0 & 0 & (\%_{res})_2 \\ 0 & 0 & C_3 & 0 & (\%_{res})_3 \\ 0 & 0 & 0 & C_4 & (\%_{res})_4 \end{bmatrix} * \begin{bmatrix} X_1[k] \\ X_2[k] \\ X_3[k] \\ X_4[k] \\ X_i[k] \end{bmatrix} + \hat{\alpha} * \begin{bmatrix} D_1 \\ D_2 \\ D_3 \\ D_4 \end{bmatrix} * u[k] \tag{7.6}$$

$$\hat{Y}[k+1] = \begin{bmatrix} \alpha_1 & 0 & \cdots & 0 & \alpha_2 & 0 & \cdots & 0 & \alpha_3 & 0 & \cdots & 0 & \alpha_4 & 0 & \cdots & 0 \\ \cdots & \alpha_1 & 0 & \cdots & 0 & \alpha_2 & 0 & \cdots & 0 & \alpha_3 & 0 & \cdots & 0 & \alpha_4 & 0 & \cdots \\ \cdots & 0 & \ddots & 0 & \cdots & 0 & \ddots & 0 & \cdots & 0 & \ddots & 0 & \cdots & 0 & \ddots & 0 \end{bmatrix} *$$
$$* \begin{bmatrix} C_1 & 0 & 0 & 0 & (\%_{res})_1 \\ 0 & C_2 & 0 & 0 & (\%_{res})_2 \\ 0 & 0 & C_3 & 0 & (\%_{res})_3 \\ 0 & 0 & 0 & C_4 & (\%_{res})_4 \end{bmatrix} * \begin{bmatrix} X_1[k] \\ X_2[k] \\ X_3[k] \\ X_4[k] \\ X_i[k] \end{bmatrix} +$$
$$+ \begin{bmatrix} \alpha_1 & 0 & \cdots & 0 & \alpha_2 & 0 & \cdots & 0 & \alpha_3 & 0 & \cdots & 0 & \alpha_4 & 0 & \cdots & 0 \\ \cdots & \alpha_1 & 0 & \cdots & 0 & \alpha_2 & 0 & \cdots & 0 & \alpha_3 & 0 & \cdots & 0 & \alpha_4 & 0 & \cdots \\ \cdots & 0 & \ddots & 0 & \cdots & 0 & \ddots & 0 & \cdots & 0 & \ddots & 0 & \cdots & 0 & \ddots & 0 \end{bmatrix}$$
$$* \begin{bmatrix} D_1 \\ D_2 \\ D_3 \\ D_4 \end{bmatrix} * u[k]$$

(7.7)

$$\begin{bmatrix} Y_1[k] \\ Y_2[k] \\ \vdots \end{bmatrix} = \begin{bmatrix} \alpha_1 C_{11} X_1[k] + \alpha_1 D_{11} u[k] + \alpha_1 (\%_{res})_{11} X_i[k]) + (\alpha_2 C_{21} X_2[k] + \alpha_2 D_{21} u[k] + \\ \alpha_1 C_{12} X_1[k] + \alpha_1 D_{12} u[k] + \alpha_1 (\%_{res})_{12} X_i[k]) + (\alpha_2 C_{22} X_2[k] + \alpha_2 D_{22} u[k] + \\ \vdots \end{bmatrix}$$
$$\begin{bmatrix} +\alpha_2 (\%_{res})_{21} X_i[k]) + (\alpha_3 C_{31} X_3[k] + \alpha_3 D_{31} u[k] + \alpha_3 (\%_{res})_{31} X_i[k]) + (\alpha_4 C_{41} X_4[k] + \\ +\alpha_2 (\%_{res})_{22} X_i[k]) + (\alpha_3 C_{32} X_3[k] + \alpha_3 D_{32} u[k] + \alpha_3 (\%_{res})_{32} X_i[k]) + (\alpha_4 C_{42} X_4[k] + \\ \vdots \end{bmatrix}$$
$$\begin{bmatrix} +\alpha_4 D_{41} u[k] + \alpha_4 (\%_{res})_{41} X_i[k]) \\ +\alpha_4 D_{42} u[k] + \alpha_4 (\%_{res})_{42} X_i[k]) \\ \vdots \end{bmatrix}$$

(7.8)

$$\begin{bmatrix} Y_1[k] \\ Y_2[k] \\ \vdots \end{bmatrix} = \begin{bmatrix} \alpha_1(C_{11}X_1[k] + D_{11}u[k] + (\%_{res})_{11}X_i[k]) + \alpha_2(C_{21}X_2[k] + D_{21}u[k] + (\%_{res})_{21}X_i[k]) + \\ \alpha_1(C_{12}X_1[k] + D_{12}u[k] + (\%_{res})_{12}X_i[k]) + \alpha_2(C_{22}X_2[k] + D_{22}u[k] + (\%_{res})_{22}X_i[k]) + \\ \vdots \end{bmatrix}$$
$$\begin{bmatrix} +\alpha_3(C_{31}X_3[k] + D_{31}u[k] + (\%_{res})_{31}X_i[k]) + \alpha_4(C_{41}X_4[k] + D_{41}u[k] + (\%_{res})_{41}X_i[k]) \\ +\alpha_3(C_{32}X_3[k] + D_{32}u[k] + (\%_{res})_{32}X_i[k]) + \alpha_4(C_{42}X_4[k] + D_{42}u[k] + (\%_{res})_{42}X_i[k]) \\ \vdots \end{bmatrix} \tag{7.9}$$

$$\begin{aligned} Y_n[k] =& \alpha_1(C_{1n}X_1[k] + D_{1n}u[k] + (\%_{res})_{1n}X_i[k]) + \alpha_2(C_{2n}X_2[k] + D_{2n}u[k] + (\%_{res})_{2n}X_i[k]) + \\ &+ \alpha_3(C_{3n}X_3[k] + D_{3n}u[k] + (\%_{res})_{3n}X_i[k]) + \alpha_4(C_{4n}X_4[k] + D_{4n}u[k] + (\%_{res})_{4n}X_i[k]) \end{aligned} \tag{7.10}$$

The full resolution of the output equation (equation 7.10) demonstrated that the proposed blending matrix was correctly formulated. This could be confirmed as the $Y_n[k]$ output was formed by the sum of the four models composing the augmented state model multiplied each one by the concerning α_x coefficient.

7.2 Appendix B - SPKF equations summary

Table 7.1: SPKF equations summary.

Nonlinear state space model	$x_k = f(x_{k-1}, u_{k-1}, w_{k-1})$ $y_k = h(x_k, u_k, v_k)$
Definitions	$x_k^a = \left[x_k^T, w_k^T, v_k^T\right]^T$ $\boldsymbol{\chi}_k^a = \left[\left(\boldsymbol{\chi}_k^x\right)^T, \left(\boldsymbol{\chi}_k^w\right)^T, \left(\boldsymbol{\chi}_k^v\right)^T\right]^T$ $p = 2\dim(x_k^a)$
Initializations	$\hat{x}_0^+ = \mathbb{E}[x_0]$ $\hat{x}_0^{a,+} = \mathbb{E}\left[x_0^a\right] = \left[\left(\hat{x}_0^+\right)^T, \bar{w}, \bar{v}\right]^T$ $\Sigma_{\tilde{x},0}^+ = \mathbb{E}\left[\left(x_0 - \hat{x}_0^+\right)\left(x_0 - \hat{x}_0^+\right)^T\right]$ $\Sigma_{\tilde{x},0}^{a,+} = \mathbb{E}\left[\left(x_0^a - \hat{x}_0^{a,+}\right)\left(x_0^a - \hat{x}_0^{a,+}\right)^T\right] = diag\left(\Sigma_{\tilde{x},0}^+, \Sigma_{\tilde{w}}, \Sigma_{\tilde{v}}\right)$
State estimate time update	$\boldsymbol{\chi}_{k-1}^{a,+} = \left\{\hat{x}_{k-1}^{a,+}, \hat{x}_{k-1}^{a,+} + \gamma\sqrt{\Sigma_{\tilde{x},k-1}^{a,+}}, \hat{x}_{k-1}^{a,+} - \gamma\sqrt{\Sigma_{\tilde{x},k-1}^{a,+}}\right\}$ $\boldsymbol{\chi}_{k,i}^{x,-} = f\left(\boldsymbol{\chi}_{k-1}^{x,+}, u_{k-1}, \boldsymbol{\chi}_{k-1,i}^{w,+}\right)$ $\hat{x}_k^- = \sum_{i=0}^{p} \alpha_i^{(m)} \boldsymbol{\chi}_{k,i}^{x,-}$
Error covariance time update	$\widetilde{\boldsymbol{\chi}}_{k,i}^{x,-} = \boldsymbol{\chi}_{k,i}^{x,-} - \hat{x}_k^-$ $\Sigma_{\tilde{x},k}^- = \sum_{i=0}^{p} \alpha_i^{(c)} \left(\widetilde{\boldsymbol{\chi}}_{k,i}^{x,-}\right)\left(\widetilde{\boldsymbol{\chi}}_{k,i}^{x,-}\right)^T$
Output estimate	$\mathrm{y}_{k,i} = h\left(\boldsymbol{\chi}_{k,i}^{x,-}, u_k, \boldsymbol{\chi}_{k-1,i}^{v,+}\right)$ $\hat{y}_k = \sum_{i=0}^{p} \alpha_i^{(m)} \mathrm{y}_{k,i}$
Estimator gain matrix	$\tilde{\mathrm{y}}_{k,i} = \mathrm{y}_{k,i} - \hat{y}_k$ $\Sigma_{\tilde{y},k} = \sum_{i=0}^{p} \alpha_i^{(c)} \left(\tilde{\mathrm{y}}_{k,i}\right)\left(\tilde{\mathrm{y}}_{k,i}\right)^T$ $\Sigma_{\tilde{x}\tilde{y},k}^- = \sum_{i=0}^{p} \alpha_i^{(c)} \left(\widetilde{\boldsymbol{\chi}}_{k,i}^{x,-}\right)\left(\tilde{\mathrm{y}}_{k,i}\right)^T$ $L_k = \Sigma_{\tilde{x}\tilde{y},k}^- \Sigma_{\tilde{y},k}^{-1}$
State estimate measurement update	$\hat{x}_k^+ = \hat{x}_k^- + L_k(y_k - \hat{y}_k)$
Error covariance measurement update	$\Sigma_{\tilde{x},k}^+ = \Sigma_{\tilde{x},k}^- - L_k \Sigma_{\tilde{y},k} L_k^T$
Calculation of updated electrochemical variables	$\boldsymbol{\chi} 2_k = \left\{\hat{x}_k^+, \hat{x}_k^+ + \gamma\sqrt{\Sigma_{\tilde{x},k}^+}, \hat{x}_k^+ - \gamma\sqrt{\Sigma_{\tilde{x},k}^+}\right\}$ $\mathrm{y}2_{k,i} = h_2\left(\boldsymbol{\chi} 2_{k,i}, u_k, \boldsymbol{\chi}_{k-1,i}^{v,+}, \boldsymbol{\chi}_{k-1,i}^{w,+}\right)$ $\hat{y}2_k = \sum_{i=0}^{p} \alpha_i^{(m)} \mathrm{y}2_i$

7.3 Appendix C - P2D model parameters

Table 7.2: P2D model parameters.

Geometry	
Electrode plate area	A
Thickness of the electrode	L^{n}, L^{s}, L^{p}
Material properties	
Particle radius	$R_{\mathrm{s}}^{\mathrm{n}}$, $R_{\mathrm{s}}^{\mathrm{p}}$
Solid phase electric conductivity	$\sigma_{\mathrm{eff}}^{\mathrm{n}}$, $\sigma_{\mathrm{eff}}^{\mathrm{p}}$
Solid phase electric conductivity activation energy	$E_{act,\sigma}^{\mathrm{n}}$, $E_{act,\sigma}^{\mathrm{p}}$
Solid phase electric conductivity Bruggeman coefficient	$brug_{\sigma^{\mathrm{n}}}$, $brug_{\sigma^{\mathrm{p}}}$
Film resistance	$R_{\mathrm{f}}^{\mathrm{n}}$, $R_{\mathrm{f}}^{\mathrm{p}}$
OCV curves	
Solid phase initial lithium concentration	$\theta_{100}^{\mathrm{n}}$, $\theta_{100}^{\mathrm{p}}$
Solid phase final lithium concentration	θ_{0}^{n}, θ_{0}^{p}
Electrolyte activity coefficient ln derivative	$\partial \ln f_{\pm} / \partial \ln c_{\mathrm{e}}$
Cationic transference number	t_{+}^{0}
Electrolyte conductivity	$\kappa_{\mathrm{eff}}^{\mathrm{n}}$, $\kappa_{\mathrm{eff}}^{\mathrm{s}}$, $\kappa_{\mathrm{eff}}^{\mathrm{p}}$
Electrolyte conductivity activation energy	$E_{act,\kappa}$
Electrolyte conductivity Bruggeman coefficient	$brug_{\kappa^{\mathrm{n}}}$, $brug_{\kappa^{\mathrm{s}}}$, $brug_{\kappa^{\mathrm{p}}}$
Maximum lithium concentration in the solid	$C_{\mathrm{s,max}}^{\mathrm{n}}$, $C_{\mathrm{s,max}}^{\mathrm{p}}$
Initial lithium concentration in the electrolyte	$c_{\mathrm{e},0}$
Volume fraction	$\varepsilon_{\mathrm{e}}^{\mathrm{n}}$, $\varepsilon_{\mathrm{e}}^{\mathrm{s}}$, $\varepsilon_{\mathrm{e}}^{\mathrm{p}}$
Specific surface area	$a_{\mathrm{s}}^{\mathrm{n}}$, $a_{\mathrm{s}}^{\mathrm{p}}$
Electrochemical reaction kinetics	
Charge transfer coefficient	α^{n}, α^{p}
Reaction rate coefficient	k_{0}^{n}, k_{0}^{p}
Reaction rate coefficient activation energy	$E_{act,k}^{\mathrm{n}}$, $E_{act,k}^{\mathrm{p}}$
Transport	
Diffusion coefficient in the solid	$D_{\mathrm{s}}^{\mathrm{n}}$, $D_{\mathrm{s}}^{\mathrm{p}}$
Diffusion coefficient in the solid activation energy	$E_{act,D_{\mathrm{s}}}^{\mathrm{n}}$, $E_{act,D_{\mathrm{s}}}^{\mathrm{p}}$
Effective diffusion coefficient in the electrolyte	$D_{\mathrm{e,eff}}^{\mathrm{n}}$, $D_{\mathrm{e,eff}}^{\mathrm{s}}$, $D_{\mathrm{e,eff}}^{\mathrm{p}}$
Diffusion coefficient in the electrolyte activation energy	E_{act,D_e}
Diffusion coefficient in the electrolyte Bruggeman coefficient	$brug_{D_{\mathrm{e}}^{\mathrm{n}}}$, $brug_{D_{\mathrm{e}}^{\mathrm{s}}}$, $brug_{D_{\mathrm{e}}^{\mathrm{p}}}$

7.4 Appendix D - P2D model equations

This appendix gather the specific equations composing the P2D model.

1. Solid-phase charge conservation:

$$\nabla \cdot (\sigma_{\text{eff}} \nabla \phi_s) = a_s F j,$$

where $\phi_s(x,t)$ is the solid-phase potential at some spatial location x in the cell at time t, σ_{eff} is the effective conductivity of the solid, a_s is the specific surface area of the solid in the electrode, F is Faraday's constant, and $j(x,t)$ is the flux of lithium leaving the solid and entering the electrolyte. In the negative electrode, $0 \leq x \leq L^{\text{n}}$, in the separator, $L^{\text{n}} \leq x \leq L^{\text{n}} + L^{\text{s}}$, and in the positive electrode $L^{\text{n}} + L^{\text{s}} \leq x \leq L^{\text{n}} + L^{\text{s}} + L^{\text{p}}$.

2. Solid-phase mass-conservation:

$$\frac{\partial c_s}{\partial t} = \frac{1}{r^2} \frac{\partial}{\partial r} \left(D_s r^2 \frac{\partial c_s}{\partial r} \right),$$

where $c_s(x,r,t)$ is the solid-phase concentration of lithium at radial position $0 \leq r \leq R_s$ within an assumed spherical particle of electrode material and D_s is the diffusivity of lithium in the solid.

3. Electrolyte-phase charge conservation:

$$\nabla \cdot \left(\kappa_{\text{eff}} \nabla \phi_e + \kappa_{D,\text{eff}} \nabla \ln c_e \right) + a_s F j = 0,$$

where $\phi_e(x,t)$ is the electrolyte-phase potential, $c_e(x,t)$ is the electrolyte-phase concentration of lithium, κ_{eff} is the effective conductivity of the electrolyte, and

$$\kappa_{D,\text{eff}} = 2RT\kappa_{\text{eff}}(t_+^0 - 1)(1 + \partial \ln f_{\pm} / \partial \ln c_e)/F$$

scales κ_{eff} to multiply a concentration dependence of ϕ_e, t_+^0 is the transference number of the positive ion in the electrolyte with respect to the solvent, and $f_{\pm}$ is the mean molar activity coefficient.

4. Electrolyte-phase mass conservation:

$$\frac{\partial(\varepsilon_e c_e)}{\partial t} = \nabla \cdot (D_{e,\text{eff}} \nabla c_e) + a_s(1 - t_+^0) j,$$

where ε_e is the porosity of the electrode and $D_{e,\text{eff}}$ is the effective diffusivity of the electrolyte. The electrolyte concentration in equilibrium is denoted as $c_{e,0}$.

5. Butler-Volmer kinetics relationship,

$$j = j_0 \left\{ \exp\left(\frac{(1-\alpha)F}{RT} \eta \right) - \exp\left(-\frac{\alpha F}{RT} \eta \right) \right\},$$

where $\eta = \phi_s - \phi_e - U_{\text{ocp}}(c_{s,e}/c_{s,\max}) - FR_{\text{f}} j$ and U_{ocp} is the open-circuit-potential function of the electrode, which in this case is evaluated at the surface concentration $c_{s,e}(x,t) = c_s(x,R,t)$ normalized by the maximum theoretic concentration of lithium $c_{s,\max}$ of the electrode materials. In this relationship, R_{f} is the resistivity of a surface film on the electrode and

$$j_0 = k_0 c_e^{1-\alpha} (c_{s,\max} - c_{s,e})^{1-\alpha} c_{s,e}^{\alpha}$$

where α is an asymmetric charge-transfer coefficient and k_0 is a kinetic parameter.

During operation, electrode stoichiometry $c_s/c_{s,\max}$ is expected to remain between θ_0 and θ_{100}. Cell electrical current density $i_{\text{app}}(t)/A$ (where A is the current-collector area) drives these equations through a boundary condition on ϕ_s. Cell voltage is the difference between ϕ_s measured at the positive and negative current collectors.

7.5 Appendix E - Power converter design

The power converter integrated in this platform was designed and implemented. The reason behind this is that few converters could be found in the market with an input voltage suitable to connect a battery, not only this, but the converters fitting in this requirement are not able to handle considerable current levels. It is important then to review the requirements considered within this thesis. The cell characteristics were first analyzed (table 7.3), what delimited the converters input ranges.

Table 7.3: Kokam cell characteristics.

Constant	Unit	Value
Nominal cell capacity $C_{\max}$	$[Ah]$	7.5
Minimum cell voltage $V_{\min}$	$[V]$	2.7
Maximum cell voltage $V_{\max}$	$[V]$	4.2
Maximum cell discharge current $I_{\max}$	$[A]$	37.5

The input voltage and current were defined accordingly as can be seen in table 7.4. The current limit was fixed higher than the continuous discharge capacity of the cell, so limitations in the converter design for higher capacity cells (as it is the case in a wide variety of applications) could be explored.

Table 7.4: Converter specifications.

Constant	Unit	Value
Minimum input voltage $V_{in,\min}$	$[V]$	2.7
Maximum input voltage $V_{in,\max}$	$[V]$	4.2
Maximum input current $I_{in,\max}$	$[A]$	50
Nominal output voltage $V_{out,nom}$	$[V]$	10

The output voltage is normally related to the application the battery is used for. In this case it was not considered an specific one as stated before. Thus, the output voltage was fixed to $10V$, as the converter output was connected to electronic source and load this voltage is inside the most used devices. Also the output current level was kept reasonable for common devices.

When input and output characteristics were defined the DC/DC converter topology was defined. The output voltage was kept constant and therefore negative gain was not needed. Between positive gain converters the *Boost* topology is one of the best know and matures and

was selected because of this reason. This topology had a series connected coil in the input as well, what made the input current ripple lower (avoiding unnecessary micro-cycles). Batteries are intended to store energy and deliver it when needed what implies that the converter had also to be bidirectional (it was needed that current could flow in and out of the battery). Taking into account all this considerations the selected final topology was a *synchronous boost* as can be seen in figure 7.2.

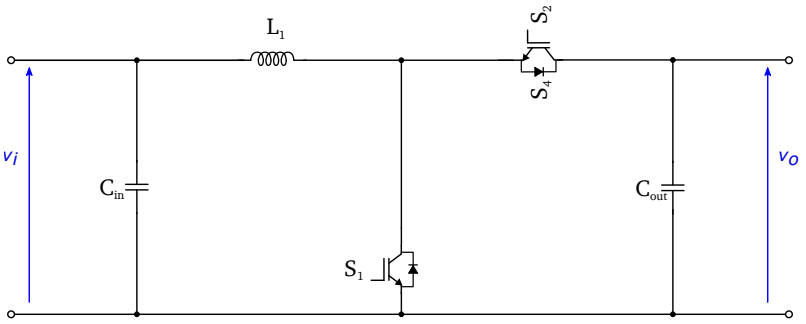

Figure 7.2: Synchronous boost converter diagram.

The current level that the converter needed to handle was also a value that conditioned the converter topology. The coils used in the converter were dimensioned according to the maximum and mean value of the current. This coils can be designed to work with the desired current, nevertheless commercially found devices are limited. A possible solution to use common commercial coils was to distribute the current in several branches with an interleaved topology (figure 7.3). After selecting the topology the converter was sized analytically based on [176], and used components can be found in figure 7.4.

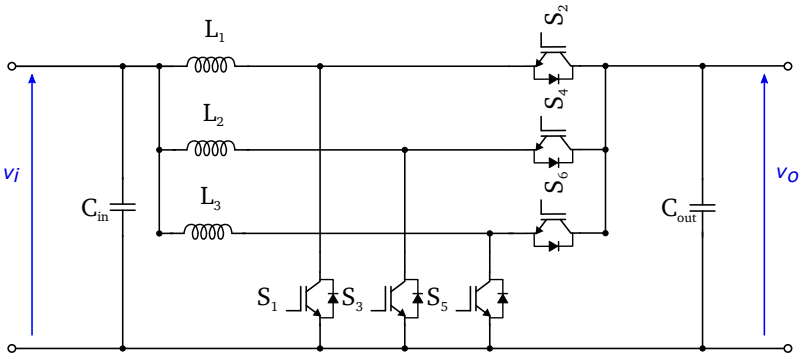

Figure 7.3: Interleaved synchronous boost converter diagram.

Current and voltage values at the converter input were measured to feed the battery cell model as explained along chapter 5, in addition output values sensors and conditionings were

also implemented for future use. Not only electric values were needed to feed the model, cell temperature measurement was also implemented in each converter. A temperature measurement dedicated "NTC" sensor (B57861S0502F040 manufactured by *TDK*) was used. The same way the current measurement was also accomplished with a dedicated device (ACS770LCB-050B-PFF-T manufactured by *Allegro MicrosSystems*) and voltages were measured with an isolated voltage sensor (ACPL-C87AT-000E commercialized by *Broadcom*).

After the validation of the converter the final schematic with the measurements conditioning and all the auxiliary electronics can be found in figure 7.4.

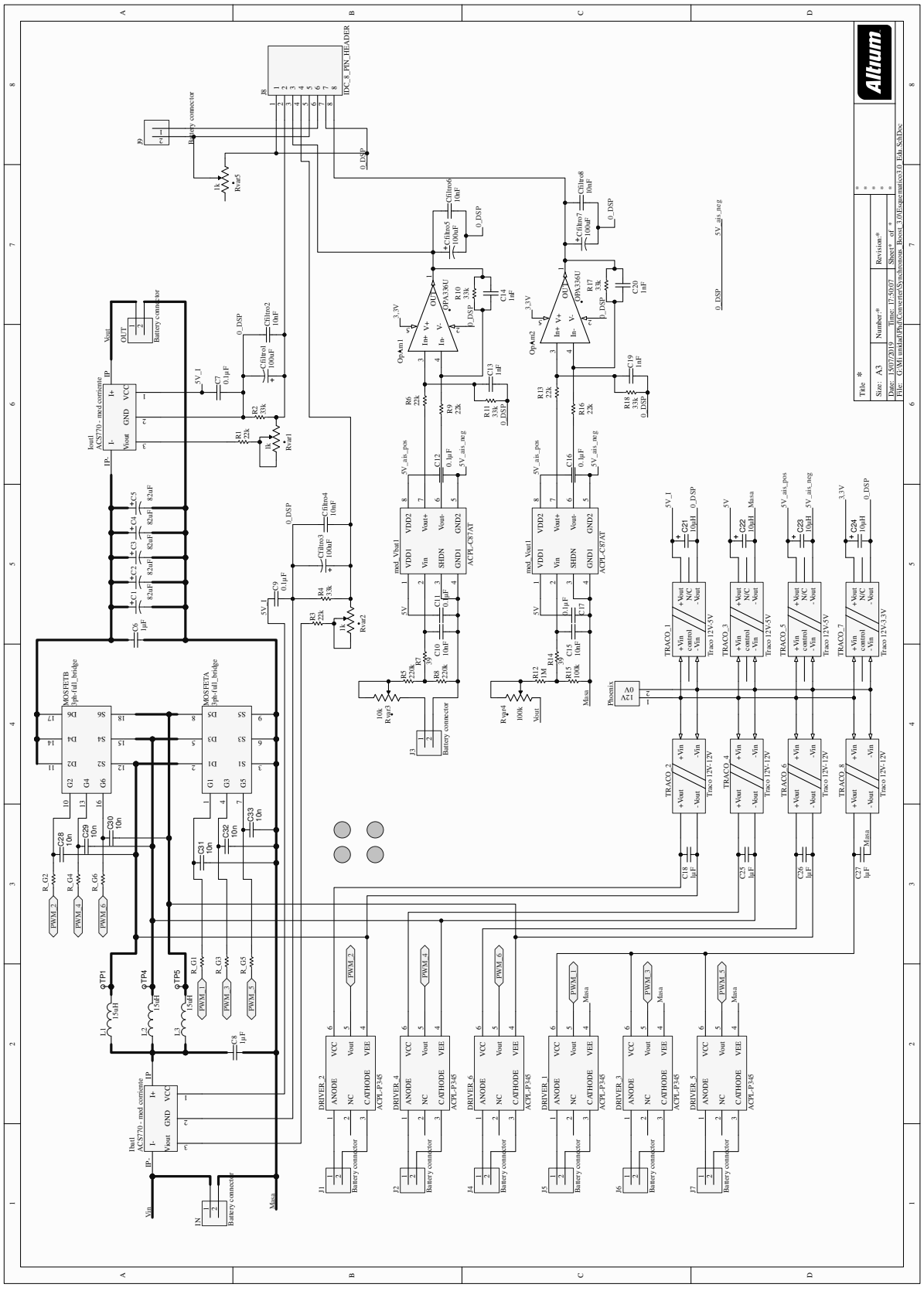

Figure 7.4: Converter schematic diagram.

7.6 Symbols used in the nonlinear corrections explanation

Some additional symbols used in the nonlinear corrections explanation can be found in the table 7.5. In addition the next notations are of interest; X^d denotes an undefined dimension, $\sim$ denotes a linear variable (after isolating the nonlinear term of the equation) and $X_{x,avg}$ denotes and average value.

Table 7.5: Symbols.

Linear voltage	v_{linear}
Solid surface concentration	$C_{s,e}^{pos}$, $C_{s,e}^{neg}$
Solid phase potential	ϕ_s^{pos}, ϕ_s^{neg}
Open circuit voltage	U_{ocp}^{pos}, U_{ocp}^{neg}
Initial lithium concentration in the electrolyte	$C_{e,0}$
Initial solid surface concentration	$C_{s,0}$
Maximum lithium concentration in the solid phase	$C_{s,\max}^{d}$
Reaction rate coefficient	k_0^d
Total thickness of the cell	L^{tot}

List of Figures

List of Tables

References

[1] International Energy Agency, “Key world energy balances,” 2019.

[2] ——, “Global Energy Transformation,” 2016.

[3] A. A. Akhil, G. Huff, A. B. Currier, B. C. Kaun, D. M. Rastler, S. B. Chen, A. L. Cotter, D. T. Bradshaw, and W. D. Gauntlett, “SANDIA REPORT DOE / EPRI Electricity Storage Handbook in Collaboration with NRECA,” 2015.

[4] Nature SP, “Climate change,” *Nature*, vol. 479, pp. 267–268, 2011.

[5] International Energy Agency, “World Energy Outlook - Special Report,” 2016.

[6] S. Sabihuddin, A. E. Kiprakis, and M. Mueller, “A Numerical and Graphical Review of Energy Storage Technologies,” *Energies*, vol. 8, pp. 172–216, 2015.

[7] J. W. Choi and D. Aurbach, “Promise and reality of post-lithium-ion batteries with high energy densities,” *Nature Reviews Materials*, vol. 1, 2016.

[8] ESA, “Energy Storage Association.”

[9] N. Nitta, F. Wu, J. T. Lee, and G. Yushin, “Li-ion battery materials: present and future,” *Materials Today*, vol. 00, no. 00, 2014.

[10] Kokam, “Kokam.”

[11] Tesla © 2019, “Tesla Gigafactory.”

[12] M. Ecker, “Lithium Plating in Lithium-Ion Batteries,” Ph.D. dissertation, RWTH Aachen University, 2016.

[13] E. Sarasketa-Zabala, "A novel approach for lithium-ion battery selection and lifetime prediction," Ph.D. dissertation, Mondragon Unibertsitatea, 2014.

[14] E. Sarasketa-Zabala, I. Gandiaga, E. Martinez-Laserna, L. M. Rodriguez-Martinez, and I. Villarreal, "Cycle ageing analysis of a LiFePO4/graphite cell with dynamic model validations: Towards realistic lifetime predictions," *Journal of Power Sources*, vol. 275, pp. 573–587, oct 2015.

[15] G. L. Plett, *Battery Management Systems, Volume II: Equivalent-Circuit Methods:*, ser. Artech House power engineering series. Artech House, 2016.

[16] H. Liu, Z. Wei, W. He, and J. Zhao, "Thermal issues about Li-ion batteries and recent progress in battery thermal management systems : A review," *Energy Conversion and Management*, vol. 150, pp. 304–330, 2017.

[17] U. IRAOLA, "Electro-thermal optimization of an energy storage system based on li-ion batteries," Ph.D. dissertation, Mondragon Unibertsitatea, 2014.

[18] M. Sufyan, N. A. Rahim, M. M. Aman, C. K. Tan, and S. R. S. Raihan, "Sizing and applications of battery energy storage technologies in smart grid system : A review," *Journal of Renewable Sustainable Energy*, vol. 11, 2019.

[19] Y. Yang, S. Bremner, C. Menictas, and M. Kay, "Battery energy storage system size determination in renewable energy systems : A review," *Renewable and Sustainable Energy Reviews*, vol. 91, pp. 109–125, 2018.

[20] E. Sarasketa-Zabala, E. Martinez-Laserna, M. Berecibar, I. Gandiaga, L. M. Rodriguez-Martinez, and I. Villarreal, "Realistic lifetime prediction approach for Li-ion batteries," *Applied Energy*, vol. 162, pp. 839–852, 2016.

[21] M. Lucu, E. Martinez-Laserna, I. Gandiaga, and H. Camblong, "A critical review on self-adaptive Li-ion battery ageing models," *Journal of Power Sources*, vol. 401, pp. 85–101, 2018.

[22] Y. Yuan, C. Sun, M. Li, S. S. Choi, and Q. Li, "Determination of optimal supercapacitor-lead-acid battery energy storage capacity for smoothing wind power using empirical

mode decomposition and neural network," *Electric Power Systems Research*, vol. 127, pp. 323–331, 2015.

[23] S. R. A. Bolonne and D. P. Chandima, "Sizing an Energy System for Hybrid Li-Ion Battery-Supercapacitor RTG Cranes Based on State Machine Energy Controller," *IEE Access*, vol. 7, pp. 71 209–71 220, 2019.

[24] E. Martinez-Laserna, E. Sarasketa-Zabala, I. Villarreal, D.-I. Stroe, M. Swierczynski, A. Warnecke, J. Timmermans, and S. Goutam, "Technical Viability of Battery Second Life : A Study from the Ageing Perspective," *IEEE Transactions on Industry Applications*, vol. 54, no. 3, 2018.

[25] E. Martinez-laserna, I. Gandiaga, E. Sarasketa-zabala, J. Badeda, and D.-I. Stroe, "Battery second life : Hype , hope or reality ? A critical review of the state of the art," *Renewable and Sustainable Energy Reviews*, vol. 93, pp. 701–718, 2018.

[26] V. I. Herrera, E. Martinez-laserna, A. Milo, H. Gaztañaga, and H. Camblong, "Techno-economic assessment of Lithium-ion battery lifetime estimation methods for sizing and operation conditions definition in railway applications," in *2017 IEEE Vehicle Power and Propulsion Conference (VPPC)*, 2017.

[27] C. Zhang, J. Marco, and T. F. Yu, "Hardware Platform Design of Small Energy Storage System using Second Life Batteries," in *2018 UKACC 12th International Conference on Control (CONTROL)*, 2018.

[28] M. Swierczynski, D. Stroe, E. Martinez-Laserna, E. Sarasketa-Zabala, J. Timmermans, S. Goutam, and R. Teodorescu, "The Second Life Ageing of the NMC/C Electric Vehicle retired Li-ion Batteries in the Stationary Applications," *ECS Transactions*, vol. 74, no. 1, pp. 55–62, 2016.

[29] A. Saez-de Ibarra, E. Martinez-Laserna, D.-I. Stroe, M. Swierczynski, and P. Rodriguez, "Sizing Study of Second Life Li-ion Batteries for Enhancing Renewable Energy Grid Integration," *IEEE Transactions on Industry Applications*, vol. 52, no. 6, 2016.

[30] J. W. A. Catton, S. B. Walker, P. Mcinnis, M. Fowler, R. A. Fraser, S. B. Young, and B. Gaffney, "Design and Analysis of the Use of Re-Purposed Electric Vehicle Batteries for Stationary Energy Storage in Canada," *Batteries*, vol. 5, no. 14, 2019.

[31] Z. Chu, X. Feng, L. Lu, J. Li, X. Han, and M. Ouyang, "Non-destructive fast charging algorithm of lithium-ion batteries based on the control-oriented electrochemical model," *Applied Energy*, vol. 204, pp. 1240–1250, 2017.

[32] Z. Chu, G. L. Plett, M. S. Trimboli, and M. Ouyang, "A control-oriented electrochemical model for lithium-ion battery , Part I : Lumped-parameter reduced-order model with constant phase element," *Journal of Energy Storage*, vol. 25, p. 100828, 2019.

[33] H. E. Perez, S. Dey, X. Hu, and S. J. Moura, "Optimal Charging of Li-Ion Batteries via a Single Particle Model with Electrolyte and Thermal Dynamics," *Journal ofThe Electrochemical Society*, vol. 164, no. 7, 2017.

[34] H. Perez, N. Shahmohammadhamedani, and S. Moura, "Enhanced Performance of Li-Ion Batteries via Modified Reference Governors and Electrochemical Models," *IEEE/ASME Transactions on Mechatronics*, 2015.

[35] P. Fortenbacher, J. L. Mathieu, and G. Andersson, "Modeling, identification, and optimal control of batteries for power system applications," in *2014 Power Systems Computation Conference*. IEEE, aug 2014.

[36] M. Xavier, G. L. Plett, and M. S. Trimboli, "Model prediction and optimization: Accurate power limit estimation for lithium-ion batteries," *Advanced Automotive Battery Conference*, 2018.

[37] G. Florentino and M. S. Trimboli, "Lithium-ion Battery Management Using Physics-based Model Predictive Control and DC-DC Converters," *2018 IEEE Transportation Electrification Conference and Expo (ITEC)*, 2018.

[38] M. S. Trimboli and M. A. Xavier, "Charging strategies for lithium-ion batteries using electrochemical based reduced-order models and predictive control," in *Advanced Automotive Battery Conference*, Detroit, MI, 2015.

[39] A. J. Smiley, "An Improved Approcah To State-Of-Age Estimation For Lithium-Ion Battery Cells Using Interacting Multiple Model Kalman Filters," Ph.D. dissertation, University of Colorado Colorado Springs (UCCS), 2019.

[40] A. Smiley and G. L. Plett, "An adaptive physics-based reduced-order model of an aged lithium-ion cell , selected using an interacting multiple-model Kalman filter," *Journal of Energy Storage*, vol. 19, pp. 120–134, 2018.

[41] D. Zhang, S. Dey, L. D. Couto, and S. J. Moura, "Battery Adaptive Observer for a Single Particle Model With Intercalation-Induced Stress," *IEEE Transactions on Control Systems Technology*, 2019.

[42] S. Park, D. Zhang, and S. Moura, "Hybrid Electrochemical Modeling with Recurrent Neural Networks for Li-ion Batteries," in *2017 American Control Conference*, Seattle, USA, 2017.

[43] A. Rodríguez, G. L. Plett, and M. S. Trimboli, "Comparing four model-order reduction techniques, applied to lithium-ion battery-cell internal electrochemical transfer functions," *eTransportation*, vol. 1, 2019.

[44] S. J. Moura, F. Bribiesca Argomedo, R. Klein, A. Mirtabatabaei, and M. Krstic, "Battery State Estimation for a Single Particle Model With Electrolyte Dynamics," *IEEE Transactions on Control Systems Technology*, vol. 25, no. 2, pp. 1063–6536, 2016.

[45] A. A. Franco, "Multiscale modelling and numerical simulation of rechargeable lithium ion batteries: concepts, methods and challenges," *RSC Advances*, vol. 3, no. 13027, 2013.

[46] D. Miranda, C. M. Costa, and S. Lanceros-Mendez, "Lithium ion rechargeable batteries : State of the art and future needs of microscopic theoretical models and simulations," *Journal of Electroanalytical Chemistry*, vol. 739, pp. 97–110, 2015.

[47] V. Ramadesigan, P. W. C. Northrop, S. De, S. Santhanagopalan, R. D. Braatz, and V. R. Subramanian, "Modeling and Simulation of Lithium-Ion Batteries from a Systems Engineering Perspective," *Journal of The Electrochemical Society*, vol. 159, no. 3, pp. R31–R45, 2012.

[48] J. L. Lee, A. Chemistruck, and G. L. Plett, "One-dimensional physics-based reduced-order model of lithium-ion dynamics," *Journal of Power Sources*, vol. 220, pp. 430–448, 2012.

[49] P. W. C. Northrop, V. Ramadesigan, S. De, and V. R. Subramanian, "Coordinate Transformation, Orthogonal Collocation, Model Reformulation and Simulation of Electrochemical-Thermal Behavior of Lithium-Ion Battery Stacks," *Journal of The Electrochemical Society*, vol. 158, no. 12, pp. A1461–A1477, 2011.

[50] F. Zhang, M. M. Ur Rehman, H. Wang, Y. Levron, G. Plett, R. Zane, and D. Maksimović, "State-of-Charge Estimation Based on Microcontroller Implemented Sigma-Point Kalman Filter in a Modular Cell Balancing System for Lithium-Ion Battery Packs," in *2015 IEEE 16th Workshop on Control and Modeling for Power Electronics (COMPEL)*, 2015.

[51] E. Miguel, "Post-mortem analysis of LP2770112 Lishen cells for an elevation application," Master thesis, Mondragon Unibertsitatea, 2015.

[52] S. Santhanagopalan, Q. Guo, P. Ramadass, and R. E. White, "Review of models for predicting the cycling performance of lithium ion batteries," *Journal of Power Sources*, vol. 156, pp. 620–628, 2006.

[53] A. Seaman, T.-S. Dao, and J. McPhee, "A survey of mathematics-based equivalent-circuit and electrochemical battery models for hybrid and electric vehicle simulation," *Journal of Power Sources*, vol. 256, pp. 410–423, 2014.

[54] M. Doyle, T. F. Fuller, and J. Newman, "Modeling of Galvanostatic Charge and Discharge of the Lithium/Polymer/Insertion Cell," *Journal of The Electrochemical Society*, vol. 140, no. 6, pp. 1526–1533, 1993.

[55] T. F. Fuller, M. Doyle, and J. Newman, "Simulation and Optimization of the Dual Lithium Ion Insertion Cell," *Journal of The Electrochemical Society*, vol. 141, no. 1, p. 10, 1994.

[56] J. Newman and W. Tiedemann, "Porous-Electrode Theory with Battery Applications," *AIChE Journal*, vol. 21, no. 1, pp. 25–41, 1975.

[57] J. Newman and K. E. Thomas-Alyea, *Electrochemical Systems*, 3rd ed., I. John Wiley & Sons, Ed. John Wiley & Sons, Inc., 2004.

[58] T. F. Fuller, M. Doyle, and J. Newman, "Relaxation Phenomena in Lithium-Ion-Insertion Cells," *Journal of The Electrochemical Society*, vol. 141, no. 4, pp. 982–990, 1994.

[59] P. Arora, M. Doyle, and R. E. White, "Mathematical Modeling of the Lithium Deposition Overcharge Reaction in Lithium-Ion Batteries Using Carbon-Based Negative Electrodes," *Journal of The Electrochemical Society*, vol. 146, no. 10, pp. 3543–3553, 1999.

[60] P. Ramadass, B. Haran, R. White, and B. N. Popov, "Mathematical modeling of the capacity fade of Li-ion cells," *Journal of Power Sources*, vol. 123, no. 2003, pp. 230–240, 2003.

[61] P. Ramadass, B. Haran, P. M. Gomadam, R. White, and B. N. Popov, "Development of First Principles Capacity Fade Model for Li-Ion Cells," *Journal of The Electrochemical Society*, vol. 151, no. 2, pp. A196–A203, 2004.

[62] P. Ramadass, "Capacity fade analysis of commercial Li-ion batteries," Ph.D. dissertation, University of South Carolina, 2003.

[63] M. Safari, M. Morcrette, A. Teyssot, and C. Delacourt, "Multimodal Physics-Based Aging Model for Life Prediction of Li-Ion Batteries," *Journal of the Electrochemical Society*, vol. 156, no. 3, pp. A145–A153, 2009.

[64] Y. Dai, L. Cai, and R. E. White, "Capacity Fade Model for Spinel LiMn2O4 Electrode," *Journal of the Electrochemical Society*, vol. 160, no. 1, pp. A182–A190, 2013.

[65] R. Narayanrao, M. M. Joglekar, and S. Inguva, "A Phenomenological Degradation Model for Cyclic Aging of Lithium Ion Cell Materials," *Journal of the Electrochemical Society*, vol. 160, no. 1, pp. A125–A137, 2013.

[66] B. S. Haran, B. N. Popov, and R. E. White, "Determination of the hydrogen diffusion coefficient in metal hydrides by impedance spectroscopy," *Journal of Power Sources*, vol. 75, pp. 56–63, 1998.

[67] G. Ning and B. N. Popov, "Cycle Life Modeling of Lithium-Ion Batteries," *Journal of The Electrochemical Society*, vol. 151, no. 10, pp. A1584–A1591, 2004.

[68] M. Guo, G. Sikha, and R. E. White, "Single-Particle Model for a Lithium-Ion Cell: Thermal Behavior," *Journal of The Electrochemical Society*, vol. 158, no. 2, pp. A122–A132, 2011.

[69] W. B. Gu, C. Y. Wang, and B. Y. Liaw, "Micro-Macroscopic Coupled Modeling of Batteries and Fuel Cells: II. Application to Nickel-Cadmium and Nickel-Metal Hydride Cells," *Journal of the Electrochemical Society*, vol. 145, no. 10, pp. 3418–3427, 1998.

[70] V. R. Subramanian, V. D. Diwakar, and D. Tapriyal, "Efficient Macro-Micro Scale Coupled Modeling of Batteries," *Journal of The Electrochemical Society*, vol. 152, no. 10, pp. A2002–A2008, 2005.

[71] K. A. Smith, C. D. Rahn, and C.-Y. Wang, "Model Order Reduction of 1D Diffusion Systems Via Residue Grouping," *Journal of Dynamic Systems, Measurement, and Control*, vol. 130, 2008.

[72] J. C. Forman, S. Bashash, J. L. Stein, and H. K. Fathy, "Reduction of an Electrochemistry-Based Li-Ion Battery Model via Quasi-Linearization and Padé Approximation," *Journal of The Electrochemical Society*, vol. 158, no. 2, pp. A93–A101, 2011.

[73] G. L. Plett, *Battery Management Systems, Volume I: Battery Modeling*. Artech House, 2015.

[74] J. L. Lee, A. Chemistruck, and G. L. Plett, "Discrete-time realization of transcendental impedance models, with application to modeling spherical solid diffusion," *Journal of Power Sources*, vol. 206, pp. 367–377, may 2012.

[75] L. Zhang, L. Wang, C. Lyu, J. Li, and J. Zheng, "Non-Destructive Analysis of Degradation Mechanisms in Cycle-Aged Graphite/LiCoO2 Batteries," *Energies*, vol. 7, pp. 6282–6305, sep 2014.

[76] B. Pilipili Matadi, "Study of the aging mechanisms of Li-ion batteries under low temperature cycling and high temperature storage: understanding of the origins and aging modeling," Ph.D. dissertation, Universite Grenoble Alpes, 2017.

[77] R. Fu, S.-Y. Choe, V. Agubra, and J. Fergus, "Development of a physics-based degradation model for lithium ion polymer batteries considering side reactions," *Journal of Power Sources*, vol. 278, pp. 506–521, mar 2015.

[78] ——, "Modeling of degradation effects considering side reactions for a pouch type Li-ion polymer battery with carbon anode," *Journal of Power Sources*, vol. 261, pp. 120–135, 2014.

[79] L. Liu and M. Zhu, "Modeling of SEI Layer Growth and Electrochemical Impedance Spectroscopy Response using a Thermal-Electrochemical Model of Li-ion Batteries," *ECS Transactions*, vol. 61, no. 27, pp. 43–61, oct 2014.

[80] L. Liu, J. Park, X. Lin, A. M. Sastry, and W. Lu, "A thermal-electrochemical model that gives spatial-dependent growth of solid electrolyte interphase in a Li-ion battery," *Journal of Power Sources*, vol. 268, pp. 482–490, dec 2014.

[81] G. L. Plett, "Algebraic Solution for Modeling SEI Layer Growth," *ECS Electrochemistry Letters*, vol. 2, no. 7, pp. A63–A65, 2013.

[82] E. Prada, D. Di Domenico, Y. Creff, J. Bernard, V. Sauvant-Moynot, and F. Huet, "Physics-based modelling of LiFePO4-graphite Li-ion batteries for power and capacity fade predictions: Application to calendar aging of PHEV and EV," in *2012 IEEE Vehicle Power and Propulsion Conference*, oct 2012.

[83] A. V. Randall, R. D. Perkins, X. Zhang, and G. L. Plett, "Controls oriented reduced order modeling of solid-electrolyte interphase layer growth," *Journal of Power Sources*, vol. 209, pp. 282–288, 2012.

[84] T. R. Tanim and C. D. Rahn, "Aging formula for lithium ion batteries with solid electrolyte interphase layer growth," *Journal of Power Sources*, vol. 294, pp. 239–247, 2015.

[85] Q. Zhang and R. E. White, "Capacity fade analysis of a lithium ion cell," *Journal of Power Sources*, vol. 179, pp. 793–798, 2008.

[86] ANSYS, "Electric Machine Design Methodology : A Revolutionary Approach."

[87] O. Zienkiewicz, R. Taylor, and P. Nithiarasu, *The finite element method for fluid dynamics*, 7th ed. Elsevier Ltd., 2014.

[88] K. D. Stetzel, L. L. Aldrich, M. S. Trimboli, and G. L. Plett, "Electrochemical state and internal variables estimation using a reduced-order physics-based model of a lithium-

ion cell and an extended Kalman filter," *Journal of Power Sources*, vol. 278, pp. 490–505, mar 2015.

[89] A. Bizeray, S. Duncan, and D. Howey, "Advanced battery management systems using fast electrochemical modelling," in *IET Hybrid and Electric Vehicles Conference (HEVC)*. Institution of Engineering and Technology, 2013.

[90] H. Binous, A. a. Shaikh, and A. Bellagi, "Chebyshev orthogonal collocation technique to solve transport phenomena problems with Matlab® and Mathematica ©," *Computer Applications in Engineering Education*, vol. 23, pp. 422–431, 2015.

[91] J. Sabatier, J. M. Francisco, F. Guillemard, L. Lavigne, M. Moze, and M. Merveillaut, "Lithium-ion batteries modeling: A simple fractional differentiation based model and its associated parameters estimation method," *Signal Processing*, vol. 107, pp. 290–301, feb 2015.

[92] A. Bizeray, S. Zhao, S. Duncan, and D. Howey, "Lithium-ion battery thermal-electrochemical model-based state estimation using orthogonal collocation and a modified extended Kalman filter," *Journal of Power Sources*, vol. 296, pp. 400–412, 2015.

[93] C.-Y. R. Christopher D. and Wang, *Battery Systems Engineering*. John Wiley & Sons Inc., 2013.

[94] G. Damblanc, S. Hartridge, R. Spotnitz, and K. Imaichi, "Validation of a new simulation tool for the analysis of electrochemical and thermal performance of lithium ion batteries," in *JSAE Annual Congress*, 2011.

[95] L. Cai and R. E. White, "Mathematical modeling of a lithium ion battery with thermal effects in COMSOL Inc. Multiphysics (MP) software," *Journal of Power Sources*, vol. 196, pp. 5985–5989, 2011.

[96] Q. Wang, P. Ping, X. Zhao, G. Chu, J. Sun, and C. Chen, "Thermal runaway caused fire and explosion of lithium ion battery," *Journal of Power Sources*, vol. 208, pp. 210–224, 2012.

[97] M. S. Rad, D. L. Danilov, M. Baghalha, M. Kazemeini, and P. H. L. Notten, "Thermal Modeling of Cylindrical LiFePO4 Batteries," *Journal of Modern Physics*, vol. 04, pp. 1–7, 2013.

[98] Y. Lai, S. Du, L. Ai, L. Ai, Y. Cheng, Y. Tang, and M. Jia, "Insight into heat generation of lithium ion batteries based on the electrochemical-thermal model at high discharge rates," *International Journal of Hydrogen Energy*, vol. 40, pp. 13 039–13 049, 2015.

[99] J. Newman, "Fortran toolbos for battery simulation," 1998.

[100] "COMSOL Multiphysics®."

[101] K. Uddin, S. Perera, W. D. Widanage, L. Somerville, and J. Marco, "Characterising Lithium-Ion Battery Degradation through the Identification and Tracking of Electrochemical Battery Model Parameters," *Batteries*, vol. 2, no. 13, 2016.

[102] S. J. Moura, "Estimation and Control of Battery Electrochemistry Models : A Tutorial," *2015 IEEE 54th Annual Conference on Decision and Control (CDC)*, 2015.

[103] S. J. Moura, N. A. Chaturvedi, and M. Krstić, "Adaptive PDE Observer for Battery SOC/-SOH Estimation via an Electrochemical Model," *Journal of Dynamic Systems Measurement and Control*, vol. 136, no. 1, pp. 011–015, 2014.

[104] S. J. Moura, "Techniques for Battery Health Conscious Power Management via Electrochemical Modeling and Optimal Control by," Ph.D. dissertation, University of Michigan, 2011.

[105] J. L. Lee, L. L. Aldrich, K. D. Stetzel, and G. L. Plett, "Extended operating range for reduced-order model of lithium-ion cells," *Journal of Power Sources*, vol. 255, pp. 85–100, jun 2014.

[106] M. P. Bonkile and V. Ramadesigan, "Power management control strategy using physics-based battery models in standalone PV-battery hybrid systems," *Journal of Energy Storage*, vol. 23, pp. 258–268, jun 2019.

[107] M. T. Lawder, B. Suthar, P. W. C. Northrop, S. De, C. M. Hoff, O. Leitermann, M. L. Crow, S. Santhanagopalan, and V. R. Subramanian, "Battery Energy Storage System (BESS)

and Battery Management System (BMS) for Grid-Scale Applications," *Proceedings of the IEEE*, vol. 102, no. 6, pp. 1014–1030, jun 2014.

[108] S. B. Lee, C. Pathak, V. Ramadesigan, W. Gao, and V. R. Subramanian, "Direct, Efficient, and Real-Time Simulation of Physics-Based Battery Models for Stand-Alone PV-Battery Microgrids," *Journal of The Electrochemical Society*, vol. 164, no. 11, pp. E3026–E3034, feb 2017.

[109] M. P. Bonkile, P. K. S, and V. Ramadesigan, "Simulation of standalone PV-battery systems using physics-based battery models," in *Computational Science Symposium, Department of Computational and Data Sciences (IISc)*, Banglore, India, 2017.

[110] M. P. Bonkile, S. Bandyopadhyay, and V. Ramadesigan, "Energy Storage Design Using Physics-Based Models in Standalone PV- Battery Hybrid Systems," in *Twelfth International Conference on Thermal Engineering: Theory and Applications*, Gandhinagar, India, 2019.

[111] S. Zhao, A. M. Bizeray, S. R. Duncan, and D. A. Howey, "Performance Evaluation Of An Extended Kalman Filter For State Estimation Of A Pseudo-2D Thermal-Electrochemical Lithium-Ion Battery Model," in *Proceedings of the ASME 2015 Dynamic Systems and Control Conference*, Ohio, USA, 2015, pp. 1–5.

[112] A. M. Bizeray, J.-H. Kim, S. R. Duncan, and D. A. Howey, "Identifiability and Parameter Estimation of the Single Particle Lithium-Ion Battery Model," in *UKACC 12th International Conference on Control*. Sheffield, UK: IEEE, sep 2018, p. 186.

[113] R. Drummond, A. M. Bizeray, D. A. Howey, and S. R. Duncan, "A Feedback Interpretation of the Doyle-Fuller-Newman Lithium-Ion Battery Model," *IEEE Transactions on Control Systems Technology*, pp. 1–12, 2019.

[114] A. M. Bizeray, J. Kim, S. R. Duncan, and D. A. Howey, "Identifiability and Parameter Estimation of the Single Particle Lithium-Ion Battery Model," *IEEE Transactions on Control Systems Technology*, vol. 27, no. 5, pp. 1862–1877, 2019.

[115] P. W. C. Northrop, B. Suthar, V. Ramadesigan, S. Santhanagopalan, R. D. Braatz, and V. R. Subramanian, "Efficient Simulation and Reformulation of Lithium-Ion Battery Models

for Enabling Electric Transportation," *Journal of The Electrochemical Society*, vol. 161, no. 8, pp. E3149–E3157, 2014.

[116] R. R. Jobman, "Identification of Lithium-Ion-Cell Physics-Model Parameter Values," Ph.D. dissertation, University of Colorado Colorado Springs (UCCS), 2016.

[117] K. D. Stetzel, "Model-Based Estimation of Battery Cell Internal Physical State," Ph.D. dissertation, University of Colorado Colorado Springs (UCCS), 2014.

[118] A. Rodríguez, "Improvements to fidelity, generation and implementation of physics-based lithium-ion reduced-order models," Ph.D. dissertation, University of Colorado Colorado Springs (UCCS), 2017.

[119] M. Ecker, T. K. D. Tran, P. Dechent, S. Kabitz, A. Warnecke, and D. U. Sauer, "Parameterization of a Physico-Chemical Model of a Lithium-Ion Battery: I. Determination of Parameters," *Journal of the Electrochemical Society*, vol. 162, no. 9, pp. A1836—-A1848, 2015.

[120] M. Ecker, S. Käbitz, I. Laresgoiti, and D. U. Sauer, "Parameterization of a Physico-Chemical Model of a Lithium-Ion Battery: II. Model Validation," *Journal of the Electrochemical Society*, vol. 162, no. 9, pp. A1849–A1857, 2015.

[121] L. Zhang, C. Lyu, G. Hinds, L. Wang, W. Luo, J. Zheng, and K. Ma, "Parameter Sensitivity Analysis of Cylindrical LiFePO4 Battery Performance Using Multi-Physics Modeling," *Journal of The Electrochemical Society*, vol. 161, no. 5, pp. A762–A776, mar 2014.

[122] B. Rajabloo, M. Désilets, and Y. Choquette, "Parameter Estimation of Single Particle Model Using COMSOL Multiphysics ® and MATLAB ® Optimization Toolbox," in *2015 COMSOL Conference*, Boston, 2015.

[123] Y. Li, C. Liao, L. Wang, L. Wang, and D. Xu, "Subspace-based modeling and parameter identification of lithium-ion batteries," *International Journal of Energy Research*, vol. 38, pp. 1024–1038, jun 2014.

[124] I. The MathWorks, "Matlab Optimization Toolbox Documentation."

[125] S. Santhanagopalan, Q. Guo, and R. E. White, "Parameter Estimation and Model Discrimination for a Lithium-Ion Cell," *Journal of The Electrochemical Society*, vol. 154, no. 3, pp. A198–A206, 2007.

[126] V. Boovaragavan, S. Harinipriya, and V. R. Subramanian, "Towards real-time (milliseconds) parameter estimation of lithium-ion batteries using reformulated physics-based models," *Journal of Power Sources*, vol. 183, pp. 361–365, aug 2008.

[127] T. Zhang, D. Li, Z. Tao, and J. Chen, "Understanding electrode materials of rechargeable lithium batteries via DFT calculations," *Progress in Natural Science: Materials International*, vol. 23, no. 3, pp. 256–272, 2013.

[128] J. C. Forman, S. J. Moura, J. L. Stein, and H. K. Fathy, "Genetic Parameter Identification of the Doyle-Fuller-Newman Model from Experimental cycling of a LiFePO4 Battery," in *2011 American Control Conference*, San Francisco, CA, USA, 2011.

[129] ——, "Genetic identification and fisher identifiability analysis of the Doyle-Fuller-Newman model from experimental cycling of a LiFePO 4 cell," *Journal of Power Sources*, vol. 210, pp. 263–275, jul 2012.

[130] A. Jokar, B. Rajabloo, M. Désilets, and M. Lacroix, "An Inverse Method for Estimating the Electrochemical Parameters of Lithium-Ion Batteries I. Methodology," *Journal of The Electrochemical Society*, vol. 163, no. 14, pp. A2876–A2886, 2016.

[131] B. Rajabloo, A. Jokar, M. Désilets, and M. Lacroix, "An Inverse Method for Estimating the Electrochemical Parameters of Lithium-Ion Batteries II: Implementation," *Journal of The Electrochemical Society*, vol. 164, no. 2, pp. A99–A105, 2017.

[132] A. Jokar, M. Désilets, M. Lacroix, and K. Zaghib, "Mesoscopic modeling and parameter estimation of a lithium-ion battery based on LiFePO4/graphite," *Journal of Power Sources*, vol. 379, pp. 84–90, 2018.

[133] V. Ramadesigan, K. Chen, N. a. Burns, V. Boovaragavan, R. D. Braatz, and V. R. Subramanian, "Parameter Estimation and Capacity Fade Analysis of Lithium-Ion Batteries Using Reformulated Models," *Journal of The Electrochemical Society*, vol. 158, no. 9, pp. A1048–A1054, 2011.

[134] M. A. Rahman, S. Anwar, and A. Izadian, "Electrochemical model parameter identification of a lithium-ion battery using particle swarm optimization method," *Journal of Power Sources*, vol. 307, pp. 86–97, 2016.

[135] S. Santhanagopalan, Q. Zhang, K. Kumaresan, and R. E. White, "Parameter Estimation and Life Modeling of Lithium-Ion Cells," *Journal of The Electrochemical Society*, vol. 155, no. 4, pp. A345–A353, 2008.

[136] J. Vazquez-Arenas, L. E. Gimenez, M. Fowler, T. Han, and S.-K. Chen, "A rapid estimation and sensitivity analysis of parameters describing the behavior of commercial Li-ion batteries including thermal analysis," *Energy Conversion and Management*, vol. 87, pp. 472–482, 2014.

[137] R. Masoudi, T. Uchida, and J. McPhee, "Parameter estimation of an electrochemistry-based lithium-ion battery model," *Journal of Power Sources*, vol. 291, pp. 215–224, 2015.

[138] Z. Deng, H. Deng, L. Yang, Y. Cai, and X. Zhao, "Implementation of reduced-order physics-based model and multi-parameters identification strategy for lithium-ion battery," *Energy*, vol. 138, pp. 509–519, 2017.

[139] T. Ashwin, A. McGordon, W. Widanage, and P. Jennings, "Modified electrochemical parameter estimation of NCR18650BD battery using implicit finite volume method," *Journal of Power Sources*, vol. 341, pp. 387–395, 2017.

[140] X. Yang, L. Chen, X. Xu, W. Wang, Q. Xu, Y. Lin, and Z. Zhou, "Parameter identification of electrochemical model for vehicular lithium-ion battery based on particle swarm optimization," *Energies*, vol. 10, no. 1811, 2017.

[141] S. Park, D. Kato, Z. Gima, R. Klein, and S. Moura, "Optimal Experimental Design for Parameterization of an Electrochemical Lithium-Ion Battery Model," *Journal ofThe Electrochemical Society*, vol. 165, no. 7, pp. A1309–A1323, 2018.

[142] A. P. Schmidt, M. Bitzer, Á. W. Imre, and L. Guzzella, "Experiment-driven electrochemical modeling and systematic parameterization for a lithium-ion battery cell," *Journal of Power Sources*, vol. 195, pp. 5071–5080, aug 2010.

[143] Y. Ye, Y. Shi, N. Cai, J. Lee, and X. He, "Electro-thermal modeling and experimental validation for lithium ion battery," *Journal of Power Sources*, vol. 199, pp. 227–238, feb 2012.

[144] J. Marcicki, M. Canova, A. T. Conlisk, and G. Rizzoni, "Design and parametrization analysis of a reduced-order electrochemical model of graphite/LiFePO4 cells for SOC/SOH estimation," *Journal of Power Sources*, vol. 237, pp. 310–324, 2013.

[145] S. Park, D. Kato, Z. Gima, R. Klein, and S. Moura, "Optimal Input Design for Parameter Identification in an Electrochemical Li-ion Battery Model," in *Annual American Control Conference (ACC)*, 2018.

[146] E. Namor, D. Torregrossa, R. Cherkaoui, and M. Paolone, "Parameter identification of a lithium-ion cell single-particle model through non-invasive testing," *Journal of Energy Storage*, vol. 12, pp. 138–148, 2017.

[147] J. Li, L. Wang, C. Lyu, E. Liu, Y. Xing, and M. Pecht, "A parameter estimation method for a simplified electrochemical model for Li-ion batteries," *Electrochimica Acta*, vol. 275, pp. 50–58, 2018.

[148] L. Zhang, L. Wang, G. Hinds, C. Lyu, J. Zheng, and J. Li, "Multi-objective optimization of lithium-ion battery model using genetic algorithm approach," *Journal of Power Sources*, vol. 270, pp. 367–378, 2014.

[149] L. Zhang, C. Lyu, L. Wang, W. Luo, and K. Ma, "Thermal-Electrochemical Modeling and Parameter Sensitivity Analysis of Lithium-ion Battery," *Chemical Engineering Transactions*, vol. 33, pp. 943–948, 2013.

[150] C. Edouard, M. Petit, C. Forgez, J. Bernard, and R. Revel, "Parameter sensitivity analysis of a simplified electrochemical and thermal model for Li-ion batteries aging," *Journal of Power Sources*, vol. 325, pp. 482–494, 2016.

[151] A. Falconi, "Electrochemical Li-Ion battery modeling for electric vehicles," Ph.D. dissertation, Universite Grenoble Alpes, 2018.

[152] M. Doyle and Y. Fuentes, "Computer Simulations of a Lithium-Ion Polymer Battery and Implications for Higher Capacity Next-Generation Battery Designs," *Journal of The Electrochemical Society*, vol. 150, no. 6, pp. A706–A713, jun 2003.

[153] W. Fang, O. J. Kwon, and C.-Y. Wang, "Electrochemical-thermal modeling of automotive Li-ion batteries and experimental validation using a three-electrode cell," *International Journal of Energy Research*, vol. 34, pp. 107–115, 2010.

[154] E. Prada, D. Di Domenico, Y. Creff, J. Bernard, V. Sauvant-Moynot, and F. Huet, "Simplified Electrochemical and Thermal Model of LiFePO4-Graphite Li-Ion Batteries for Fast Charge Applications," *Journal of The Electrochemical Society*, vol. 159, no. 9, pp. A1508–A1519, 2012.

[155] M. Safari and C. Delacourt, "Modeling of a Commercial Graphite/LiFePO4 Cell," *Journal of The Electrochemical Society*, vol. 158, no. 5, pp. A562–A571, 2011.

[156] M. Doyle, J. Newman, A. S. Gozdz, C. N. Schmutz, and J.-M. Tarascon, "Comparison of Modeling Predictions with Experimental Data from Plastic Lithium Ion Cells," *Journal of Electrochemical Society*, vol. 143, no. 6, pp. 1890–1903, 1996.

[157] J. Schmalstieg, C. Rahe, M. Ecker, and D. U. Sauer, "Full Cell Parameterization of a High-Power Lithium-Ion Battery for a Physico-Chemical Model: Part I. Physical and Electrochemical Parameters," *Journal of The Electrochemical Society*, vol. 165, no. 16, pp. A3799–A3810, 2018.

[158] J. Schmalstieg and D. U. Sauer, "Full Cell Parameterization of a High-Power Lithium-Ion Battery for a Physico-Chemical Model: Part II. Thermal Parameters and Validation," *Journal of The Electrochemical Society*, vol. 165, no. 16, pp. A3811–A3819, 2018.

[159] M. Doyle and J. Newman, "The use of mathematical modeling in the design of lithium/polymer battery systems," *Electrochimica Acta*, vol. 40, no. 13-14, pp. 2191–2196, 1995.

[160] A. Kwade and W. Haselrieder, "Effect of Electrode and Cell Production Steps on Lithium-Ion Battery Cell Performance and Costs," in *AABC Europe*, 2017.

[161] T. Waldmann, A. Iturrondobeitia, M. Kasper, N. Ghanbari, F. Aguesse, E. Bekaert, L. Daniel, S. Genies, I. Jiménez Gordon, M. W. Löble, E. De Vito, and M. Wohlfahrt-Mehrens, "Review - Post-Mortem Analysis of Aged Lithium-Ion Batteries: Disassembly Methodology and Physico-Chemical Analysis Techniques," *Journal of The Electrochemical Society*, vol. 163, no. 10, pp. A2149–A2164, 2016.

[162] T. G. Zavalis, "Mathematical Models for Investigation of Performance , Safety , and Aging in Lithium- Ion Batteries," Ph.D. dissertation, School of Chemical Science and Engineering, 2013.

[163] M. Ebner and V. Wood, "Tool for Tortuosity Estimation in Lithium Ion Battery Porous Electrodes," *Journal ofThe Electrochemical Society*, vol. 162, no. 2, pp. A3064–A3070, 2015.

[164] M. Park, X. Zhang, M. Chung, G. B. Less, and A. M. Sastry, "A review of conduction phenomena in Li-ion batteries," *Journal of Power Sources*, vol. 195, pp. 7904–7929, 2010.

[165] Y.-H. Chen, C.-W. Wang, X. Zhang, and A. M. Sastry, "Porous cathode optimization for lithium cells : Ionic and electronic conductivity , capacity , and selection of materials," *Journal of Power Sources journal*, vol. 195, pp. 2851–2862, 2010.

[166] C. W. Wang, A. M. Sastry, K. A. Striebel, and K. Zaghib, "Extraction of Layerwise Conductivities in Carbon-Enhanced, Multilayered LiFePO4 Cathodes," *Journal ofThe Electrochemical Society*, vol. 152, no. 5, pp. A1001–A1010, 2005.

[167] Y. Li and Y. Han, "Power electronics integration on battery cells," in *2014 IEEE Applied Power Electronics Conference and Exposition - APEC 2014*, vol. 2, 2014, pp. 3318–3322.

[168] C. R. Birkl, D. F. Frost, A. M. Bizeray, R. R. Richardson, and D. A. Howey, "Modular Converter System for Low-cost Off-grid Energy Storage Using Second Life Li-ion Batteries," in *Global Humanitarian Technology Conference (GHTC), IEEE*, 2014.

[169] M. M. U. Rehman, M. Evzelman, K. Hathaway, R. Zane, G. L. Plett, K. Smith, E. Wood, and D. Maksimovic, "Modular approach for continuous cell-level balancing to improve performance of large battery packs," in *2014 IEEE Energy Conversion Congress and Exposition (ECCE)*, Pittsburgh, PA, USA, 2014.

[170] I. Aizpuru Larrañaga, "Energy efficiency improvement of Li-ion battery packs via balancing techniques," Ph.D. dissertation, Mondragon Unibertsitatea, 2015.

[171] N. Mukherjee, "Distributed Control Structures and their Comparison in Cascaded Hybrid Battery Energy Storage Systems," in *2015 50th International Universities Power Engineering Conference (UPEC)*, 2015.

[172] M. A. V. Nilanjan Mukherjee, Dani Strickland, "Adaptive Control of Hybrid Battery Energy Storage Systems under Capacity Fade," *Journal of European Power Electronics and Drives (EPE)*, vol. 25, no. 4, pp. 25–33, 2014.

[173] F. Helling, J. Glück, A. Singer, and T. Weyh, "Modular Multilevel Battery (M2B) for Electric Vehicles," in *EPE'16 ECCE Europe*, 2016.

[174] Y. Li and Y. Han, "Control of Input-Series and Output-Independent Power Converter Building Block System Based on Buck Converter Topology," in *2015 IEEE Applied Power Electronics Conference and Exposition (APEC)*, Charlotte, NC, USA, 2015.

[175] ——, "Evaluation of a Module-Integrated Distributed Battery Energy Storage System," in *2015 IEEE Energy Conversion Congress and Exposition (ECCE)*, Montreal, QC, Canada, 2015.

[176] R. Taylor and W. Liu, "Phase Shifting Optimizes Multistage Buck Converters," pp. 1–31, 2007.